Andraž Kocjan

HYDROGEN ABSORPTION IN Ti-Zr-Ni ALLOYS

Doctoral Dissertation

ABSORPCIJA VODIKA V ZLITINAH Ti-Zr-Ni

Doktorska disertacija

Supervisor: Prof. dr. Spomenka Kobe

Co-Supervisor: Dr. Paul J. McGuiness

June 2009

MEDNARODNA PODIPLOMSKA ŠOLA JOŽEFA STEFANA
JOŽEF STEFAN INTERNATIONAL POSTGRADUATE SCHOOL
Ljubljana, Slovenia

Index

1 Introduction 2
1.1 Quasicrystals 3
1.1.1 Ti-Zr-Ni quasicrystals 4
1.1.2 Cell parameter calculation 9
1.2 Metallic glasses 12
1.3 Crystalline phases 13
1.3.1 C14 Laves phase 13
1.4 Hydrogen absorption 14
1.4.1 Hydrogen storage 14
1.4.2 Hydrogen in Ti-Zr-Ni quasicrystals 15

2 Materials and methods 18
2.1 Preparation 18
2.1.1 Mechanical alloying 18
2.1.1.1 Introduction 18
2.1.1.2 Experimental overview 19
2.1.1.3 Mechanical alloying in a hydrogen atmosphere 19
2.1.2 Melt spinning 19
2.1.2.1 Introduction 19
2.1.2.2 Experimental overview 20
2.1.2.2.1 Melt-Spinner Edmund Bühler GmbH 21
2.1.3 Hydriding 22
2.1.3.1 Introduction 22
2.1.3.1.1 Sievert's apparatus 22
2.1.3.2 Hydrogenation of ball-milled powders 23
2.1.3.3 Hydrogenation of melt spun-ribbons 23
2.1.3.4 Dehydrogenation of melt-spun ribbons 23
2.1.3.5 Deuterization of melt-spun ribbons 23
2.1.4 Arc-melting 24
2.1.5 Quenched rods 25
2.2 Characterization 25
2.2.1 X-Ray Diffraction (XRD) 25
2.2.2 X-ray Photoelectron Spectroscopy (XPS) 26
2.2.3 Scanning Electron Microscopy (SEM) 26
2.2.4 Transmission Electron Microscopy (TEM) 27
2.2.5 Differential Scanning Calorimetry (DSC) 28
2.2.6 Thermo-gravimetry (TG) 29
2.2.7 Mass spectrometry (MS) 29
2.2.8 Vibrating-Sample Magnetometer (VSM) 29
2.2.9 Superconducting Quantum Interference Device (SQUID) 30
2.2.10 ^{2}H NMR 31
2.2.10.1 Dynamic NMR lineshape 31
2.2.10.2 NMR spin-lattice relaxation 31
2.2.11 Density measurement 31

3 Results 32
3.1 Mechanical alloying 32

3.1.1 X-ray diffraction 32
3.1.2 SEM and EDS analysis 33
3.1.3 DSC measurements 34
3.1.3.1 Activation energy of crystallization 35
3.1.4 Magnetic measurements 37
3.1.5 Heat treatment 38
3.1.6 Mechanical alloying in hydrogen atmosphere 39
3.2 Melt spinning 40
3.2.1 Wheel speed effect 40
3.2.2 Composition effect on the structure and the cell parameters 42
3.2.2.1 Copper addition effect 43
3.2.3 SEM analysis 44
3.2.4 TEM analysis 46
3.2.4.1 Quasicrystalline sample 46
3.2.4.2 Crystalline sample 47
3.2.5 Crucible effect 48
3.2.6 XPS analysis 49
3.2.7 SQUID measurements 53
3.3 Hydriding 54
3.3.1 Thermogravimetry of desorbed hydrogen 54
3.3.2 Mass spectrometry of desorbed hydrogen 55
3.3.2.1 Hydrogen in the i-phase 57
3.3.2.2 Hydrogen in the amorphous phase 59
3.3.2.3 Hydrogen in crystalline phases 61
3.3.2.4 Partial dehydrogenation of i-phase 62
3.3.2.5 Low pressure hydrogenation of ribbons 63
3.3.2.6 Hydrogen induced i-phase formation 65
3.3.2.7 Dehydrogenation of powders mechanically alloyed in hydrogen 66
3.3.3 Hydrogen effect on the magnetization 67
3.3.3.1 I-phase 67
3.3.3.2 Amorphous phase 69
3.3.3.3 Crystalline phases 70
3.3.4 ^{2}H NMR study 70
3.3.5 Hydriding of quenched rods 73
3.4 Quenched rods 75
3.4.1 X-ray diffraction 75
3.4.2 SEM/EDS analysis 77
3.4.3 VSM results 80
3.5 Arc-melting 81
3.5.1 X-ray diffraction of cross-section 81
3.5.2 SEM/EDS analysis 82
3.5.3 VSM results 83
3.5.4 Density measurements 84

4 Discussion 85
4.1 Mechanical alloying 85
4.2 Melt spinning 85
4.3 Hydriding 86
4.4 Quenched rods 87
4.5 Arc-melting 88

5 Conclusions 89

6 Acknowledgements 90

7 References 92
Bibliography 103

Abstract

Our research focused on the formation of $Ti_{40}Zr_{40-x}Ni_{20}Cu_x$ (x=3, 5), $Ti_{45}Zr_{38-x}Ni_{17}Cu_x$ (x=3, 5), $Ti_{53}Zr_{27-x}Ni_{20}Cu_x$ (x=3, 5) and $Ti_{58}Zr_{24-x}Ni_{18}Cu_x$ (x=3, 5) icosahedral (i-phase) quasicrystals by three different techniques and their subsequent characterization and high-pressure hydrogenation. The quasicrystals of this system are thermodynamically stable and they have a relatively good affinity for hydrogen absorption. The aim of this research was to study the influence of processing parameters on the structure, morphology and magnetic properties of the material, before and after hydrogen absorption. With a thermogravimeter and an attached mass-spectrometer we studied the weight percent of desorbed hydrogen and the distribution of desorption temperatures, which gave us an insight into the hydrogen bonding energies (sites) in the material, depending on the structure, composition and hydrogen content.

The icosahedral samples were produced by high-energy planetary ball-milling with subsequent annealing at temperatures around 500°C in vacuum. The temperatures and activation energies of crystallization were measured by differential scanning calorimetry (DSC) and calculated using the Kissinger equation, respectively. A strong decrease of the magnetization during the mechanical alloying was observed due to a modification of the nickel d-states. Scanning electron microscopy (SEM) revealed the formation of non-homogeneous agglomerates during the mechanical treatment, with an average size of 100 μm.

For the preparation of alloys with different structures, from crystalline, quasicrystalline and amorphous, we used the melt-spinning technique. First, the process parameters, i.e., pressure, temperature, distance between nozzle and cooling wheel, rotation speed, material and the geometry of the crucible, had to be optimized. We studied the dependence of the ribbons' thickness, structure and magnetic properties on the cooling-wheel speed. As expected, the thickness of the ribbons decreases, from about 120 μm at a surface speed of 12 m/s to 30 μm at speeds above 40 m/s. Also, at low wheel speeds mainly the hexagonal C14 Laves phase and cubic solid solution of titanium and zirconium are formed, at middle speeds the icosahedral quasicrystalline phase is formed, whereas at speeds above 35 m/s we get fully amorphous ribbons. Regardless of the effect of rotation frequency on the structure, the magnetization (at 1 Tesla) is constant, within the experimental uncertainty. A linear decrease of quasi-lattice cell parameter due to higher amounts of titanium and copper instead of zirconium was observed. Using transmission electron microscopy (TEM) we confirmed that the ribbons (spun at 22 m/s) contain grains of icosahedral phase imbedded in an amorphous matrix with the same composition. The average particle size of the i-phase on the wheel side of the ribbon was approximately 50 nm, whereas on the argon side the maximum grain size was up to 500 nm. The 5-fold symmetry (besides 3- and 2-fold) was confirmed by selected-area electron diffraction and high-resolution TEM, which is basic characteristic of icosahedral quasicrystals. X-ray photoelectron spectroscopy (XPS) analysis showed that the thickness of an (zirconium and titanium) oxide layer on the surface of the ribbons was around 7 nm. Using temperature and loading time we have a rough influence on the extent of hydrogen in the sample, where hydrogen in the i-phase was determined from the shift in the XRD peaks and the linear dependence between the [H]/[M] ratio and the quasi-lattice constant a_q. To measure the overall amount (wt. %) of hydrogen desorbed and to obtain the hydrogen bonding sites distribution thermo-gravimetry (TG) with an attached mass-spectrometer of these materials has been applied. We also studied how the loaded hydrogen affects the magnetic properties of these alloys.

At the end we did a series of vacuum-casting experiments with different sizes of copper cold molds, 3, 2 and 1.5 mm, for samples with the same compositions we used for the melt-spinning. Three milimetre quenched rods of various compositions were hydrided and studied by vibrating sample magnetometer (VSM) to see how the magnetic properties are affected by the absorbed hydrogen. Also, we compared the mass-spectra of hydrogen from the quenched rods with those from the melt-spun ribbons to see how the cooling regime affects the hydrogen-bonding energy distribution.

Povzetek

Delo v sklopu te doktorske disertacije je obsegalo raziskave zlitin na osnovi elementov titana, cirkonija, hafnija, niklja in bakra kot dopanta, s sledečimi sestavami: $Ti_{40}Zr_{40-x}Ni_{20}Cu_x$ (x=3, 5), $Ti_{45}Zr_{38-x}Ni_{17}Cu_x$ (x=3, 5), $Ti_{53}Zr_{27-x}Ni_{20}Cu_x$ (x=3, 5) in $Ti_{58}Zr_{24-x}Ni_{18}Cu_x$ (x=3, 5). Študirali smo različne tehnike za pripravo t.i. ikozaedrične kvazikristalne faze (i-faza), ki je za razliko od ostalih kvazikristalov termodinamsko stabilna in kaže relativno dobro afiniteto za absorpcijo vodika. Namen te disertacije je razkriti vpliv različnih procesnih parametrov na strukturo, morfologijo in magnetne lastnosti materiala, pred in po absorpciji vodika. Z metodo termo-gravimetrije s pripetim masnim spektrometrom preučevali masni delež desorbiranega vodika in odvisnost temperatur desorpcije oz. vezavnih energij vodika od strukture in sestave materiala ter deleža vodika.

V prvem sklopu raziskovalnega dela smo se ukvarjali z mehanskim litjem elementarnih prahov v visoko-energijskem planetarnem mlinu, kjer smo z metodo rentgenske difrakcije opazovali hitrost nastajanja amorfne faze, iz katere smo po termični obdelavi pri temperaturi 500°C dobili i-fazo. Z DSC metodo smo prej določili temperaturo kristalizacije in s pomočjo Kissingerjeve enačbe tudi izračunali aktivacijsko energijo le-te. Opazili smo zmanjšanje magnetizacije po mehanski obdelavi, kar gre pripisati izraziti modifikaciji nikljevih d-stanj. Vrstična elektronska mikroskopja je razkrila, da med mletjem nastajajo aglomerati, katerih povpreča velikost je bila 100 μm, njihova sestava pa nehomogena, saj je notranjost aglomeratov bogata s cirkonijem.

Za pripravo i-faze, pa tudi amorfne in kristalne, smo uporabili tudi ultra-hitro ohlajevanje taline s t.i. rotacijskim kaljenjem (ang. »melt-spinning«). Sprva smo morali optimizirati obratovalne parametre: temperaturo, tlak, razdaljo med šobo in hladilnim valjem, hitrost vrtenja le-tega ter material in geometrijo talilnega lončka. S to tehniko priprave smo študirali vpliv hitrosti hladilnega valja na debelino, strukturo in magnetne lastnosti tako dobljenih trakov. Kot smo pričakovali se debelina trakov zmanjša, in sicer z okoli 120 μm pri obodni hitrosti 12 m/s na 30 μm pri hitrostih nad 40 m/s. Prav tako lahko s frekvenco rotacije kontroliramo strukturo materiala; od heksagonalne C14 Lavesove in kubične trdne raztopine titana in cirkonija, preko ikozaedrične kvazikristalne faze pri srednjih hitrostih, do popolnoma amorfne faze pri hitrostih nad 35 m/s. Ne glede na to, da se struktura spreminja s frekvenco rotacije, pa je magnetizacija, merjena pri gostoti zunanjega polja 1 Tesla, konstanta v okviru eksperimentalne napake. Opazili smo tudi linearno manjšanje konstante kvazikristalne rešetke z večanjem deleža titana in bakra. S transmisijsko elektronsko mikroskopijo smo pokazali, da trakovi (pripravljeni pri 22 m/s) vsebujejo zrna ikozaedrične faze v amorfni matrici enake sestave. Povprečna velikost zrn i-faze v traku na strani hladilnega valja je okoli 50 nm, medtem ko je velikost zrn na strani argona kar desetkrat večja, torej 500 nm. Z elektronsko difrakcijo izbranega področja (SAED) in visoko-ločljivostno transmisijsko elektronsko mikroskopijo (HRTEM) smo neposredno potrdili obstoj 5-števne simetrije (poleg 3- in 2-števne) v materialu, ki je značilna za ikozaedrične kvazikristale. XPS analiza je pokazala, da je debelina (cirkonijeve in titanove) oksidne plasti na površini trakov okoli 7 nm. S temperaturo in časom lahko grobo kontroliramo delež absorbiranega vodika, ki ga za i-fazo izračunamo iz premika rentgenskih uklonov in linearne odvisnosti med razmerjem [H]/[M] in kvazi-mrežne konstante a_q. S termogravimetrom (TG) s pripetim masnim spektrometrom je bilo mogoče določiti celokupno količino desorbiranega vodika (utežni delež) in porazdelitev vezavnih mest vodika. Študirali smo tudi vpliv vodika na magnetne lastnosti teh zlitin.

Na koncu smo opravili še serijo poskusov vakuumskega kaljenja z bakrenimi modeli, pri čemer smo dobili vzorce paličastih oblik različnih premerov; in sicer 3, 2 in 1.5 mm, z enakimi sestavami kot smo jih uporabili za ultra-hitro rotirajoče kaljenje. Vzorce premera 3 mm različnih sestav smo navodičili ter študirali vpliv navodičenja na magnetne lastnosti, z masno spektrometrijo pa preverili vpliv načina kaljenja na porazdelitev vodikovih vezavnih energij, v primerjavi z masnimi spektri vodika iz trakov.

Abbreviations

BCC	=	body-centered cubic
BMG	=	bulk metallic glasses
BSE	=	back-scattered electrons
CCD	=	charge-coupled device
DOE	=	Department of Energy
DOS	=	density of states
DSC	=	differential scanning calorimetry
DTA	=	differential thermal analysis
EDS	=	energy dispersive spectroscopy
EFG	=	electric field gradient
e.g.	=	for example
ESCA	=	electron spectroscopy for chemical analysis
et al.	=	and co-workers
FCC	=	face-centered cubic
FFT	=	fast Fourier transformation
FWHM	=	full width at half-maximum
GFA	=	glass-forming ability
HRTEM	=	high-resolution transmission electron microscopy
HT	=	heat treatment
i.e.	=	that is
JJ	=	Josephson junction
JSI	=	Jožef Stefan Institute
MA	=	mechanical alloying
NMR	=	nuclear magnetic resonance
PEM	=	proton-exchange membrane
RF	=	radio-frequency
rpm	=	revolutions per minute
SAED	=	selected-area electron diffraction
SEM	=	scanning electron microscopy/microscope
SEI	=	secondary-electron imaging
SQUID	=	superconducting quantum interference device
TEM	=	transmission electron microscopy/microscope
TG	=	thermo-gravimetry
TTT	=	temperature-time-transformation
VSM	=	vibrating-sample magnetometer
XPS	=	X-ray photoelectron spectroscopy
XRD	=	X-ray diffraction
WD	=	working distance

1 Introduction

As we know, matter can exist in four states, i.e. solid, liquid, gas and plasma, depending on its free energy. Since this energy tends to spontaneously minimize, plasma turns into gas by cooling, gas condenses into liquid and by further cooling liquid solidifyies into solid matter, which is the ground state of every known element or compound at absolute zero. In this thesis we will focus on the last mentioned transition, namely liquid-solid. At this transition atoms often tend to form crystal structures, since the free energy of crystals is often lower than of disordered matter. Depending on the cooling rate by which the liquid condenses into the solid state, one can get different crystallographic modifications. For instance, all metals form crystallites upon cooling. If we have multiple phase system, one must set the proper cooling rate to get the majority of the desired phase, according to phase diagram of this system. To grow phases with lower free energies, one must apply lower cooling rates, and vice versa. Beside free energy, nucleation rate of single phases affects the final microstructure of the material as well. If we increase the cooling rate to the point of undercooling, we end up with amorphous or so-called glassy materials, where atoms are in positions as they were in the liquid state. This is done by rapid quenching, where cooling rates are much higher than the crystal growth and even nucleation. Some materials exist only in this modification (glass) or have higher so-called glass forming ability (GFA), which means that the cooling rate can be much lower to achieve the amorphous modification. This class of materials belong to, normally, ternary alloys and are known as bulk metallic glasses (BMG). Amorphous materials are metastable and thus crystallize at elevated temperatures. The third state of solid materials is quasicrystalline state, which is metastable modification between amorphous and crystalline modification, from free energy and crystallographic point of view. Namely, some ternary metallic systems form metastable phases upon proper cooling, which show 5-, 8-, 10- and 12-fold rotation symmetries, which were "forbidden" in classical crystallography until 1984, when this third, quasicrystalline state of matter was discovered.

Two dimensional patterns and crystals can be built up from a single unit of pattern called a basis, by repeated translations, due to two vector operators, known as unit vectors. Unit vectors outline a repeated area of a pattern called a unit cell. Repeated translations of unit vectors mark out a grid of identical points in space, called a lattice. The definition of a lattice is very important and is given as: a repeating pattern of points, each point having the same surroundings. The concept that patterns and crystals can be built by associating an identical basis in the same way with each point of a lattice is a feature of periodic or commensurate crystal structures. Such structures have no interstitials and have 2, 3, 4 and 6-fold rotational symmetries that are allowed in »classical« crystallography, see Figure 1.

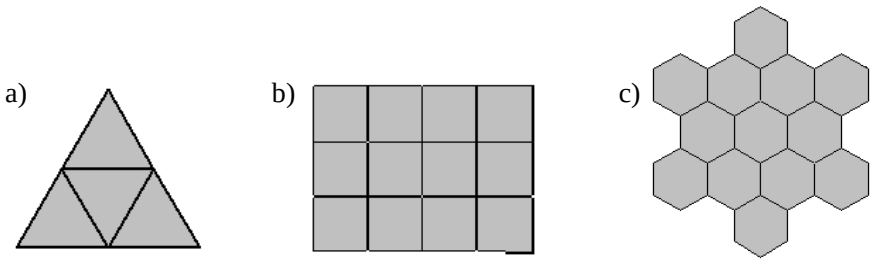

Figure 1: Schematic representation of a) 3-fold, b) 4-fold and c) 6-fold crystallographic symmetry.

On the other hand, quasicrystals show rotational and long-range translational symmetry only. Thus they possess so-called incommensurate periodicity, related to irrational number τ, golden section, which originates from five-fold geometry, shown in Figure 2. In many years of researching quasicrystals and complex metallic alloys in general, scientists have explained the metastability of these structures and found few cases of thermodynamically stable quasicrystals.

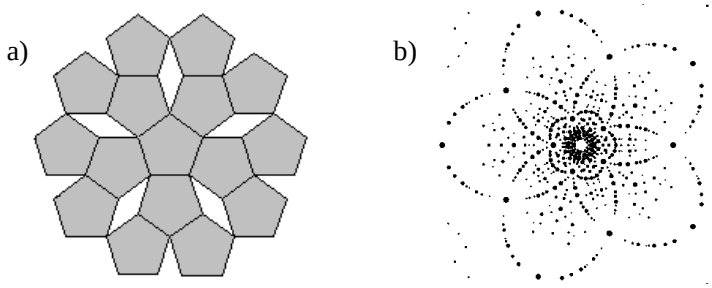

Figure 2: a) Illustration of »forbbiden« 5-fold symmetry shows that rhomboedral interstitials are formed while trying to fill 2D plane with regular pentagons, b) simulation for a Laue pattern (X-ray) from an icosahedral quasicrystal, whereby the X-ray beam is along one of the five-fold axes.

1.1 Quasicrystals

Since the discovery of Al-Mn quasicrystals by Dan Shechman in 1984, great interest in the examination and application of these materials has been shown. Namely, the revolution that followed, with its unavoidable and probably fruitful controversies, forced new progress in our understanding of the atomic arrangements in solids, since that order in condensed matter is not necessarily imposed by simple translation symmetry as was thought before. This revolutionary concept turned into a more general crystallography, which proves very useful nowadays to understand complex intermetallic systems comprising hundreds or thousands of atoms per unit cell. Quasicrystals are very interesting and comparatively new phase of solids, they possess strange and unique mechanical, physical and chemical properties, and what is the most important, from the crystallographic point of view, they show just long-range translational periodicity and "forbidden" 5-, 8-, 10- or 12-fold rotational symmetries, depending on the composition and the cluster type, respectively. The quasicrystalline state is a third form of solid matter beside the crystalline and the amorphous. Due to their position between the disordered and the crystalline systems, they show strict sphericity (clusters) as well as planarity, even though the aperiodic one. From quasiperiodicity, new localization properties of electrons and phonons were derived. Thermodynamically stable icosahedral (5-fold symmetry) alloys have been found in Al-Li-Cu (Ball et al., 1985), Al-Cu-Fe (Tsai et al., 1987), Ti-Zr-Ni (Viano et al., 1995), Zn-Mg-Dy (Sato et al., 1997) systems, etc. Today, some hundred quasicrystalline phases are known, some tens of which are stable and therewith candidates for single-quasicrystal growth approaches. Quasicrystals have high tensile strength and hardness, but they are brittle at room temperature. At elevated temperatures they become plastic. Semiconductor-like behaviour and low thermal conductivity is another interesting feature of quasicrystalline alloys, which makes them good candidates as thermo-power materials. From their complexity, a pseudo-gap near the Fermi level arises, which makes these materials stable and gives them unique electronic structures that cause other interesting physical properties, such as catalytic and bio-activity, low surface friction, etc.

The origin of the pseudo-gap at the Fermi level comes from two facts: first, is that the Fermi surface and the Jones zone coincide. This is well known Hume-Rothery matching rule (Mizutani et al., 2004), by which the stability of quasicrystals and complex metallic alloys is governed. This rule is denoted as $k_p \sim 2k_f$, where k_f is the momentum of electrons at the Fermi level, and k_p is the width of the predominant Brillouin zone. Among them, k_p can be defined experimentally by the X-ray diffraction technique based on an Equation 1,

$$k_p = 4\pi \sin\theta/\lambda \tag{1}$$

where λ is the wavelength of the XRD radiation and θ is the diffraction angle of the most intense diffraction peak. On the other hand, k_f can be calculated by the following expression,

$$k_f = (3\pi^2 N_v)^{1/3} \tag{2}$$

based on the nearly-free electron theory (Mizutani et al., 2004), where $N_v = (e/a)(N_0\rho/M)$, e/a is the number of valence electrons per number of atoms, N_0 is the Avogadro constant, ρ the mass density and M atomic weight of an alloy, respectively. By using the Hume-Rothery matching rule most of the complex metallic alloys and quasicrystals were discovered in the past 25 years.

Furthermore, partial 3p density of states (DOS) of aluminium alloys in crystal structures show no energy gap near the Fermi energy and thus these alloys possess metallic behaviour. But, if the structure

becomes quasicrystalline (of the same composition), the 3p density of states moves away from the Fermi level and pseudo-gap shows up, giving these materials semiconductor-like nature.

The second reason for pseudo-gap formation in quasicrystalline alloys is hybridization of sp-d electrons, moving valence d-states of transition metals from the Fermi surface. This phenomenom has an optimal effect on phase stability, since only the occupied states get shifted to lower energies, whereas those shifted to higher energies are empty. Subsequently, the total system tends to self-organize into the optimal state.

If we summarize the Hume-Rothery rule it says, the more complex the alloy is, the larger pseudo-gap it forms and thus the more stable the structure is (Poon, 1992, Stadnik, 1999). It is well known that the e/a-constant and e/a-variant lines are common features in quasicrystalline systems, and the ideal composition of quasicrystals in a given ternary system lies at the crossing point of these two lines. These lines constitute the empirical criteria to search for ideal ternary quasicrystals compositions, (Qiang, 2004).

One of the most interesting challenges in quasicrystal research has been the finding of connections among the unique structural and determined physical properties of these materials. Especially, substancial posibility existed that the non-periodicity of the atomic arrangement may influence the electronic and magnetic properties of quasicrystals. Gavilano et al., 2004, investigated magnetic susceptibilities $\chi(T)$ and electrical resistivities of well-characterized icosahedral and amorphous phases of $Al_{75}Cu_{15}V_{10}$ between 2 and 350 K. A temperature-independent Pauli-type susceptibility was observed for the icosahedral phase, above 100 K, whereas below 100 K it decreases with decreasing temperature, implying there is a small gap in the DOS at the Fermi level. The authors also revealed that the icosahedral structure does not favor the formation of localized V magnetic moments, since the χ of amorphous and icosahedral phases are different. On the other hand, no major changes in the electrical resistivities of those two phases were observed.

Furthermore, Chernikov et al., 1993, investigated quasicrystalline $Al_{70}Mn_9Pd_{21}$ and discovered only a very small fraction of the Mn ions participate in a spin glass transition. And yet more generally, several authors (Lasjaunias et al., 1995, Gavilano et al., 2002, Rau, 0304262) have reported in quasicrystalline Al-Pd-Mn alloys, only a very small fraction of the Mn ions are magnetic.

1.1.1 Ti-Zr-Ni quasicrystals

Among the many quasicrystals, the Ti-Zr-Ni alloy appears particularly interesting due to the formation of a stable and well-ordered icosahedral phase (Stroud et al., 1996, Kelton et al., 1997, Davis et al., 2000). Ti-Zr-Ni quasicrystals have been mainly prepared by rapid quenching, e.g. melt spinning (Kelton et al., 1997, Huttunen-Saarivirta, 2004, Dubois, 2000, Rud et al., 2005), or powder metallurgy, e.g. mechanical alloying (MA) with subsequent annealing (Konstanchuck, 2001, Takasaki, 2004).

In 2001 Konstanchuck et al. reported that the $Ti_{45}Zr_{38}Ni_{17}$ icosahedral phase can be formed directly by mechanical alloying at the acceleration of 400 ms^{-2}, where after 1 hour practically all XRD peaks of initial mixture of elements vanish, and only two very broad peaks of the icosahedral phase are observed. After 2 hours of MA i-phase peaks become more intense, even though they still remain broadened substantially. The heat-treatment of this sample in an inert atmosphere for 5 hours at 440 °C causes the narrowing of i-phase peaks.

Three years later, in 2004, Takasaki et al. reported observations that are in contrast to Konstanchuck's results. Namely, Takasaki performed mechanical alloying of the same material, i.e. $Ti_{45}Zr_{38}Ni_{17}$ and revealed the XRD peaks of elemental metals are dramatically decreased after MA for 2.5 hours, showing the elemental powders become alloyed at an early stage of MA. The same observation as Konstanchuck's only without any sign of broad i-phase diffraction peaks. Furthermore, Takasaki reported that amorphous state appears after MA for more than 7 hours. But what is more important and contradictory is his claim that the i-phase could not be formed directly by mechanical alloying, since dynamic force (mechanical collision) leads to chemical inhomogenity of the final products, making it difficult to produce a single quasicrystal phase powder. The only logical explanation for this discrepancy between the results obtained by these two authors are the experimental conditions of the mechanical treatment. Namely, Takasaki used ball-to-powder weight ratio 8:1 and acceleration 150 ms^{-2}, whereas Konstanchuck used ball mass to sample mass ratio 20:1 and acceleration of 400 ms^{-2}. Clearly, i-phase can be formed upon mechanical alloying, but only at more severe conditions.

In 2002 Kelton et al. constructed a cut of the Ti-Zr-Ni ternary phase diagram for equal Ti and Zr concentrations, Figure 3. The high temperature body-centered cubic (BCC) β-Ti/Zr solid solution phase (a= 0.343 nm for equal Ti:Zr content) is the primary solidification phase for alloys made with a low Ni content, since the solubility of nickel in Ti/Zr solid solutions is poor. Eutectic at [Ni] ~ 21 at. % has been revealed. For higher nickel contents, the polytetrahedral C14 Laves phase (hexagonal $P6_3/mmc$, a= 0.529 nm and c=

0.842 nm) is the primary solidification phase. At [Ni] ~ 17 at. %, i-phase is formed by a solid-state transformation from the hexagonal α-Ti/Zr solid solution ($P6_3/mmc$, a= 0.311 nm and c= 0.492 nm) and the C14 Laves phases at around 570°C, (Kelton and Gibbons, 1997).

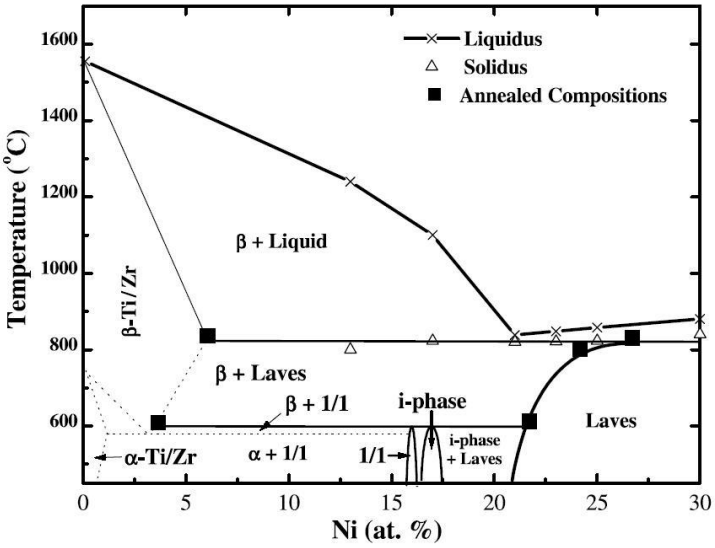

Figure 3: Schematic vertical section of Ti-Zr-Ni phase diagram along a line of equal Ti and Zr, showing the phases that form in equilibrium (Kelton et al., 2002).

Molokanov and Chebotnikov, 1990, have shown Ti-Zr-Ni i-phase is formed in the wide concentration interval by melt spinning, which is associated with a wide range of Laves phase existence, Figure 4. It appears that quasicrystalline phase is formed upon the interaction between C14 Laves phase and BCC β-(Ti/Zr) solid solution, since icosahedral coordination shells dominate in the structure of former one.

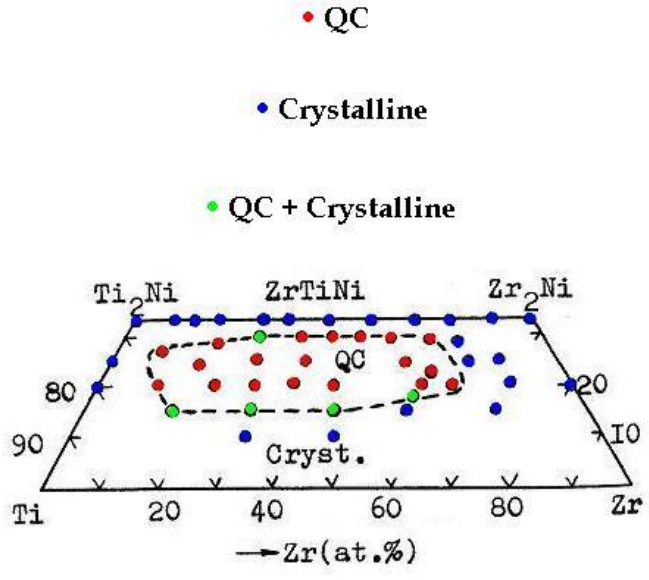

Figure 4: Compositional range for the formation of quasicrystalline phases in rapidly solidified Ti-Ti_2Ni-Zr_2Ni-Zr alloys is denoted by dash line, Molokanov and Chebotnikov, 1990.

Qiang et al., 2004, have reported they revealed a broad bulk-quasicrystal-forming region in Ti-Zr-Ni system as well, described by the general formula $(Ti_xZr_{100-x})_{100-y}Ni_y$ ($43.75 < x < 81.25$, y = 17, 20 at. %). Among these, $Ti_{40}Zr_{40}Ni_{20}$ is the optimal composition, where a nearly pure bulk quasicrystalline sample can be achieved, Figure 5. Also, the α- and β-(Ti/Zr) solid solution phases and/or C14-type Laves phase are found to coexist with the majority i-phase, though as minority phases, with a slight deviation from the ideal composition. Crystallographic data of Ti/Zr-rich phases in Ti-Zr-Ni alloy system are given in Table 1.

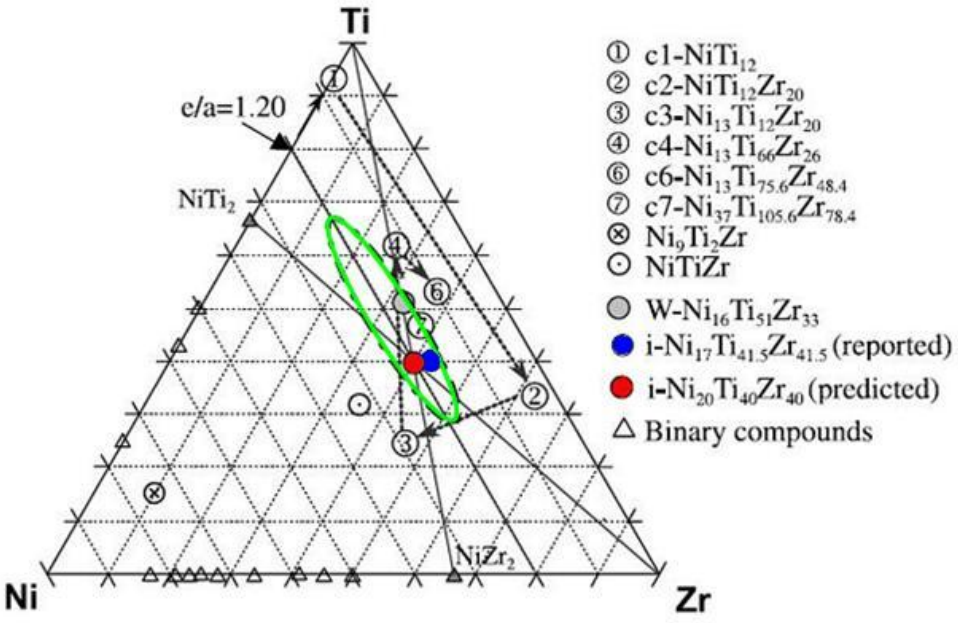

Figure 5: Ternary phase formation section for Ti-Zr-Ni alloys. Green line denotes the phase field of Ti-Zr-Ni quasicrystals revealed by Qiang et al., 2004. Their predicted ternary i-$Ti_{40}Zr_{40}Ni_{20}$ (red point), located at the crossing point of two e/a-variant lines Ti_2Ni-to-Zr and Zr_2Ni-to-Ti, is just slightly different from reported (Kelton et al., 2002) ternary quasicrystals composition i-$Ti_{41.5}Zr_{41.5}Ni_{17}$ (blue point).

Phase	Crystallographic data/nm		Compositions (at.%)
α-(Ti,Zr)	hP2, $P6_3/mmc$	α-(Ti): $a = 0.295$, $c = 0.468$	Ti_xZr_{100-x}
		α-(Zr): $a = 0.326$, $c = 0.515$	($x = 0$–100)
β-(Ti,Zr)	cI2, Im $\bar{3}$ m,	β-(Ti): $a = 0.3306$	Ti_xZr_{100-x}
		β-(Zr): $a = 0.3545$	($x = 0$–100)
Ti_2Ni	cF96, Fd $\bar{3}$ m, $a = 1.1278$		$Ti_{66.7}Ni_{33.7}$
Zr_2Ni	tI12, I4/mcm, (0.6477, 0.5243)		$Zr_{66.7}Ni_{33.7}$
1/1-W phase	cI162, Im $\bar{3}$, $a = 1.4317$		$Ti_{51}Zr_{33}Ni_{16}$
			$Ti_{44}Zr_{40}Ni_{16}$
C14-TiZrNi	hP12, $P6_3/mmc$,	$a = 0.5142$–0.5191	$(Ti_{100-x}Zr_x)_2Ni$
	$MgZn_2$ type	$c = 0.8433$–0.8520	($x = 21$–30)
B-IQC	Metastable icosahedral phase		Ti_2Ni
I phase	Low-temperature stable	$a_R = 0.512$	$Ti_{53}Zr_{27}Ni_{20}$
	Icosahedral	$a_R = 0.516$	$Ti_{45}Zr_{38}Ni_{17}$
			$Ti_{43}Zr_{40}Ni_{17}$
			$Ti_{41.5}Zr_{41.5}Ni_{17}$

Table 1: Crystallographic data of the reported Ti/Zr-rich phases in the Ti-Zr-Ni alloy system, (Qiang et al., 2004).

Icosahedral quasicrystals have large density of tetrahedrally coordinated interstitial sites, which are believed to be structurally favourable for hydrogen absorption and thus give these novel materials challenging opportunities from the technological point of view (Stroud et al., 1996, Takasaki et al., 2006). Since hydrogen atoms prefer sites close to hydrogen-friendly atoms like Ti and Zr, this suggests that the Ni–Ti–Zr icosahedral phase should be a good, relatively low-cost candidate for hydrogen-storage and hydrogen battery materials. Previous reports (Viano et al., 1998; Kelton and Gibbons, 1997) have described how Ti–Zr–Ni quasicrystals can absorb large amounts of hydrogen, equivalent to H/M value close to 1.7. This is significantly higher than the well-known value of H/M ≈ 1 for $LaNi_5$-type materials. However, hydrogen absorption from the gas phase in the Ni–Ti–Zr i-phase requires pressures of up to 40 bar and elevated temperatures to overcome the thin, surface-oxide barrier, which is inherent to the compounds in both the crystalline and quasicrystalline states (Viano et al., 1995, Kim et al., 1998).

Like in other quasicrystalline systems, Ti-Zr-Ni alloys can as well undergo phase transformations upon

thermal treatment, from amorphous with the highest free energy to quasicrystalline phase and finally crystalline, i.e. C14 Laves phase and α-(Ti, Zr) solid solution, with the lowest Gibbs free energy, Figure 6. With sufficient undercooling, metastable i(TiZrNi) nucleates in preference to a polytetrahedral C14 Laves phase, suggesting a local icosahedral order in the liquid. Namely, the fact that the formation of the i-phase is favored over even the polytetrahedral C14 phase is strong evidence for icosahedral order in these liquids.

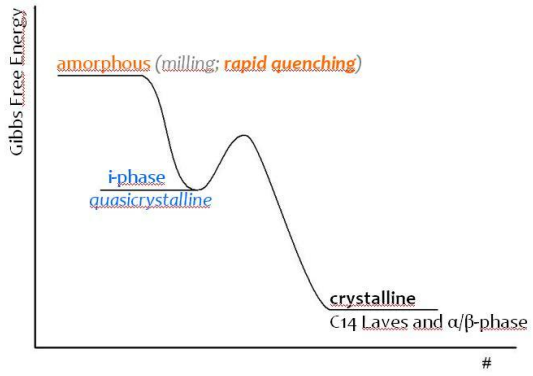

Figure 6: Thermodynamic stability of phases in Ti-Zr-Ni alloy system.

The earliest reports of copper-containing Ni–Ti–Zr alloys were by Wang et al. (Wang and Inoue, 2001) in 2001. They prepared amorphous alloys with 10 at. % Cu and crystallised them through multiple-step exothermic reactions. The metastable i-phase was found to be approximately 20 nm in size, and at higher temperatures this phase decomposed into stable crystalline phases. In 2002 the same group reported on melt-spun $Ti_{60}Zr_{15}Ni_{15}Cu_{10}$ (Wang et al., 2002). They found that with low wheel speeds of 10 m/s stable α-Ti/Zr, Ti_2Ni and Ti_2Cu phases were formed, at 15–20 m/s an i-phase was formed directly, and at higher speeds the ribbons consisted of a mixture of i-phase and increasing amounts of amorphous phase. In 2003 the group expanded their investigations to look at a range of copper-containing alloys $Ti_{45}Zr_{35}Ni_{20-x}Cu_x$ (x= 0, 1, 3, 5 and 7) produced by melt spinning (Wang et al., 2003a). They reported that the formation of the i-phase, Laves phases and the amorphous phase depended on the thickness of the ribbons, i.e. the cooling wheel speed, Figure 7.

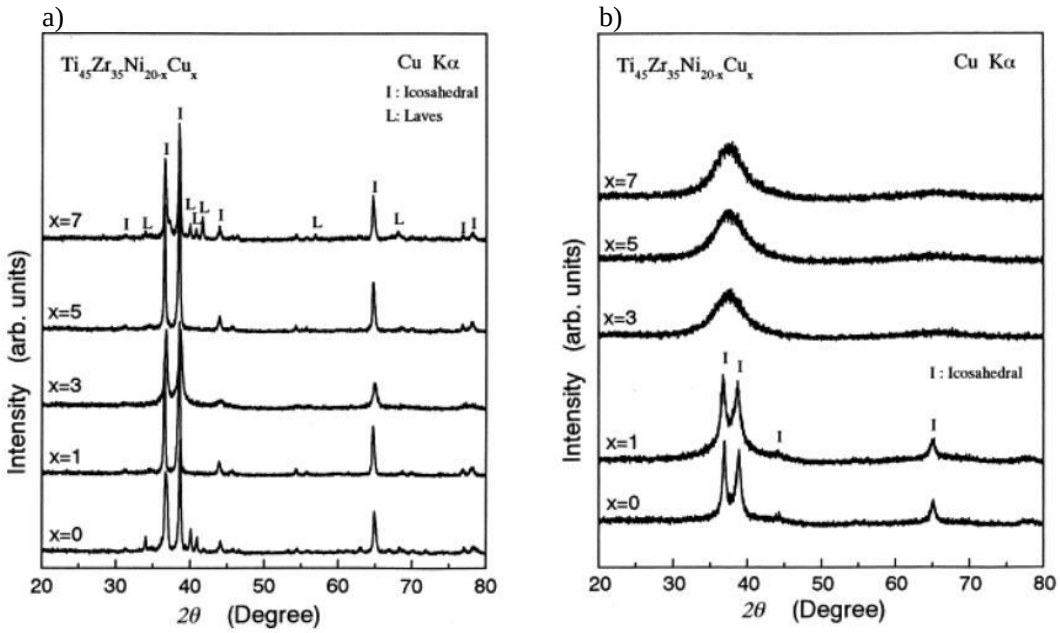

Figure 7: XRD patterns of $Ti_{45}Zr_{35}Ni_{17}Cu_3$ ribbons, melt-spun at a) 10 m/s (86 ± 5 μm thick), and b) 35 m/s (20 ± 2 μm thick); Wang et al. 2003a.

They also reported that the cooling rate, i.e. the diameter of the cooling copper cold mould, has a strong influence on the phases formed in cast rods, Figure 8. EDS measurements indicated that the i-phase had an approximate composition of $Ti_{49}Zr_{36}Ni_{13}Cu_2$.

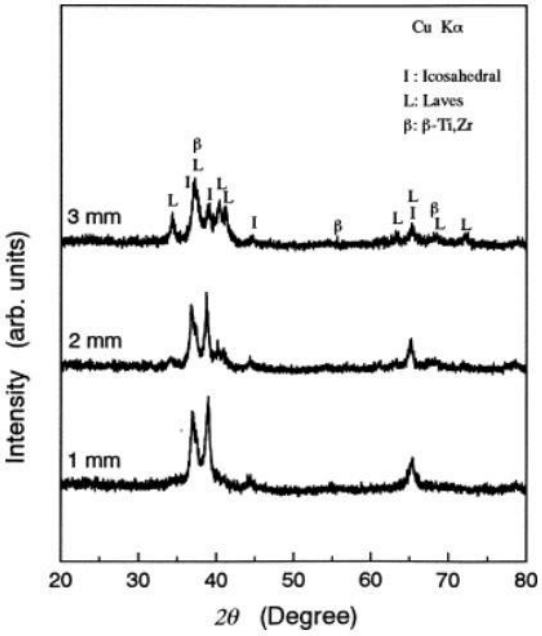

Figure 8:XRD patterns of cast $Ti_{45}Zr_{35}Ni_{17}Cu_3$ bulk samples with diameters of 3, 2 and 1 mm (Wang, 2003a).

Liu et al., 2008, have reported about the amorphous forming ability of $Ti_{45}Zr_{30}Ni_{25}Y_x$ (x = 1, 3, 5 and 7) alloys improved with increasing Y content.

In 2006 Mechler et al. reported on the stability of the icosahedral quasicrystalline alloy $Zr_{64.5}Ti_{11.4}Ni_{13.8}Cu_{10.3}$ under radiation with swift heavy ions and characterised the microstructure of the quasicrystalline phase with X-ray diffraction and transmission electron microscopy (TEM). In the same year the crystallographic and electrochemical characteristics of a $Ti_{45}Zr_{35}Ni_{17}Cu_3$ + xNi (x= 0, 5, 10, 15, and 20 mass %) quasicrystalline alloy ball milled with nickel powder were investigated by Liu et al. (Liu and Wang, 2006a). The powders consisted of amorphous, i-phase and Ni-based phases. The Ni was suggested to improve the electrochemical characteristics and indirectly enhance the hydrogen diffusivity in the bulk alloy. The kinetic and electrochemical properties of an icosahedral quasicrystalline $Ti_{45}Zr_{35}Ni_{17}Cu_3$ alloy powder as a negative electrode material for a Ni–MH battery were investigated at different temperatures by Liu et al. (Liu et al., 2006b). The exchange current density and the diffusion coefficient of hydrogen in the bulky electrode were found to rise with increasing temperature.

More recent studies by Liu et al. (Liu et al., 2006c) have looked at icosahedral quasicrystalline $Ti_{45}Zr_{35}Ni_{17}Cu_3$ alloy powder that was ball-milled with 20 mass % Ni. They found that the amounts of icosahedral quasicrystalline and Ni phases decreased when the ball-milling time increased from 30 to 180 min. In 2007 Qiang et al. (Qiang et al., 2007) reported that single-phase quasicrystals can be obtained by the casting method for compositions of $Ti_{40}Zr_{40}Ni_{20}$ and $Ti_{33}Zr_{44}Ni_{18}Cu_5$, and a bulk glassy alloy is formed at the composition of $Ti_{12}Zr_{55}Ni_{13}Cu_{20}$.

However, Lefaix et al., 2008, have reported that the phase selection criterion as a function of solidification route remains unclear from the structural point of view. By performing a series of planar flow casting experiments of the $Ti_{45}Zr_{38}Ni_{17}$ alloy, using different processing parameters, they obtained a mixture of nanoscale β and amorphous phases at a high cooling rate. The icosahedral phase precipitated at an intermediate cooling rate or after annealing a crystallized amorphous matrix. The formation of quasicrystals in the amorphous matrix containing β particles is shown in the competition between icosahedral and body-centered cubic (BCC) phases during the solidification process. The β phase seems to have a lower nucleation barrier than the quasicrystalline for this composition. These observations coincide with the phase diagram of Ti-Zr-Ni alloys detailed by Kelton et al., 2002, for an equal ratio of Ti and Zr, Figure 3.

Reports of the interaction of Ni–Ti–Zr copper-containing phases and their interaction are restricted to a report by Guo et al. (Guo et al., 2002) They looked only at amorphous and crystalline ribbons, and found that the amorphous material could absorb hydrogen to a maximum H/M value of 1.41, some 17.6 times more than in the corresponding crystalline phase. They attributed this to the electronic structure and the favourable chemistry for hydrogen in the amorphous alloy.

In the present Ph.D work we investigated the formation of mechanically alloyed and thermally-treated,

melt-spun and vacuum-cast icosahedral Ti-Zr-Ni and Ti-Zr-Ni-Cu phases and the material's ability to absorb hydrogen from a gaseous environment. To our best knowledge no reports on the magnetic properties, i.e., hysteresis curves, the temperature dependence of magnetization, the temperature dependence of susceptibility, the magneto-resistance, etc., have been reported for Ti-Zr-Ni alloys, so far. With this dissertation we thus tried to explain the magnetic nature of the Ti-Zr-Ni-based quasicrystalline, amorphous and crystalline phases, as well.

1.1.2 Cell parameter calculation

By using well-established mathematical model for indexing icosahedral structures (Cahn et al., 1986) we were able to index our X-ray and electron diffraction spectra with six Miller indices and calculate corresponding i-phase cell parameter a_q.

The most common symmetry of quasicrystals is icosahedral, which is decribed by the icosahedral $m\bar{3}\bar{5}$ space group, containing 6 five-fold axes, 10 three-fold axes and 15 two-fold axes. These axes are schematically shown on a ployhedron called an icosahedron, which describes the icosahedral quasicrystalline structure, Figure 9, and has 15 triangular faces joining in 12 vertices.

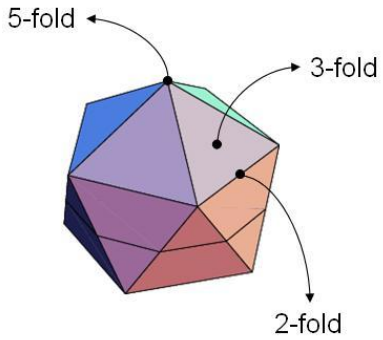

Figure 9: Icosahedron, with corresponding 5-, 3- and 2-fold rotation zone axes.

1st Brillouin zone of icosahedral quasicrystal, Figure 10, is almost a sphere, thus this structure is energetically favourable despite its complexity. This is an answer why nature favours complex structures. Of course, icosahedral structure is not enough for stability of particular quasicrystalline system, namely substancial pseudo-gap at the Fermi level should form as well. Another important fact should be mentioned and explained at this point, related to sphere-like 1st Brillouin zone of icosahedral quasicrystals. Namely, quasicrystals do not have conventional cells, like we know from classic crystallography, since due to the lack of translational periodicity size of their cells is infinite, and thus their 1st Brillouin zone converges to a perfect sphere. And so number of X-ray, electron or neutron diffraction spots converges to infinite as well. It should be noted that icosahedral clusters (Bergman type in Ti-Zr-Ni system) are glued together by so-called glue atoms, again forming icosahedral structure of larger scale, which is repeated to the limit of the grain, by preserving this quasicrystalline order. We use a_q to characterize an average or relative interatomic distance in such quasilattice and can be thought as a side of a Bergman cluster.

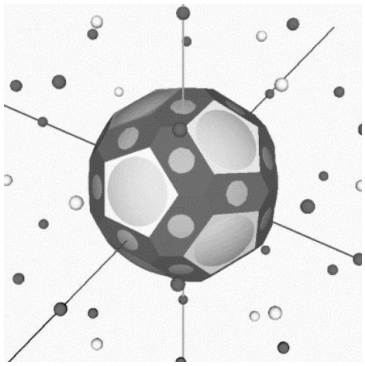

Figure 10: The first Brillouin zone of icosahedral quasicrystal.

As mentioned before, icosahedral quasicrystals have a forbidden 5-fold symmetry and the lack of translational periodicity makes it difficult to index the "crystal" planes by using conventional 3-index

Miller indexation in a cubic coordinate system.

If we consider a plane or reciprocal space position with an index of the form

$$(h+h'\tau, k+k'\tau, l+l'\tau) \tag{3}$$

that is where

$$H= h+h'\tau\,, \quad K= k+k'\tau\,, \quad L= l+l'\tau \tag{4}$$

in which the h, h', k, k', l and l' are all integers. We introduce the six-index notation (h/h', k/k', l/l') to designate such reflections. τ denotes the golden section or golden mean, infinitive rational number (like π), which is unavoidable for describing and indexing icosahedral quasicrystal structures, and is closely related to fivefold symmetry, since this is the ratio between the length of the diagonal in a pentagon and its side. Thus it can be calculated as $\tau = 2\cos 36° = (1+\sqrt{5})/2 = 1.618034$. The golden mean is also related to the Fibbonacci chain ($a_{n+1} = a_n + a_{n-1}$), and can be obtained as a_{n+1} / a_n, when n limits to ∞. Because τ originates from this chain the following identities are characteristic for it, and were used for the matrix calculation of fivefold rotation about [1τ0] axis, which is not mentioned in this thesis.

$$\tau^2 = 1+\tau$$
$$\frac{1}{\tau} = \tau - 1 \tag{5}$$

What is more important is the imposition of the so-called parity conditions that the three sums h+k', k+l' and l+h' are even: after fivefold rotation the six integer indices remain integers and the parity rules are conserved. If all diffraction spots are in this form, the pattern comes from the quasiperiodic structure. Furthermore, we then focus on indexing of the main directions. The six fivefold axes are all of the form (1τ0), which corresponds to the six-index notation (1/0 0/1 0/0). The ten threefold axes have two different denotations: four are along (111) or (1/0 1/0 1/0) and six along ($\tau^2$10) or (1/1 1/0 0/0). Three of the twofold axes are along the cube axes, and the remaining 12 have the form (0.5τ 0.5τ^{-1} 0.5) or (0/1 -1/1 1/0).

Every spot in the reciprocal three-dimensional quasilattice occurs as a sum of the integer multiples of a finite number (more than 3) of vectors. For instance, there exist 6 vectors along the fivefold axes, given by Equation 6.

$$Q = \sum_{i=1}^{6} n_i q_i \tag{6}$$

where the n_i are integers and q_i are (1τ0), which in 6-index notation is

q_1= (1/0 0/1 0/0)
q_2= (0/1 0/0 1/0)
q_3= (0/0 1/0 0/1)
q_4= (-1/0 0/1 0/0)
q_5= (0/1 0/0 -1/0)
q_6= (0/0 -1/0 0/1) (7)

The set of six numbers (n_i) can be considered as the indexing of *Q*. The same set can also be considered to be a six-dimensional lattice vector. To express Q in terms of the three-dimensional cubic coordinates we substitute set (7) in Equation (6) and perform the summation,

$$Q = ((n_1 - n_4)/(n_2 + n_5), (n_3 - n_6)/(n_1 + n_4), (n_2 - n_5)/(n_3 + n_6)) \tag{8}$$

This transformation enables us to go from the six-dimensional vector (n_1, n_2, n_3, n_4, n_5, n_6) to the six-index three-dimensional vector *(h/h', k/k', l/l')*.

$$\begin{aligned} h &= n_1 - n_4 \\ h' &= n_2 + n_5 \\ k &= n_3 - n_6 \\ k' &= n_1 + n_4 \\ l &= n_2 - n_5 \\ l' &= n_3 + n_6 \end{aligned} \tag{9}$$

and vice versa

$$\begin{aligned} 2n_1 &= h + k' \\ 2n_2 &= l + h' \\ 2n_3 &= k + l' \\ 2n_4 &= -h + k' \\ 2n_5 &= -l + h' \\ 2n_6 &= -k + l' \end{aligned} \tag{10}$$

The form of Equations 10 shows that *Q* in the six-index notation obeys the parity rules, which originate from extinction rules and lead to four kinds of positions:

1. six even indices,
2. four even indices (odd/even, even/odd, even/even),
3. two even indices (even/odd, odd/even, odd/odd),
4. six odd indices

Furthermore, the square of Q is in the form

$$Q^2 = N + M\tau \tag{11}$$

$$N = 2\sum_{i=1}^{6} n_i^2 = h^2 + h'^2 + k^2 + k'^2 + l^2 + l'^2 \tag{12}$$

$$M = h'^2 + k'^2 + l'^2 + 2(hh' + kk' + ll')$$

In three dimensions the six vectors along the fivefold axes are not orthogonal. Thus we can pick the 6D cubic space in which each of these vectors is a basis vector along a hypercube axis that is perpendicular to all others. Six n_i numbers then represent a position of vector in 6D cubic reciprocal lattice, where Equation 15 gives the correlation among the positions in 3D and 6D spaces.

Q is a dimensionless parameter, so we must introduce a three-dimensional quasilattice constant d_0 such that the three-dimensional diffraction vector *k* and the interplanar spacing are given by

$$k = \frac{Q}{d_0} \tag{13}$$

$$d(h/h', k/k', l/l') = \frac{d_0}{\sqrt{N + \tau M}} \tag{14}$$

The length of the six-dimensional reciprocal lattice constant a_6^* is related to d_0 by

$$a_6^* d_0 = \sqrt{2(2+\tau)} \tag{15}$$

and the length of the three-dimensional lattice constant a_q in real space is derived from a_6^* as

$$a_q = \left(a_6^* \sqrt{2} \right)^{-1} \tag{16}$$

Dimensionless parameters for six-index notation of the four most intense icosahedral peaks in X-ray diffraction patterns are given in Table 2.

dimensionless				indexation		zone-axis
N	M_0	Q_0^2	Q_C	(h/h',k/k',l/l')	(n_i)	-fold
18	29	64.92	0.45	(1/2,2/3,0/0)	100000	5
20	32	71.78	0.76	(0/0,2/4,0/0)	110000	2
52	84	187.91	0.47	(1/0,1/1,0/1)	101000	2
72	116	259.69	0.90	(2/4,4/6,0/0)	200000	2

Table 2: Table of dimensionless parameters for 6-index notation of the four most intense i-phase XRD peaks.

A fit parameter d_0 is set so that the calculated 2ϑ values match to the observed ones. For this operation it is enough to take just the first four most intense peaks: (100000), (110000), (101000) and (200000). Table 3 shows an example of such semi-empirical calculation of a_q for $Ti_{45}Zr_{35}Ni_{17}Cu_3$ i-phase. Results of this indexation are described in detail in section 4.3. For this particular case d_0 is set to 1.960 nm and from Equation (15) a_6^* is then 1.372 nm^{-1}. Using Equation (16) a_q is calculated to be 5.15 Å. XRD data were measured by Cu-Kα radiation with 1.5405 Å wavelength.

(n_i)	$d^{-1}\,(nm^{-1})$	2ϑ
100000	4.11	36.9
110000	4.32	38.9
101000	6.99	65.2
200000	8.22	78.6

Table 3: Indexation of $Ti_{45}Zr_{35}Ni_{17}Cu_3$ i-phase XRD spectrum for quasi-lattice cell parameter a_q determination.

1.2 Metallic glasses

To achieve the formation of an amorphous structure even during slower cooling, the alloy has to be made of three or more components, leading to complex crystal units with higher potential energy and a lower chance of formation. The atomic radius of the components has to be significantly different (over 12%), to achieve a high packing density and a low free volume. The combination of components should have a negative heat of mixing, inhibiting crystal nucleation and prolonging the time the molten metal stays in the supercooled state. Amorphous alloys have a variety of potentially useful properties. In particular, they tend to be stronger than crystalline alloys of similar chemical composition, and they can sustain larger reversible ("elastic") deformations than crystalline alloys. Amorphous metals derive their strength directly from their non-crystalline structure, which does not have any of the defects (such as dislocations) that limit the strength of crystalline alloys. One modern amorphous metal, known as Vitreloy, has a tensile strength that is almost twice that of high-grade titanium. However, metallic glasses at room temperature are not ductile and tend to fail suddenly when loaded in tension, which limits the material applicability in reliability-critical applications, as the impending failure is not evident. Therefore, there is considerable interest in producing metal matrix composite materials consisting of a metallic glass matrix containing dendritic particles or fibers of a ductile crystalline metal. The thermal conductivity of amorphous materials is lower than that of crystals. As formation of amorphous structure relies on fast cooling, this limits the maximum achievable thickness of amorphous structures. Amorphous metal is usually an alloy rather than a pure metal. The alloys contain atoms of significantly different sizes, leading to a low free volume (and therefore up to orders of magnitude higher viscosity than other metals and alloys) in the molten state. The viscosity prevents the atoms moving enough to form an ordered lattice. The material structure also results in low shrinkage during cooling, and resistance to plastic deformation. The absence of grain boundaries, the weak spots of crystalline materials, leads to better resistance to wear and corrosion. Amorphous metals, while technically glasses, are also much tougher and less brittle than oxide glasses and ceramics.

This term refers to amorphous metallic materials, with a disordered atomic-scale structure. In contrast to most metals, which are crystalline and therefore have a highly ordered arrangement of atoms, metallic glasses are non-crystalline. There are several ways in which amorphous metals can be produced, including physical vapor deposition, solid-state reaction, ion irradiation, melt spinning, and mechanical alloying. We used the last two mentioned techniques to prepare Ti-Zr(Hf)-Ni-(Cu) amorphous alloys.

In the past, small batches of amorphous metals have been produced through a variety of quick-cooling methods. For instance, amorphous metal wires have been produced by sputtering molten metal onto a spinning metal disk. The rapid cooling, of the order of millions of degrees a second, is too fast for crystals to form and the material is "locked in" a glassy state. More recently a number of alloys with critical cooling rates low enough to allow formation of amorphous structure in thick layers (over 1 millimeter) have been produced, these are known as bulk metallic glasses (BMGs), which show strengths much greater than conventional steel alloys. Even though these materials are very hard, they suffer from a lack of ductility. In the scientific community there is great interest to increase the plasticity of metallic glasses, which would increase their technological application potential. Perhaps the most useful property of bulk amorphous alloys is that they are true glasses, which means that they soften and flow upon heating. This allows for easy processing, such as by injection molding, in much the same way as polymers. As a result, amorphous alloys have been commercialized for use in sports equipment, medical devices, and as cases for electronic equipment. For instance, they are widely used for golf-club coatings, since the elastic energy stored inside the metallic glasses (high Young modulus) increases the speed of the golf ball by up to 20 % compared to conventional materials.

BMGs always possess strong glass-forming abilities, which makes it more easy to achieve the amorphous state even at the intermediate cooling rate, for instance from 1 to 100 K/s (Inoue, 2000, Wang et al., 2004, Löffler et al., 2003). The formation of the BMG alloy and its glass-forming ability are dependent on the composition and design technique, as well. Based upon different considerations several composition rules for BMGs have been reported by Wang et al. in 2004. Dong and co-workers (Wang et al., 2003b, Chen et al., 2003, Dong et al., 2004) proposed a quantitative criteria to optimize and design the proper composition of various BMGs by using the specific e/a (valence electron per atom) and R_a (average atomic diameter) parameters in the given alloy phase diagram. They claim, for a particular system, BMGs, quasicrystals and corresponding crystalline counterparts belong to a series of electron phases having a very similar e/a value, which can then be used as an e/a-constant criterion for the formation of BMGs (Wang et al., 2003b). Qiang et al., 2007, have verified the validity of this criterion on a series of Ti-Zr-Ni-Cu alloys, having a constant e/a value. They studied the relationship between BMG and its crystalline counterparts from the viewpoint of electronic and atomic structures. The samples used were as-quenched 3 mm rods. Their experimental results and theoretical analysis revealed that all phases match the Hume-Rothery rule, and they are a group of e/a-constant electron phases. They confirmed that the e/a-constant criteria for BMGs is valid in the Ti-Zr-Ni-Cu glass-forming system, which implies the e/a factor has an important role in stabilizing the amorphous phase together with its related phases (i-phase, C14 Laves, and solid solutions).

The first metallic glass was an alloy $Au_{80}Si_{20}$ produced by Pol Duwez in 1957. This and other early glass-forming alloys had to be cooled extremely rapidly (of the order of one megakelvin per second, 10^6 K·s^{-1}) to avoid crystallization. An important consequence of this was that metallic glasses could only be produced in a limited number of forms (typically ribbons, foils, or wires) in which one dimension was small so that the heat could be extracted quickly enough to achieve the necessary cooling rate. As a result, metallic glass specimens (with a few exceptions) were limited to a thicknesses of less than one hundred micrometres.

1.3 Crystalline phases

1.3.1 C14 Laves phase

Laves phases have the general formula AB_2, where the A atoms are ordered as in hexagonal diamond, and the B atoms form tetrahedra around the A atoms. Ti-Zr-Ni alloys exist in stable C14 hexagonal modification, where Ni atoms are located on the sites of the hexagonal diamond (lonsdaleite) structure. This structure is often called $MgZn_2$-type Laves phase, since it is present in this alloy. The Pearson symbol of this structure is hP12, which refers to the hexagonal space group $P6_3/mmc$. C14 denotes the corresponding structure in »Strukturbericht« designation. Other compounds with this structure are $CaMg_2$, $ZrRe_2$, KNa_2, $TaFe_2$, $NbMn_2$, UNi_2. Figure 11 represents the C14 structure in a few perspectives. If we think of Ti-Zr-Ni system, then red spheres are Ti and Zr atoms (B), and green spheres are Ni atoms (A).

General formula of C14 Ti-Zr-Ni Laves phase was proposed by Qiang et. al in 2004. Ni content is always 33 at. %, whereas ratio Ti/Zr varies from 3.76 to 2.33, which gives Ti content 52 – 46 at. % and Zr 15 – 21 at. %. These numbers are given by the formula $(Ti_{100-x}\ Zr_x)_2Ni$ (x = 21-30). Since the ratio of Ti and Zr in the structure varies as mentioned, lattice parameters a and c vary as well; a = 5.142 – 5.191 Å and c = 8.433 – 8.520 Å, Qiang et al., 2004. These crystallographic data are in contrast with reports of Davis et al. in 2000, since the authors claim that the lattice constants for the C14 phase have a small composition dependence around the values a = 5.23 Å and c = 8.55 Å.

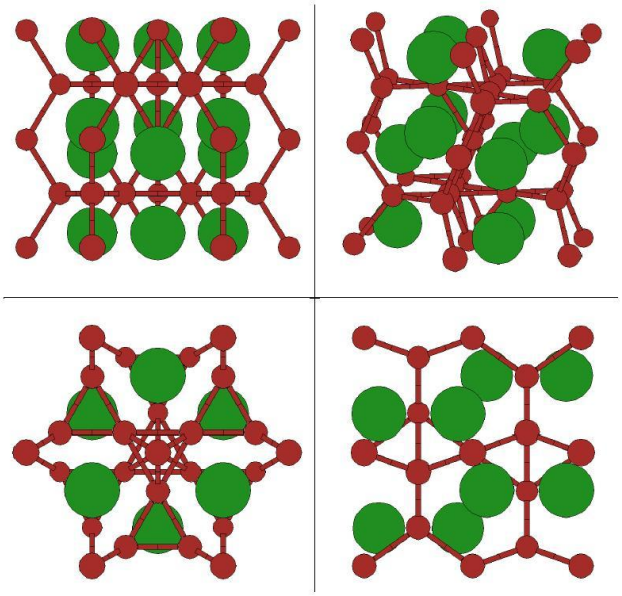

Figure 11: C14 Laves phase structure from several perspectives. Green spheres denote A (Ni) atoms.

Depending on the ordering of A atoms, there are three more Laves phase types: cubic C15 Cu_2Mg-type (diamond structure of A atoms), hexagonal C36 $MgNi_2$-type (moissanite-4H CSi structure of A atoms) and cubic $C15_b$ $MgSnCu_4$-type (Mg and Sn represent A atoms, which form so-called zincblende B3 structure).

1.4 Hydrogen absorption

1.4.1 Hydrogen storage

Global oil sources are running out, but the demand for this economically important source of energy is growing from day to day, especially in Asia and other countries with growing population and economy. This does not mean only higher prices of crude oil and consequently prices of fuel on petrol stations, but also means higher level of air pollution, i.e. global warming, photochemical smog in cities with high population, etc. To keep our planet clean and to provide low-cost traveling and stationary power stations, independent of oil sources, alternative sources and technologies of clean or so-called green energy should be commercialized as soon as possible. One of the potential clean energy technologies is hydrogen fuel cells, which convert the enthalpy of the reaction between hydrogen and oxygen into electricity, where only water is formed as a side product.

But prototype hydrogen fuel cell vehicles at the moment cost approximately hundred times more than conventional vehicles with internal combustion drive. This is partially upon platinum impregnated proton-exchange membrane (PEM), which is used in fuel cells as catalyst that ensure faster hydrogen dissociation of H2 molecule into protons that diffuse through the PE membrane, which is the main feature of hydrogen fuel cell. The membrane is usually NaF-ion based polymer that conducts protons at a certain humidity. Price of such material is again relatively high, that is around $30 per 100 cm². Another problem to commercialize this technology is hydrogen storage, which might be the most crucial issue so far. Namely, pressurized hydrogen at 800 bar is far too risky and dangerous option, since vast explosion may occur in the case of a crash. Cooled liquid hydrogen at lower pressure is safer but non-economical, since extreme cooling is required (4 K) and relative fast evaporation of hydrogen from the storage tank takes place. The most promising, rational and safe way to store substancional quantities of hydrogen is absorption in intermetallic alloys of a transition-metal/rare-earth system, such as $LaNi_5$ with dopants (Al, Zn, Cu, Co,

etc,) in order to create more interstitial space where protons can bond. The [H]/[M] ratio is the basic characteristic of hydrogen storage materials, since this number tells us how many protons (H) are bonded to one metal atom (M) on average, when the material is normally saturated with hydrogen. For $LaNi_5$ this ratio is approximately 1.2. Some transition metals and their alloys have the ability to reversibly absorb considerable amounts of hydrogen, since d-elements are active catalysts of the dissociative adsorption of hydrogen. The amount of absorbed hydrogen and the absorption kinetics depend on interactions between the hydrogen atoms and the alloy. Titanium and zirconium both show a high affinity for hydrogen, and Ti–Zr–Ni alloys with amorphous, quasicrystalline or crystalline structures have proved to be excellent absorbers of hydrogen.

In 2003 the U.S. Department of Energy (DOE) stated demand hydrogen storage materials must absorb at least 6 wt. % of hydrogen for transportational use by the year 2006, and even 9 wt. % of H by the year 2012. Well, up to now no breaktrough in hydrogen storage has been made so far, even though some materials absorb more than 15 wt. % of hydrogen. Sooner or later we come to an obstacle, such as too high desorption temperature (the most common), unstable structure during hydrogen cycling, non-economical preparation, cost of starting materials, slow kinetics, life time, etc. Future investigations are needed to improve hydrogen absorbtion performance of hydrogen storage materials in order to begin the commercialization of hydrogren fuel cells. What concerns Ti-Zr-Ni alloys, they can only absorb 2-2.5 wt. % of hydrogen, which makes them applicable only for stacionary use, heavy transportation (boats, trains, etc.) or for nickel metal-hydride batteries.

From the scientific point of view metal hydrides are interesting for hydrogen mobility studies by means of nuclear magnetic resonance. Namely, by this technique one is able to determine the activation energy of proton or deuteron hopping in the material, depending on the crystal or electronic structure. Also, different local environments of protons can be detected, which have different bonding energies.

1.4.2 Hydrogen in Ti-Zr-Ni quasicrystals

Ti-Zr-Ni-based quasicrystals show as good hydrogen storage performance as conventional alloys, or better. Sadoc et al. (2002) have discovered the [H]/[M] for $Ti_{45}Zr_{38}Ni_{17}$ i-phase is 1.7 for loading from gas phase and even 1.9 for electrolytic loading. These materials are able to reversibly store important amounts of hydrogen without forming stable hydrides and they conserve the icosahedral structure as well. They also have a lower density compared to conventional hydrogen storage intermetallics, thus increasing important parameter of these materials, namely the wt. % of desorbed hydrogen.

Several authors have investigated hydrogen positions and dynamics in the hydrogenated icosahedral $Ti_{45}Zr_{38}Ni_{17}$ phase and revealed that the positions occupied by hydrogen in the icosahedral structure can not be equivalent, crystallographically or energetically. Shastri et al., 1998, have discovered by ^{1}HNMR that hydrogen atoms occupy tetrahedral sites within Bergman clusters, which consist of two concentric icosahedra, and are not closer than 0.21 nm, which is the theoretical limit of the distance between two protons. Upon the discrepancy between experimental ([H]/[M] = 1.88) and theoretical Bergman cluster model data of hydrogen concentration ([H]/[M] = 1.1) they concluded a substancial amount of hydrogen probably occupies the linkages (glue atoms) between the Bergman clusters. Thus, at least two kinds of hydrogen atoms exist in the icosahedral structure of the hydrogenated $Ti_{45}Zr_{38}Ni_{17}$ phase. This hypothesis was also confirmed by the time-of-flight neutron scattering investigation of hydrogen dynamics, done by Coddens et al., 1997.

Konstanchuck et al., 2001, revealed the hydrogenation of a mechanically alloyed $Ti_{45}Zr_{38}Ni_{17}$ i-phase started without an induction time at the maximum rate and H_2 pressure below 1 bar (at 230°C), Figure 12, whereas hydriding of the same material obtained by melt spinning usually starts after a long induction period, at 230-260 °C and hydrogen pressure 27- 40 bar, due to reports in several papers (Viano et al., 1995, Stroud et al., 1996, Kelton and Gibbons, 1997). They think the surface of i-phase samples prepared by mechanical alloying may contain more defects than rapidly quenched one, and the surface of the MA samples can contain clusters of either metal nickel or nickel oxide, which is easily reduced by hydrogen at 230 °C. These nickel insertions act as the centers of dissociative adsorption of hydrogen, which is the rate limiting step of hydrogen absorption in metals. We paid attention to nickel clusters, since the magnetic properties of amorphous alloys prepared by mechanical alloying and melt spinning can be different.

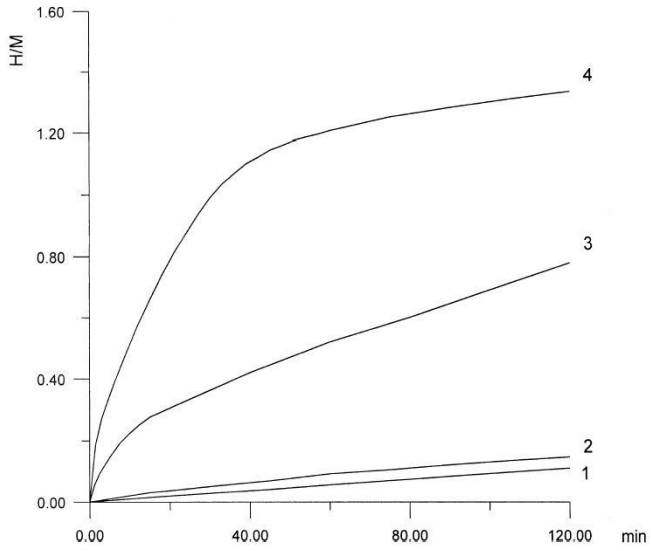

Figure 12: Hydrogenation kinetics of the $Ti_{45}Zr_{38}Ni_{17}$ i-phase at 230°C: (1, 3) 2 hours of mechanical alloying only, (2, 4) MA (2 h) and annealing at 440 °C in Ar for 5h; (1, 2) $P(H_2)$ = 0.8 bar, (3, 4) $P(H_2)$ = 13.5 bar (Konstanchuck et al., 2001).

Several authors have reported about the formation of a surface oxide layer either on melt-spun ribbons or mechanically alloyed powders (Viano et al., 1998, Takasaki and Kelton, 2002). This layer was reported to act as a barrier to hydrogen uptake, since hydrogen molecule dissociation occurs on a metal surface and not on an oxide one.

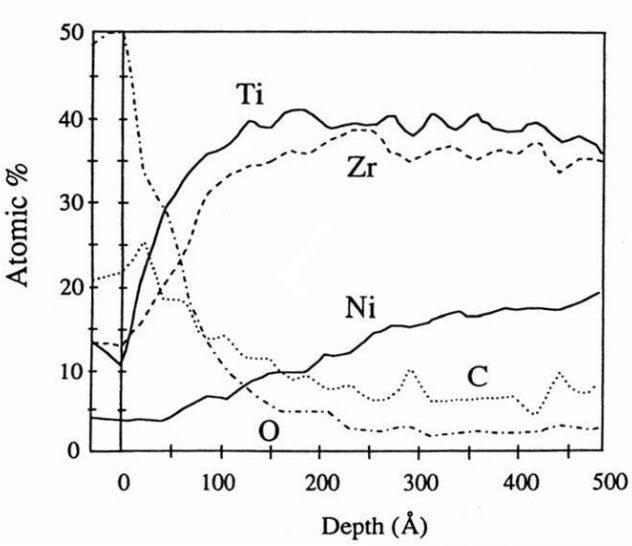

Figure 13: Auger depth profile for icosahedral $Ti_{45}Zr_{38}Ni_{17}$ stored in air for 30 days. Oxide coating is approximately 15 nm thick (Viano et al., 1998).

Even though a combination of plasma etching and palladium coating drastically reduces the loading time of hydrogen in Ti-Zr-Ni melt-spun ribbons, allowing absorption at room temperature and enabling reversible desorption of the stored hydrogen (Kim et al., 1998), such a treatment is not economical for the mass-production of this hydrogen storage material. Takasaki et al., 2002, have seen a dramatic decrease of the induction time for hydrogen loading into pre-milled Ti-Zr-Ni amorphous powders in a hydrogen atmosphere. Namely, it is expected that the formation of a surface oxide barrier can be substancially reduced during preparation under a hydrogen atmosphere.

Viano et al., 1998, have demonstrated the shift of i-phase peaks to a lower angle with increasing hydrogen content, indicating the expansion of the quasilattice as hydrogen is loaded into the material, Figure 14. These data were then used to calculate the quasilattice expansion as a function of hydrogen

concentration. The volume fraction of crystalline $(Ti/Zr)H_2$ phase is negligible and they assumed that the measured hydrogen content reflects the amount of hydrogen stored in the i-phase

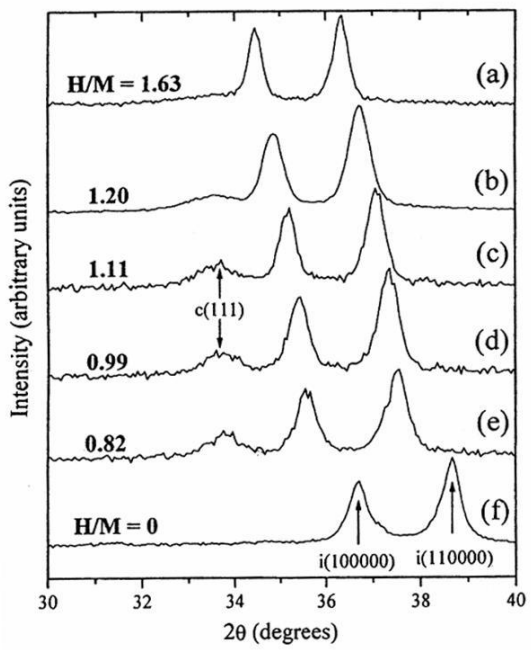

Figure 14: XRD spectra of $Ti_{45}Zr_{38}Ni_{17}$ i-phase with different contents of hydrogen ([H]/[M]). Patterns from b) to e) were obtained by desorbing hydrogen at 400 °C for b) 5, c) 10, d) 30 and e) 180 min. The peak denoted by c(111) is a reflection from the FCC $(Ti/Zr)H_2$ phase (Viano et al., 1998).

The measured content of desorbed hydrogen, expressed as [H]/[M] ratio (number of H atoms per metal atom), was then projected on the expansion of quasilattice constant (a_q), calculated from XRD patterns by the method of Elser, 1985. They found the a_q increases linearly with the hydrogen concentration, as happens in crystalline metal-hydride systems. The calculated formula of this line for this particular composition is

$$\frac{H}{M} = \frac{a_q^H - a_q^0}{0.1974} \tag{17}$$

Where a_q^H denotes the measured quasilattice constant at the certain hydrogen concentration and a_q^0 the quasilattice parameter for the as-prepared i-phase (both in Å). Equation 17 was obtained by linear fit of experimental data, given in Figure 15.

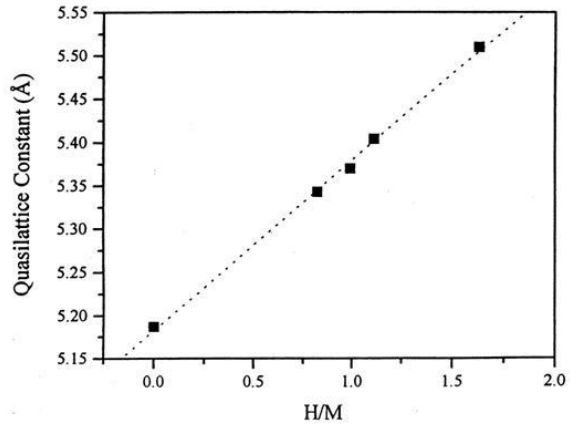

Figure 15: Expansion of the quasilattice constant a_q as a function of hydrogen concentration in icosahedral $Ti_{45}Zr_{38}Ni_{17}$ icosahedral phase.

2 Materials and methods

2.1 Preparation

2.1.1 Mechanical alloying

2.1.1.1 Introduction

Mechanical alloying performed by high energy planetary ball-milling is a mechanical operation where the kinetic energy of milling bodies (stainless-steel balls, 6 mm in diameter in our case) is used to alloy separate elements in form of powders together. Also, this kinetic energy is used for another important feature, namely when applied for long enough time it can destroy the crystal structure of the material. So, by using this technique one is able to get amorphous alloy in the powder form. Two main disadvantages occur during this method, first is the loss of the material, since more than half of it sticks (welds) on the mill wall and on the milling balls. And second, powder particles agglomerate, preventing full amorphization inside agglomerates.
Schematic presentation of planetary ball-milling is shown in Figure 16. The name planetary comes from the planet-like motion of the milling pot, since it is attached on the rotating disk with diameter *R*, which rotates with the angular velocity Ω. Like the revolution of the planet around the Sun. And then the vial with diameter d_m rotates around its axis with the angular velocity of rotation ω. When a ball moves from A spot to B, the potential energy at A spot by the acceleration of disk revolution is equivalent to the kinetic energy at B, as given by Equation 18, Mio et al., 2004.

$$\frac{1}{2}mv^2 = m\alpha d_m \qquad (\alpha = R\Omega^2) \tag{18}$$

where, α means the acceleration acting on a ball during moving from A to B and can be expressed by the revolution radius and the angular velocity of revolution, Ω.

a) b)

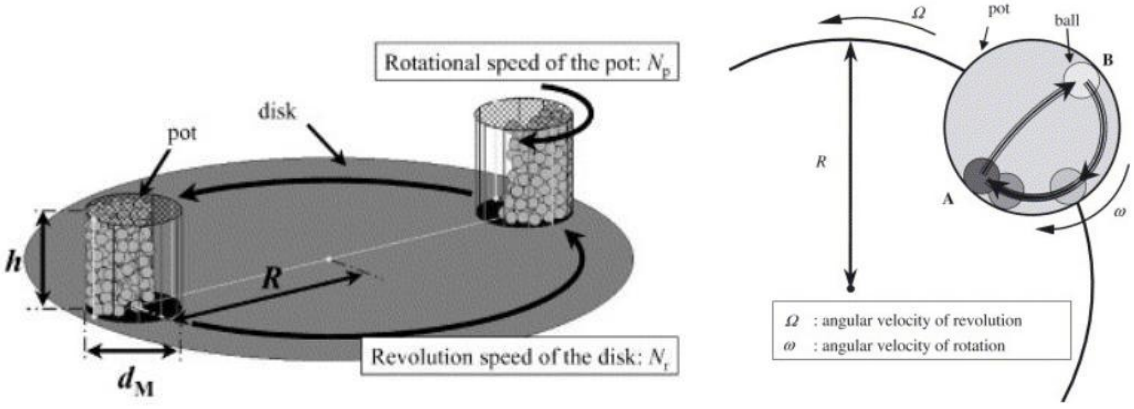

Figure 16: a) schematic diagram of the planetary ball-mill b) the movement of a ball in a pot, (Mio et al., 2004).

Mechanical alloying experiments for the purpose of this dissertation were done with a Fritsch Pulverisette Ball-Mill 5 with R = 0.125 m, d_m = 0.055 m and rotation-to-revolution speed ratio equal to 1.25, where the revolution speed of the disk was always set to 200 rpm. From Equation 18 (in brackets) we calculated the acceleration (α) on a ball in position A from given data, which equals to 55 ms^{-2}.

2.1.1.2 Experimental overview

The $Ti_{40}Zr_{40}Ni_{20}$ and $Ti_{40}Hf_{40}Ni_{20}$ glassy and quasicrystalline phases were synthesized by mechanical alloying of commercially pure Ti, Zr, Hf and Ni elemental powders, where an average grain size of the powder particles was 35 μm. The mechanical treatment was carried out in a high-energy planetary stainless steel ball mill (*Fritsch Pulverisette Ball-Mill 5*) for different times, namely 20, 40, 60, 80 and 100 hours. Ball mass-to-sample mass ratio was approximately 15:1 and the acceleration 55 ms^{-2}. The fully amorphous samples, obtained after 100 hours of mechanical alloying, were subsequently annealed at various temperatures in dynamic vacuum of 10^{-5} mbar for 2 hours in order to form the icosahedral structure. Heating rate was set to 10 K/min. After 2 hours of annealing at constant temperature the furnace was quickly removed in order that the sample cooled down naturally. In Table 4 a set of these experimental conditions is shown.

material	milling [h]	annealing	temperature of annealing [°C]				
$Ti_{40}Zr_{40}Ni_{20}$	0, 20, 40, 60, 80	-	-	-	-	-	-
$Ti_{40}Zr_{40}Ni_{20}$	100	2 hrs.	500	525	550	575	600
$Ti_{40}Hf_{40}Ni_{20}$	0, 20, 40, 60, 80	-	-	-	-	-	
$Ti_{40}Hf_{40}Ni_{20}$	100	2 hrs.	420	500	550	700	

Table 4: Preparation conditions for the $Ti_{40}Zr_{40}Ni_{20}$ and $Ti_{40}Hf_{40}Ni_{20}$ quasicrystals by mechanical alloying with subsequent annealing.

2.1.1.3 Mechanical alloying in a hydrogen atmosphere

Planetary ball-milling under hydrogen atmosphere was performed at the same conditions as the mechanical alloying under an argon atmosphere. The initial hydrogen pressure of 1 bar decreased upon absorption during the alloying process. After each sampling in protective argon atmosphere, the milling vial was evacuated and refilled with hydrogen up to 1 bar. After that the pressure dropped rapidly for about 80% due to hydrogen absorption (at room temperature!) into the metal powder inside the vial, which became quite warm, since hydrogenation is an exothermic reaction. In order to reach a constant pressure of 1 bar, the vial had to be refilled with hydrogen twice more. This routine was repeated 5 times, after each sampling, which means substantial amount of hydrogen was absorbed during the mechanical alloying in hydrogen atmosphere.

2.1.2 Melt spinning

2.1.2.1 Introduction

Melt spinning is a technique used for the rapid quenching of liquids. The cooling wheel is made of copper, which enables optimal heat-removal, and rotated at tangential speeds between 10 and 50 m/s. A thin stream of liquid is then continuously ejected onto the wheel and cooled, causing rapid solidification, Figure 17. This technique is used to develop materials that require extremely high cooling rates in order to form, such as metallic glasses. The cooling rates achievable by melt-spinning are of the order of 10^4–10^6 Kelvins per second (K/s). Its high and variable cooling rates make it suitable for the production of metallic materials with different crystallographic structures.

The melt spinner was invented in 1969 by Pond and Maddin, where the liquid was quenched on the inner side of a rolling drum (Cahn, 1983), then later as a continuous casting method by Liebermann and Graham (Liberman et al., 1976). However, because the melt spinner is only capable of producing small, thin ribbons, some as thin as 10 micrometres, melt spinning is limited to mainly production of research specimens for alloys with a high critical cooling rate, which are difficult to fabricate with other techniques.

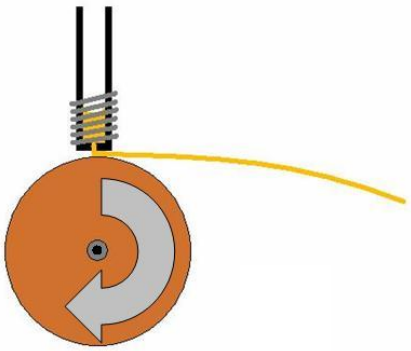

Figure 17: Schematic presentation of melt spinning performance. After the alloy is melted by RF coil induction, it is ejected through the crucible nozzle onto the rotating copper cooling wheel, producing long and thin ribbons.

Melt spinning is an alternative method for the preparation of metallic glasses, which can be used as precursors for the synthesis of quasicrystals. But according to temperature-time-transformation (TTT) diagram in Figure 18, which describes the state of the material after melt spinning, the i-phase can be produced directly from the melt, if the right cooling rate (cooling wheel speed) is set, shown by the arrows. Melt spinning is similar in someways to mechanical alloying; however, there are a number of important differences. Because the precursor is a liquid the process is much quicker, and less sample is required for one batch (about 10 grams instead of 20).

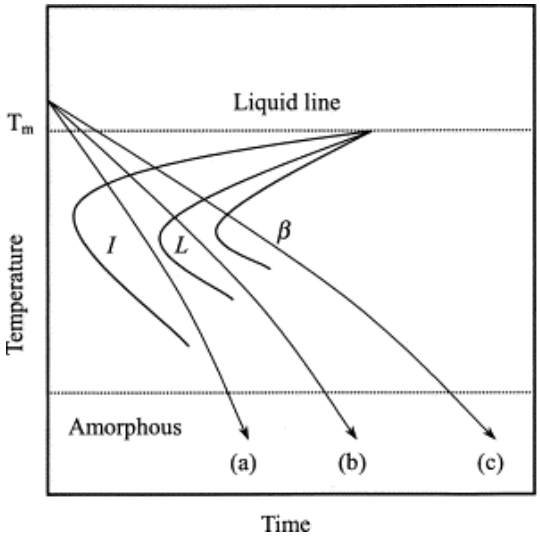

Figure 18: Temperature-time-transformation diagram of Ti-Zr-Ni alloy system (Wang et al., 2003a).

2.1.2.2 Experimental overview

The precursors for the melt spinning were prepared by arc-melting a $Zr_{65.9}Ni_{34.1}$ alloy and Ti (99%) and Cu (99, 99%) powders pressed pellets, in such ratios that the final material compositions were $Ti_{40}Zr_{40}Ni_{20}$ and $Ti_{45}Zr_{35}Ni_{17}Cu_3$. The mass of the arc-melted precursors for the melt spinning was approximately 9 grams (two ingots). The ingots were placed in graphite and boron-nitride melting crucibles with a 1.5-mm nozzle diameter. After evacuating to $5 \cdot 10^{-5}$ mbar with turbo diffusion pump the chamber of the melt-spinner (Edmund Bühler, Melt Spinner SC), Figure 20, was refilled with 99.99 % pure argon gas. The precursor samples were then heated up to 1400 °C by radio-frequency (RF) induction. The temperature was detected with a pyrometer that was attached to a crucible holder. The melt was injected through the nozzle by 200 mbar of argon over-pressure onto a rotating copper wheel of 200 mm diameter. We repeated the experiment at 10 different wheel speeds: 12, 16, 20, 24, 28, 32, 36, 40, 45 and 50 m/s. Figure 19 shows the transformation of the arc-melted precursors (buttons) to melt-spun ribbons via the melt spinning processing route. The arc-melting technique is described in Chapter 2.1.4.

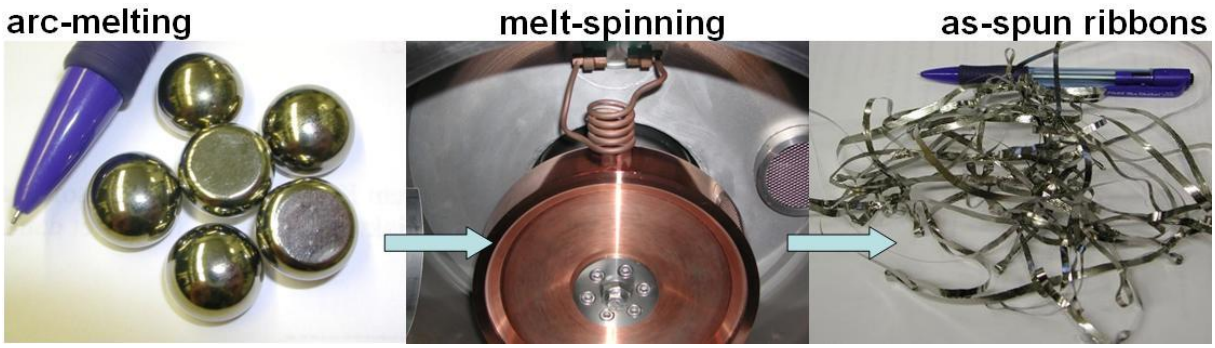

Figure 19: Processing route of melt-spun ribbons.

2.1.2.2.1 Melt-Spinner Edmund Bühler GmbH

This device requires only 10 grams of input material, whereas for mechanical alloying the minimum amount of powder for one batch is more than 20 grams. The diameter of copper cooling wheel is 200 mm, which can be rotated up to 80 Hz (50 m/s). A combination of rotary and turbo-pump provides a high vacuum down to 10^{-5} mbar. Melt-spinning chamber is then refilled with an inert gas, such as argon or helium. Usually 200 mbar overpressure is used to inject the melt through the nozzle of the crucible on a rotating copper cooling wheel. According to melting point of the sample different crucibles are used. Quartz crucibles resist temperatures up to 1300°C, boron-nitride up to 1600°C and graphite up to 1900°C. The distance between the wheel and the crucible can also be varied from 0.05 to 1 mm. Normally, it is set to 0.2 mm. Samples are melted by RF induction provided by 6 kW generator. Temperature is measured with an infra-red pyrometer.

Figure 20: Edmund Bühler, Melt Spinner SC device.

By varying all these parameters, i.e. wheel speed, pressure, nozzle size and shape, distance, and finally the temperature, one can produce ribbons of different lengths, thicknesses and widths, crystallographic structures, grain sizes, etc. All these properties are a consequence of various cooling rates, which can go up to 10^6 K/min. Besides these parameters the result of a melt-spinning experiment is strongly dependent on the sample composition.

2.1.3 Hydriding

2.1.3.1 Introduction

2.1.3.1.1 Sievert's apparatus

Sievert's apparatus allows the study of the hydrogen absorption and desorption kinetics as well as the determination of the pressure–composition–temperature (*P–C–T*) diagram of the material–hydrogen gas phase system. The apparatus can operate over a wide range of temperature, 300–700 K, and H_2 pressures, 1– 60 bar.

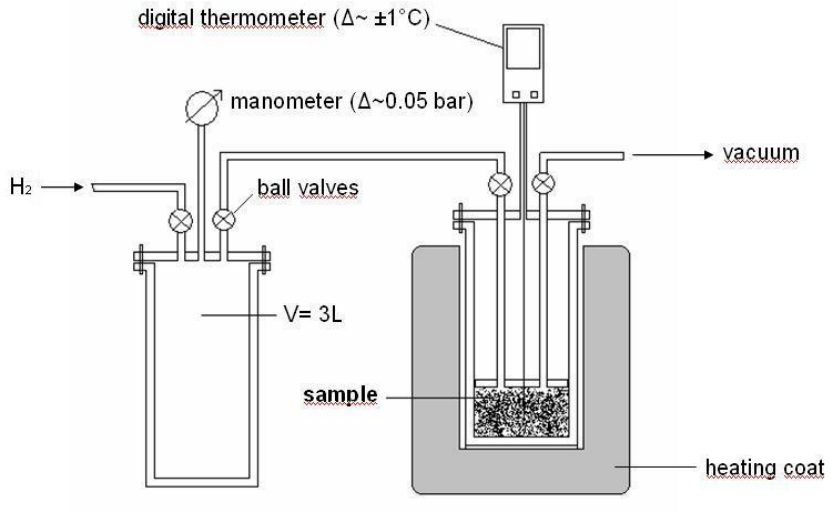

Figure 21: Schematic presentation of Sievert's apparatus for hydrogen absorption from gas phase.

Figure 21 shows a schematic of the device we used for our hydrogen absorption experiments. It was designed and made at Jožef Stefan Institute for the purpose of this Ph.D work. It is made completely out of stainless-steel AISI 316 L, which is well known to have very low hydrogen permeability, even at high temperatures and pressures. At this point it should be noted we did not perform any P-C-T measurements, since too small amount of samples were used to be able to detect any significant pressure drop. And this was not our primary aim. Thus we rather varied temperature and time of hydrogenation, where the pressure was always more or less around 45 bar. The content of hydrogen was measured by mass change by thermogravimetry, described in Chapter 2.2.6.

Before starting the experiment the complete installation was evacuated (5 min) and refilled with hydrogen three times. For safety reasons, hydrogen sensor was placed in the space where this instalation was situated. The alarm turns-on if the level of hydrogen exceeds 20 % of LEL (= low explosion level), which is 4 vol. % for hydrogen in air. This level must be exceeded at least for 2 minutes before the alarm switches on. At the beginning, when the device was installed we had some small leakages of hydrogen gas at threaded joints, which were all eliminated and fixed before experiments took place. Not just for safety reasons, but to ensure isostatic conditions during the whole experiment as well. There is a photograph of our Sievert's device in Figure 22.

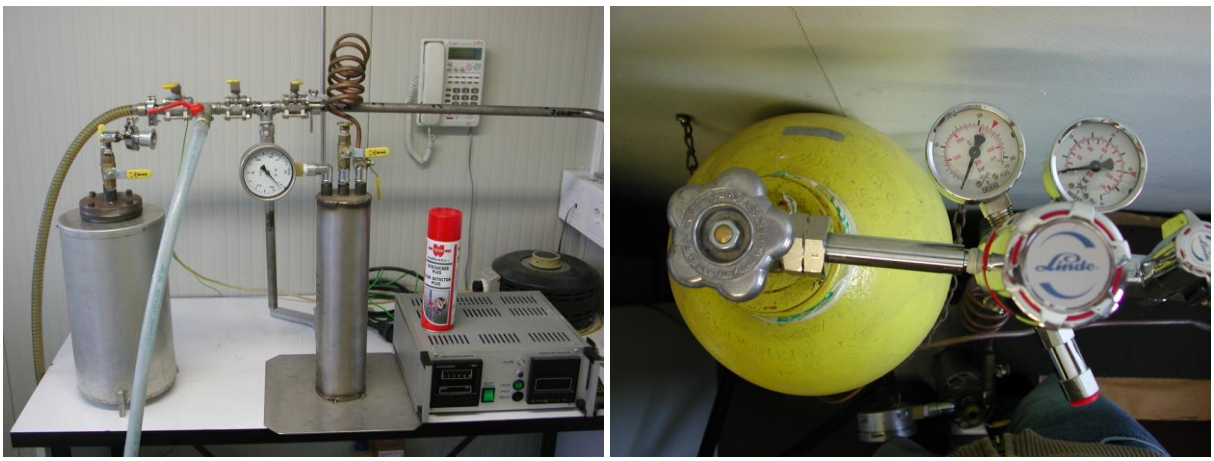

Figure 22: Photography of our stainless-steel Sievert's apparatus for high-pressure hydrogen absorption.

2.1.3.2 Hydrogenation of ball-milled powders

Powders obtained by mechanical alloying were described in details in Chapter 3. As we have seen we were able to produce icosahedral structure by mechanical amorphization and subsequent annealing, but we could not manage to load any hydrogen into the material with the low-pressure Sievert's apparatus. Thus this topic does not appear in the Results section.

2.1.3.3 Hydrogenation of melt spun-ribbons

Before the high-pressure stainless-steel device for hydrogen absorption from the gas phase was constructed, we tried to load hydrogen in melt-spun ribbons in our low-pressure Sievert's apparatus, as we did for mechanically alloyed and annealed powders. As expected, XRD showed no i-phase lattice expansion due to interstitial hydrogen. For this reason we built a high-pressure device for hydrogen aborption, in order to overcome the oxide layer barrier.

2.1.3.4 Dehydrogenation of melt-spun ribbons

Samples that were successfully loaded with hydrogen, which was checked by X-ray diffraction peaks shift to lower angles due to lattice expansion, were analyzed by TG-DTA/DSC with Gas Analytical System QMS 403 C Aëolos (STA 449 C/6/G Jupiter® - QMS 403 C, Netzsch, Germany) thermal analyzer with attached mass spectrometer. Around 25 mg of the sample was placed in an alumina pot and attached to a thermocouple on a microbalance. After three evacuation/argon refill cycles sample was heated from 30°C up to 800°C with 20 K/min heating rate. The mass change of samples and hydrogen molecule counts by the mass spectrometer were measured simultaneously. In Results (Chapter 3.3.1) we decided to show just an example of three curves, each corresponding to the amorphous, icosahedral and crystalline samples, since the shapes of these TG curves are very much alike. When loaded all three samples were subjected to the same hydrogenation conditions, i.e. 300°C, 45 bar for 500 minutes. The amount of desorbed hydrogen was measured by TG, since counts of H_2 are expressed in arbitrary units, which are good only for a quick, relative comparison, meaning, more hydrogen, higher intensities. For a calculation of the exact hydrogen content from the area under mass-spectra one should use standards and rather complex computational methods. Our device was not equiped with a standardization part.

2.1.3.5 Deuterization of melt-spun ribbons

By this method we investigated deuterium dynamics in the icosahedral and amorphous phases of the $Ti_{40}Zr_{40}Ni_{20}$ melt-spun ribbons (Gradišek, 2008). Results were analysed by dynamic lineshape and spin-lattice relaxation models that assume deuterium thermally activated hopping within a manifold of different chemical environments. The reason why deuterium has been used instead hydrogen is that during ^{1}H NMR H–H interactions prevail over H–alloy interactions.

Deuterim loading was performed from the gas phase by exposing the material to the D_2 atmosphere at room temperature and a pressure of 10 bar for i-phase sample and 20 bar for the amorphous sample. In order to perform ^{2}H NMR experiments, melt-spun samples were loaded with deuterium. This work was done at the Korea Basic Science Institute by our partners in the billateral project Korea-Slovenia Hydrogen Storage.

2.1.4 Arc-melting

By this technique one can easily prepare metallic samples of desired composition. The aim is to melt preliminarily pressed pellets of elements in the form of powders or small solid pieces pieces. These lumps are then placed on a specially designed water cooled copper plate, acting as the cathode. When the current is switched on, argon plasma arc is formed between the cathode (sample on a copper plate) and anode (typically tungsten rod), also predominantly water cooled. Upon a current flowing through the sample, it melts because of the resistance heating. Current of argon ions (plasma) in our Edmund Bühler Arc-Melter Type MAM-1, Figure 23, can be electronically controlled from 3 to 180 A. Typical batches of samples we used are around 5 grams, but depending on the density of the sample one could put even 20 grams of material in one sample casting mould. Depending on the quantity of sample its temperature can reach up to 3500°C.

a) b)

Figure 23: a) Edmund Bühler MAM-1 Arc-Melter, and b) melting chamber.

When the cathode plate is loaded with samples it is attached to a glass chamber, which is then evacuated (~5 min) and refilled with argon gas for two-three times. In order to completely remove the residual oxygen from the argon atmosphere we first melt a piece of titanium metal, the so-called getter, which reacts with residual oxygen forming TiO_2 that can be easily removed afterwards.

To analyze the structure of arc-melted buttons by XRD, those were cut in half horizontally. After that we polished the cross-section surface and expose it to X-rays. Arc-melted buttons of Ti-Zr-Ni alloys are shown in Figure 24.

Figure 24: Arc-melted buttons of Ti-Zr-Ni alloys. Each weights about 5 grams.

2.1.5 Quenched rods

Vacuum-casting, often called suction-casting or cold mould casting, is the last technique used for the preparation of quasicrystalline material in this dissertation, where cooling rate is simply controled by the diameter of the copper cold mould. The principle of rapid quenching of this method is similar to the melt-spinning one, only cooling rates are of the order of 10^2–10^3 K/s, which is comparable to those achived by melt spinning at the lowest wheel speeds, i.e., roughly estimated, somewhere between 10 and 20 m/s for our particular melt-spinner. This method has an advantage in the preparation of bulk metallic glasess (Chapter 1.2) or, though, bulk quasicrystalline samples, whereas by melt spinning one is able to produce only ribbons of such structures, that are appropriate for further characterization, but often not appropriate for application purposes. A smaller disadvantage of vacuum-casting is one gets smaller amount of the sample with one batch, aroung 1 gram, whereas by melt spinning we can get from 10 up to 20 grams of material during one run.

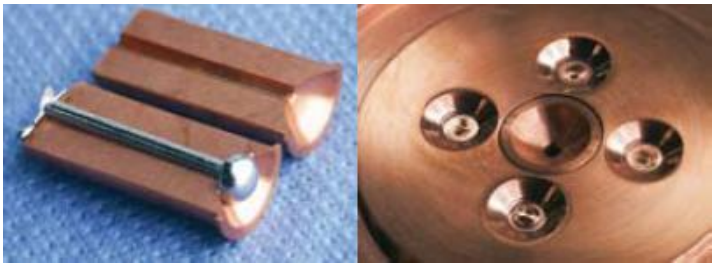

Figure 25: 3 mm rod cast in arc-melter MAM 1, and suction casting copper crucible plate.

Preparation of quenched rods looks very alike arc-melting (Chapter 2.1.4). The only difference is in the copper cathode plate, which has integrated a copper cooling mould of desired diameter (1.5, 2 and 3 mm in our case), attached to a vacuum chamber, Figure 25. So, when the sample is molten, we open the valve to the vacuum chamber and by this the melt is quickly sucked in the mould and quenches with the cooling rate, corresponding to the diameter of the copper mould used. For further analysis, as-cast rods were crushed in the mortar, where no liquid nitrogen cooling was required, since the rods were brittle enough at room temperature.

2.2 Characterization

2.2.1 X-Ray Diffraction (XRD)

X-ray diffraction is a method of determining the arrangement of atoms within a crystal, in which a beam of X-rays strikes a crystal and scatters into many different directions. From the angles and intensities of these scattered beams, a crystallographer can produce a three-dimensional picture of the density of electrons within the crystal. From this electron density, the mean positions of the atoms in the crystal can be determined, as well as their chemical bonds, their disorder and other sundry information.

An intuitive understanding of X-ray diffraction can be obtained from the Bragg model of diffraction. In this model, a given reflection is associated with a set of evenly spaced sheets running through the crystal, usually passing through the centers of the atoms of the crystal lattice. The orientation of a particular set of sheets is identified by its three Miller indices (*h, k, l*), and their spacing is denoted by *d*. William Lawrence Bragg proposed a model in which the incoming X-rays are scattered specularly (mirror-like) from each plane; from that assumption, X-rays scattered from adjacent planes will combine constructively (constructive interference) when the angle θ between the plane and the X-ray results in a path-length difference that is an integer multiple n of the X-ray wavelength λ, Equation 19.

$$2d\sin\theta = n\lambda \tag{19}$$

A reflection is said to be indexed when its Miller indices (or, more correctly, its reciprocal lattice vector components) have been identified from the known wavelength and the scattering angle 2θ. Such indexing gives the unit-cell parameters, the lengths and angles of the unit-cell, as well as its space group. Since Bragg's law does not interpret the relative intensities of the reflections, however, it is generally inadequate for solving the arrangement of atoms within the unit-cell; for that, a Fourier transform method must be applied.

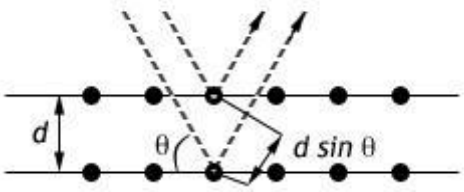

Figure 26: Interference of X-ray light, scattered on crystal planes.

XRD spectra of our samples were taken by Bruker AXS, D4 Endeavor spectrometer by using Cu-Kα radiation in the range from 30 to 80 degrees. Raw results were processed by Diffrac Plus Evaluation and Poudrix computer programmes.

2.2.2 X-ray Photoelectron Spectroscopy (XPS)

X-ray photoelectron spectroscopy (XPS) was applied to analyse the surface composition, chemical states and depth distribution of elements in the $Ti_{45}Zr_{35}Ni_{17}Cu_3$ ribbons. Surface analyses with similar technique of the oxide layers on Zr-based alloys were reported in the literature (Baunack et al., 2005).
The X-ray photoelectron spectroscopy (XPS or ESCA) analyses were carried out on the PHI-TFA XPS spectrometer produced by Physical Electronics Inc., Figure 27. In order to follow the depth distribution of the elements, XPS sputter depth profiling was applied. Ion sputtering was performed with a 1 keV Ar^+ beam rastered over a 3 x 3 mm^2 area. For these parameters a sputtering rate of about 1 nm/min was measured on the reference Ni/Cr multilayer structure. The analysed area was 0.4 mm in diameter and the analysed depth was about 3 nm. XPS spectra were excited by X-ray radiation from an Al-standard source. The base pressure in the spectrometer was 2 x 10^{-8} Pa. Relative sensitivity factors 2.08 for Ti 2p, 2.77 for Zr 3d, 2.31 for Ni $2p_{3/2}$, 2.63 for Cu $2p_{3/2}$, 0.31 for C 1s and 0.73 for O 1s, provided by the instrument producer were used to calculate the surface concentrations (Moulder et al., 1995). We estimate that the relative error for the calculated concentrations is about 20%. The XPS method is not sensitive for H and He.

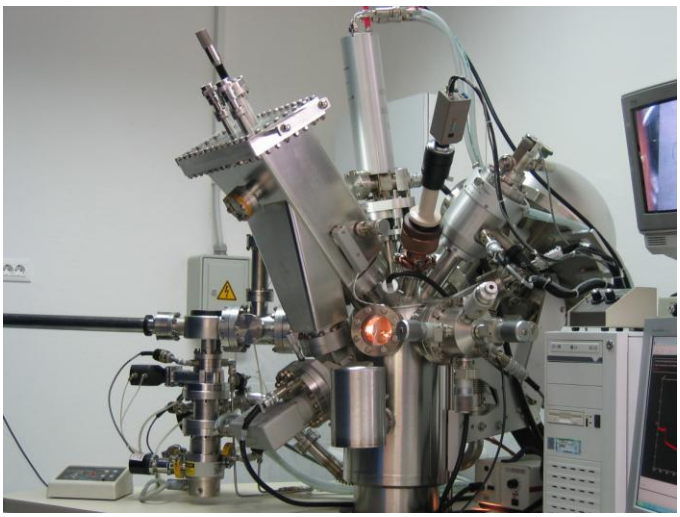

Figure 27: PHI-TFA XPS spectrometer produced by Physical Electronics Inc.

2.2.3 Scanning Electron Microscopy (SEM)

The scanning electron microscope (SEM) is a type of electron microscope that images the sample surface by scanning it with a high-energy beam of electrons in a raster scan pattern. The electrons interact with the atoms that make up the sample producing signals that contain information about the sample's surface topography, composition and other properties, such as electrical conductivity.

The types of signals produced by an SEM include secondary electrons, back scattered electrons (BSE), characteristic x-rays, light (cathodoluminescence), specimen current and transmitted electrons. These types

of signal all require specialized detectors for their detection that are not usually all present on a single machine. The signals result from the interactions of the electron beam with atoms at or near the surface of the sample. In the most common or standard detection mode, secondary electron imaging or SEI, the SEM can produce very high-resolution images of a sample surface, revealing details about 1 to 5 nm in size. Due to the way these images are created, SEM micrographs have a very large depth of field yielding a characteristic three-dimensional appearance useful for understanding the surface structure of a sample. A wide range of magnifications is possible, from about x 25 (about equivalent to that of a powerful hand-lens) to about x 250,000, about 250 times the magnification limit of the best light microscopes. Back-scattered electrons (BSE) are beam electrons that are reflected from the sample by elastic scattering. BSE are often used in analytical SEM along with the spectra made from the characteristic x-rays. Because the intensity of the BSE signal is strongly related to the atomic number (Z) of the specimen, BSE images can provide information about the distribution of different elements in the sample. For the same reason BSE imaging can image colloidal gold immuno-labels of 5 or 10 nm diameter, that would otherwise be difficult or impossible to detect in secondary electron images in biological specimens. Characteristic X-rays are emitted when the electron beam removes an inner shell electron from the sample, causing a higher-energy electron to fill the shell and release energy. These characteristic x-rays are used to identify the composition and measure the abundance of elements in the sample. Working principle of SEM, i.e. electrons path, detectors, lenses, etc., is shown in Figure 28.

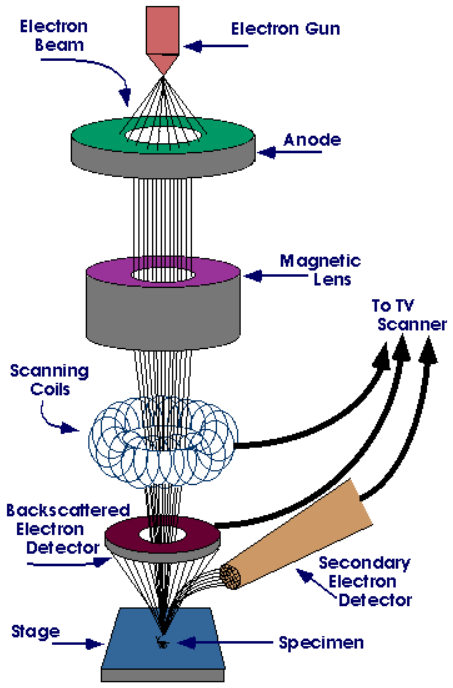

Figure 28: Scanning electron microscope (purdue.edu).

For observation of non-polished sample the powder was sputtered on conductive sticky tape impregnated with graphite powder and placed on the sample holder, which was then fixed in vacuum column of the microscope and evacuated for about 20 minutes until the pressure was ~10^{-4} bar.

For the preparation of polished sample the powder was moulded in metallographic specimen with Technovit resin. After polishing the specimen Technovit resin was removed, sample placed on the holder. Then the conductive graphite paste was sputtered between the sample and sample holder. After graphite paste dried the holder was placed in vacuum column and evacuated. After the high voltage was set (20 kV), the sample holder was moved from the initial to the central position. The apperture of the column was set to 100 μm. Finally, before switching the high-voltage on, the spot size of electron beam and working distance (WD) were set, where WD must be at least 10 mm for safety reasons and for optimal EDS analysis angle, as well.

2.2.4 Transmission Electron Microscopy (TEM)

Transmission electron microscopy (TEM) is a microscopy technique whereby a beam of electrons is transmitted through an ultra thin specimen, interacting with the specimen as they pass through. An image is formed from the interaction of the electrons transmitted through the specimen, which is magnified and

focused onto an imaging device, such as a fluorescent screen, as is common in most TEMs, on a layer of photographic film, or to be detected by a sensor such as a CCD camera. The first TEM was built by Max Knoll and Ernst Ruska in 1931, with this group developing the first TEM with resolving power greater than that of light in 1933 and the first commercial TEM in 1939, Figure 29.

TEMs are capable of imaging at a significantly higher resolution than light microscopes, owing to the small de Broglie wavelength of electrons. This enables the instrument to be able to examine fine detail -- even as small as a single column of atoms, which is tens of thousands times smaller than the smallest resolvable object in a light microscope. TEM forms a major analysis method in a range of scientific fields, in both physical and biological sciences. At smaller magnifications TEM image contrast is due to the absorption of electrons in the material, due to the thickness and composition of the material. At higher magnifications complex wave interactions modulate the intensity of the image, requiring expert analysis of observed images. Alternate modes of use allow for the TEM to observe modulations in chemical identity, crystal orientation, electronic structure and sample induced electron phase shift as well as the regular absorption based imaging.

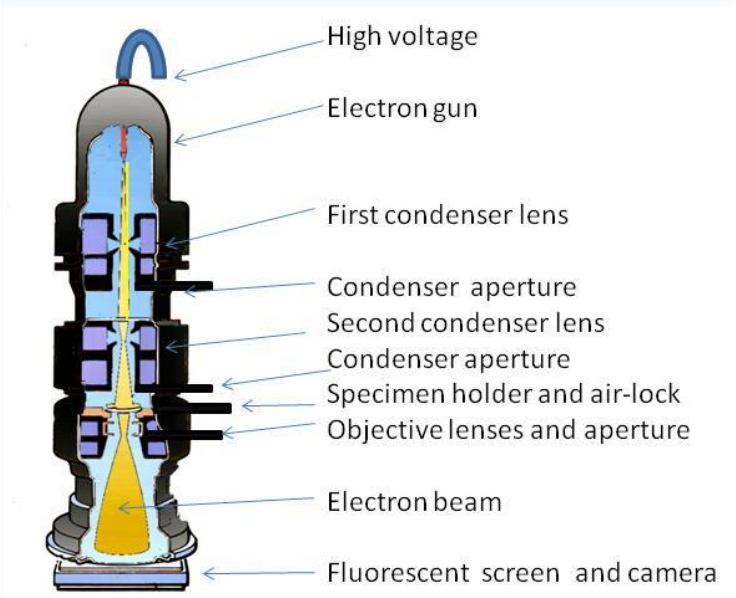

Figure 29: Transmission electron microscope, (findtarget.com).

The powders with an average grain size from 10 to 15 μm were dispersed in ethanol and deposited on carbon-coated Cu grid using ultrasonic sputtering. After the grid was dried we put it inside the column of transmission electron microscope 2010F (Jeol Ltd., Japan) operated at 200 kV and equipped with an ultra-high resolution pole-piece having the resolution limit at 0.11 nm. Preparation of melt-spun ribbons was more complicated, since they are very brittle. Since they are already quite thin (50 μm), we skipped the dimpling step, because otherwise we would introduce too much stress to the sample and it would break. To solve this problem we cut the melt-spun ribbon into a disc of 3 mm diameter and put it directly in the argon ion-mill (RES 010, Bal-Tec AG, Balzers, Liechtenstein) and etch it with 6 keV Ar^+ ions at an incidence angle of 10° until perforation of the disk in central area. This was followed by ion-polishing using 2 keV Ar^+ ions to produce large, electron-transparent regions with low ion damage at the specimen surface. TEM analysis (selected-area electron diffraction and bright-field imaging) was made with a Jeol JEM-2100 (Jeol Ltd., Tokyo, Japan) at 200 kV accelerating voltage.

2.2.5 Differential Scanning Calorimetry (DSC)

Differential scanning calorimetry (DSC) is a technique for recording the energy necessary to establish a zero temperature difference between a substance and a reference material against either time or temperature, as the two specimens are subjected to identical temperature regimes in an environment heated or cooled at a controlled rate.

It therefore follows that in DSC the sample and reference materials must be equipped with separate heating elements and have separate temperature-sensing devices, usually either thermocouples or temperature-sensitive resistors. The two materials are maintained at an identical temperature by electronically controlling the rate at which heat is supplied electrically to the test and reference samples respectively. The ordinate of a DSC curve thus represents the rate of energy absorption by the test sample,

relative to that of the reference material; this rate naturally depends on the heat capacity of the sample.

The thermal properties and the kinetics of the crystal phases that crystallised from the amorphous alloy were investigated using a differential scanning calorimeter, *TA Instruments*, Model DSC–2910.

2.2.6 Thermo-gravimetry (TG)

Thermo-gravimetry is an experimental technique in which the mass change of a substance is measured as a function of temperature whilst the substance is subjected to a controlled temperature program. The temperature program must be taken to include holding the sample at a constant temperature other than ambient, when the mass change is measured against time. Mass loss is only seen if a process occurs where the volatile component is lost. Results are presented as a plot of relative mass change, $\Delta m/m$, against temperature, T or time, t. It should be noted that although most mass loss occurs around one temperature, where the line is steepest, some reaction starts well before the main reaction temperature and, similarly, there is still some residual mass loss well after the main reaction. Picture of our TG device is shown in Figure 30 on the left.

2.2.7 Mass spectrometry (MS)

Hydrogen desorption experiments were performed by simultaneous TG-DTA/DSC with Gas Analytical System QMS 403 C Aëolos (STA 449 C/6/G Jupiter® - QMS 403 C, Netzsch, Germany) thermal analyzer with attached mass spectrometer. About 25 mg of loaded sample was placed in the alumina pot and fixed on a thermocouple attached on the microbalance with 0.1 μg accuracy. After chamber was evacuated and refilled with argon three times the heating and argon flow were turned on. Heating rate was set to 20 K/min and the final temperature was 800°C. The carrying argon flow was set to 30 ml/min.

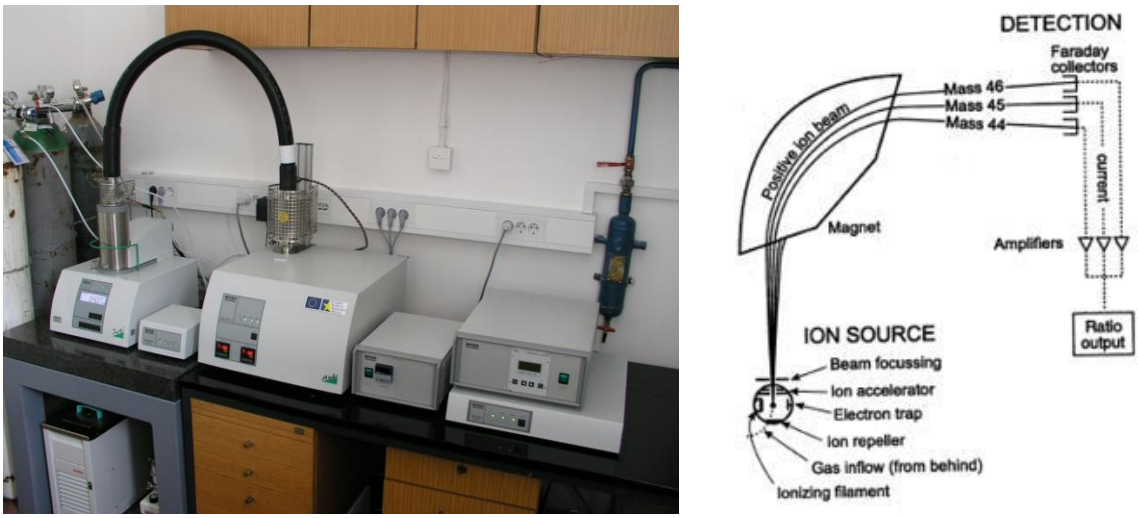

Figure 30: TG-DTA/DSC with Gas Analytical System QMS 403 C Aëolos (STA 449 C/6/G Jupiter® - QMS 403 C, Netzsch, Germany) thermal analyzer with attached mass-spectrometer. On the right, corresponding schematics is shown.

2.2.8 Vibrating-Sample Magnetometer (VSM)

Maybe the most commonly used method of characterization for magnetic materials is the Vibrating-Sample Magnetometer (VSM) that uses an induction technique, Figure 31. In a VSM the sample is mounted at the end of a rigid rod attached to a mechanical resonator, which oscillates the sample, usually in a vertical direction, at a fixed frequency, ω. In the current VSM ω= 80 Hz. Surrounding nearby the sample is a set of pick-up coils. As the sample moves, its magnetic field which is proportional to its magnetic moment, *M*, alters the magnetic flux through the coils, *dM/dt*. This induces a current directly proportional to *dM/dt*, which can be amplified and detected using lock-in amplifiers. The external magnetizing field is provided by a horizontal electromagnet. Magnetic hysteresis loops were measured by VSM LakeShore 7003 device at room temperature in field range from 10 KOe (1 T) to – 10 kOe back to 10 kOe.

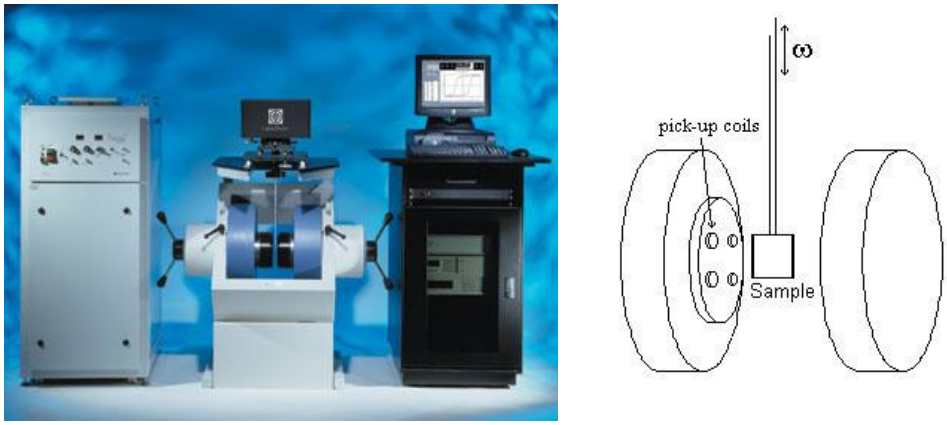

Figure 31: LakeShore vibrating-sample magnetometer and related schematics on the right.

2.2.9 Superconducting Quantum Interference Device (SQUID)

Since the signal-to-noise ratio in the VSM was too low, when performing temperature-dependent measurements at 0.5 T external field, these experiments were done by Quantum Design MPMS-XL magnetometer, which can operate at maximum external magnetic field 5 T in 1.9 – 400 K temperature range. Field uniformity is 0.01 % over 4 cm and sensitivity up to 10^{-14} T. The main advantage of this magnetometer is very high sensitivity, since it can measure the magnetic field of neural currents in the brain at 10^{-13} Tesla. The main disadvantage are costs related to consumption of liquid helium, which enables superconducting loop, based on a triple layer of aluminum and niobium, to be cooled on 5 K.

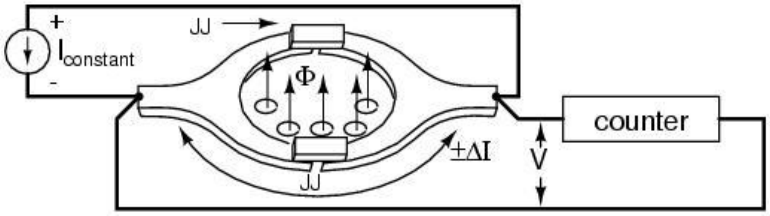

Figure 32: Superconducting quantum interference device (SQUID): Josephson junction pair within a superconducting ring. A change in flux produces a voltage variation across the JJ pair.

The JJ in Figure denotes a so-called Josephson junction, tri-layer of aluminum and niobium superconductor, bridged by a thin insulator. Electrons can tunnel through the insulator even with zero voltage applied across the superconductors. If a voltage is applied across the junction, the current decreases and oscillates at a high frequency proportional to the voltage. The relationship between applied voltage and frequency is so precise that the standard volt is now defined in terms of Josephson junction oscillation frequency. The Josephson junction can also serve as a hyper-sensitive detector of low level magnetic fields. It is also very sensitive to electromagnetic radiation from microwaves to gamma rays.

A constant current bias is forced across the ring in parallel with both Josephson junctions. The current divides equally between the two junctions in the absence of an applied magnetic field and no voltage is developed across the ring. While any value of magnetic flux (Φ) may be applied to the SQUID, only a quantized value (a multiple of the flux quanta) can flow through the opening in the superconducting ring. If the applied flux is not an exact multiple of the flux quanta, the excess flux is cancelled by a circulating current around the ring which produces a fractional flux quanta. The circulating current will flow in that direction which cancels any excess flux above a multiple of the flux quanta. Changing the applied flux linearly causes the circulating current to vary as a sinusoid. This can be measured as a voltage across the SQUID. As the applied magnetic field is increased, a voltage pulse may be counted for each increase by a flux quanta.

2.2.10 ²H NMR

2.2.10.1 Dynamic NMR lineshape

Our choice to perform NMR measurements on the ²H nuclei instead of ¹H is based on the following difference between the two isotopes. Protons (spin-1/2 nuclei) possess a strong nuclear magnetic dipole moment but no electric quadrupole moment, so that protons are strongly dipolarly coupled among themselves, but much more weakly to the lattice. In a motional process, the resonance frequency of a proton is predominantly affected by the fluctuating magnetic fields of other protons, thus this interaction is not specific to a particular lattice site. Deuterons (spin-1 nuclei) make nuclear dipole-dipole interaction between themselves by a factor 42 smaller and due to the nonzero electric quadrupole moment, deuterons interact with the electric field gradient (EFG) tensor of the neighbouring charges and the quadrupole interaction dominates over the dipolar one. The EFG is specific to each lattice site. Fast isotropic molecular motions average these interactions to zero, producing a complete motional narrowing of the NMR spectrum at high temperatures, whereas at low temperatures, a static spectrum is observed. The dynamic lineshape transition from the fast- to the slow-motion regime allows the extraction of the physical parameters of the motional processes - the correlation time, and the activation energy of hopping. The ²H NMR lineshape measurements were performed in a cooling run from 400 to 77 K at the deuterium Larmor frequency ν_0 (²H)=30.701 MHz.

2.2.10.2 NMR spin-lattice relaxation

While the dynamic NMR lineshape is sensitive to molecular motions in the 1-100 kHz frequency window, the NMR spin-lattice relaxation rate $1/T_1$ probes motions with MHz frequencies in the vicinity of the nuclear Larmor frequency. For the thermally activated hopping, $1/T_1$ is expected to sense the same motion as the dynamic NMR lineshape, but at higher temperatures, when the hopping frequencies speed up from the kHz to the MHz range. The ²H T_1 experiments were performed in the temperature range between 430 and 77 K.

2.2.11 Density measurement

Using the so-called Archimedes' technique (Figure) we were able to measure the densities of our bulk samples (arc-melted buttons and quenched rods). The principle is to measure the mass of the sample in an ambient air atmosphere (dry mass) and its mass in the water (wet mass), in order to calculate the volume of the sample from the difference between dry and wet mass of the sample. This is the mass of displaced water on account of the sample's volume and so due to buoyancy it is lighter in the water. Since the density of pure water is very close to 1 g/cm³, we can take the mass difference as the volume of the sample, and calculate its density by dividing its dry mass by the volume of the sample. The tricky part of these measurements is to fix the sample with the human hair loop and hang it on the balance. And to make the loop with the human hair can be very challenging as well.

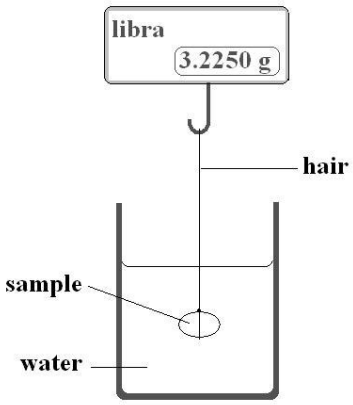

Figure 33: Archimedes' principle of volume measurement via displaced water mass.

3 Results

3.1 Mechanical alloying

3.1.1 X-ray diffraction

The XRD spectra in
Figure 34 indicate that the mixture was to a large extent amorphous when it was alloyed for more than 40 h; for 20 h and less the material still exhibited crystalline properties, as Lee et al. (2002) have also observed. The sharp peaks present in the XRD spectra of both samples at 38.5° belong to the aluminium sample holder.

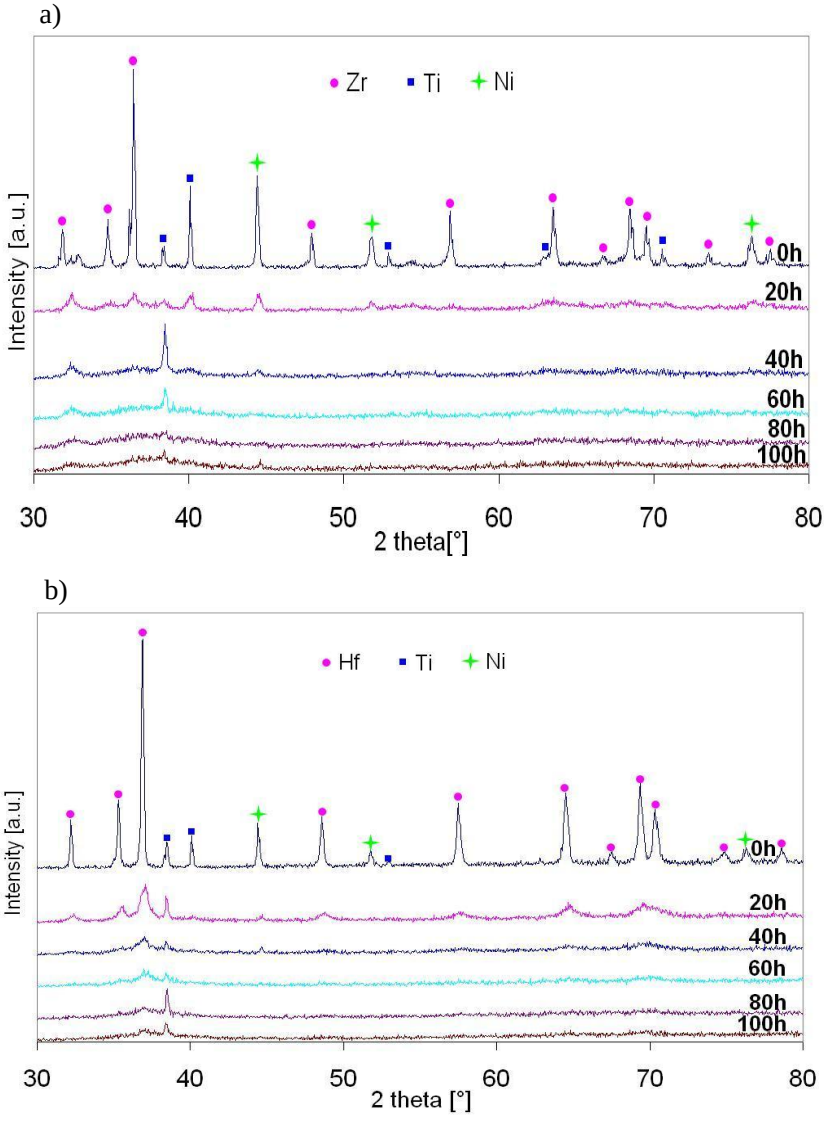

Figure 34: XRD patterns (a) of the $Ti_{40}Zr_{40}Ni_{20}$ and (b) $Ti_{40}Hf_{40}Ni_{20}$ after alloying for 0, 20, 40, 60, 80 and 100 h.

3.1.2 SEM and EDS analysis

For observations of the non-polished sample the powder was sputtered on conductive graphite sticky tape and placed on a sample holder, which was then fixed in the vacuum column of a Jeol JSM-5800 microscope and evacuated until the pressure was 10^{-4} bar. The working voltage of the SEM filament was 20 kV. The energy-dispersive X-ray spectrometer was a Link ISIS 300, Oxford Instruments. Observation of the non-polished sample using the secondary-electron detector, Figure 35a, gave us information about the topography of ball-milled powder particles. We saw that during mechanical alloying the agglomeration of submicrometer particles occurs. The size distribution of the agglomerates goes approximately from 10 to 200 μm and their average size is estimated to be around 100 μm.

Figure 35b reveals the cross-section z-contrast of the agglomerates with a back-scattered electrons detector. For this purpose the powder was moulded into fenol-formaldehide resin inside glass tube and then ground and polished. EDS analysis of bright areas in the inner part of agglomerates showed this is a Zr-rich phase.

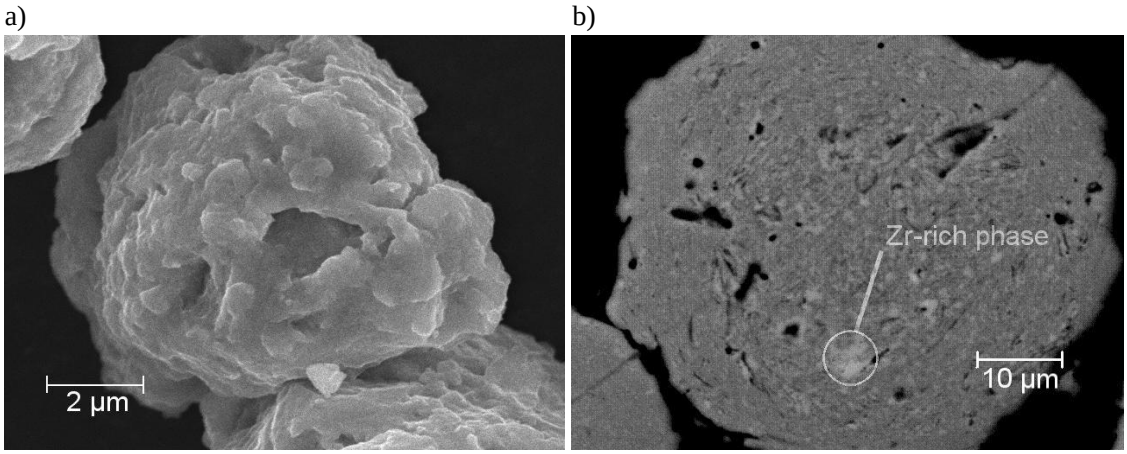

Figure 35: SEM micrographs of a) agglomerated non-polished powder particle, consisting of much smaller particles, and b) z-contrast image of polished agglomerate revealed presence of Zr-rich phase in the bulk.

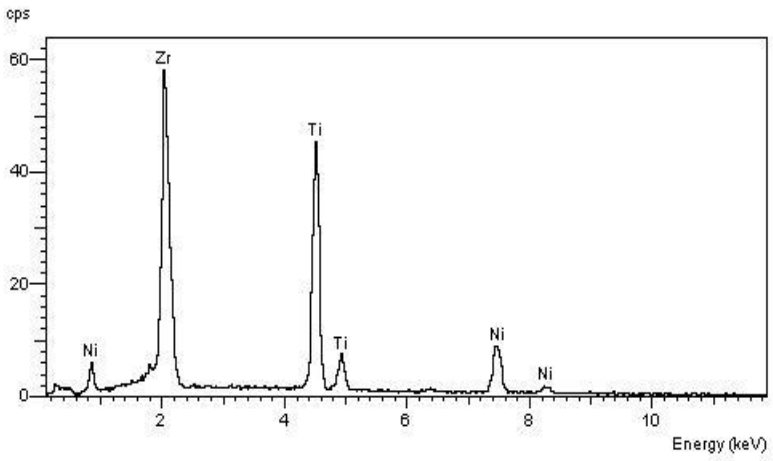

Figure 36: EDS spectrogram of polished $Ti_{45}Zr_{38}Ni_{17}$ agglomerate of ~ 5 μm² dark grey area, shown in Figure 35b.

	Ti	Zr	Ni
Stoichiometric at. %	45	38	17
EDS at. % 1.area	47,2	33,7	19,1
EDS at. % 2.area	49,7	30,1	20,2
EDS at. % 3.area	48,3	31,3	20,4

Table 5: Quantitative analysis of energy-dispersive spectrum (EDS) of three random ~ μm² areas on $Ti_{45}Zr_{38}Ni_{17}$ polished aglomerate.

3.1.3 DSC measurements

The DSC curves (Figure 37) were obtained by placing the samples of about 20 mg in open platinum sample pans, and using a heating rate of 10 K/min in an argon atmosphere at a flow rate of 100 ml/min. The DSC was calibrated with indium. For the purposes of the kinetic calculation of crystallization the alloys were heated from room temperature to 700°C using five different heating rates: 2, 5, 10, 15 and 20 K/min, Figure 39.

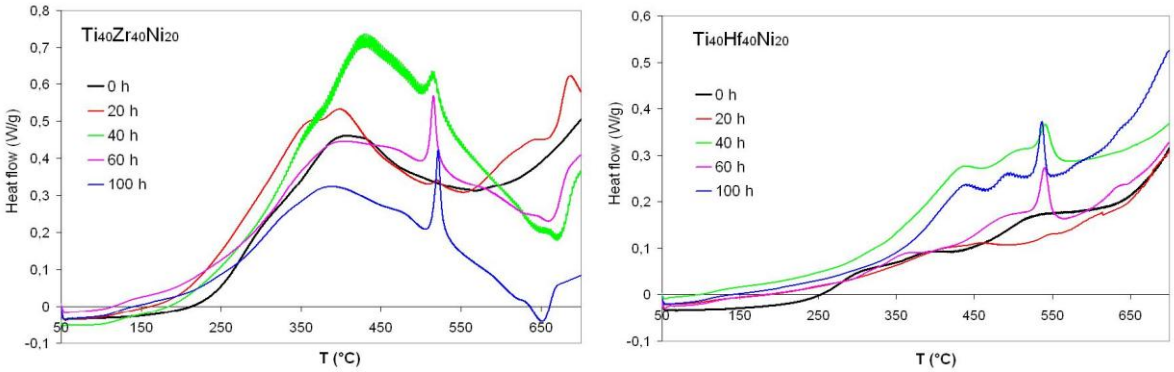

Figure 37: DSC results of $Ti_{40}Zr_{40}Ni_{20}$ and $Ti_{40}Hf_{40}Ni_{20}$ samples, mechanically alloyed for various times, recorded at heating rate 10 K/min.

For each mixture measured with a different heating rate the heat of crystallisation was observed. The heat of crystallisation is calculated as the sum of the peak segment area divided by the average temperature of the segment and multiplied by the differential scanning calorimeter's cell constant, Equation 20,

$$H = \frac{1.2218}{m} \int_{T_0}^{T_f} A(T)dT \tag{20}$$

where H is the heat of crystallisation, K the cell constant, m the mass of the sample and $A(T)$ is the segment area of the peak.

The calculated heats of crystallisation for the measured samples are shown graphically in Figure 38. For the $Ti_{40}Hf_{40}Ni_{20}$ mixture the heat of crystallisation does not show a significant change for different alloying times, while the heat of crystallisation for the $Ti_{40}Zr_{40}Ni_{20}$ mixture increases with alloying time.

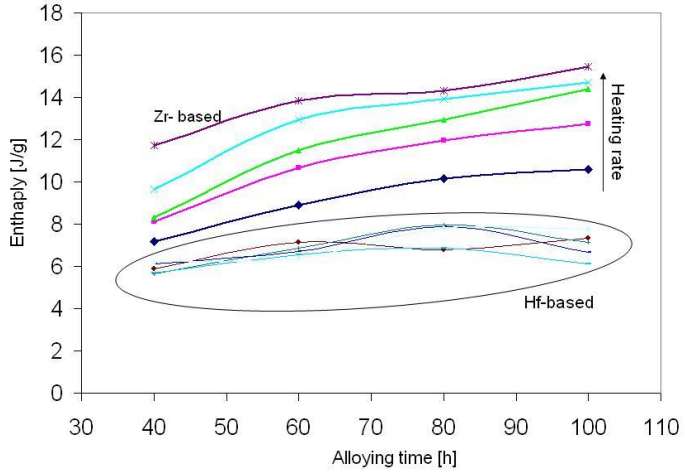

Figure 38: Heat of crystallisation vs. alloying time, for both compositions, measured at five different heating rates: 2, 5, 10, 15 and 20 °C/min.

This increase in the enthalpy of the crystallization for $Ti_{40}Zr_{40}Ni_{20}$, which can be described by the exponential model, is in accordance with the increasing content of amorphous phase, which can also be seen as an effect in Figure 37.

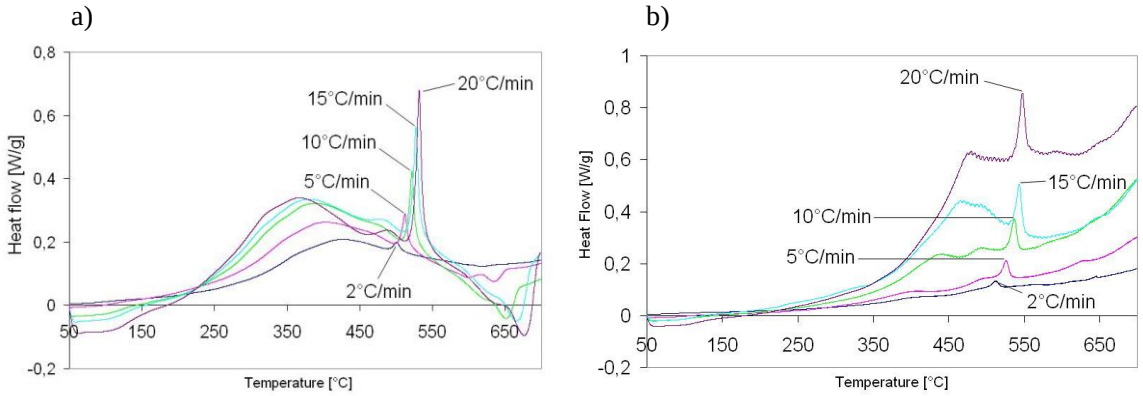

Figure 39: DSC curves recorded at five different heating rates for (a) $Ti_{40}Zr_{40}Ni_{20}$ and (b) $Ti_{40}Hf_{40}Ni_{20}$ powder mechanically alloyed for 100 h.

3.1.3.1 Activation energy of crystallization

Non-isothermal experiments that use a constant heating rate until the crystallisation is complete are preferred over isothermal experiments. Such experiments are frequently used to study crystallisation kinetics. Several kinetic methods are employed to determine the activation energy for crystallization from DTA and DSC data, of these the Kissinger equation (Equation 21) is one of the most widely used

$$\ln\left(\frac{\Phi}{T_p^2}\right) = \frac{-E_a}{RT_p} + a \tag{21}$$

where T_p is the peak temperature, Φ the DTA heating rate, R is the gas constant, and a is fit parameter. A plot of $\ln(\Phi/T_p^2)$ versus $1/T$ should be a straight line, the slope of which provides the activation energy for the crystallisation. A linear relationship between $\ln(\Phi/T_p^2)$ and $1/T_p$ for the dominant high-temperature peak was obtained in accordance with Equation 21, see Figure 40, for the $Ti_{40}Hf_{40}Ni_{20}$ material. Activation energies E_a for crystallization of Zr- and Hf-based alloys, mechanically alloyed for various times, were determined as the slope of the corresponding Kissinger plots, Figure 41.

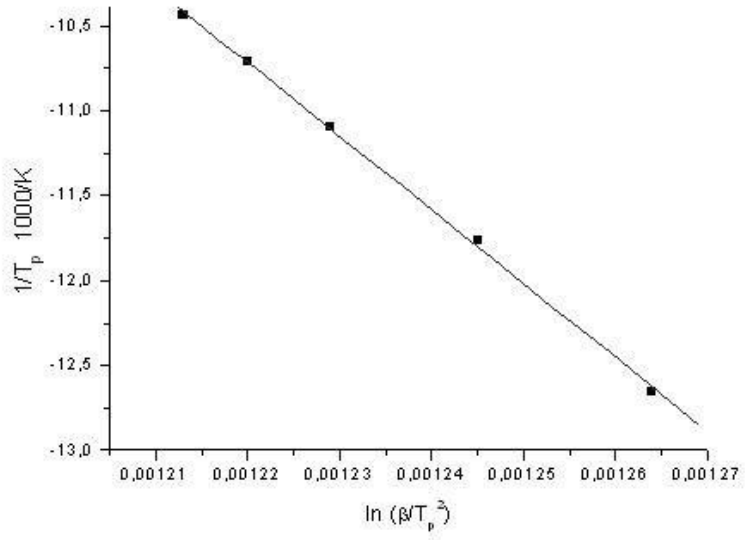

Figure 40: An example of the Kissinger plot of $Ti_{40}Hf_{40}Ni_{20}$ (after 100 h of mechanical alloying) for determining the activation energies.

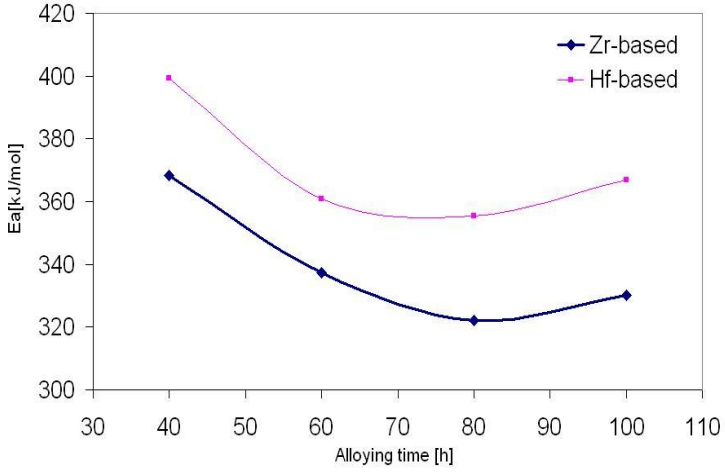

Figure 41: Dependence of activation energy of crystallization on alloying time for Zr- and Hf-based alloys.

The value of the Avrami time exponent, *n*, in the well-known Johnson–Mehl–Avrami equation for the time dependence of a nucleation-and-growth transformation was determined from the Ozawa equation (Equation 22), rearranged as:

$$\frac{d\left[\ln(-\ln(1-X))\right]}{d\ln\Phi} = -n \tag{22}$$

where X is the volume fraction crystallized at a fixed temperature T when heated at heating rate Φ. X is taken as the ratio of the partial area at a certain temperature to the total area of the crystallization exotherm. The volume fraction crystallized was calculated at a fixed temperature of 530 °C and the Ozawa plot of $\ln(-\ln(1-X))$ versus $\ln\Phi$ is not shown. The value of n determined from the slope of the plot was 3. A value of 1, representing a fixed number of nuclei and one-dimensional diffusion-controlled growth, is usually found for surface crystallization. In addition, when surface crystallization predominates, $m = n = 1$ and Equation 23 essentially reduces to the Kissinger equation, Equation 21. The value of $n = 3$ suggests that the crystallization did not occur on a fixed number of nuclei. The value of m is related to n as $m = n - 1$, when nucleation occurs during DSC and the number of nuclei in the sample is inversely proportional to the heating rate.

Matusita and Sakka stated that the Kissinger model is only valid when crystal growth occurs on a fixed number of nuclei. They modified the Kissinger equation to account for nucleation and crystal growth occurring simultaneously to be

$$\ln\left(\frac{\Phi^n}{T_p^2}\right) = \frac{-mE}{RT_p} + const. \tag{23}$$

where E_c is the activation energy of the crystallization and m represents the dimensionality of the crystalline phase. The calculated value of m is 2. When the surface crystallization predominates, $m = 1$, and when the crystallization is predominantly bulk, $m = 3$. Moreover, for a constant heating rate a broad crystallization peak indicates surface crystallization, whereas a sharp peak signifies a bulk crystallization process. Based on their interpretation and results, Figure 39 shows that bulk crystallization dominates in the measured samples.

Substituting the values of m and n into the modified equation yielded an activation energy, Figure 41, which is considerably higher than the value of the Kissinger model.

The calculated activation energies resulting from the Kissinger and the modified Kissinger equations for all of the measured samples are shown in Figure 41. These values are in good agreement with the other results obtained in this study. The dependence of the activation energies on the alloying time shows the same shape for both samples, i.e., it decreases with alloying time. From these curves we can say that the alloying process has the same influence on the activation energy of the crystallization in both cases.

The activation energy is a measure of the thermal energy needed for an atom to overcome the barrier of crystallisation. These results show that the crystallisation of the i-phase can occur relatively easily for

$Ti_{40}Hf_{40}Ni_{20}$ materials, and rather less so for $Ti_{40}Zr_{40}Ni_{20}$ materials. On the other hand, the crystallisation of $Ti_{40}Zr_{40}Ni_{20}$ more easily occurs after shorter times of alloying, which is a measure of the stored energy introduced to the system during the mechanical alloying.

3.1.4 Magnetic measurements

Figure 43 shows a decrease of magnetization, measured at 1 Tesla, for $Ti_{40}Zr_{40}Ni_{20}$ and $Ti_{40}Hf_{40}Ni_{20}$ samples after different alloying times. Since the major magnetic moment carrier are Ni d electrons, the reason for this decrease must be a modification of Ni d states upon alloying. Belin-Ferré et al., 2002, have shown that the electronic structure of icosahedral Ti-Zr-Ni quasicrystal is dominated by the metals d bands with a complete mixing of Ti and Zr states. And further more the authors claim: "With respect to the pure metal, Ni d states appear to be strongly modified upon alloying". They did the calculation just for Zr-based alloys, but according to our measurements, the Ni d states are modified in the Hf-based alloys as well.

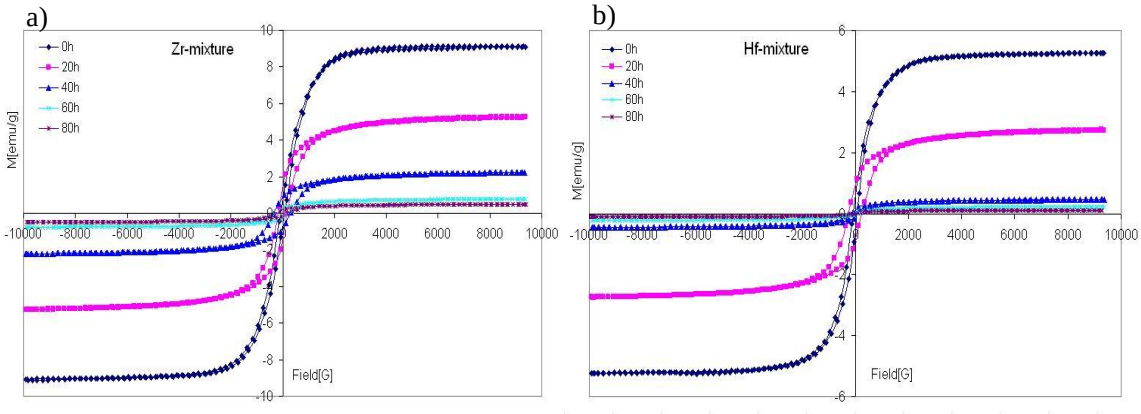

Figure 42: VSM hysteresis curves of a) Zr-based and b) Hf-based alloys, measured after 0, 20, 40, 60 and 80 hours of milling.

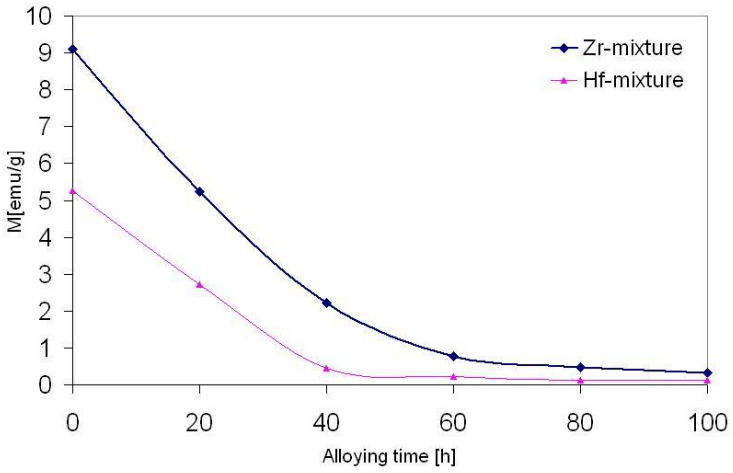

Figure 43: Magnetization (at 1 Tesla) of Zr- and Hf-based alloys decreases with alloying time. After 100 hours it is reduced for more than 95 %.

The magnetization drop, measured at 1 Tesla, is for both alloys more than 95 % after 100 hours of mechanical alloying in a planetary ball-mill, Figure 43. After that time the magnetization practically does not change anymore. A question arises from these results, namely, could the amorphisation of nickel cause this decrease of magnetization. For that reason we ball-milled pure nickel powder and measured the magnetic response every 20 hours. The results in Figure 44 show that the saturation magnetization of nickel (at 1 Tesla) remains constant and independent of the alloying time and its amorphization as the consequence of ball-milling.

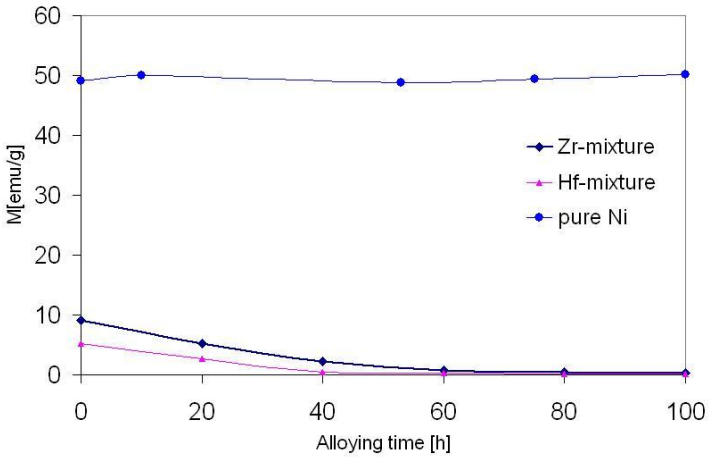

Figure 44: Magnetization (at 1 Tesla) plot of $Ti_{40}Zr_{40}Ni_{20}$, $Ti_{40}Hf_{40}Ni_{20}$ and pure Ni samples versus alloying time.

3.1.5 Heat treatment

As already mentioned in the introduction the amorphous phase has the highest Gibbs free energy, which means it tends to crystallize in energetically more favourable icosahedral quasicrystalline phase at 500°C and later on at 700°C in FCC (Ti/Zr)- or (Ti/Hf)-rich solid solutions, respectively. In the case of Zr-based alloy we observed a small amount of BCC β-(Ti, Zr) and Zr_2Ni (I4/mcm) as well, Figure 45.

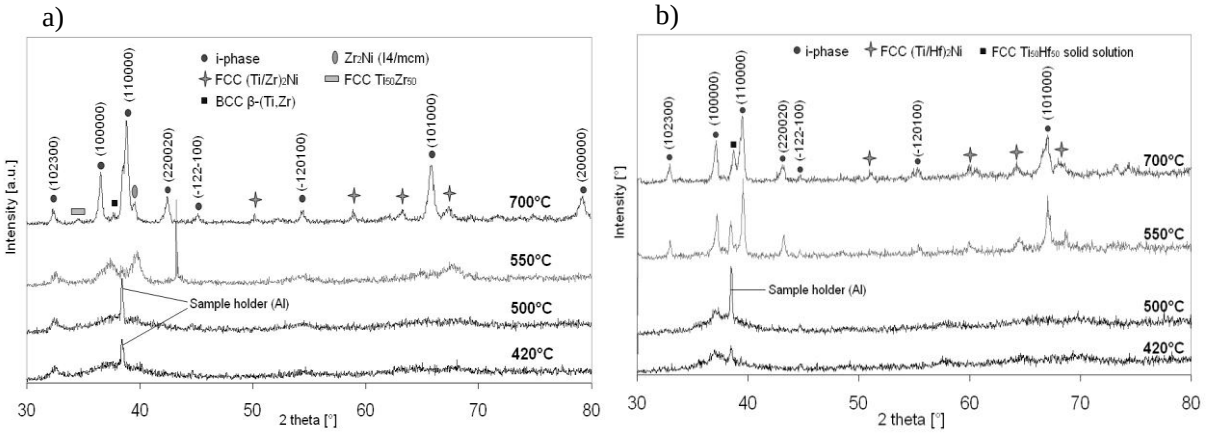

Figure 45: XRD patterns (a) of the $Ti_{40}Zr_{40}Ni_{20}$ and (b) $Ti_{40}Hf_{40}Ni_{20}$ after alloying for 60 h and heat treating at various temperatures. The heating rate was 10 K/min.

As mentioned before, we did not manage to hydride these samples using the low-pressure Sievert's apparatus, since at the time these experiments were performed, high-pressure device was not manufactured yet. To avoid the oxidation of the powder during mechanical alloying in technical argon (still contains some oxygen) we did the same experiment in hydrogen atmosphere, as was reported by Takasaki and Kelton in 2002, only starting with elemental powders. Results of these experiment are described in the following section.

3.1.6 Mechanical alloying in hydrogen atmosphere

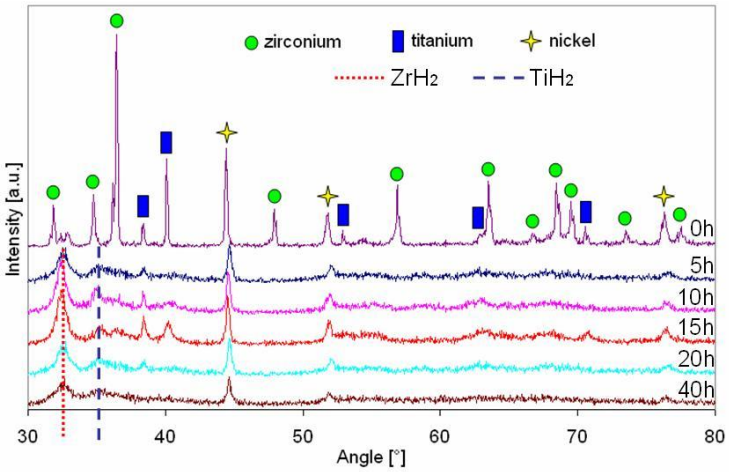

Figure 46: XRD spectra of samples mechanically alloyed in a hydrogen atmosphere.

After 40 hours of milling in hydrogen the particle size reduced to submicrometer level, mainly due to the decrepitation and increased internal tensions, due to lattice expansion, that secondary forces glued all powder particles onto the milling vial preventing any further contact between the milling bodies and most of the sample, Figure 47. Thus the amorphization of these alloys is not fully possible in a hydrogen atmosphere, Figure 46. In particular, the nickel peak around 44° and the zirconium hydride peak around 32.5° are quite obvious. The fact that nickel XRD peaks are still present prooves our observation that particle size reduction comes mainly from the reactions with hydrogen, mentioned above. Since there is no sign of nickel hydride, nickel grains were diminished to a smaller extent, also protected from the milling bodies inside the TiH_2 and ZrH_2 matrix, which made a protective layer around the bigger nickel particles.

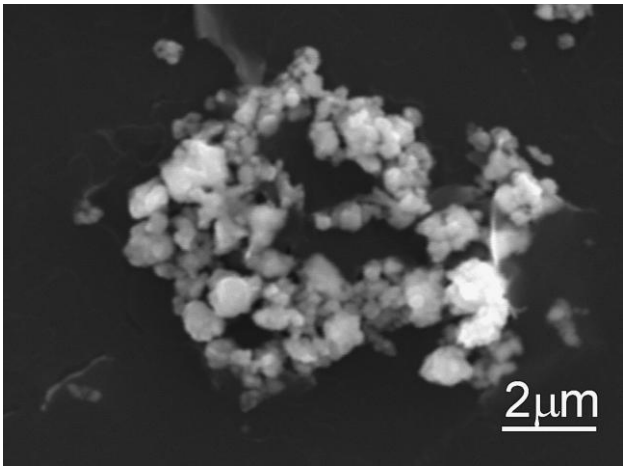

Figure 47: SEM image of submicrometer particles of $Ti_{40}Zr_{40}Ni_{20}$ powder after 40 hours of mechanical alloying in a hydrogen atmosphere.

The VSM results in Figure 48 have provided us with additional proof that the modification of magnetization (at 1 Tesla) comes from alloying ferromagnetic nickel with paramagnetic titanium and zirconium and thus changing the electronic structure, more precisely the Ni d-states, which give a major magnetic contribution to this alloy. Since Zr and Ti react with hydrogen, Ni remains unmodified, as mentioned before, which we showed by XRD analysis as well.

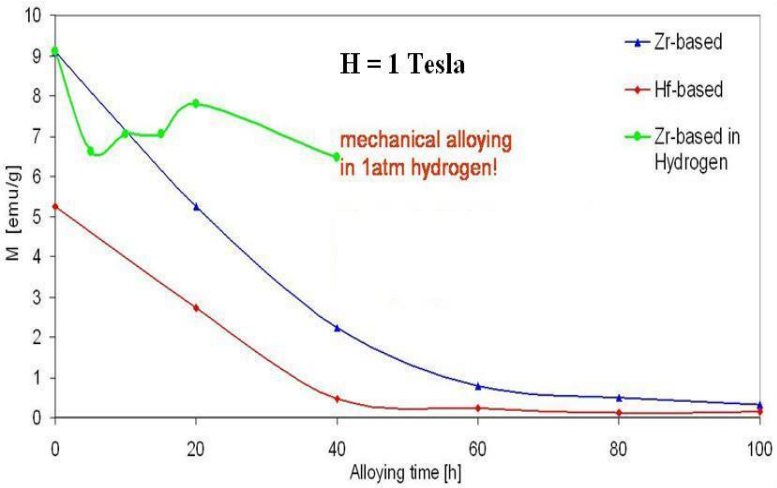

Figure 48: Magnetization (at 10 kOe) decrease is significant when alloyed in argon, but not so significant when alloyed in hydrogen.

3.2 Melt spinning

3.2.1 Wheel speed effect

According to Figure 18 we expected big influence of cooling rate on the crystallographic structure of melt-spun ribbons. According to that TTT diagram by rapid quenching one always ends up with at least two phases, except amorphous phase can be on its own in the system. In Figure 49 are the XRD spectra of the ribbons, melt-spun at various wheel speeds. For the $Ti_{45}Zr_{35}Ni_{17}Cu_3$ material we observed the i-phase is formed over a large interval of wheel speeds, from 14 m/s up to 50 m/s, where signs of nanoquasicrystallinity are evident, since the amorphous halo of the predominant amorphous phase still contains small i-phase peaks, implying nano i-phase grains are embedded in an amorphous matrix. A graphite crucible was used to perform the melt spinning experiments on $Ti_{45}Zr_{35}Ni_{17}Cu_3$ material.

On the other hand, we have got quite surprising XRD results from the $Ti_{40}Zr_{40}Ni_{20}$ material melt-spun at different wheel speeds as well, only by using a BN crucible. At low wheel speeds, around 15 m/s, there is practically no difference in the structure of the $Ti_{45}Zr_{35}Ni_{17}Cu_3$ and $Ti_{40}Zr_{40}Ni_{20}$ material. In both cases the C14 Laves phase peaks show up. But when we increase the wheel speed the $Ti_{40}Zr_{40}Ni_{20}$ ribbons, as-spun by BN crucible, become amorphous already at 32 m/s. We suspected this phenomenom has nothing to do with the composition, and that it should be connected with the crucible. That is why we performed additional experiments to proove this hypothesis. The results are shown in Chapter 3.2.5.

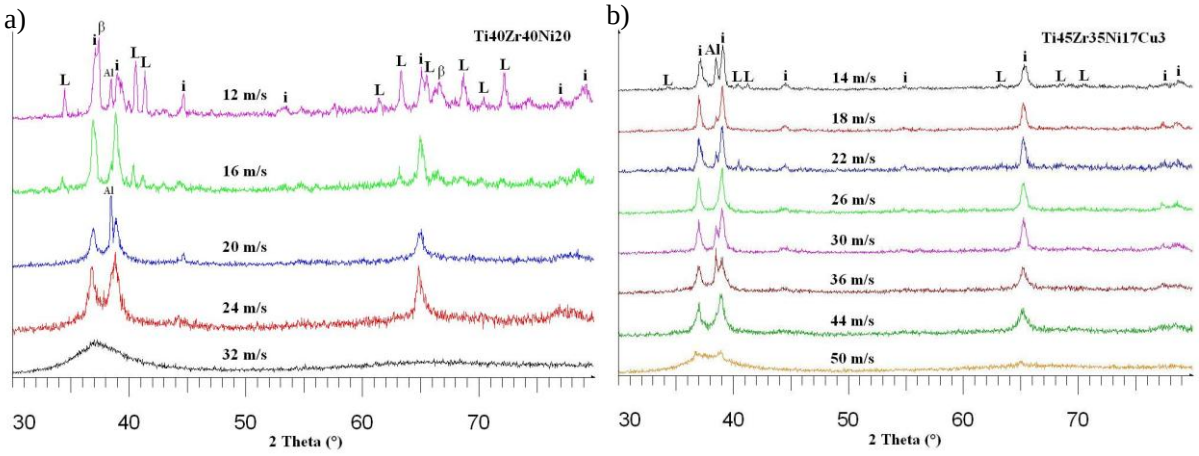

Figure 49: XRD spectra of a) $Ti_{40}Zr_{40}Ni_{20}$ and b) $Ti_{45}Zr_{35}Ni_{17}Cu_3$ ribbons melt-spun at different wheel speeds.

Figure 50 contains VSM hysteresis curves of $Ti_{40}Zr_{40}Ni_{20}$ samples, melt-spun at various wheel surface velocities, i.e. 12, 16, 20, 22, 24, 28, 32, 36 and 40 m/s, by using BN crucible.

Furthermore, Figure 51 shows that the thickness of the ribbons decreases with wheel speed from 120 to 30 micrometers, but the magnetizations of the samples, measured at 1 Tesla, of both materials seem to be largely independent of the wheel speed, and, consequently, the structure and thickness of the ribbons. All of the measured values for the magnetization, for both compositions and for all eight wheel speeds, were between 0.02 and 0.03 emu/g. For all the materials, straight-line magnetisation curves with the absence of any remanence were indicative of paramagnetic behaviour.

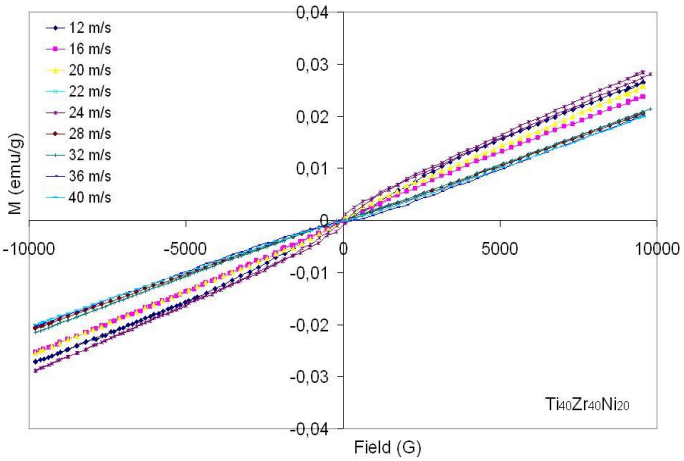

Figure 50: VSM data of $Ti_{40}Zr_{40}Ni_{20}$ samples, melt-spun at series of wheel speeds and therefore having diffrrent structural states.

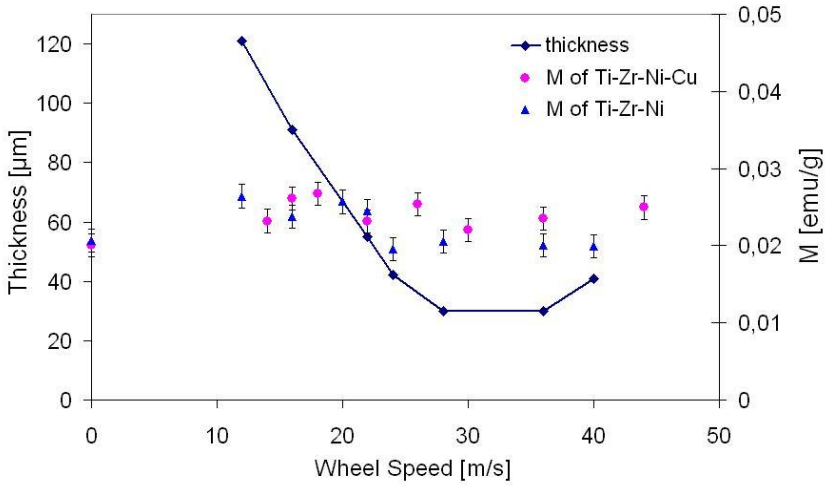

Figure 51: Thickness and magnetization at 1 Tesla of ribbons spun at various wheel speeds for the $Ti_{40}Zr_{40}Ni_{20}$ and $Ti_{45}Zr_{35}Ni_{17}Cu_3$ materials.

By results, shown in Figure 52, we have even better insight in C14 Laves phase formation, namely at wheel speeds above 30 m/s there are no Laves phase peaks present, whereas when we decrease wheel speed from 30 m/s down to 18 m/s we observe those crystalline peaks get sharper and more intense (all not marked peaks). At the same time, i-phase peaks (marked by *i*) become less difuse at the bottom, which implies on diminishing of amorphous phase (around 38°) and on bigger i-phase grains, when the wheel speed decreases.

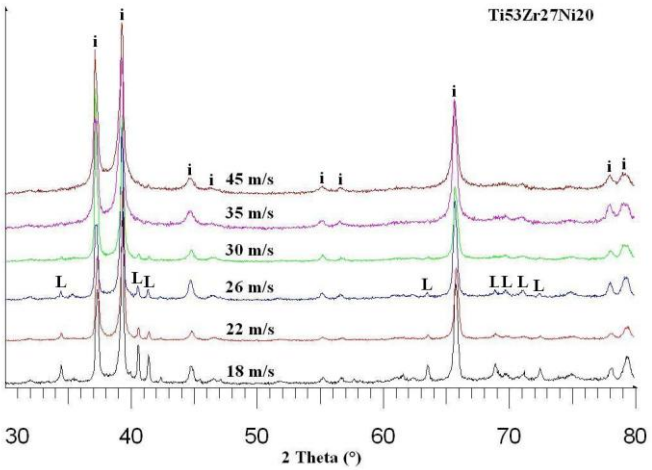

Figure 52: XRD spectra of $Ti_{53}Zr_{27}Ni_{20}$ ribbons, melt-spun at various wheel speeds.

3.2.2 Composition effect on the structure and the cell parameters

By performing a large number of melt-spinning experiments we saw that the optimal wheel speed for i-phase formation and ideal shape of ribbons is 22 m/s. We investigated the range of compositions in which i-phase is formed, at optimal melt-spinning conditions. Figure 53 shows XRD data of this investigation. Clearly, i-phase is formed over a relatively wide compositional area, where the Ti concentration varies from 40 to 58 atomic % by substituting Zr. Also, we substituted Zr with 3 and 5 at. % Cu. Clearly, the i-phase cell constant a_q decreases with Ti content, since i-phase XRD peaks move to higher 2 theta values. Even lattice parameters of secondary phases shrink, though not to such an extent as i-phase.

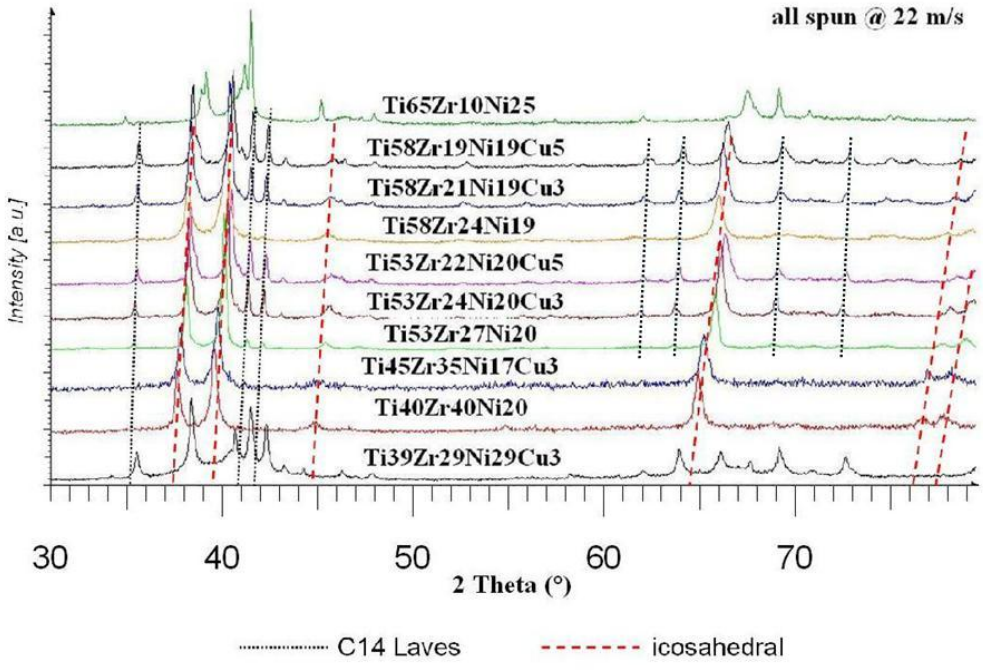

Figure 53: XRD data of ribbons with various compositons, all spun at 22 m/s.

For better presentation we put all the compositions of data from Figure 53 in a ternary phase diagram, Figure 54. I-phase zone area (green stars) in Ti-Zr-Ni ternary phase diagram we constructed upon samples, melt-spun at 22 m/s, coincides with the i-phase zone in Figure 4 and Figure 5, constructed by Molokanov (1990) and Qiang et al. (2004) upon melt-spinning and 6 mm as-quenched rods in a water-cooled copper mold, respectively.

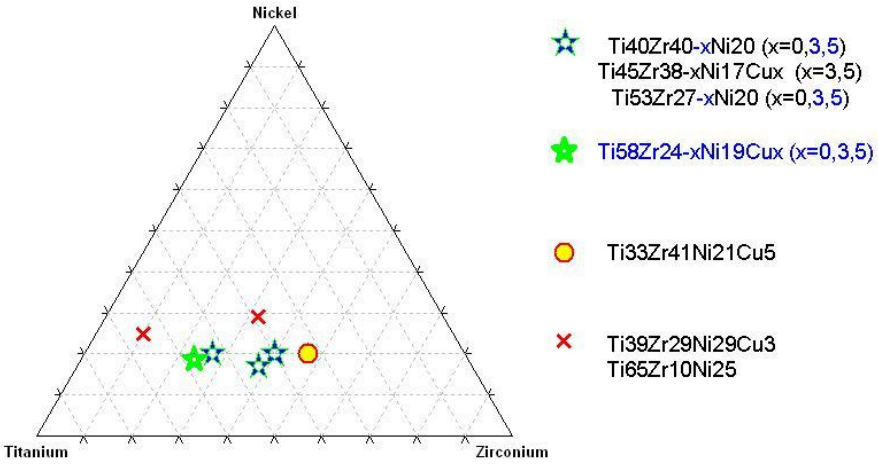

Figure 54: Ternary phase diagram. Alloys marked with blue and green stars form i-phase when melt-spun around 22 m/s. Alloy marked with yellow circle forms i-phase by vacuum-casting only (Chapter 3.4). Red crosses denote compositions at which i-phase is not formed at any wheel speed. On the right side of the figure is a list of compositions. Blue color denotes compositions that have not been published yet.

Using Cahn et al., 1986, model for indexing icosahedral diffraction peaks we could not just index XRD spectra of i-phase samples shown in Figure 53, but we were able to calculate i-phase cell constants a_q as well. We calculated a_q of as-spun (22 m/s) and fully hydrided i-phase samples, Figure 55.

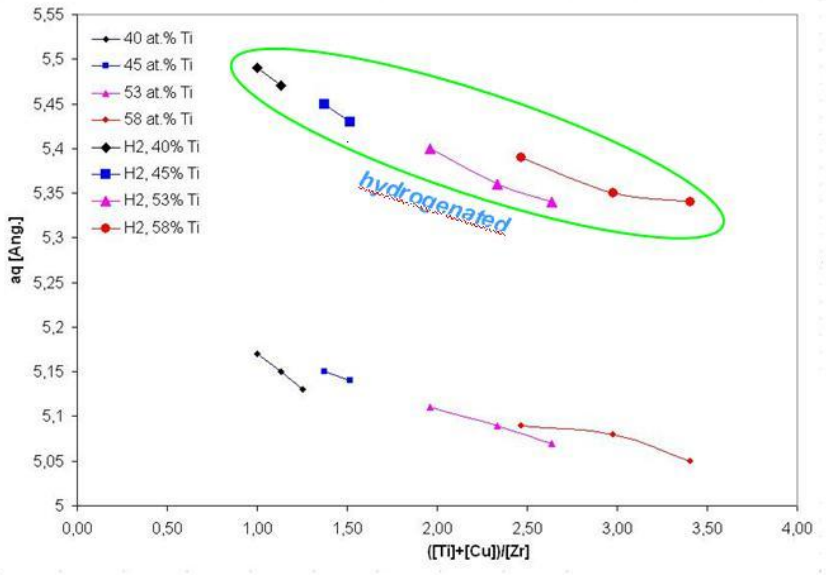

Figure 55: Decrease of icosahedral cell parameter a_q with Ti and Cu content by substituting Zr. The same trend is preserved for an expanded quasilattice with the highest amount of hydrogen we could obtain for each sample.

Our calculated i-phase cell constants a_q are in good accordance with the literature reports, namely in 2004 Qiang et al. have reported a_q of $Ti_{45}Zr_{35}Ni_{17}Cu_3$ and $Ti_{53}Zr_{27}Ni_{20}$ alloys to be 0.516 and 0.512 nm, respectively.

3.2.2.1 Copper addition effect

Due to reports of Wang et al. (2001, 2003a) copper enhances amorphous and i-phase formation in Ti-Zr-Ni system, according to higher stability of the icosahedral atomic clusters, thus lowering the activation energy of nucleation. The same group reported about improved hydrogen storage ability and the mechanical properties of amorphous and i-phase Ti-Zr-Ni-Cu system alloys as well, Liu et al. 2006d and 2006e. They investigated $Ti_{45}Zr_{35}Ni_{20-x}Cu_x$ (x= 0, 1, 3, 5 and 7) system by melt-spinning technique and discovered that x=0 and 7 at.% Cu alloys contain i- and C14 Laves phases, whereas the x=1, 3 and 5 at.% Cu alloys were single i-phase.

Thus, we focused on $Ti_{40}Zr_{40-x}Ni_{20}Cu_x$ (x= 0, 3, 5), $Ti_{45}Zr_{38-x}Ni_{17}Cu_x$ (x=0, 3, 5), $Ti_{53}Zr_{27-x}Ni_{20}Cu_x$ (x=0, 3, 5) and $Ti_{58}Zr_{24-x}Ni_{18}Cu_x$ (x=0, 3, 5) alloys to investigate their i-phase and hydrogen storage abilities.

XRD results of this analysis are shown in Figure 56. We see slight decrease of C14 Laves peaks in $Ti_{40}Zr_{40-x}Ni_{20}Cu_x$ alloy when 3 and 5 at. % of zirconium is substituted by copper. For $Ti_{45}Zr_{38-x}Ni_{17}Cu_x$ alloys system we observed the lowest C14 phase content at x=0, whereas for x=3 and 5 that content slightly increased. Our results show opposite effect as was reported by Wang et al. in 2001, 2003a. For the rest two alloys system with higher Ti/Zr ratio we observed similar effect, namely low amount of C14 phase in samples without Cu, but the effect of copper addition was more severe in these two systems, since the ratio C14/i-phase was higher than in $Ti_{45}Zr_{38-x}Ni_{17}Cu_x$ system.

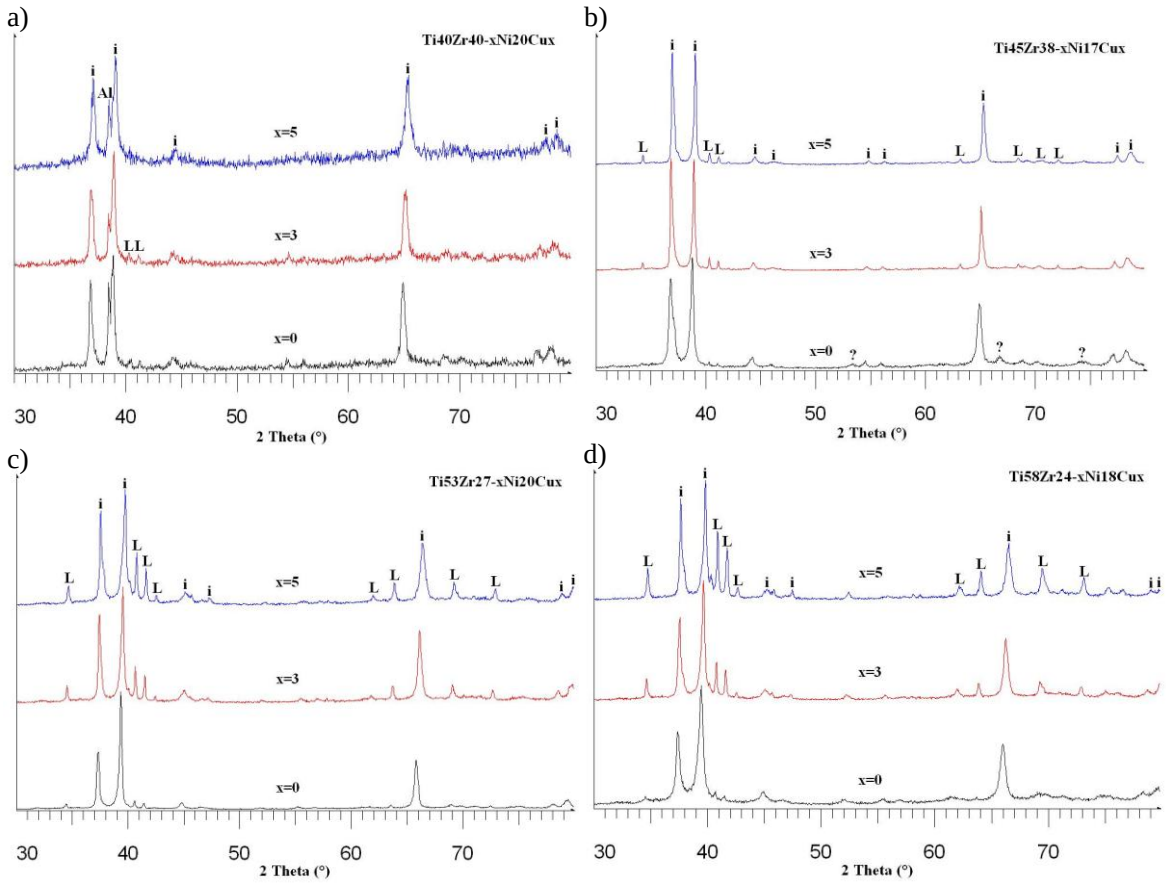

Figure 56: XRD spectra of ribbons melt-spun at 22 m/s, a) $Ti_{40}Zr_{40-x}Ni_{20}Cu_x$ (x= 0, 3, 5), b) $Ti_{45}Zr_{38-x}Ni_{17}Cu_x$ (x= 0, 3, 5), c) $Ti_{53}Zr_{27-x}Ni_{20}Cu_x$ (x= 0, 3, 5) and d) $Ti_{58}Zr_{24-x}Ni_{18}Cu_x$ (x= 0, 3, 5).

3.2.3 SEM analysis

Using the scanning electron microscope (SEM) we were able to observe the morphology of the melt-spun ribbons (see Figure 57). The photographs reveal a uniform ribbon thickness of the individual ribbons, which varies with the wheel speed from 120 to 30 micrometers, Figure 51. Furthermore, SEM images reveal the presence of both ductile and brittle failure. The hydrided materials were not observed to be any different from the as-crushed melt-spun materials, suggesting that even the relatively large hydrogen uptake associated with an H/M ratio of 1.5 did not result in any inter- or trans-granular fracture as part of a decrepitation process.

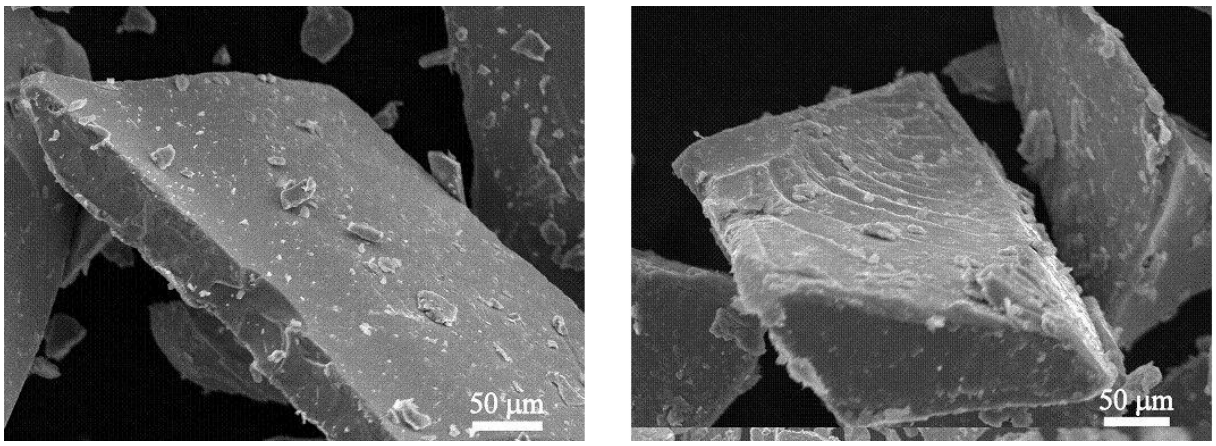

Figure 57: SEM images of melt-spun ribbons

Energy-dispersive spectroscopy (EDS) analysis, Table 6, shows the composition of $Ti_{58}Zr_{24}Ni_{18}$ melt-spun ribbons was close to the nominal composition on the free- as well as on the wheel-side, namely in the area of experimental error, estimated at 1-2 %. Z-contrast imaging by back-scattered electrons, Figure 58, showed seconardy phases are present in the melt spun ribbons. Even though with XRD results we confirmed the existence of a minor extent of seconardy phases in the $Ti_{58}Zr_{24}Ni_{18}$ ribbon, z-contrast imaging showed a contradictory and confusing situation, implying on high content of secondary phase, especially in the Figure 58b.

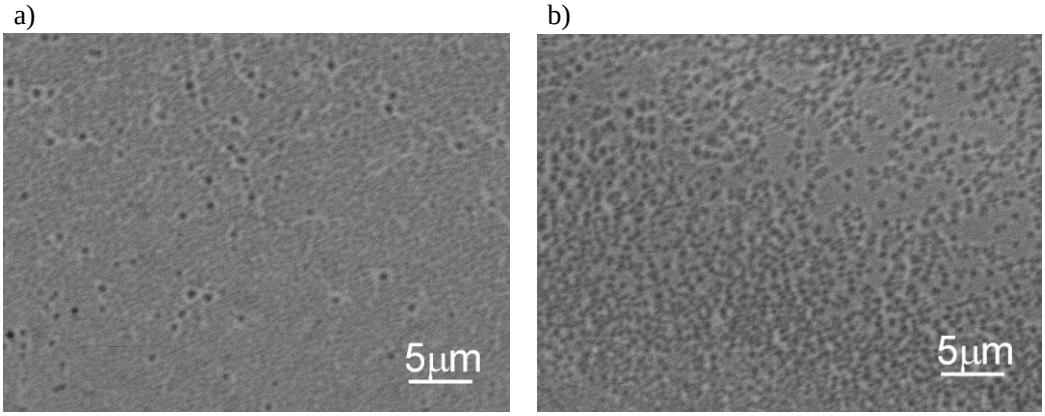

Figure 58: BSE image of a) free side and b) wheel side of $Ti_{58}Zr_{24}Ni_{18}$ melt-spun ribbon.

	Ti	**Zr**	**Ni**
nominal composition	*58.0*	*24.0*	*18.0*
free side of ribbon	59.3	21.4	19.2
	59.3	21.4	19.2
wheel side of ribbon	58.6	21.6	19.8
	58.8	21.4	19.8

Table 6: EDS data on free- and wheel-side of the melt-spun $Ti_{58}Zr_{24}Ni_{18}$ ribbon, predominantly containing i-phase.

In order to verify and to be totally sure we are not dealing with secondary phases we scanned the same area on the free side of $Ti_{58}Zr_{24}Ni_{18}$ ribbon with SE and BSE, Figure 59. With this we confirmed the black areas in Figure 58b are topological features, valleys in this case, whereas the black dots in Figure 58a are pores.

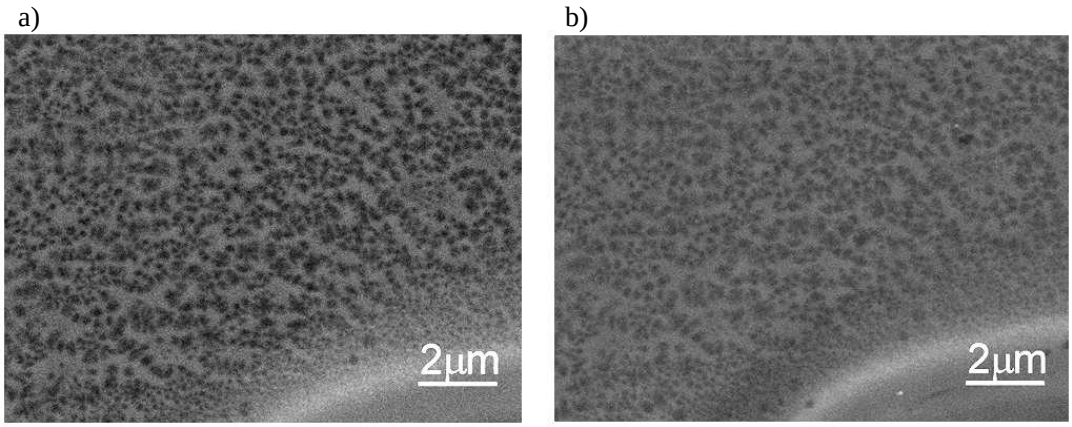

Figure 59: SEM images of the same area on the free-side of $Ti_{58}Zr_{24}Ni_{18}$ melt-spun ribbon, taken by a) back-scattered electrons, and b) secondary electrons.

The minority of secondary phases could not be observed by SEM z-contrast imaging, since these areas are either too small to observe, too finely distributed in i-phase/amorphous matrix or have a similar composition and thus the z-contrast is not so evident.

3.2.4 TEM analysis

3.2.4.1 Quasicrystalline sample

TEM investigations of the melt-spun ribbons revealed a large increase in the grain size when the wheel speed was decreased. For the $Ti_{40}Zr_{40}Ni_{20}$ material melt-spun at 22 m/s we observed ~20-nm i-phase grains imbedded in an amorphous matrix. Whereas for the $Ti_{45}Zr_{35}Ni_{17}Cu_3$ material melt-spun at 18 m/s we observed much less amorphous phase and the average i-phase grain size was ~ 50 nm. A bright-field TEM micrograph in Figure 60 shows the crystallites of the $Ti_{45}Zr_{35}Ni_{17}Ti_3$ phase scattered in an amorphous matrix, which formed due to rapid cooling of the melt. From typical selected-area electron diffraction (SAED) patterns in the 5-fold, 3-fold and 2-fold zone-axes we found that the vast majority of these crystallites were the icosahedral phase. I-phase grains are apparently equiaxed and show no preferential orientation, neither along the direction of the wheel rotation nor normal to the wheel surface. Cross-sections of the ribbons showed that close to the copper wheel the average grain size is much smaller than those close to the surface of the ribbon, where cooling is slower and the crystals had ample time for their growth. On the other hand, it is obvious that the nucleation rate was much higher on the wheel side than it was on the argon side. Even though the grains are bigger on free side, they are not so popular and consequently more amorphous phase is present here than in the regions with a high density of smaller grains.

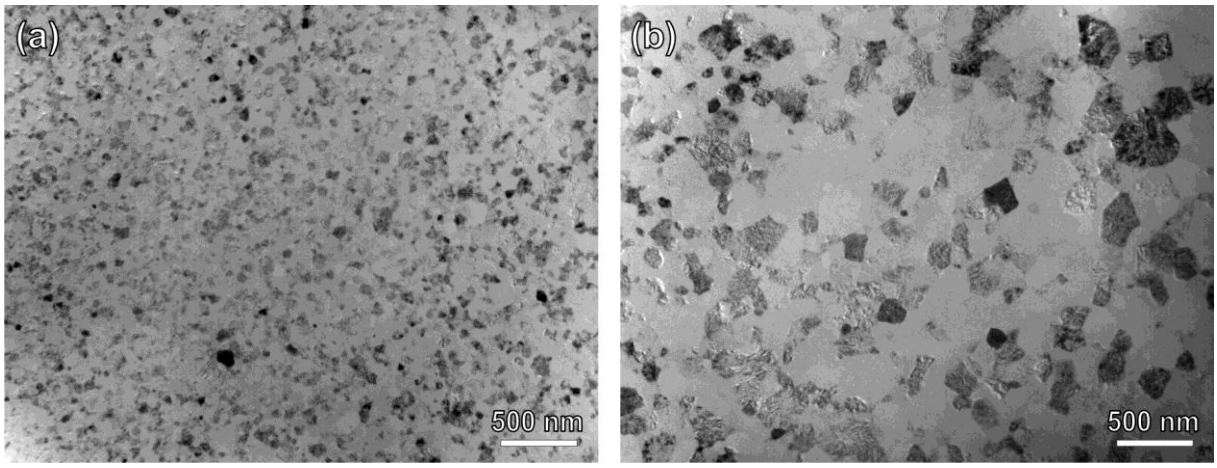

Figure 60: Crystallites of the $Ti_{45}Zr_{35}Ni_{17}Cu_3$ phase scattered in an amorphous matrix.

The quasicrystalline nature of the grains was additionally confirmed by high-resolution TEM imaging. Nanosized i-phase crystallites were recorded and oriented close to the 5-, 3- and 2-fold zone axes, as shown

in Figure 61a, Figure 61c and Figure 61e, respectively. In order to enhance the contrast the images were Fourier filtered using a Bragg mask. SAED patterns of the processed HRTEM images are shown in Figure 61b, Figure 61d and Figure 61f.

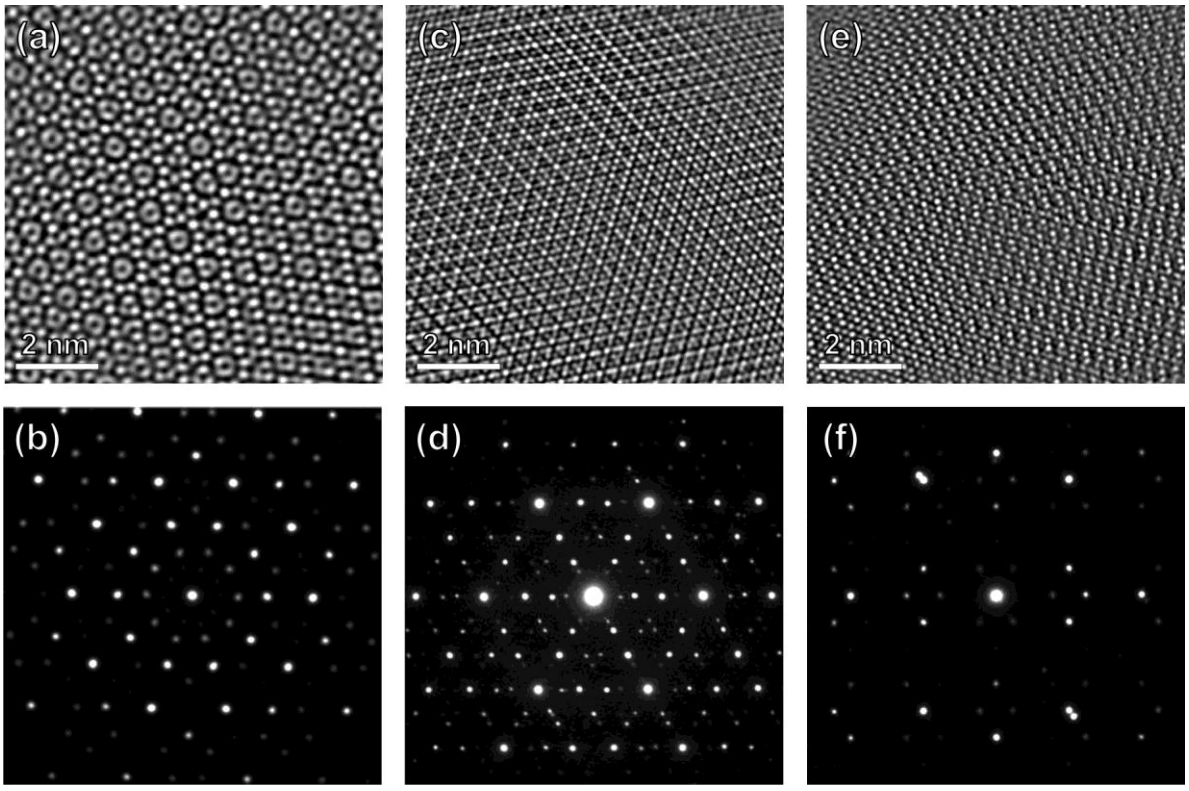

Figure 61: HRTEM images of i-phase grain and corresponding SAED patterns in a), b) 5-fold, c), d) 3-fold and e), f) 2-fold zone axes, respectively.

3.2.4.2 Crystalline sample

With a TEM investigation of the crystalline material we wanted to show the SAED patterns and HRTEM images as a proof that the quasicrystalline order no longer exists. The aim of TEM research was to find and identify d-spacings of corresponding crystal planes and combine those with the XRD data, Figure 62, by choosing the appropriate space group and the lattice parameters.

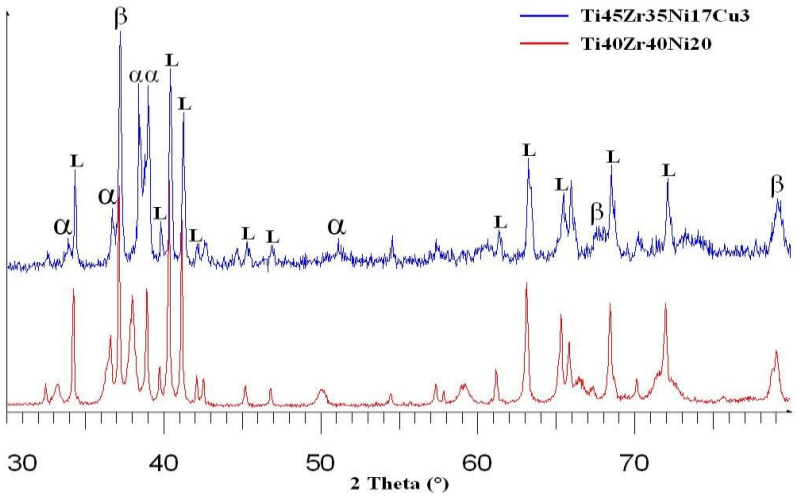

Figure 62: XRD spectra of $Ti_{40}Zr_{40}Ni_{20}$ and $Ti_{45}Zr_{35}Ni_{17}Cu_3$ crystalline alloys, obtained by annealing of the i-phase ribbons at 700 °C for 2 hours and 800°C for 4 hours in high vacuum, respectively.

Since we were not interested in the position and the size distribution of the crystalline grains in the as-

spun and annealed ribbons, we did not prepare the sample in the same way as we did for the i-phase observation. Namely, we crushed crystalline ribbons in the mortar, then we added similar volume fraction of fenol-formaldehide resin and mixed it with sample. By hot press we pressed the mixture at 150 °C and 100 Mpa for about 30 min. From the cooled pellet (1-mm thick) we cut 3-mm disc and prepared TEM sample by conventional method (grinding, dimpling, ion-etching).

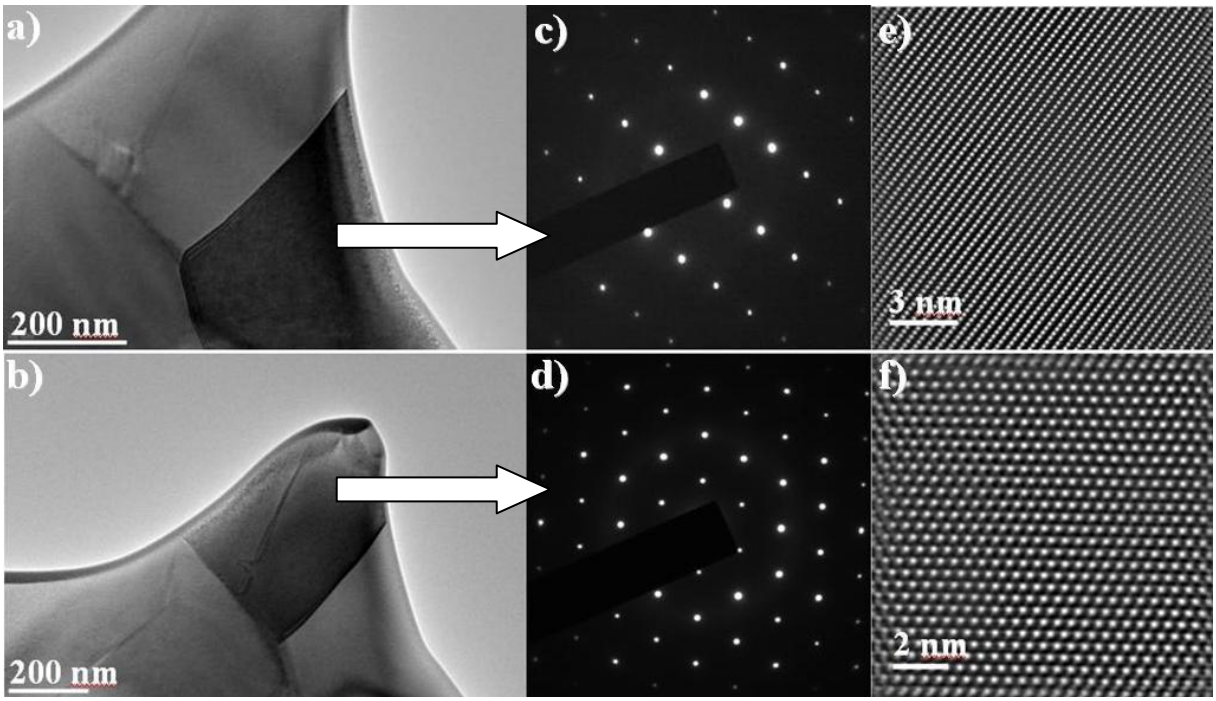

Figure 63: TEM characterization of crystallized $Ti_{40}Zr_{40}Ni_{20}$ sample upon annealing at 700°C for 2 hours. BF images a) and b) show the same area only differently tilted, namely dark grain is in the zone axis.

3.2.5 Crucible effect

By coincidence we discovered the effect of the crucible on the structure of melt-spun ribbons. As said before, two different crucibles have been used when performing melt-spinning experiments, i.e. boron-nitride (BN) and graphite. A series of melt-spinning experiments were done on $Ti_{40}Zr_{40}Ni_{20}$ alloy using BN crucible. For the $Ti_{45}Zr_{35}Ni_{17}Cu_3$ alloy we used a graphite crucible. Both crucibles performed well at operating conditions (1400°C) and no macroscopic signs of any reaction between the crucible and the melt were noticed. But when we studied XRD of ribbons we saw that $Ti_{40}Zr_{40}Ni_{20}$ sample was already amorphous at relatively low cooling wheel speeds, namely at 32 m/s. On the other hand, $Ti_{45}Zr_{35}Ni_{17}Cu_3$ sample was still not fully amorphous at the highest possible wheel speed our device can achieve, 50 m/s, Figure 49a.

Since the composition difference is not so drastic we suspect crucible material must affect the structure. From XRD data we could not detect if any new compound had been formed. Both carbon and boron are well known to have good glass forming ability (GFA), Wu et al. (2009).

To show this phenomenom better we plot just XRD data of ribbons melt-spun at 40 m/s, using boron-nitride and graphite crucibles, Figure 64. There is a huge structural difference depending upon the material of the crucible used. In case of $Ti_{40}Zr_{40}Ni_{20}$ alloy we end up with single amorphous phase when BN crucible have been used, and predominant i-phase (there is always some amorphous phase left) with no secondary crystalline phases if graphite crucible is used.

On the other hand, story is not so simple for $Ti_{45}Zr_{35}Ni_{17}Cu_3$ alloy, since nano-scaled BCC β-(Ti, Zr) solid solution grains are formed in the case of BN crucible, namely XRD presents the superposition of a characteristic BCC β phase peak over a diffuse diffraction hump spreading out the angular range 32–45° and corresponding to an amorphous phase. The lattice constant of this BCC phase, a_β is 0.339 nm. The shoulder observed at amorphous halo around 39° and at higher angular values at 65° might have been due to nanoquasicrystalline grains precipitation. Lefaix et. al, 2008, performed melt spinning experiments on $Ti_{45}Zr_{38}Ni_{17}$ alloy by using quartz crucible and got such a shoulder-like diffraction hump of amorphous phase and a superposition of a characteristic BCC β-(Ti,Zr) solid solution phase, with slightly bigger cell

constant as we obtained, namely a_β = 0.343 nm.

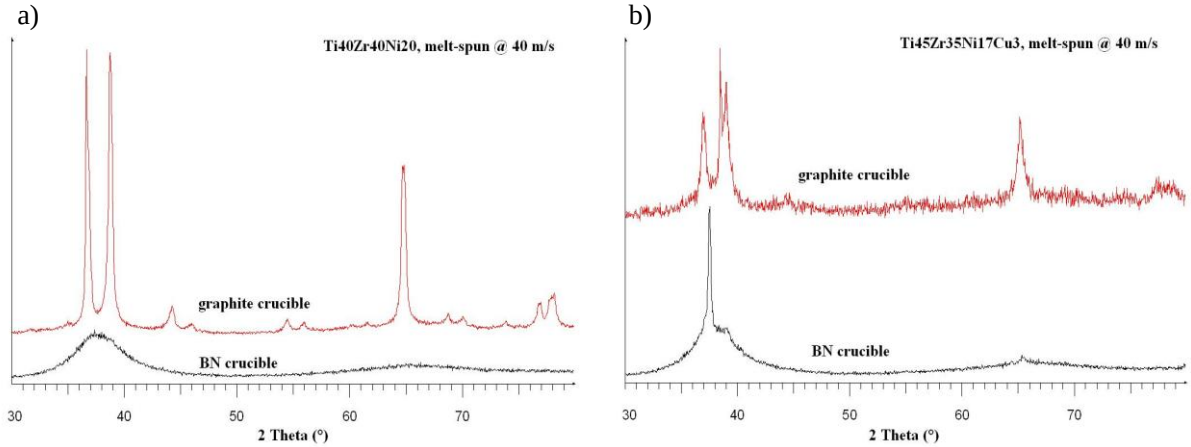

Figure 64: XRD spectra of ribbons, melt-spun at 40 m/s. Material of the crucible has obvious effect on the structure of both a) $Ti_{40}Zr_{40}Ni_{20}$ and b) $Ti_{45}Zr_{35}Ni_{17}Cu_3$ samples.

In addition, in the beginning of our melt spinning experimental work we were using quartz crucibles only, for production of $Ti_{40}Zr_{40}Ni_{20}$ ribbons. As said before, before ejecting a melt through the nozzle, we heated-up the melt to 1400 °C, which is too high for quartz crucibles. We have obtained ribbons, though, only we could use them only once. Namely, quartz crucibles are normally used only up to 1200 °C, but this temperature was too low to obtain an optimal amount of uniformly shaped ribbons. But, what is more important at this point is that $Ti_{40}Zr_{40}Ni_{20}$ ribbons were amorphous already at 32 m/s, when quartz crucible had been used. Rud et al., 2005, have discovered that even a small amount of Si (0.2-0.3 at. %) in the Ti-Zr-Ni alloy strongly affects the ribbon structural state in the sense of promoting the formation of an amorphous or a mixed amorphous-quasicrystalline state. They quenched the melt of $Ti_{37.2}Zr_{38.9}Ni_{23.9}$ at 1400 °C on a Cu cooling wheel at surface velocities 44 and 30 m/s. Chemical analysis showed the presence of a small amount of Si in the ribbons, fully amorphous at 44 m/s and amorphous on the wheel side at 30 m/s. They say the most probable source of silicon in the ribbons is the quartz quenching tube (crucible) used during the melt spinning procedure, due to reports of Viano et al., 1995, and Davies et al., 2000.

XRD analysis of our $Ti_{40}Zr_{40}Ni_{20}$ ribbons melt-spun at 32 m/s using quartz crucible, in Figure 65, show the ribbons were fully amorphous on both sides. Namely there was only one spectrum recorded on ribbons, alternately laid on the holder, air-side up, wheel-side up, respectively.

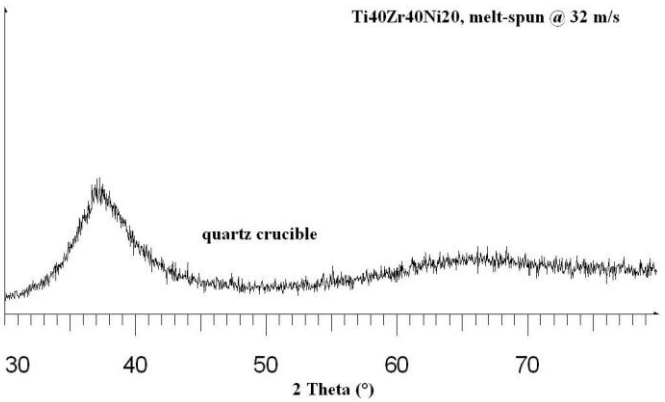

Figure 65: XRD spectrum of $Ti_{40}Zr_{40}Ni_{20}$ ribbons, melt-spun at 32 m/s using quartz crucible.

3.2.6 XPS analysis

A surface oxide layer was reported to act as a barrier to hydrogen absorption in i-phase ribbons produced by melt spinning, Viano et al., 2002. Authors (Huang et al., 2008) have given just the values of the surface oxide layer thicknesses, but showed no corresponding XPS depth profiles, oxidation states of elements, etc. And even more, they reported that the thickness of a surface oxide layer on as-cast $Ti_{45}Zr_{35}Ni_{17}Cu_3$ rods is no less than 70 nm. This result is in contrast to our findings, namely by XPS we measured the surface oxide

film thickness on $Ti_{45}Zr_{35}Ni_{17}Cu_3$ melt-spun ribbons was only 7 nm, Figure 66.

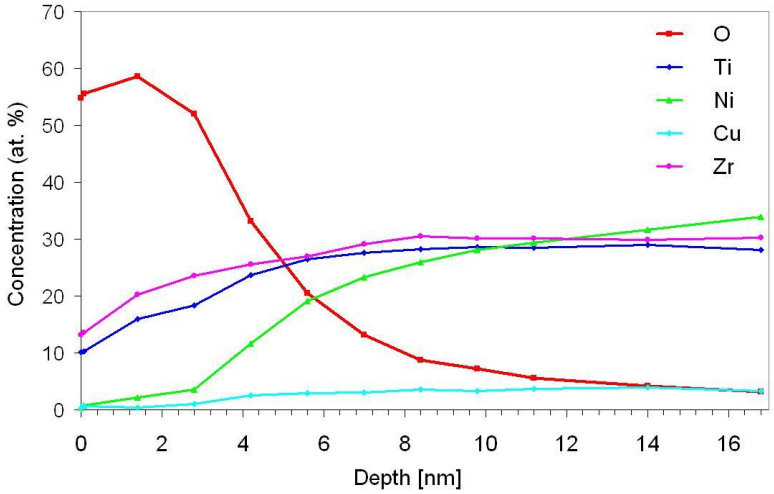

Figure 66: Depth profile of elements in $Ti_{45}Zr_{35}Ni_{17}Cu_3$ melt-spun ribbon.

In order to investigate crucible effect as well, described in the previous Chapter 3.2.5, we used the same samples for XPS analysis, namely first spun by the BN crucible and other by the graphite one. Unfortunately, we were not able to see any boron signal in the first 3 nm of the sample, spun by BN crucible, since boron photoelectron binding energy peak overlapps with the zirconium (Zr^{4+}) 3d peak at 182.75 eV.

No difference between the XPS spectra recorded on the surface (3 nm) of the ribbons, melt-spun by the BN and the graphite crucible has been observed, Figure 67. Except traces of fluorine were found on the surface of ribbons obtained using boron-nitride crucible, even though fluorine could not come from the boron-nitride. The only possible explanation for the origin of fluorine is from the polishing paste for polishing the copper cooling wheel. Namely, it seems some paste remained on the wheel, and it is known that metal polishing paste contains fluoride components.

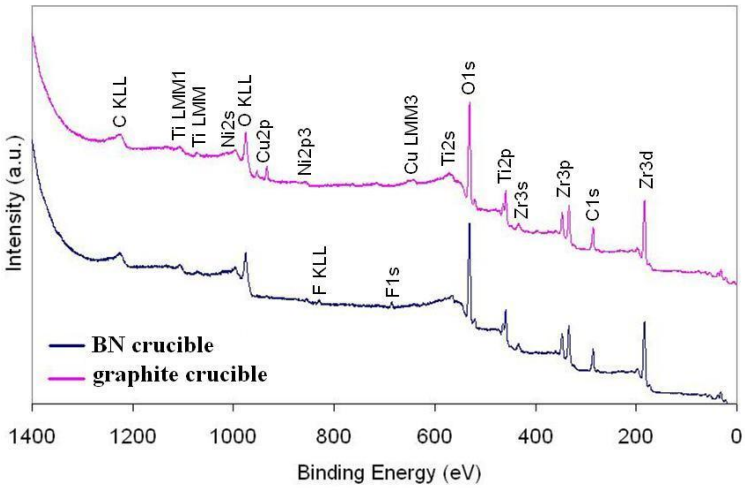

Figure 67: 3-nm-deep XPS binding energy analysis of ribbons melt-spun by BN and graphite crucibles.

Another useful information we obtained by XPS is the oxidation state of the elements in the oxide film. We found we are dealing with zirconium (Zr^{4+}) and titanium (Ti^{4+}) oxide. Nickel and copper are unoxidised, and they substancially show up only after the first 3 nanometers of material is etched, Figure 68.

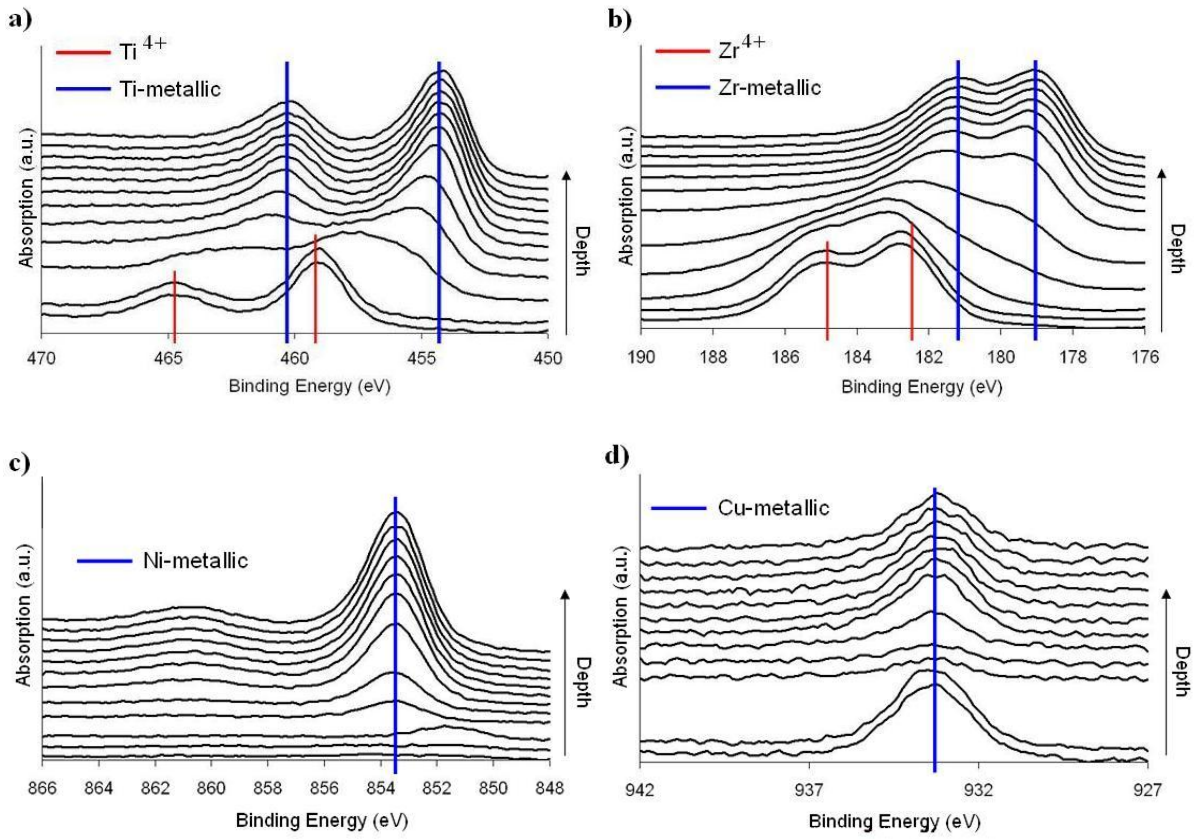

Figure 68: X-ray photoelectron absorption peaks of a) Ti 2p, b) Zr 3d, c) Ni 2p, and d) Cu $2p_{3/2}$ electrons. Intervals correspond to etching depths that are roughly 1.5 nm apart, same as points in Figure 66.

Ti 2p and Zr 3d peaks are shifted to slightly higher energies due to the oxidation of elements, forming a thin surface oxide layer. Nickel is not oxidized and not even present in first atomic layers. Shift of its 2p absorption peak at depth 1.4 nm is related to the discharge of the sublayer, which happens quite often during XPS analysis of conductive samples. Monolayer of seggregated copper was observed when recording Cu $2p_{3/2}$ absorption peak, since the first two spectra in all the diagrams are taken from the same depth. Then we get very weak Cu signals at depths of 1.4 and 2.8 nm, after that the copper concentration quickly reaches stoichiometric value 3 atomic %.

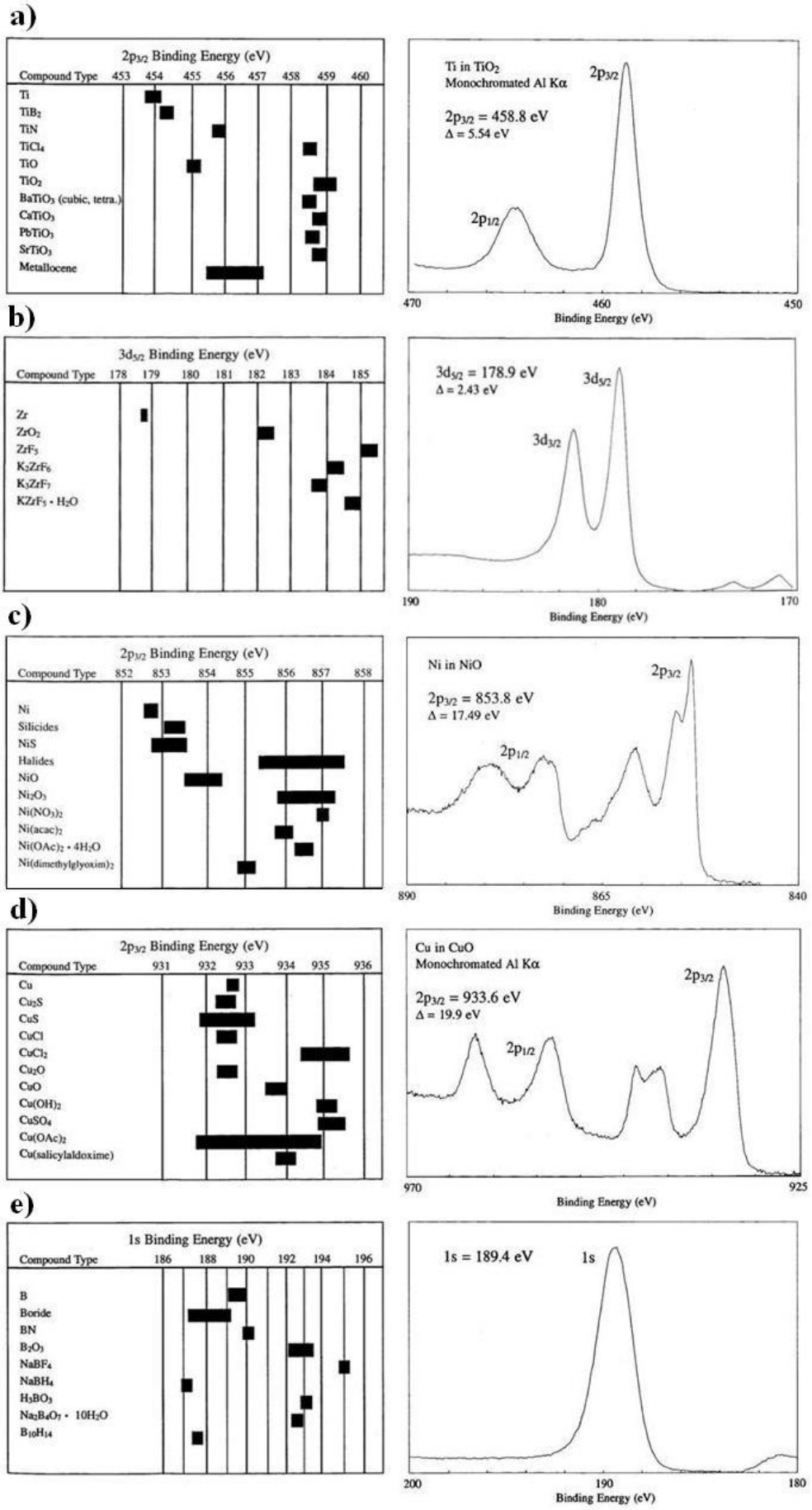

Figure 69: Typical X-ray photoelectron spectra and binding energies of a) titanium, b) zirconium, c) nickel, d) copper, and e) boron. Data were obtained by monochromated Al Kα radiation (from Moulder et al., 1995).

3.2.7 SQUID measurements

With a superconducting-quantum-interference device (SQUID) we performed temperature-dependent measurements of magnetization. For this purpose we prepared three $Ti_{40}Zr_{40}Ni_{20}$ samples, amorphous, quasicrystalline and crystalline, Figure 70. There are nano i-phase precipitates present in the amorphous sample, even though it was prepared by melt spinning at the highest wheel speed our machine can undergo, namely 50 m/s. This precipitation happened, because the graphite crucible had been used.

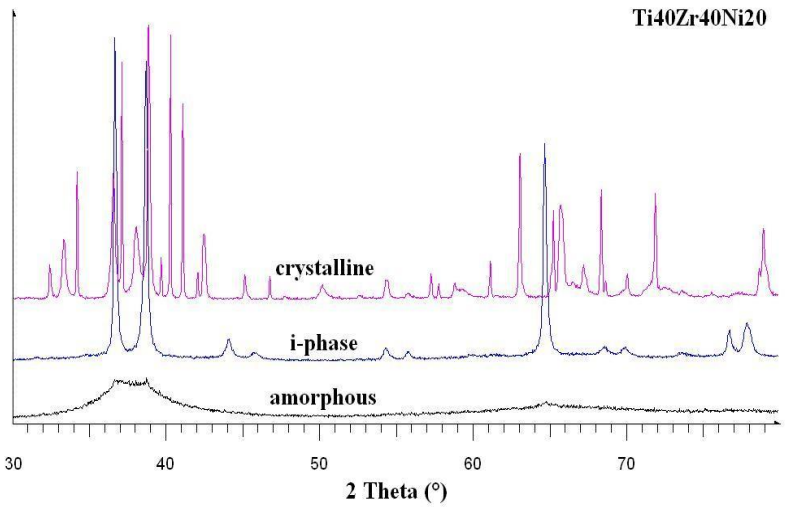

Figure 70: XRD spectra of $Ti_{40}Zr_{40}Ni_{20}$ samples, amorphous, i-phase and crystalline, that were used for SQUID (and VSM) experiments.

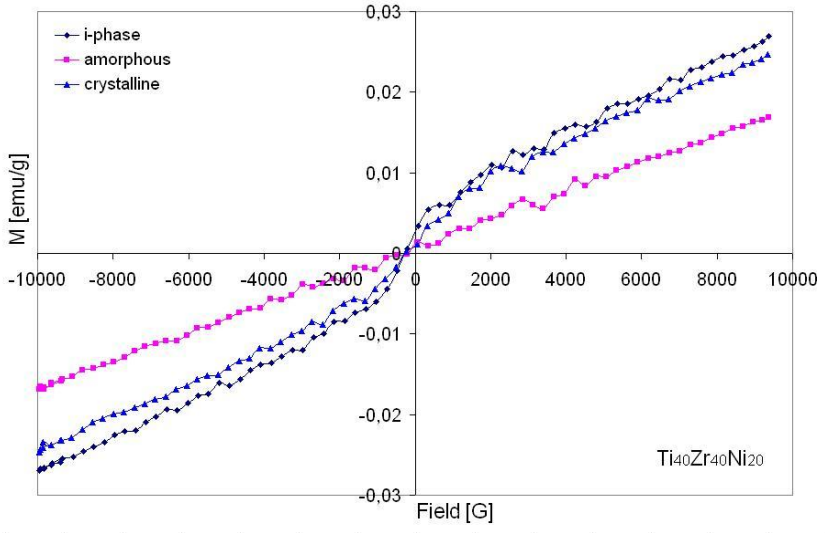

Figure 71: VSM hysteresis curves of amorphous, icosahedral and crystalline $Ti_{40}Zr_{40}Ni_{20}$ samples.

All three samples were analyzed by VSM first, Figure 71, and then by SQUID technique, Figure 72. By VSM we have got hysteresis curves recorded at room temperature and external magnetic field varying from 1 T to -1 T, whereas by SQUID we were able to perform very low noise temperature dependent measurements of the magnetization. The external magnetic field in SQUID device was set at constant value, 0.1 T and the temperature varied from 400 K to 4 K and back to 400 K.

Even though the structure of these samples is different, they all show paramagnetic behaviour with similar susceptibilities, only i-phase and crystalline samples are showing small ferromagnetic contribution as well. In order to verify which type of paramagnetism we have in these alloys we performed temperature dependent measurements of magnetization by SQUID, Figure 72, since cooling system of VSM is not capable to achieve 4 K and the signal-to-noise ratio is very poor for this type of experiment as well. Amorphous sample is showing spin glass-like behaviour, since its magnetization depends on whether the sample is being heated or cooled. This effect is also well known as thermal memory, which is the reason for

the hysteresis of corresponding SQUID curve.

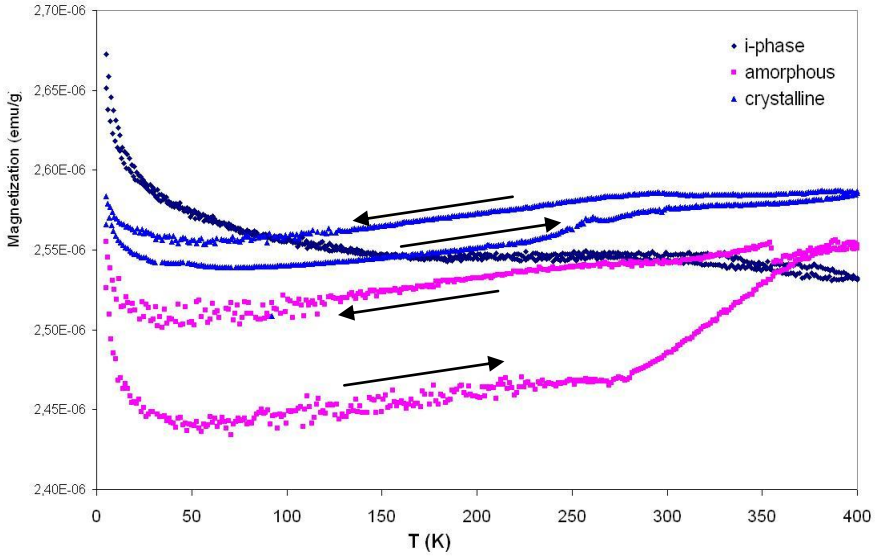

Figure 72: Results of SQUID analysis of amorphous, icosahedral and crystalline $Ti_{40}Zr_{40}Ni_{20}$ samples. Black arrows denote cooling and heating, respectively.

3.3 Hydriding

3.3.1 Thermogravimetry of desorbed hydrogen

Figure 73 represents the case how we measured the content of desorbed hydrogen by thermogravimetry, where we traced the mass drop due to hydrogen release at certain temperatures. We chose to show just three examples of TG curves of three different structures (amorphous, quasicrystalline and crystalline) with different amounts of hydrogen desorbed, in order to demonstrate how the mass content of hydrogen was measured. Raw data were processed by corresponding Netsch Proteus software by choosing the highest and the lowest point of the curve and subtracting them. The resulting number was the mass % of desorbed hydrogen.

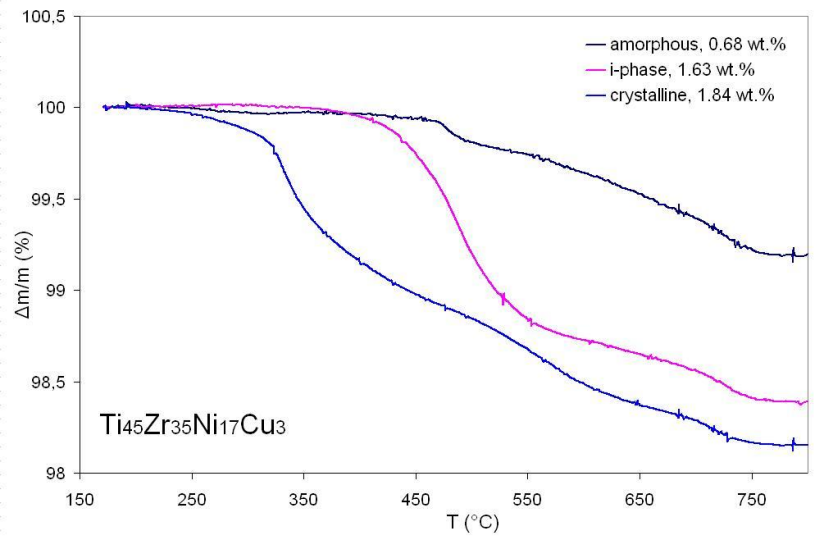

Figure 73: TG curves of hydrogen desorption from amorphous, icosahedral and crystalline $Ti_{45}Zr_{35}Ni_{17}Cu_3$ samples, all subjected to the same loading conditions.

To verify the accuracy and precision of TG data we did desorption of hydrogen from five different samples (structurally and stoichiometrically), where we weighed the samples (around 300 mg) before and after the desorption. It should be noted that for TG measurements we used about 25 mg of sample and a

microbalance with 0,1 μg precision, whereas in the case of the desorption by electric furnace (*Carbolite*) attached on turbo-vacuum system via a silica tube we were using standard digital balance with 0,1 mg precision, which is 1000-times less than at TG.

Regardless of such discrepancy in precision of balances, we were able to successfully demonstrate the correlation between mass % values of desorbed hydrogen, obtained by two different methods. From Figure 74 we see these results are quite well correlated, where contents of hydrogen, obtained by Carbolite desorption, are always higher than the values achieved by the conventional TG route.

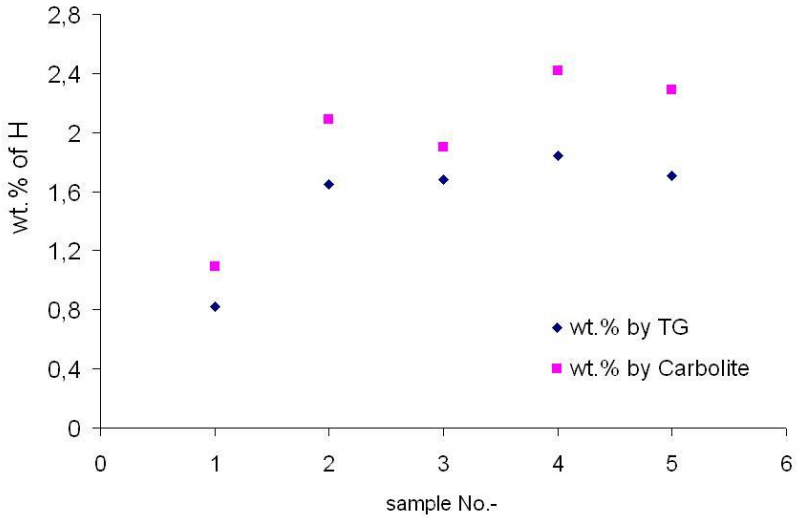

Figure 74: Comparison of mass contents of desorbed hydrogen from five different samples, obtained by TG and by weighing before and after desorption using Carbolite furnace attached to dynamic vaccum via silica tube.

3.3.2 Mass spectrometry of desorbed hydrogen

The aim of these measurements was to investigate the distribution of hydrogen desorption temperatures, i.e. hydrogen bonding sites in different samples, depending either on chemical composition or structure. For various reasons quantification of these spectra (integration) in order to determine the amount of desorbed hydrogen is not accurate and reproducible. First, to measure the exact amount of hydrogen coming in the mass spectrometer, we should use internal standards, i.e. samples like $LaNi_5H_x$ with known content of hydrogen. But even this would not give us correct values since part of hydrogen reacts with oxygen that difuses through polyethylene pipes for argon-carrying gas and so water comes in the mass spectrometer instead of hydrogen. This oxygen income affects TG results as well, even though not to such extent as mass-spectra intensities, in sense of increasing sample mass due to its oxidation, which starts at similar temperatures as water formation does. Namely, we had observed this effect when performed the same experiment with either an empty sample or sample with a very small amount of hydrogen. Thus, we think the released hydrogen prevents oxidation of the sample to some critical ratio released H_2 / input of O_2. When this ratio is reached, mass % of H_2 starts to decrease since the subsequent oxidation of the sample occurs. This explains higher weight contents of hydrogen obtained by weighing the samples before and after desorption using the same temperature program, but in a high dynamic vacuum (10^{-5} mbar) instead of in argon flow. Also, 10-times more material was used in this case to ensure better precision.

And second, electronics that measures very small currents (10^{-11}A) of charged species (H_2) in quadrupolar column is subjected to drift, which means intensities of mass-spectra should be taken in arbitrary units like XRD spectra. But this drift is not so strong so we can roughly compare areas under mass-spectra and predict the amounts of desorbed hydrogen from different samples. In order to do this all the spectra were divided by the corresponding sample mass.

So, basically both results, TG mass change and area under mass-spectrum are always affected by oxidation to the same extent, since there is always same residual oxygen content present in Argon 5.0 bottle and the diffusion of oxygen through PE pipes is presumably constant. But, if we plot area/sample mass (A*s/mg) versus mass % of hydrogen obtained by TG (Figure 75), we get a linear response with huge scattering, which is exclusively due to the electronic drift of mass spectrometer electronics, mentioned before. When recording samples with no or negligible amount of hydrogen desorbed, we detected ~ 0.2 % weight increase, which is due to oxidation, thus points in Figure 75 should have plus 0,2 mass % of H error

bars. Nevertheless, this discrepancy was shown in Figure 74 as well, namely the numbers there are higher, since hydrogen desorption there occured in a high dynamic vacuum. Estimated relative experimental error of the mass-spectra area size normalized to sample mass is about 40 %. If we divide experiments into different periods, we see that the relative error is practically two times smaller. Of course, oxidation affects mass-spectra as well, so all areas should be systematicaly bigger (like TG data), but this is not the reason for such scattering.

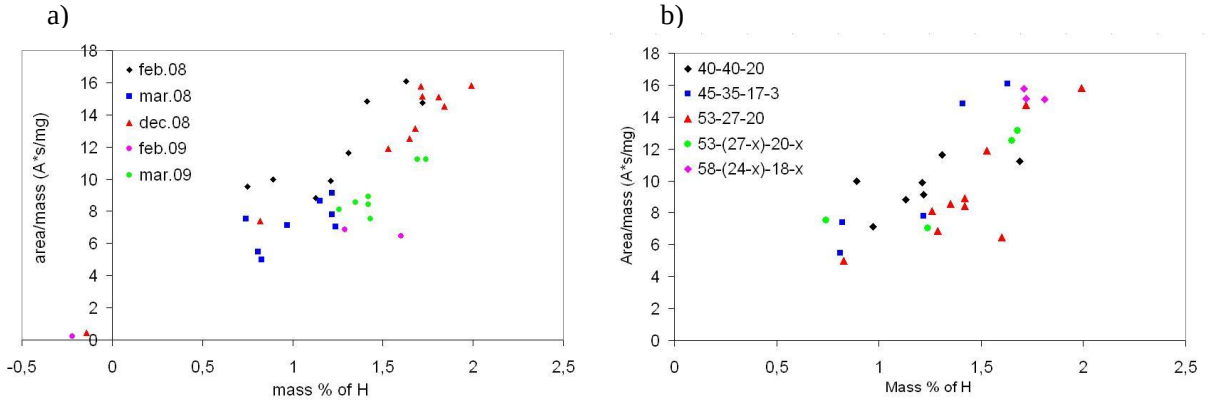

Figure 75: Plot of areas under mass-spectra normalized to sample mass versus mass content of desorbed hydrogen, measured by TG. In graph a) points are divided according to date of measurement, whereas in b) points are sorted due to composition (density).

By Figure 76 we want to demonstrate the shape of mass-spectra is strongly dependent just on the crystallographic structure of the sample and to minor extent on its composition and hydrogen content.

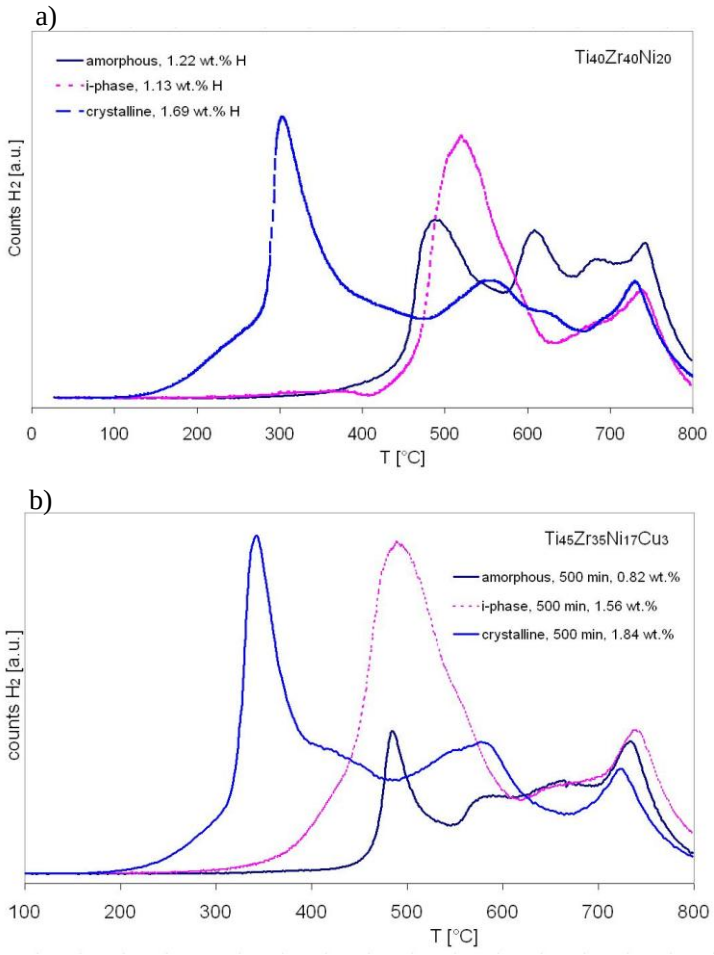

Figure 76: Mass-spectra of desorbed hydrogen are strongly dependent just on the structure of samples, and only slightly dependent on the composition or hydrogen content; a) $Ti_{40}Zr_{40}Ni_{20}$ and b) $Ti_{45}Zr_{35}Ni_{17}Cu_3$.

3.3.2.1 Hydrogen in the i-phase

As seen before, hydrogen bonding site distribution for i-phase phase has a characteristic shape and thus can be easily separated from amorphous and crystalline one. In other words hydrogen desorption temperature distribution rather strongly depends on the structure of measured sample.

Next logical question that arises is whether the shape of such distribution is somehow affected by the content of bonded hydrogen in the material. Figure 77 shows the answer to that question. We can see that the peak intensity ratios between low (500°C) and high (740°C) temperature are hydrogen content dependend. Namely, this ratio is increasing with the hydrogen content. Physical explanation of this phenomenom is rather simple, since protons first bond to energetically favorable sites, represented by high temperature of desorption (740°C). When these sites are taken, protons go to thermodynamically less stable sites, increasing low temperature desorption peak at 500°C.

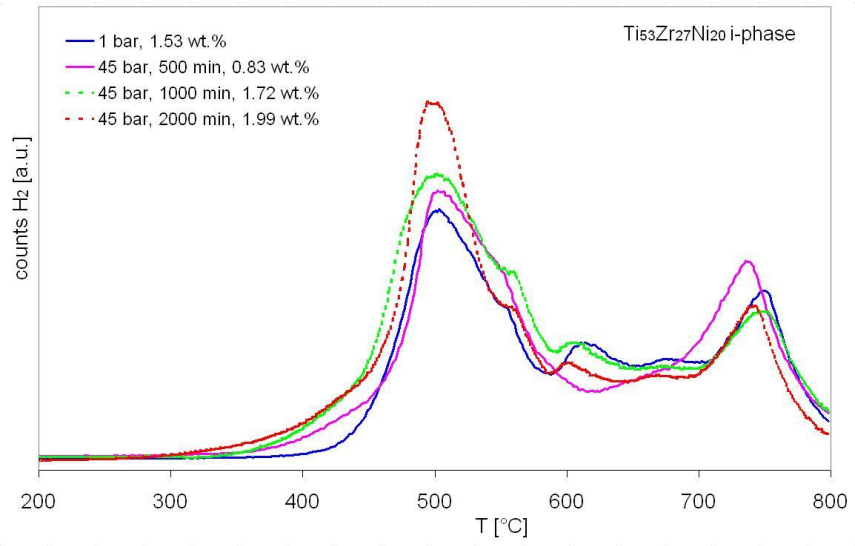

Figure 77: Mass-spectra of desorbed hydrogen from $Ti_{53}Zr_{27}Ni_{20}$ i-phase samples, containing different amount of hydrogen, i.e. hydrided for various extent of time.

Furthermore, we compared hydrogen site distributions of i-phase samples with different compositions, and with highest mass contents of hydrogen, Figure 78.

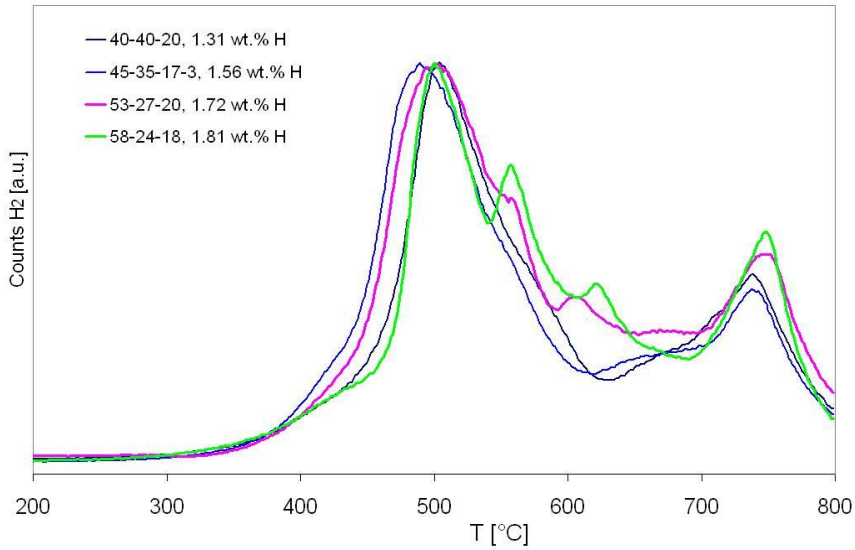

Figure 78: Mass-spectra of desorbed hydrogen from i-phase samples with different compositions and highest content of hydrogen.

From above results we may conclude that all i-phases with different compositions and thus cell-parameters as we have seen them in Chapter 4.3.2 have similar shape of hydrogen mass-spectrum. Namely all four compositions contain two main desorption peaks, first around 500 °C and second around 740 °C.

The position of these two peaks slightly varies with the composition, though. Samples with highest contents of titanium (and hydrogen) poses two additional peaks, where the lower ones almost coincide and are placed around 560 °C, the rest of the peaks are placed at 610 °C for $Ti_{53}Zr_{27}Ni_{20}$ and at 625 °C for $Ti_{58}Zr_{24}Ni_{18}$, respectively. One might ask, whether these two peaks appear because of different composition and thus electronic structure, which enables protons to bond to two additional sites, or they are more related to the fact that these two compositions contain higher weight % of hydrogen. The answer is rather simple, namely if we compare the spectra of the last two mentioned samples we see that the 560 °C peak is more expressed for $Ti_{58}Zr_{24}Ni_{18}$ alloy, even though they contain comparable amount of hydrogen. And since peaks at 610 °C and 625 °C do not coincide this phenomenom must be more due to the electronic structure of the material rather than due to hydrogen content. Especially when we think of $Ti_{40}Zr_{40}Ni_{20}$ and $Ti_{45}Zr_{35}Ni_{17}Cu_3$ mass-spectra that do not have even these two small peaks. Not even a sign.

Interesting results were obtained with the investigation of hydrogen desorption temperature distribution of samples with the same basic composition, where only the content of dopant (Cu) was slightly varied, Figure 79.

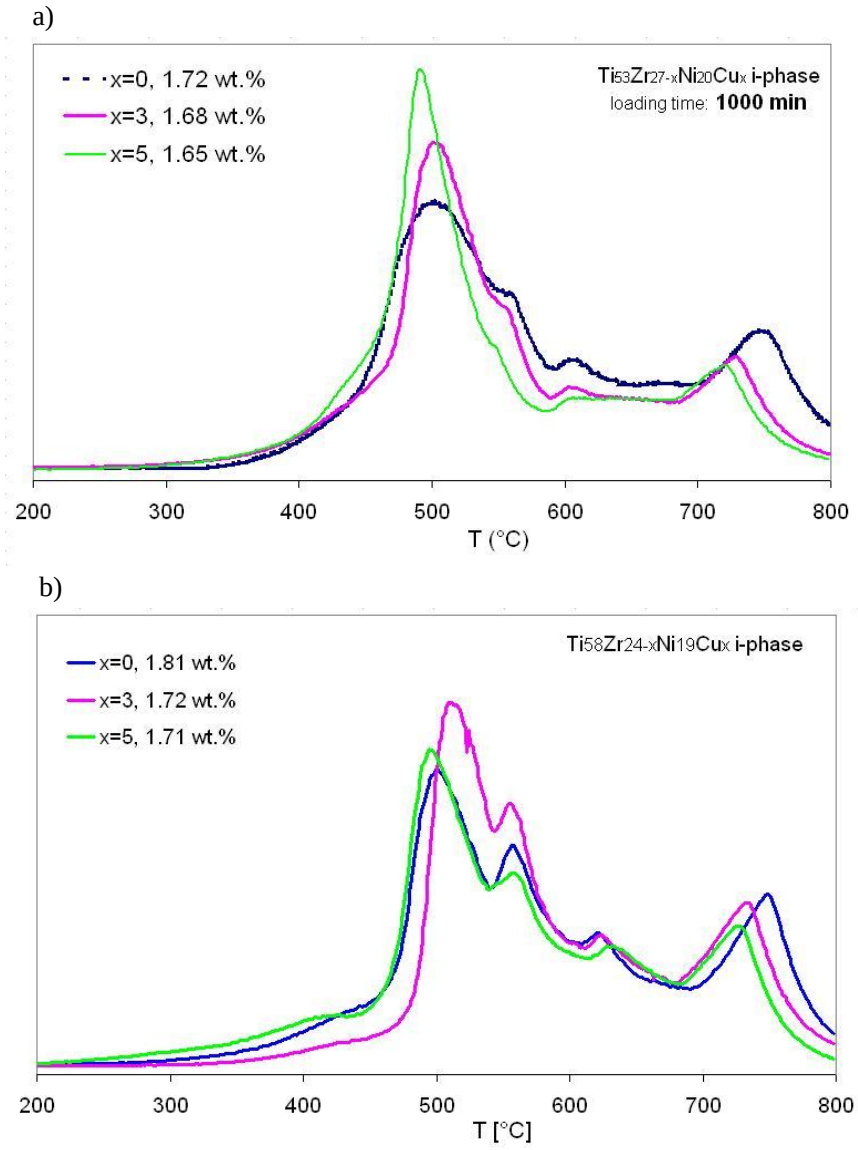

Figure 79: H_2 mass-spectra of a) $Ti_{53}Zr_{27-x}Ni_{20}Cu_x$ and b) $Ti_{58}Zr_{24-x}Ni_{18}Cu_x$ samples loaded with comparable amount of hydrogen.

Obvious difference between $Ti_{53}Zr_{27-x}Ni_{20}Cu_x$ and $Ti_{58}Zr_{24-x}Ni_{18}Cu_x$ mass-spectra is that the second highest peak (~ 560 °C) is much more expressed for the $Ti_{58}Zr_{24-x}Ni_{18}Cu_x$. This difference comes from different electronic structure dependent on the composition. Also, dependence of peak positions around 500 °C on the copper content is different for observed basic compositions. But if we take a closer look on the peaks placed around 740°C, we can see that copper lowers not only this temperature for desorption of highly bonded protons, but its content as well. Values of these desorption temperatures are shown in

Table 7.

x	$Ti_{53}Zr_{27-x}Ni_{20}Cu_x$	$Ti_{58}Zr_{24-x}Ni_{18}Cu_x$
0	749°C	749°C
3	729°C	732°C
5	720°C	726°C

Table 7: Desorption temperatures of highly bonded protons from two different compositions with 0, 3 and 5 atomic % of copper addition.

3.3.2.2 Hydrogen in the amorphous phase

Amorphous material was processed in two steps. First step was melt-spinning at 40 m/s, producing brittle ribbons with small i-phase grains as we anticipated. Brittleness of ribbons allowed us further mechanical amorphisation of the material as the second step, which we performed by planetary ball-milling for 60 hours. XRD results in Figure 80 showed that no stable hydrides (TiH_2 and ZrH_2) were formed upon high-pressure hydrogenation of amorphous material, as reported elsewhere (Takasaki et al., 2004). Peaks at around 38.4° in all four spectra belong to aluminium holder, since amorphous powder is formed out of agglomerated granules, formed upon milling, and thus can not cover the whole surface of the holder.

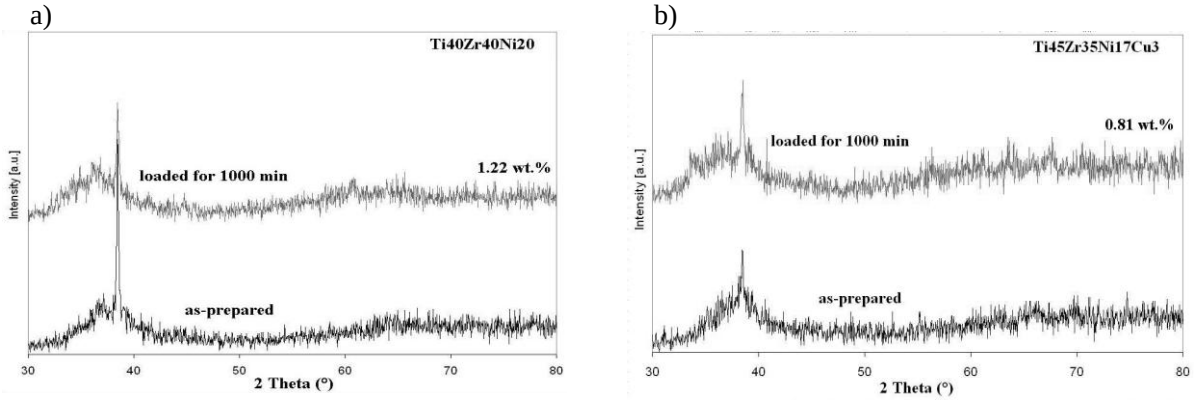

Figure 80: XRD spectra of amorphous $Ti_{40}Zr_{40}Ni_{20}$ and $Ti_{45}Zr_{35}Ni_{17}Cu_3$ powders, hydrided for 1000 min at 300°C and 45 bar.

In order to clearly see the shift of XRD amorphous halo, all four spectra were filtered by fast Fourier transformation (FFT), using Diffrac Plus Evaluation (Eva) software package, Figure 81.

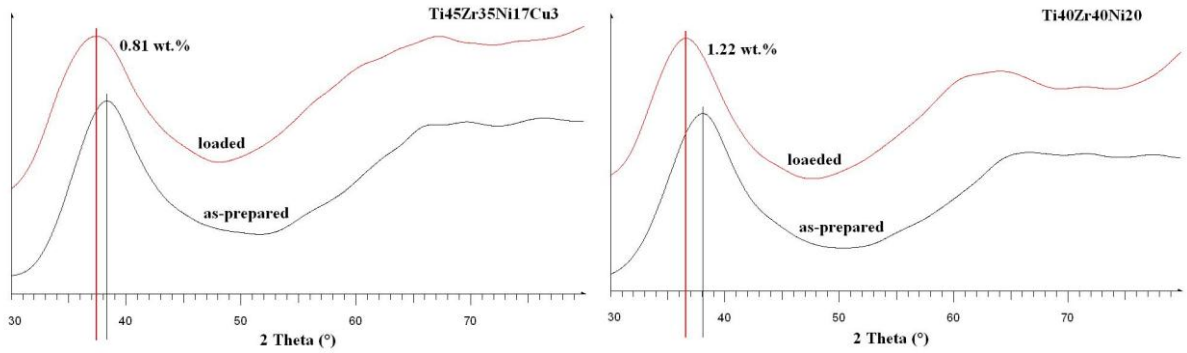

Figure 81: FFT of amorphous XRD spectra. The shift of amorphous halo indicates the interatomic distances increased upon interstitial protons, and it is proportional with the content of hydrogen obtained by TG.

In case of $Ti_{40}Zr_{40}Ni_{20}$ amorphous material this shift was 1.5° and it contained 1.22 wt. % of hydrogen, whereas the shift for $Ti_{45}Zr_{35}Ni_{17}Cu_3$ amorphous material was less than 0.9°, containing 0.81 wt. % H_2. According to Westlake rule we were able to calculate or at least estimate [H]/[M] value for these two samples. Since in metallic glasses there is no crystallographic order we do not have any unit cells either. There is only one average interatomic distance, which can be used as alternative to conventional cell constant, and the volume of this alternative cell is a sphere with a radius of that average interatomic distance. We do not even need the absolute values of these parameters, since [H]/[M] value can be calculated using only volume (sphere) expansion. The Westlake equation (Equation 24) is universal for all

hydrogen absorbing metals. It says, when the volume expansion of metal's unit cell is 20 %, there is one proton bonded to a metal atom. Using Bragg's law (Equation 19) we can calculate average interatomic distance in our amorphous alloys from the position of amorphous halo peak in Figure 81.

$$[H]/[M] = 5 \times \Delta V \quad (24)$$

For $Ti_{40}Zr_{40}Ni_{20}$ as-prepared material d is 0.2365 nm and 0.2456 nm for loaded one. The difference is 0.0091 nm. For $Ti_{45}Zr_{35}Ni_{17}Cu_3$ as-prepared amorphous material d is 0.2348 nm and 0.2404 nm for loaded one. The difference, 0.0056 nm, is smaller as expected due to lower wt. % obtained by TG. From these numbers we can calculate volumes of spheres with radii calculated above, using Equation 25.

$$V = 4/3\ \pi\ r^3 \quad (25)$$

First, for $Ti_{40}Zr_{40}Ni_{20}$ material volumes of spheres are:

V (as-prepared) = 0.055381 nm³
V (loaded) = 0,062023 nm³

which means volume expansion equals to 12 %, which corresponds to [H]/[M] = 0.60. We did the same calculation for $Ti_{45}Zr_{35}Ni_{17}Cu_3$ material and the volume expansion was 7 %, giving [H]/[M] value equal to 0.37. XRD results imply that 1.7 times more hydrogen have been stored in $Ti_{40}Zr_{40}Ni_{20}$ amorphous material than in $Ti_{45}Zr_{35}Ni_{17}Cu_3$ at the same loading conditions: temperature 300°C, pressure 45 bar and time 1000 minutes. TG results gave us similar picture, namely mass content of desorbed hydrogen was 1.5 higher from $Ti_{40}Zr_{40}Ni_{20}$ sample. Mass-spectra of these two samples are shown in Figure 82.

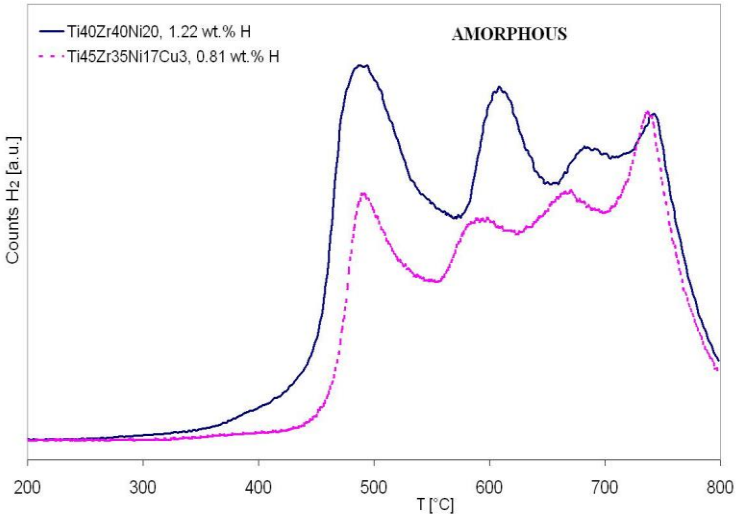

Figure 82: Mass-spectra of desorbed hydrogen from amorphous $Ti_{40}Zr_{40}Ni_{20}$ and $Ti_{45}Zr_{35}Ni_{17}Cu_3$ samples, both loaded at 300°C and 45 bar for 1000 min.

TG and mass-spectrometry of desorbed hydrogen from the same amorphous $Ti_{45}Zr_{35}Ni_{17}Cu_3$ sample, gave the same desorbed hydrogen mass %, even though one loaded for 500 min and the other for 1000 min. By these results we confirmed that all hydrogen is already absorbed in less than 8 hours.

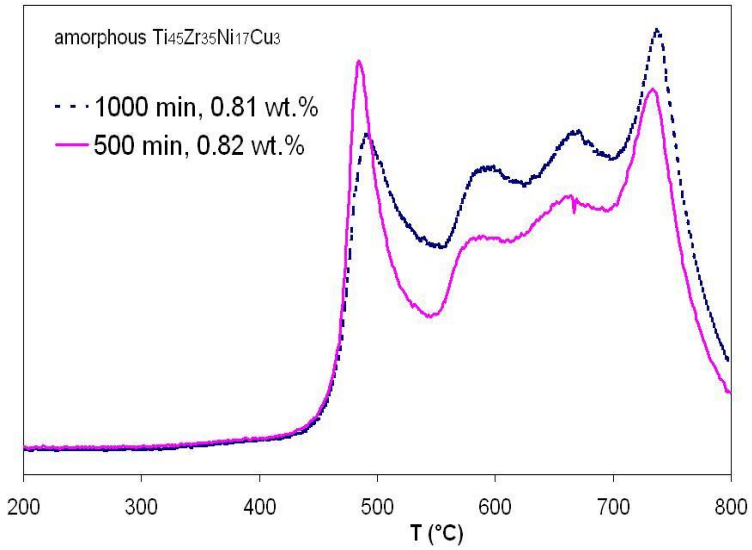

Figure 83: Mass-spectra of hydrogen desorption from $Ti_{45}Zr_{35}Ni_{17}Cu_3$ amorphous samples, loaded for 500 and 1000 min. The same amount of hydrogen was desorbed from both samples.

3.3.2.3 Hydrogen in crystalline phases

The production of crystalline, i.e. C14 Laves phase and (Zr, Ti) solid solutions samples by melt-spinning was rather unefficient, since very small amount of ribbons was useful for subsequent crushing in the mortar to get the powder, with which it is much easier to perform further investigations. To avoid this step we produced crystalline material by annealing of melt-spun i-phase ribbons at 700°C for 2 hours in dynamic 10^{-5} mbar vacuum. XRD spectra of as-prepared and loaded $Ti_{45}Zr_{35}Ni_{17}Cu_3$ samples are shown in Figure 84. With this material we did two hydriding experiments at 300°C and 45 bar, first sample was subjected to hydrogen gas for 500 min and second for 1000 min.

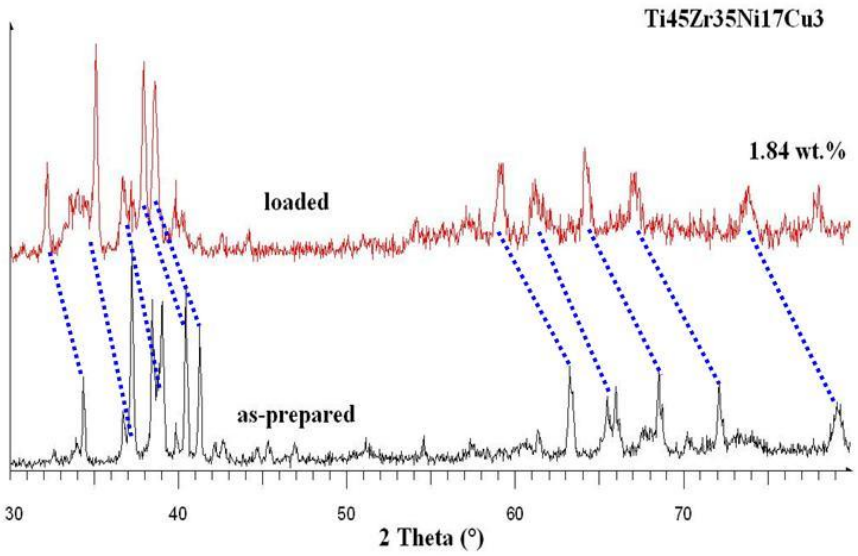

Figure 84: Lattice expansion of hexagonal C14 Laves phase and cubic (Zr, Ti) solid solutions due to interstitially bonded protons.

We have got interesting results by mass-spectrometer, where analysis on crystalline $Ti_{40}Zr_{40}Ni_{20}$ and $Ti_{45}Zr_{35}Ni_{17}Cu_3$ samples was done, Figure 85. TG of $Ti_{45}Zr_{35}Ni_{17}Cu_3$ sample showed that they contained comparable amounts of hydrogen: namely first sample loaded for 500 min contained 1.84 wt. %, but the second one contained slightly less hydrogen, 1.74 wt. %, even though it was loaded for twice as long, 1000 min.

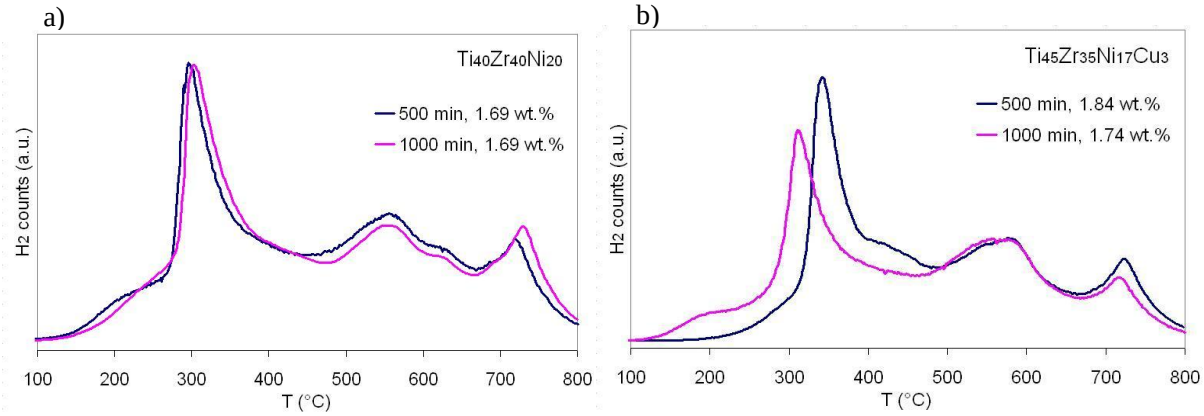

Figure 85: Mass-spectra of desorbed hydrogen from crystalline a) $Ti_{40}Zr_{40}Ni_{20}$ and b) $Ti_{45}Zr_{35}Ni_{17}Cu_3$ samples, loaded for 500 and 1000 min.

3.3.2.4 Partial dehydrogenation of i-phase

Since there are two hydrogen bonding sites in the icosahedral material, related to two desorption temperatures, we asked ourselves how partial hydrogen desorption from low bonding energy sites at 500°C affects XRD spectrum. Would this desorption appear in X-ray diffraction just as partial or as complete desorption of hydrogen from i-phase? The answer is given in Figure 86, which implies that hydrogen was fully desorbed from the icosahedral grains, since the diffraction peaks of desorbed material returned back to the initial state of the as-spun material peaks. Two questions arise from that result, namely is it possible that hydrogen from high bonding energy sites (desorption at 740°C) somehow re-distributes to low energy sites from where it is simultaneously desorbed? Or, could that second peak in i-phase mass-spectrum belong to hydrogen in the amorphous matrix, because this hydrogen could not be seen by XRD. To get better insight if there is still some hydrogen trapped inside the material, we measured magnetic properties as well. Results shown in Figure 87 reveal that the magnetization of partially desorbed sample is still higher than the magnetization of the initial sample. Nevertheless, another important feature can be observed in Figure 86, namely no stable hydrides, such as ZrH_2 and TiH_2, were formed after desorption, which means that this material has reversible hydrogenation characteristics.

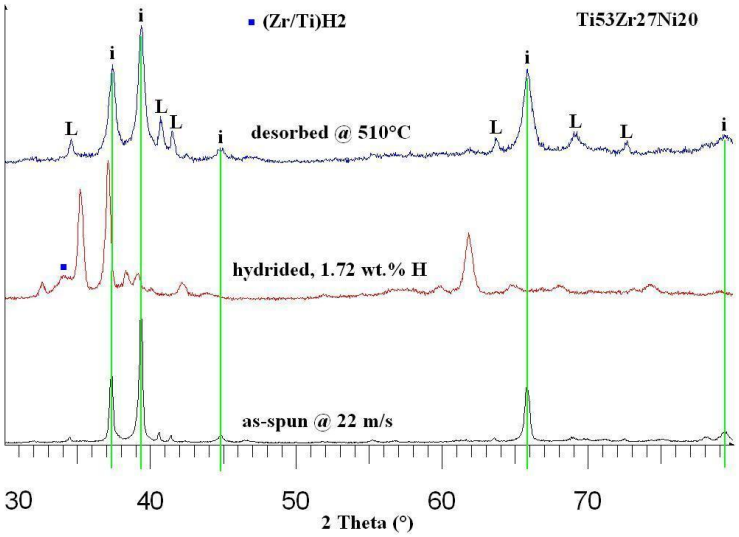

Figure 86: XRD spectra of as-prepared, loaded and unloaded $Ti_{53}Zr_{27}Ni_{20}$ i-phase implies that this material can be already fully unloaded at low desorption temperature (see Figure 77). No stable hydrides have been formed.

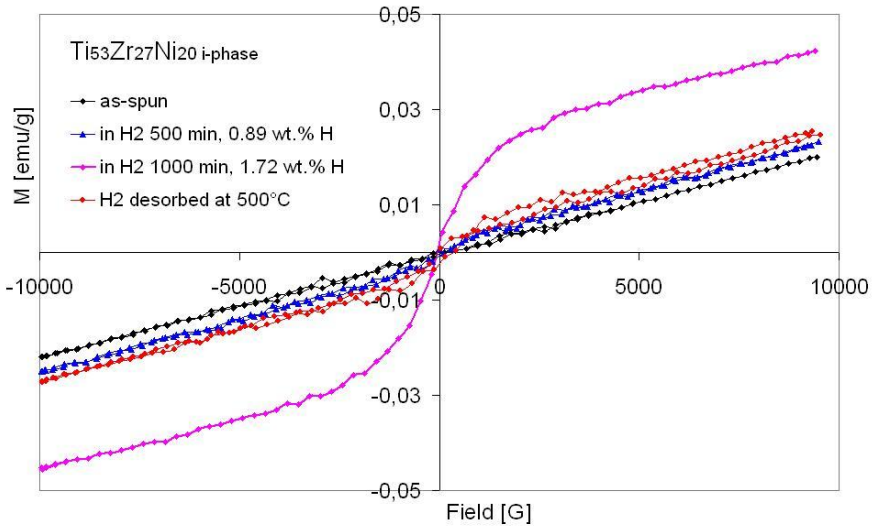

Figure 87: VSM data of $Ti_{53}Zr_{27}Ni_{20}$ i-phase ribbons; as-prepared, loaded with two different H_2 contents, and finally desorbed at 500°C. Even though almost all hydrogen was desorbed, by VSM measurements we can see irreversible magnetic response (red curve).

To see if there is really any hydrogen left in the material after desorption at 510°C for 50 minutes as Figure 87 implies, we did mass-spectrometry of residual hydrogen by heating the sample up to 800°C. Results in Figure 88 show that there is a small amount of hydrogen starting to desorb at 600°C. The amount of desorbed hydrogen was too small to be detected by TG, since the experimental error is estimated around 0.05 wt. %. These results confirmed that all hydrogen was desorbed already at 510°C after 50 minutes.

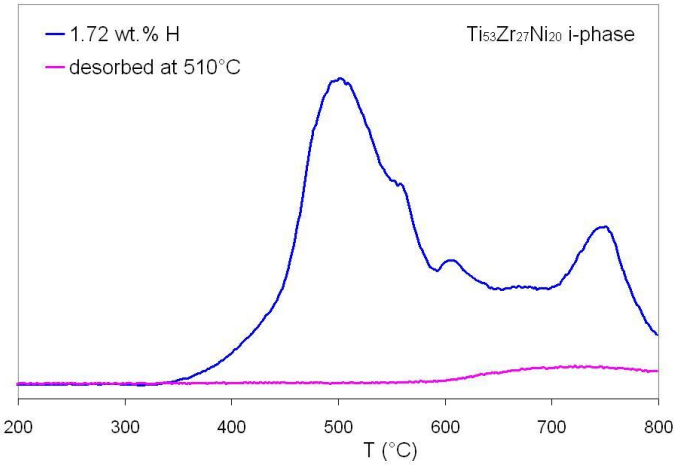

Figure 88: Mass-spectra of desorbed hydrogen from fully loaded $Ti_{58}Zr_{24}Ni_{18}$ i-phase (1.81 wt. %) and the same sample, after hydrogen was desorbed at the first and most intense desorption peak (510 °C).

3.3.2.5 Low pressure hydrogenation of ribbons

Due to the reports of Konstanchuk et al. (2001) titanium and zirconium alloys undergo activation as a result of heating in vacuum or at low hydrogen pressure before hydriding. During the annealing, rupture of the surface oxide film occurs, either because of cracking due to the differences in the thermal expansion coefficients of metal and oxide, or because of partial dissolution of the oxide. The rupture of the oxide film causes the formation of additional hydrogen adsorption centers and, as a consequence, the increase of hydriding rate.

To verify this theory on our material we did series of hydrogenating experiments at normal hydrogen pressure (1 bar), which included activation steps at different conditions. First, we melt-spun $Ti_{53}Zr_{27}Ni_{20}$ ribbons at 22 m/s to get the icosaherdal structure, see Figure 89. We have not even crushed the ribbons in the mortar, but whole flakes were placed inside silica tube, attached to vacuum system and hydrogen gas.

When we annealed ribbons at 450°C in hydrogen for 6 hours substacial amount of expanded C14 and β-phase formed simultaneously with the i-phase expansion. Similar happened with the sample annealed at 500 and 300°C for two hours, respectively, only that the i-phase expansion was bigger in this case. But, in both cases a lot of (Zr/Ti)H_2 solid solution phase has formed. On the other hand, during hydrogen absorption via "complicated program" described in the next paragraph, no new phases were formed, only i-phase expansion occurred.

From these findings we may conclude that the low pressure hydrogen uptake in Ti-Zr-Ni icosahedral alloy is very sensitive on selected activation route. First, we did so-called "complicated program" activation, which contained few activation steps: 4 hours at 450°C in hydrogen (first absorption), natural cooling in hydrogen flow for 24 hours, 2 hours at 500°C in high dynamic vacuum (desorption), second absorption in hydrogen for 6 hours at 300°C. Logical question that arises from this result is whether we can skip the last two activation steps and obtain the same amount of hydrogen in the material just after the first step. The answer is no, since secondary crystalline and hydride phases are formed in case of loading the sample without activation.

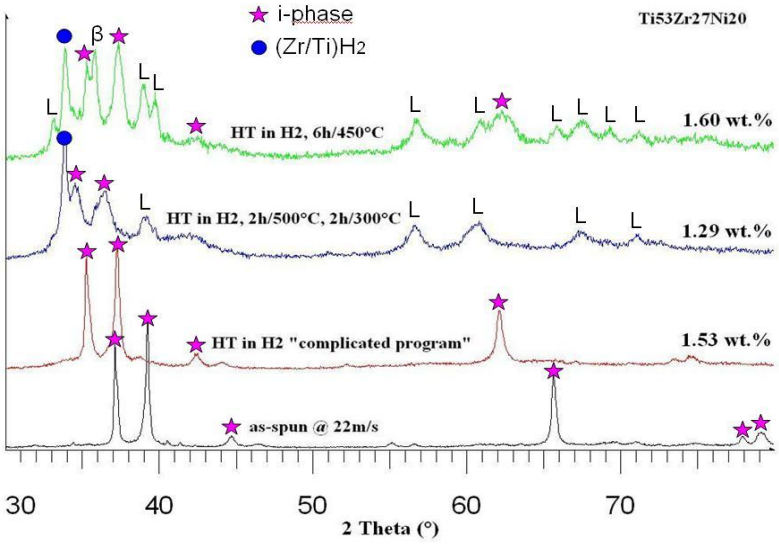

Figure 89: XRD spectra of ribbons hydrogenated at normal hydrogen pressure, subjected to various thermal activation regimes. HT denotes heat-treatment.

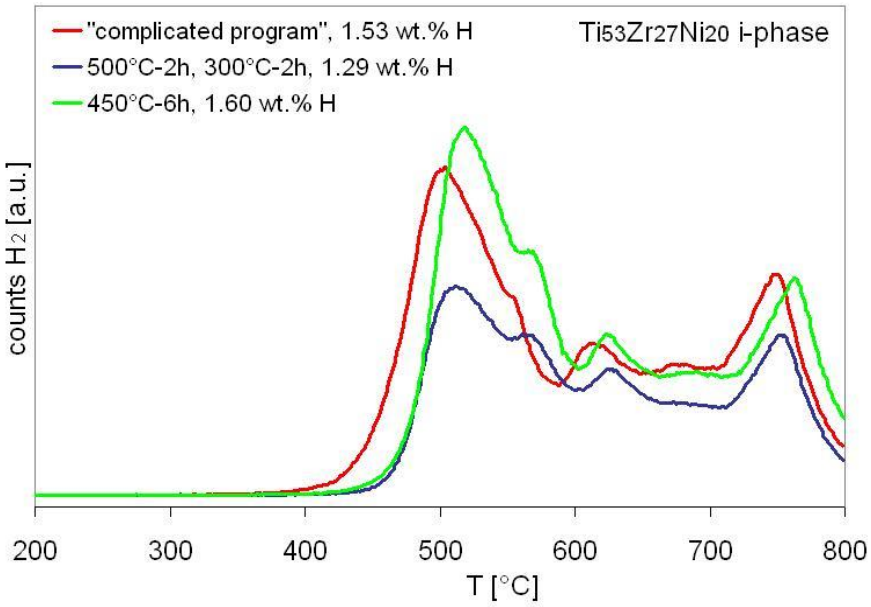

Figure 90: Mass-spectra of desorbed hydrogen from icosahedral samples, hydrided at normal hydrogen pressure, at different heating regimes.

As we measured mass-spectra of desorbed hydrogen from $Ti_{53}Zr_{27}Ni_{20}$ i-phase loaded at high pressure (45 bar), which contained 1.72 wt. % of hydrogen, and from the same starting material, only loaded at normal hydrogen pressure by using "complicated" activation program, containing 1.53 wt. %, we saw that the hydrogen desorption temperature distribution is practically independent of the route the sample was loaded, Figure 91.

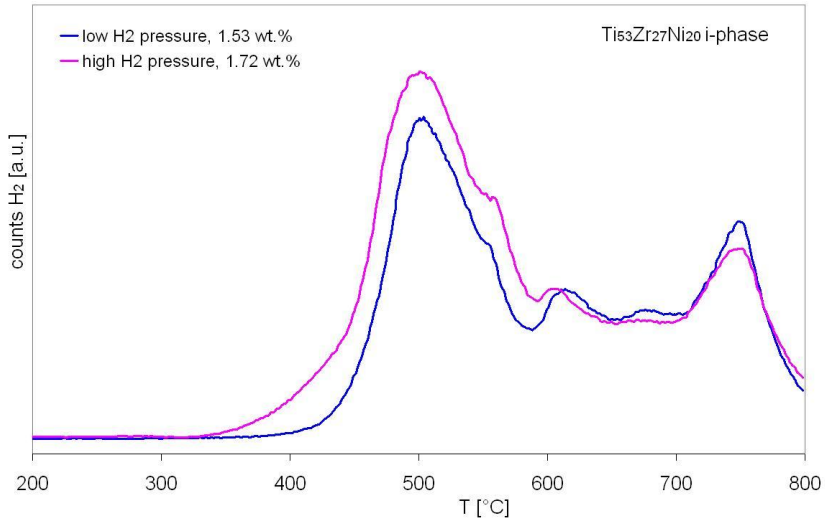

Figure 91: Hydrogen desorption temperature distribution is practically independent of the way the sample was loaded, i.e. high (45 bar) or low (1 bar) pressure loading.

Another low-pressure loading experiment has been performed, only not in a pure hydrogen gas but in a mixture of 7 vol. % H_2 in Ar, with commercial name Inoxmix. I-phase $Ti_{45}Zr_{35}Ni_{17}Cu_3$ ribbons, spun at 26 m/s were subjected to this atmosphere at normal pressure and 400°C for 16 hours. X-ray analysis showed modest quasilattice expansion due to hydrogen absorption, Figure 92.

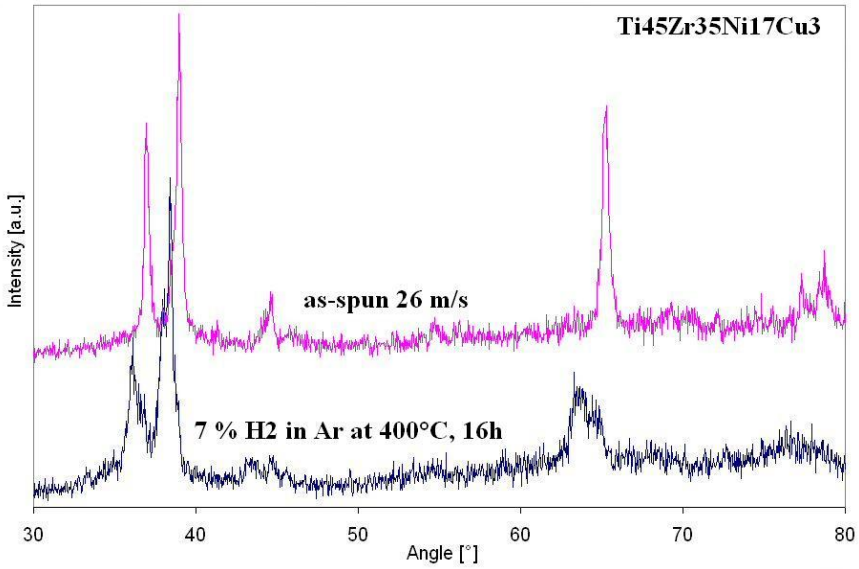

Figure 92: XRD spectra of as-spun and loaded $Ti_{45}Zr_{35}Ni_{17}Cu_3$ i-phase ribbons.

3.3.2.6 Hydrogen induced i-phase formation

We performed this experiment to show the catalytic influence of hydrogen on transformation of C14 Laves phase to icosahedral quasicrystalline phase, Figure 93. Namely, in all Ti-Zr-Ni samples we have loaded, we observed diminishing of crystalline phase peaks upon hydrogen absorption and thus lattice expansion of all present phases. To be sure that this effect is due to hydrogenation, we thermally treated one of the samples that contains high amount of Laves phase, using the same temperature (i.e. 1000 min at 300°C) as for hydriding, only in vacuum. The content of crystalline phase has even slightly increased after heat-treatment in vacuum. When we performed the same experiment again, only in hydrogen ambient, we observed

substancial decrease of Laves phase peaks and its expansion as expected. Quasilattice has expanded for 5.75 % ([H]/[M] = 1.44).

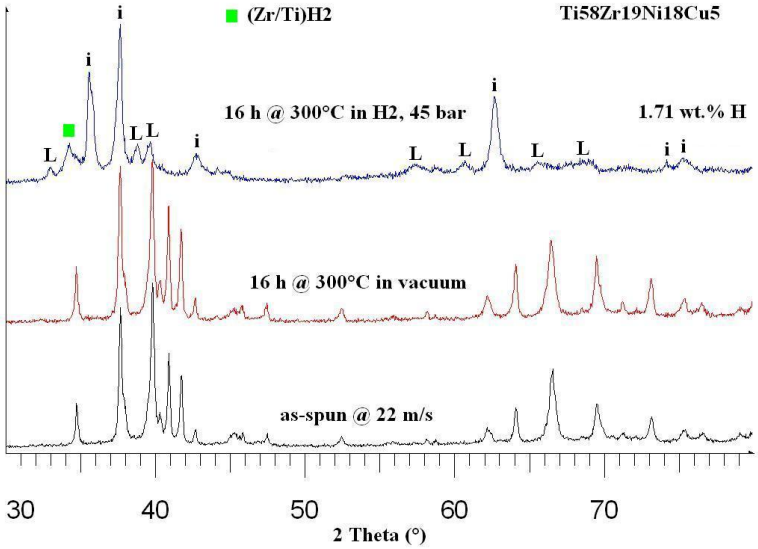

Figure 93: XRD spectra of $Ti_{58}Zr_{19}Ni_{18}Cu_5$ melt-spun material indicates mixture of icosahedral and Laves phase in as-spun and vacuum annealed samples. Clearly, hydrogen induces Laves phase-to-icosahedral phase transformation.

3.3.2.7 Dehydrogenation of powders mechanically alloyed in hydrogen

Since substancial amounts of hydrogen were absorbed in $Ti_{40}Zr_{40}Ni_{20}$ powder during mechanical alloying in hydrogen, starting with elemental powders and normal pressure of hydrogen, which was refilled 5 times, after every sampling, we performed mass-spectrometry analysis of desorbed hydrogen from the sample, mechanically alloyed in H_2 for 40 hours. As said before, full amorphization did not occur, since size of the powder particles decreased to submicrometer level, enabling Van der Walls forces to stick particles on the milling vial, which prevented further contact of majority of the material with the milling balls. Thus, remaining nickel peaks can be observed, since it did not react with hydrogen. Zirconium and titanium reacted with hydrogen forming predominant amorphous hydride phase, but part of the sample is still crystalline TiH_2 and ZrH_2, as well as crystalline Ni, because that part of sample in the mill was isolated from milling balls, Figure 94b.

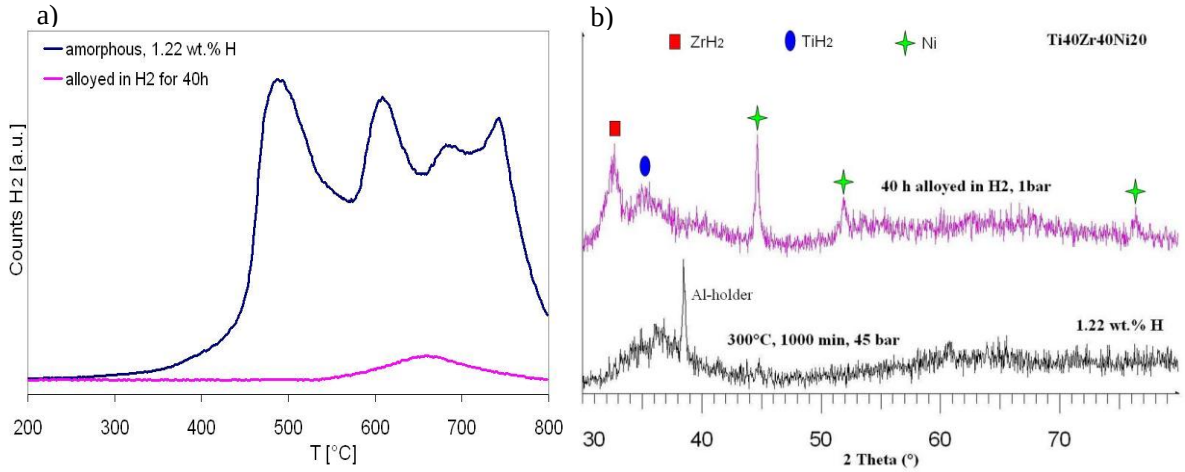

Figure 94: a) Comparison of H_2 mass-spectra from sample mechanically alloyed in hydrogen for 40 hours by 5-times refilling of hydrogen, and amorphous sample with the same composition, loaded with hydrogen from gas phase at 300°C, 1000 min and 45 bar; b) corresponding XRD spectra.

By mass-spectrometry we determined that a negligible amount of hydrogen came out of the sample, which was mechanically alloyed for 40 hours in hydrogen, Figure 94a. Very broad H_2 desorption peak

around 660°C indicates rather strongly bounded H atoms and broad distribution of bonding energies. This broadening refers to many different local chemical environments of interstitial protons. Corresponding TG data showed 0.22 mass % increase of the sample, which we think is due to oxidation and water formation, both related to submicrometer powder particles.

By mechanical alloying of elemental powders in hydrogen we could not get hydrided amorphous powder, as we did by MA in Ar and subsequent high-pressure hydrogenation, but rather a mixture of Ti/Zr stable hydrides solid solution phases and partially crystalline nickel.

3.3.3 Hydrogen effect on the magnetization

3.3.3.1 I-phase

Magnetic measurements of as-prepared and hydrided Ti-Zr-Ni alloys are a real added value of this doctoral dissertation, since to our best knowledge no reports on this topic have been published, yet. Its primar purpose was to measure the content of hydrogen in alloys via modified magnetic properties, e.g. magnetization, measured by VSM device.

In several investigated samples an increase of the magnetization and transition from paramagnetic to ferromagnetic + paramagnetic behaviour has been observed upon bonded hydrogen. For instance, $Ti_{45}Zr_{35}Ni_{17}Cu_3$ i-phase showed no change of magnetization after thermal treatment for 16 hours at 400°C in vacuum, in order to increase size of icosahedral grains, embedded in the amorphous matrix. However, the magnetization at 10 kOe have increased for about 30 % and ferromagnetic contribution was revealed as well after 1.56 mass % of hydrogen was loaded into the pre-annealed sample, Figure 95a. It is interesting that magnetic properties were not modified upon annealing, as one would expected due to the formation of (hexagonal!) crystalline phases, which are well-known to posess magneto-crystalline anisotropy.

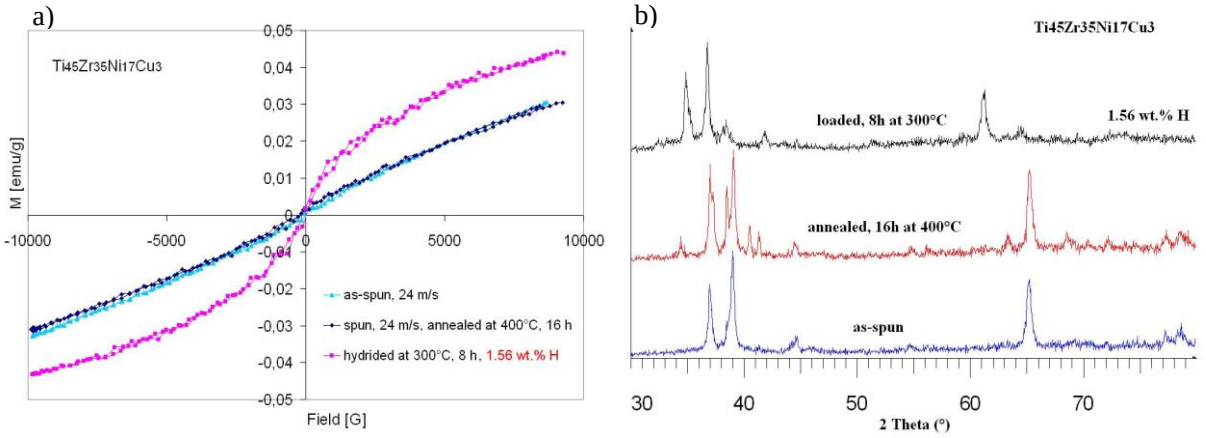

Figure 95: a) VSM curves of as-spun, annealed and hydrided $Ti_{45}Zr_{35}Ni_{17}Cu_3$ i-phase samples. Approximately 30 % increase of magnetization at 10 kOe has been observed for hydrided sample, containing 1.56 wt. % H; b) corresponding XRD spectra reveal the formation of crystalline phases upon annealing of the i-phase ribbons, which disappear after hydrogenation.

Magnetization increased when those crystalline phases disappeared and expanded icosahedral quasilattice showed-up after substancial amount of hydrogen has been absorbed, namely 1.56 mass %, at 300 °C and 45 bar after 8 hours.

Similar behaviour showed $Ti_{53}Zr_{27}Ni_{20}$ i-phase sample that was loaded via multi-step thermal activation in 1 bar hydrogen atmosphere, namely this sample contained 1.53 mass % of hydrogen after absorption and showed slight magnetization increase, though not to such extent as $Ti_{45}Zr_{35}Ni_{17}Cu_3$ i-phase sample, Figure 96.

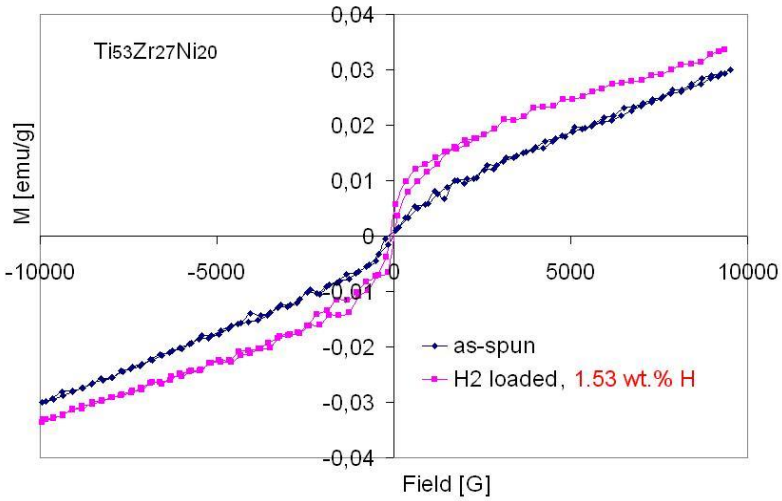

Figure 96: VSM curves of as-spun (22 m/s) $Ti_{53}Zr_{27}Ni_{20}$ i-phase and hydrided at 1 bar of hydrogen by multi-step thermal activation, containing 1.53 wt. % H.

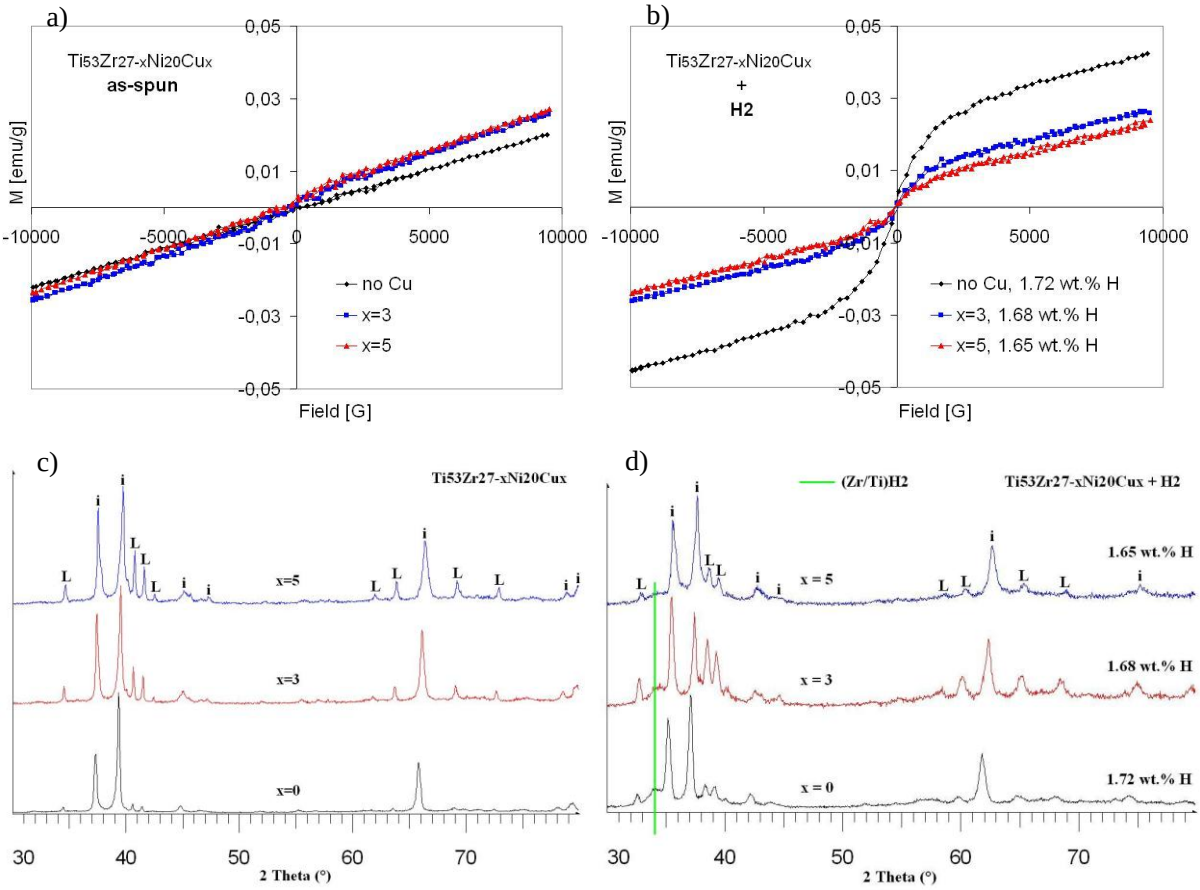

Figure 97: VSM and XRD data of $Ti_{53}Zr_{27-x}Ni_{20}Cu_x$ (x= 0, 3, 5) predominantly icosahedral alloys; a) and c) as-spun at 22 m/s, b) and d) hydrided at 300 °C for 16 hours, all containing comparable amounts of hydrogen.

Figure 97 and Figure 98 are showing VSM and XRD data of as-spun and hydrided $Ti_{53}Zr_{27-x}Ni_{20}Cu_x$ (x= 0, 3, 5) and $Ti_{58}Zr_{24-x}Ni_{18}Cu_x$ (x= 0, 3, 5) predominantly icosahedral alloys. All samples were obtained by melt-spinning at 22 m/s and subsequently hydrided at 300°C for 16 hours. We see that more copper the alloys contain the more C14 phase is formed in as-spun samples, but all exhibiting paramagnetic behaviour with practically the same susceptibilities. When those samples are hydrided, huge difference of magnetic properties can be observed between the basic compositions. All samples become more ferromagnetic upon loading, but for $Ti_{53}Zr_{27-x}Ni_{20}Cu_x$ alloy the ferromagnetic contribution decreases with copper content, whereas for $Ti_{58}Zr_{24-x}Ni_{18}Cu_x$ alloy it is vise versa and the maximum magnetization increase (at 1 Tesla) is

5-times bigger than the maximum magnetization increase (at 1 Tesla) of the $Ti_{53}Zr_{27-x}Ni_{20}Cu_x$ sample. From XRD data we can further examine the formation of $(Zr/Ti)H_2$ phase, which seems to be inhibited by copper addition and has no influence on modified magnetic properties of these alloys.

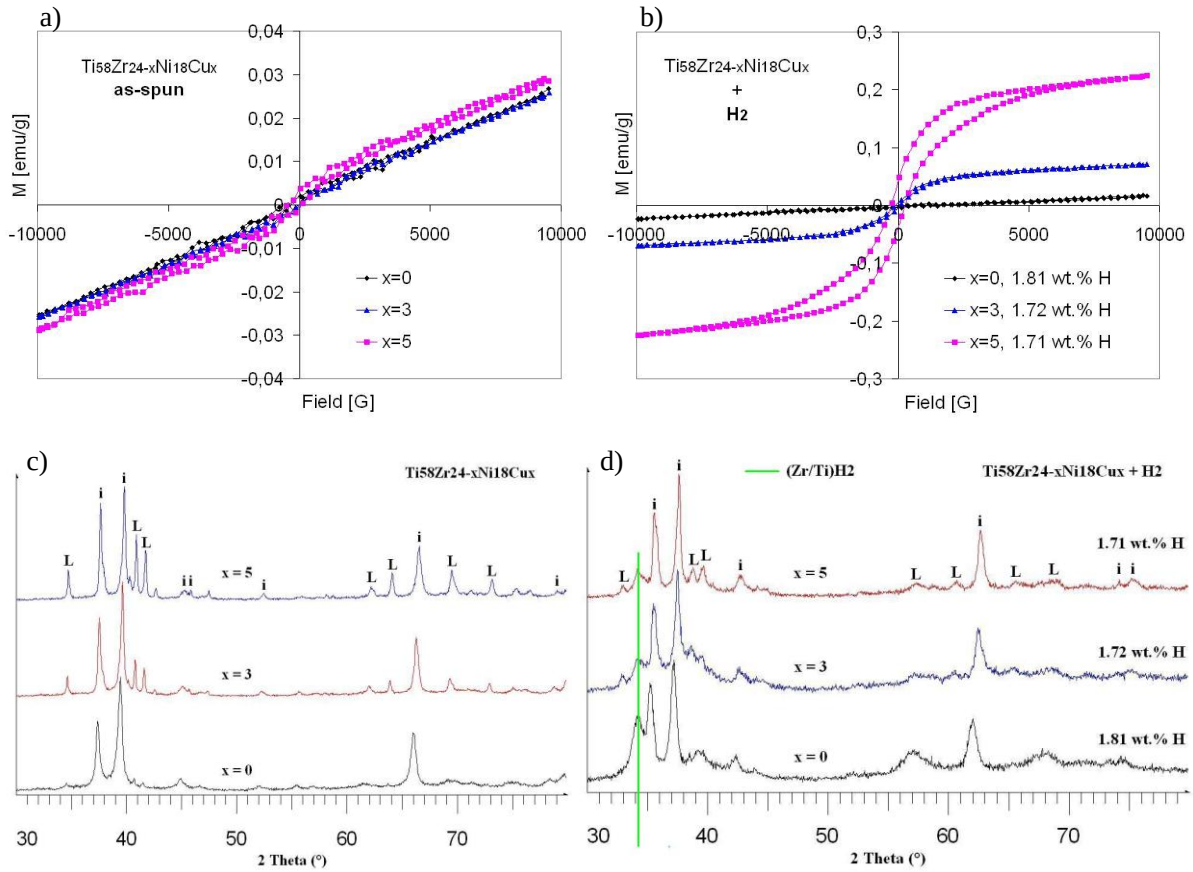

Figure 98: VSM and XRD data of $Ti_{58}Zr_{24-x}Ni_{18}Cu_x$ (x= 0, 3, 5) predominantly icosahedral alloys; a) and c) as-spun at 22 m/s, b) and d) hydrided at 300 °C for 16 hours, all containing comparable amounts of hydrogen.

3.3.3.2 Amorphous phase

We studied hydrogen effect on magnetic properties of mechanically alloyed amorphous powders only, since we were not able to load any hydrogen in melt-spun amorphous ribbons by high-pressure Sievert's device. XRD patterns are shown in Figure 80. VSM data of these experiments are shown in Figure 99. These two graphs reveal that hydrogenation of the amorphous material does not modify its magnetic properties, independent of the composition and the loading time. All samples show paramagnetic + ferromagnetic response with similar extent of magnetization.

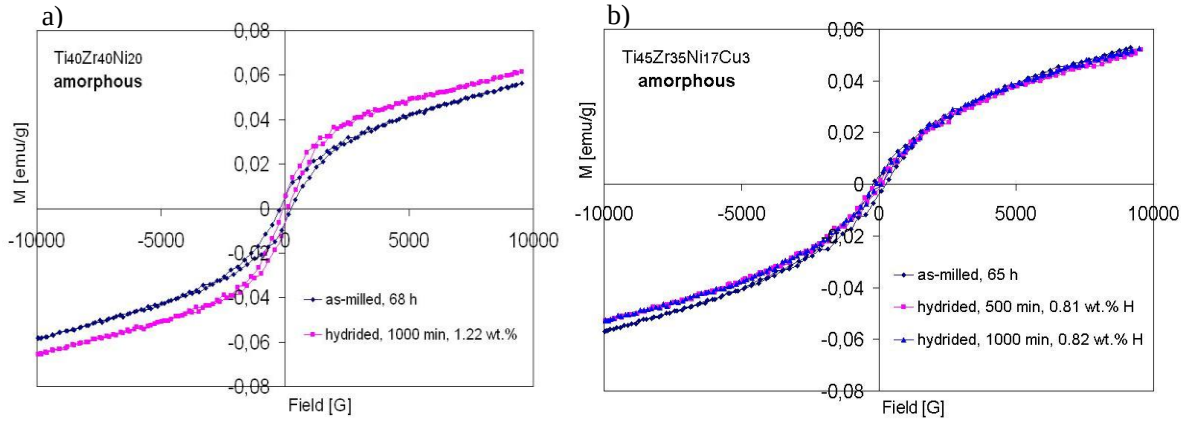

Figure 99: VSM study of hydrided and as-prepared amorphous a) $Ti_{40}Zr_{40}Ni_{20}$ and b) $Ti_{45}Zr_{35}Ni_{17}Cu_3$ samples, obtained by mechanical alloying of melt-spun ribbons.

3.3.3.3 Crystalline phases

In Figure 100 VSM data of as-annealed and hydrided crystalline $Ti_{40}Zr_{40}Ni_{20}$, $Ti_{45}Zr_{35}Ni_{17}Cu_3$ and $Ti_{53}Zr_{27}Ni_{20}$ samples are shown. All three were loaded for 500 and 1000 min at 300°C and pressure 45 bar. Only difference is that $Ti_{45}Zr_{35}Ni_{17}Cu_3$ sample was annealed at 800°C for 4 hours, whereas the other two were heat treated at 700°C for 2 hours. But nevertheless, according to previously shown XRD data all samples exibit crystalline structure, containing predominantly mixture of C14 and α/β-phase. However, when $Ti_{40}Zr_{40}Ni_{20}$ and $Ti_{45}Zr_{35}Ni_{17}Cu_3$ samples were hydrided they showed different magnetic response, depending on the loading time, even though this did not affect the amount of desorbed hydrogen much. They become more ferromagnetic with respect to as-annealed samples. Interestingly, susceptibility of $Ti_{53}Zr_{27}Ni_{20}$ sample was not affected by hydrogen absorption, neither after 500 or 1000 min of loading.

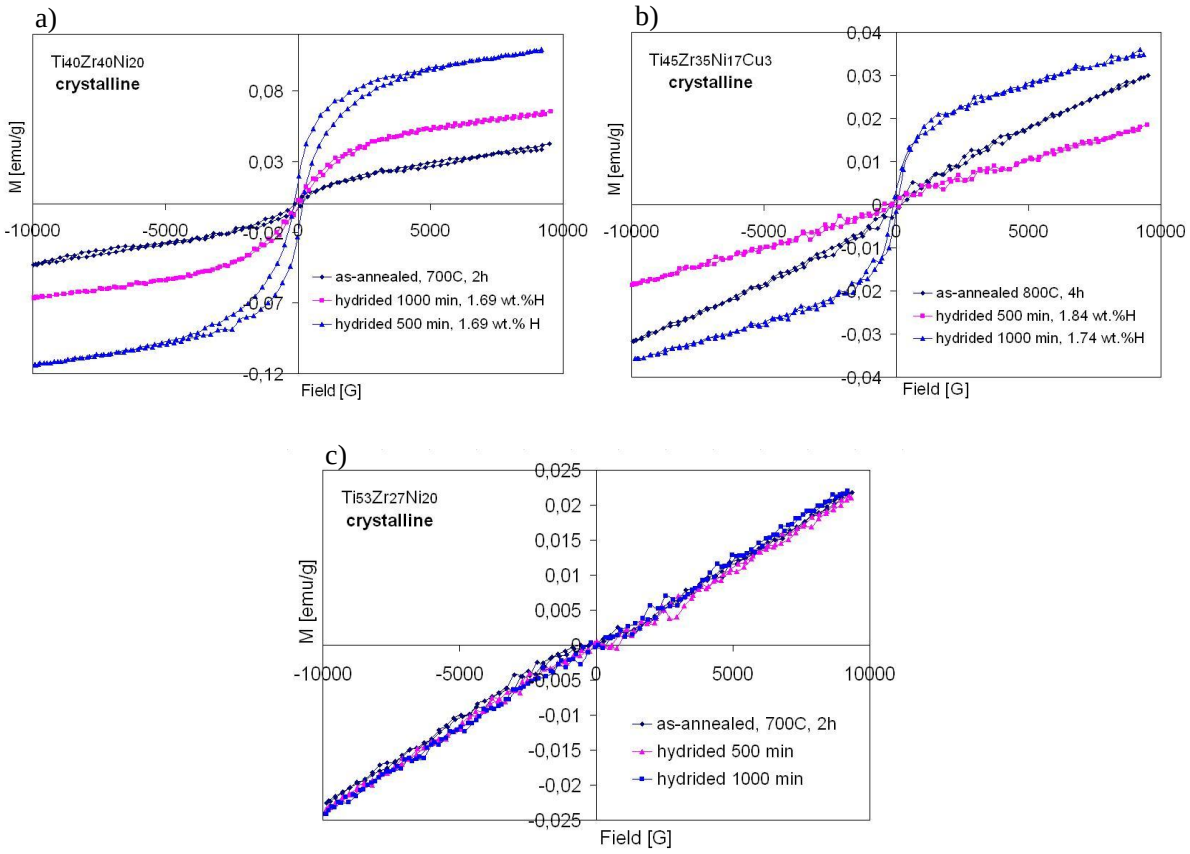

Figure 100: VSM data of as-annealed and hydrided crystalline a) $Ti_{40}Zr_{40}Ni_{20}$, b) $Ti_{45}Zr_{35}Ni_{17}Cu_3$ and c) $Ti_{53}Zr_{27}Ni_{20}$ samples.

3.3.4 ^{2}H NMR study

Under these conditions, the icosahedral sample absorbed 1.89 wt. % of D_2, which equals to deuterium-to-metal ratio [D]/[M] = 0.64, whereas amorphous sample absorbed 4.3 wt. % of D_2 or [D]/[M] = 1.48. The XRD spectra of loaded and unloaded samples are shown in Figure 101.

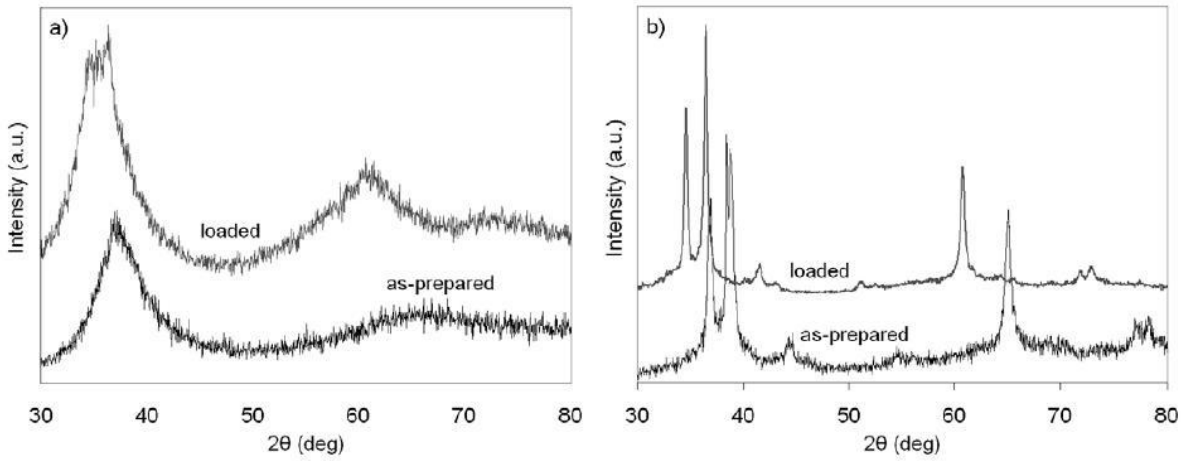

Figure 101: XRD spectra of a) amorphous and b) icosahedral $Ti_{40}Zr_{40}Ni_{20}$ samples in unloaded state and after deuterium loading.

The shift of the peaks to lower angles due to the lattice expansion upon deuteration is observed for both samples. The XRD of loaded amorphous sample shows an additional feature: the high peak at $2\theta \sim 36°$ due to the first-neighbour atomic shell shows some additional structure of sharp lines at its top, demonstrating that a small amount of a crystalline phase (perhaps a stable metal hydride phase) formed within the amorphous matrix upon deuteration.

Figure 102 shows a dynamic transition from motionally narrowed ^2H NMR spectra of amorphous and icosahedral samples above 300 K to static spectra below 200 K. The shape of the asymptotic high-temperature lineshape (400 K) is Lorentzian-like, whereas low temperature static spectrum (80 K) has shape of Gaussian curve.

The temperature-dependent full width at half-maximum (FWHM) of the ^2H NMR spectra from Figure 102 are shown in Figure 103. Transition from the fast-to the slow-motion of deuterons regime occurs between 300 and 200 K. This means that deuterium hopping frequencies between neighbouring interstitial sites slow down upon cooling and cross the 1-10 kHz range between 300 and 200 K.

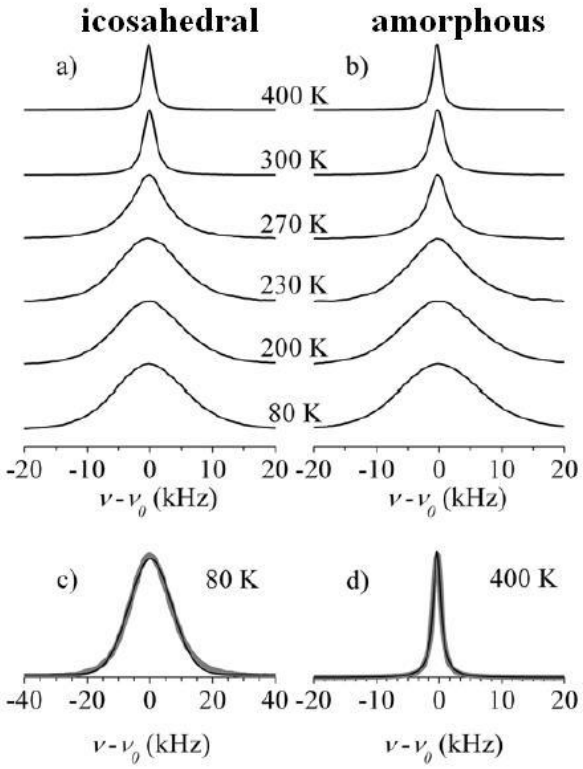

Figure 102: The temperature-dependent deuterium NMR spectra of a) icosahedral and b) amorphous sample. For amorphous sample, the Gaussian fit of the static spectrum at T = 80 K is shown in c), whereas a Lorenzian fit of the motionally narrowed spectrum at T = 400 K is shown in d).

Comparing FWHM curves in Figure 103 shows that the corresponding fit parameters of icosahedral and amorphous samples are practically the same. Based on the Arrhenius thermally activated form of the autocorrelation time, described by Equation 25, activation energy, E_a, could be calculated for both samples. 230 ± 10 meV and 250 ± 10 meV are activation energies for deuterim hopping in icosahedral and amorphous sample, respectively.

$$\tau_c = \tau_0 \exp(E_a/k_B T) \tag{25}$$

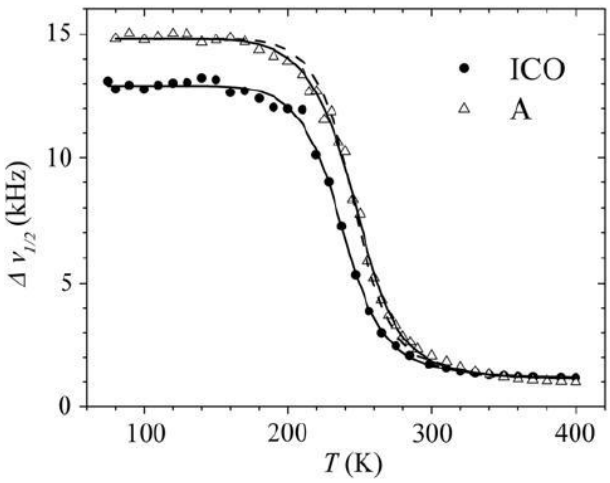

Figure 103: The temperature-dependent full width at half-maximum $\Delta\nu_{1/2}$ of the ^{2}H NMR spectra of the icosahedral (ICO) and amorphous (A) samples.

Considering experimental error, these values are practically the same. On the other hand this small difference in activation energies (8 %) can be understood in terms of substancially different contents of

deuterim loaded in both samples, since there is over 100 % more deuterium absorbed in the amorphous material. Thus, for realistic influence of the structure, i.e. chemical environment, on the activation energy for deuterium hopping, both samples should be loaded to the same or at least similar extent.

Similarly, amorphous sample exhibits about 10 % bigger static spectrum width (due to higher inhomogeneous broadening), implying on a larger density of different local chemical environments in the amorphous material. Again, this difference might come from the fact that amorphous sample contains roughly twice as much ^2H than icosahedral, since higher deuterium loading results in larger expansion of the lattice and creation of more defects, acting as different local chemical environments. This prooves that we should analyze samples with similar contents of absorbed deuterium.

3.3.5 Hydriding of quenched rods

Quenched rods with 3 mm in diameter and with compositions $Ti_{33}Zr_{41}Ni_{21}Cu_5$, $Ti_{40}Zr_{40}Ni_{20}$, $Ti_{45}Zr_{35}Ni_{17}Cu_3$ and $Ti_{53}Zr_{27}Ni_{20}$ were crushed in the mortar to increase specific surface for hydrogen dissociation, like we did for hydrogen absorption in melt-spun ribbons. Then, these powders were placed in a stainless steel hydrogenation device for 1000 minutes at 300°C and 45 bar of technical hydrogen. After that we performed mass-spectrometry of desorbed hydrogen, using the same experimental conditions as for loaded melt-spun ribbons, Figure . Like we expected, the more crystalline secondary phases the sample contains, the more distorted gets its spectrum from the »ideal« i-phase spectrum. For instance, if we compare mass-spectra of $Ti_{40}Zr_{40}Ni_{20}$, which contains practically no Laves or solid solution phase, but predominantly icosahedral one, with $Ti_{45}Zr_{35}Ni_{17}Cu_3$ one, we see these two spectra differ quite a lot, since $Ti_{45}Zr_{35}Ni_{17}Cu_3$ rod contains much more Laves and β-phase. The same is true for the other two compositions, only not so drastically.

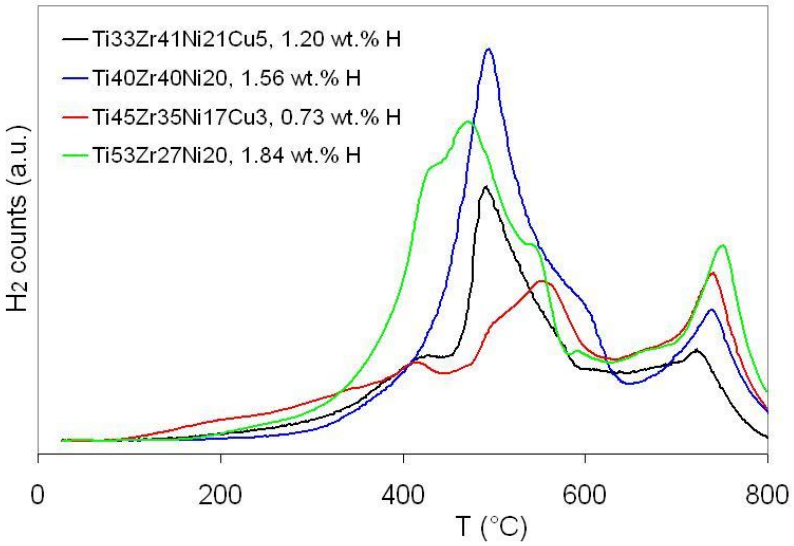

Figure 104: Mass-spectra of desorbed hydrogen from 3 mm quenched rods with different compositions, all loaded under same conditions, i.e. 300°C and 45 bar for 1000 minutes.

When we checked XRD patterns of these rods, i.e. as-cast and hydrided, we saw no diminishing of C14 Laves or β phase peaks, as was the case for melt-spun samples, Figure 105. Namely, there we claim hydrogen induces i-phase formation from those crystalline phases. We observed no diminishing of these peaks in fully crystalline and hydrided samples either. So, the only logical explanation for Laves and β phase transformation into icosahedral phase upon hydrogenation is the presence of amorphous phase (matrix) in melt-spun ribbons. Consequently we my say that there is no amorphous phase present in 3 mm quenched rods. These observations are in good accordance with reports of Wang et al., 2003a, where they investigated microstructures of quenched $Ti_{45}Zr_{35}Ni_{17}Cu_3$ rods of different diameters by TEM. In 3 mm rods there were just C14, β and i-phase grains present, without any amorphous areas. In 2 mm rods they found mainly C14 and i-phase, whereas 1 mm rods consisted of homogenously distributed i-phase grains below 5 μm, embedded in amorphous matrix.

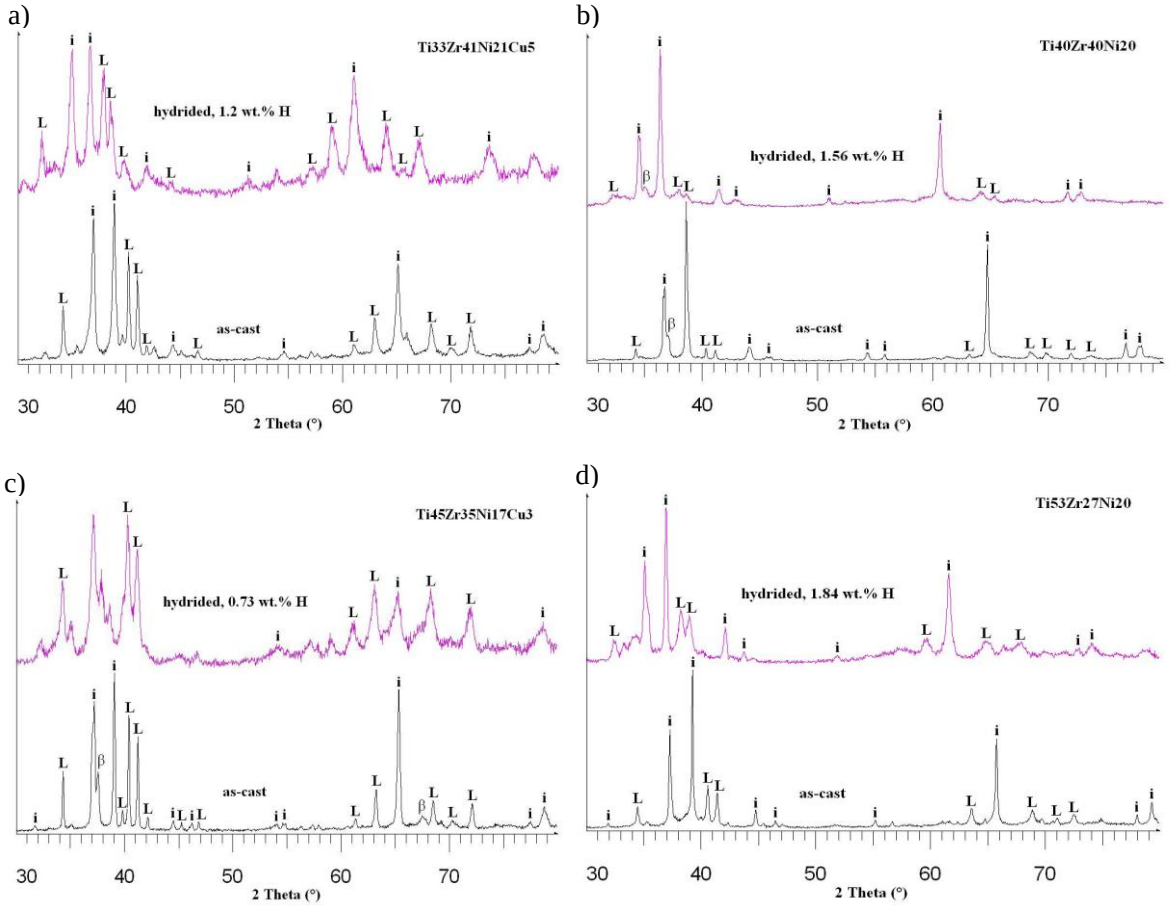

Figure 105: XRD spectra of as-cast and hydrided (300°C, 1000 min) 3 mm rods of four different compositions; a) $Ti_{33}Zr_{41}Ni_{21}Cu_5$, b) $Ti_{40}Zr_{40}Ni_{20}$, c) $Ti_{45}Zr_{35}Ni_{17}Cu_3$ and d) $Ti_{53}Zr_{27}Ni_{20}$.

3.4 Quenched rods

3.4.1 X-ray diffraction

As-quenched rods were crushed in the mortar at room temperature to analyze the structure by powder XRD. In Figure 106 we present X-ray diffraction data of as-quenched rods with constant diameter and different compositions, namely those used for melt spinning experiments, except for $Ti_{33}Zr_{41}Ni_{21}Cu_5$.

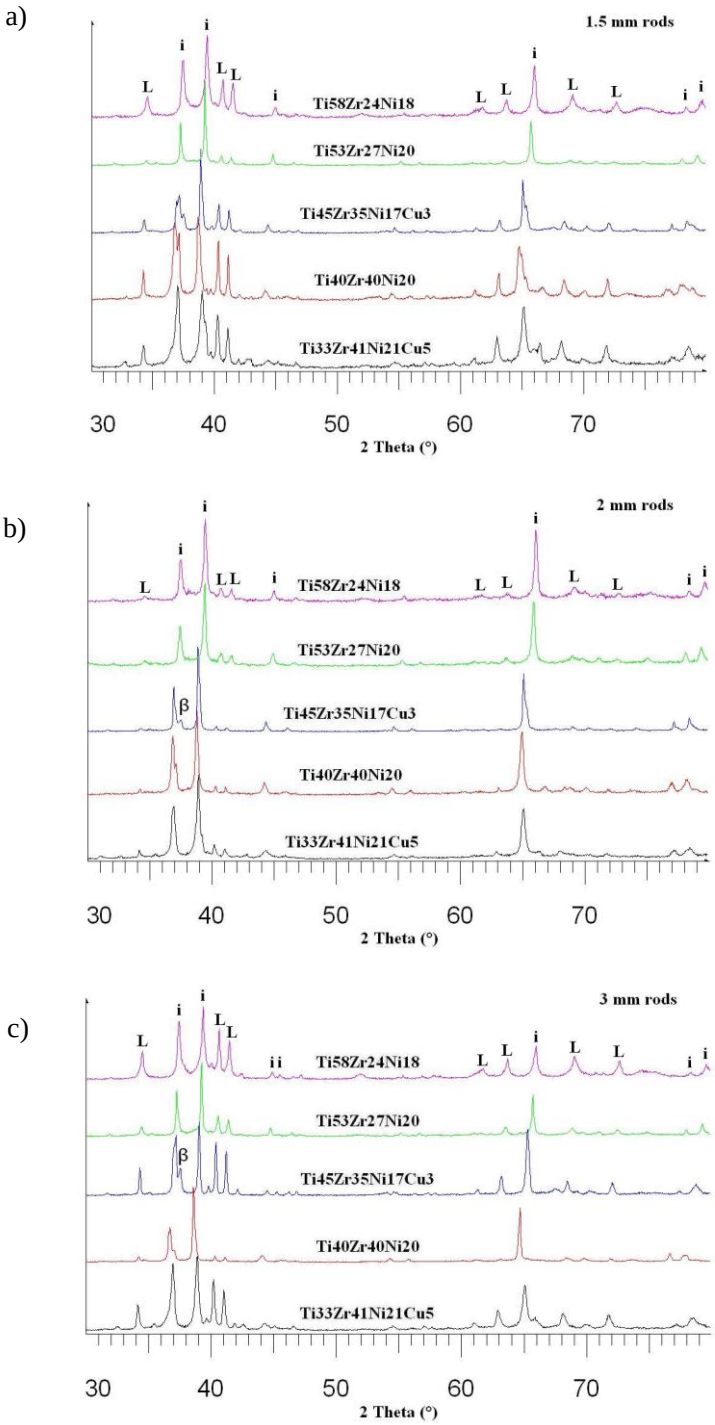

Figure 106: XRD spectra of a) 1.5 mm, b) 2 mm and c) 3 mm vacuum-cast rods of various compositions, all predominantly containing icosahedral phase and minority of hexagonal C14 Laves and FCC β-(Ti, Zr) solid solution.

The same results are shown in Figure 107 in order to stress out the optimal cooling conditions for i-phase formation were achieved by using 2 mm copper mould.

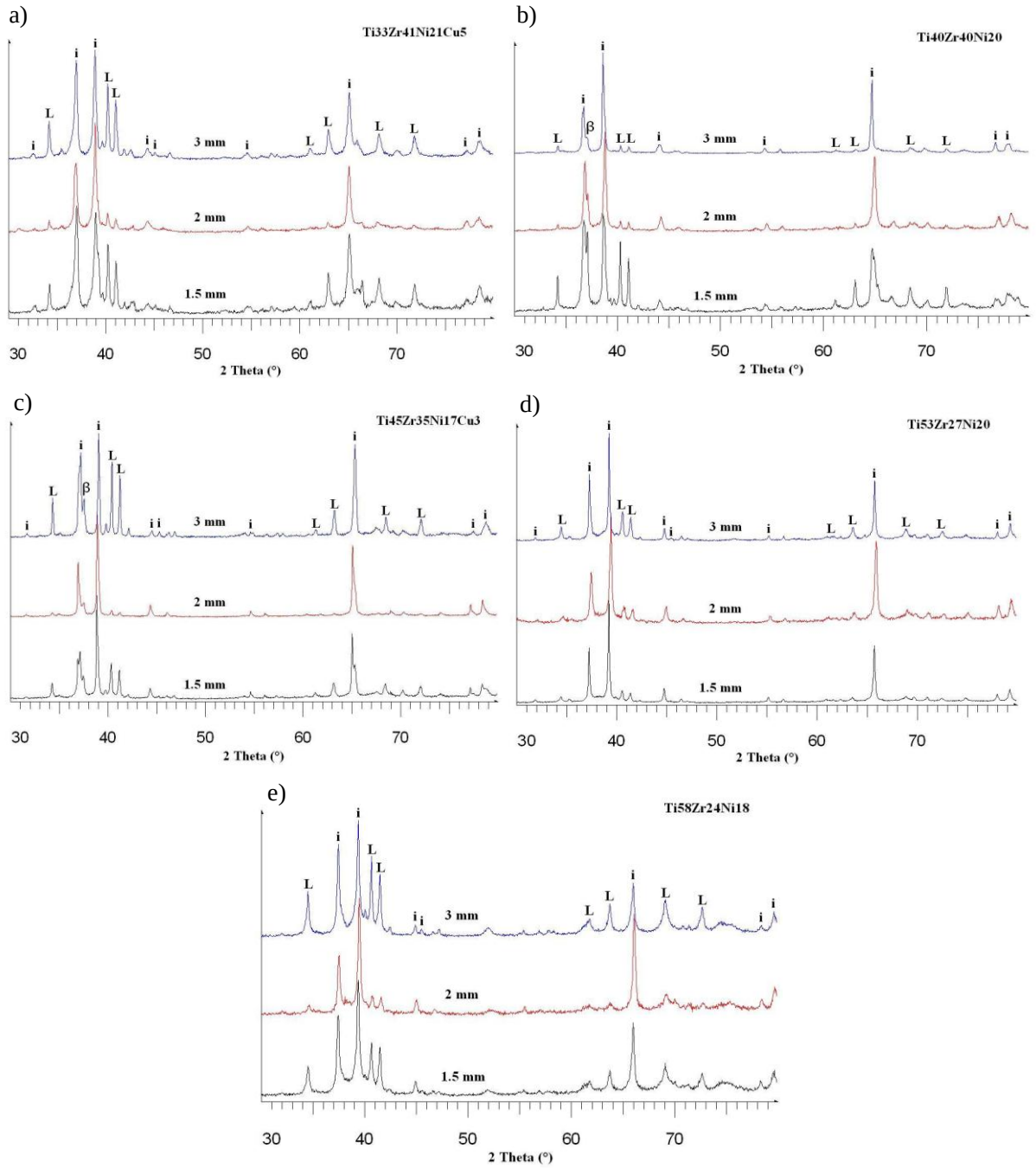

Figure 107: XRD spectra of quenched rods with five different compositions: a) $Ti_{33}Zr_{41}Ni_{21}Cu_5$, b) $Ti_{40}Zr_{40}Ni_{20}$, c) $Ti_{45}Zr_{35}Ni_{17}Cu_3$, d) $Ti_{53}Zr_{27}Ni_{20}$, e) $Ti_{58}Zr_{24}Ni_{18}$. Rods with three different diameters (3, 2 and 1.5 mm) were quenched for each composition.

As already commented before, cooling rates in melt spinner are obviously too high for $Ti_{33}Zr_{41}Ni_{21}Cu_5$ alloy to form icosahedral structure. This is why we used vacuum casting technique for preparation of i-phase with this material as did Qiang et al., 2007. Figure 108 shows that $Ti_{33}Zr_{41}Ni_{21}Cu_5$ alloy contains significant amount of amorphous phase when melt-spun at 22 m/s, which is the lower wheel speed limit before crystalline phases begin to form in all other alloys, which we used for this Ph.D research. Actually, we observed α and Laves-phase coexisting with an icosahedral and amorphous phase, which implies rate of i-phase formation compared to crystalline phases one is much lower in $Ti_{33}Zr_{41}Ni_{21}Cu_5$ alloy. In order to get more i-phase we need to lower the cooling rate, which was successfully achieved by vacuum-casting in 2 mm copper moulds. These observations are similar to reports of Davis et al. in 2000, where they confirmed that the Ti-Zr-Ni quasicrystal phase is thermodynamically stable, forming near 600°C over a

narrow composition range, i.e. $Ti_{41.5}Zr_{41.5}Ni_{17}$ and $Ti_{50}Zr_{35}Ni_{15}$, by a solid-state reaction from the C14 and α(Ti/Zr) phase. Which means that i-phase grows from these two precursors, that are formed directly from the liquid phase. Our results thus give new insight in this phenomenom, since we showed this happens for $Ti_{33}Zr_{41}Ni_{21}Cu_5$ alloy as well. Surprisingly, no β-phase had been found, which should form before α-phase. Moreover, our results are in contrary with reports of Qiang et al. (2004), who claim:"In the Ti-rich quasicrystalline alloys, the Ti(Zr) solid solution always has the form of α-Ti(Zr) (hP2), while the β-Ti(Zr) (cI2) is formed in the Zr-rich quasicrystalline alloys." All our results, shown to this point, are giving just the opposite situation. But nevertheless, these authors conclude very general by saying that α- and β-Ti(Zr) solid solution phases and/or C14 Laves phase coexist with the majority i-phase, with a small deviation from the ideal composition.

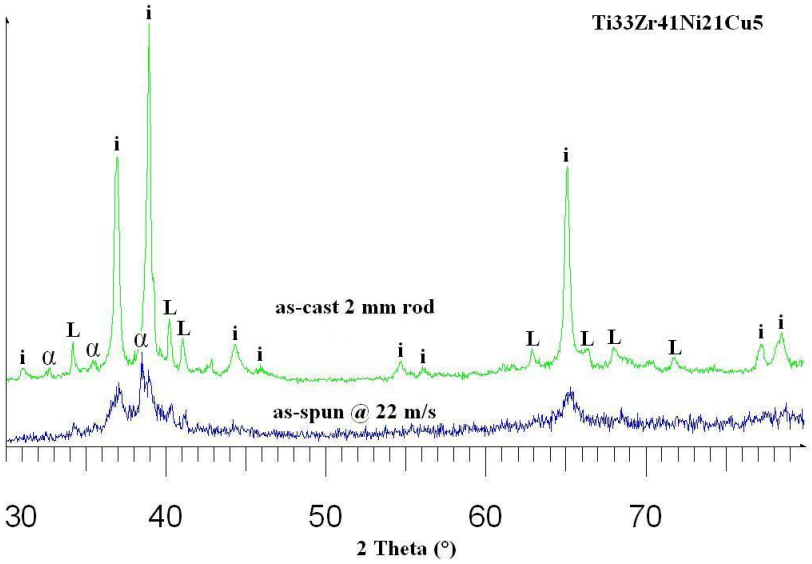

Figure 108: XRD spectra of as-spun (22 m/s) and as-cast (2 mm rod) $Ti_{33}Zr_{41}Ni_{21}Cu_5$ alloy.

3.4.2 SEM/EDS analysis

By topography investigation of fractured surfaces of crushed suction-cast rods (3 mm), Figure 109, we observed that these materials undergo brittle fracture, which is expected due to known brittleness of icosahedral phase that is present in the majority in this particular sample. Also, interesting features were observed after crushing those rods, i.e. spherical, few micrometer big inclusion of quenched melt; and non-spherical one as well.

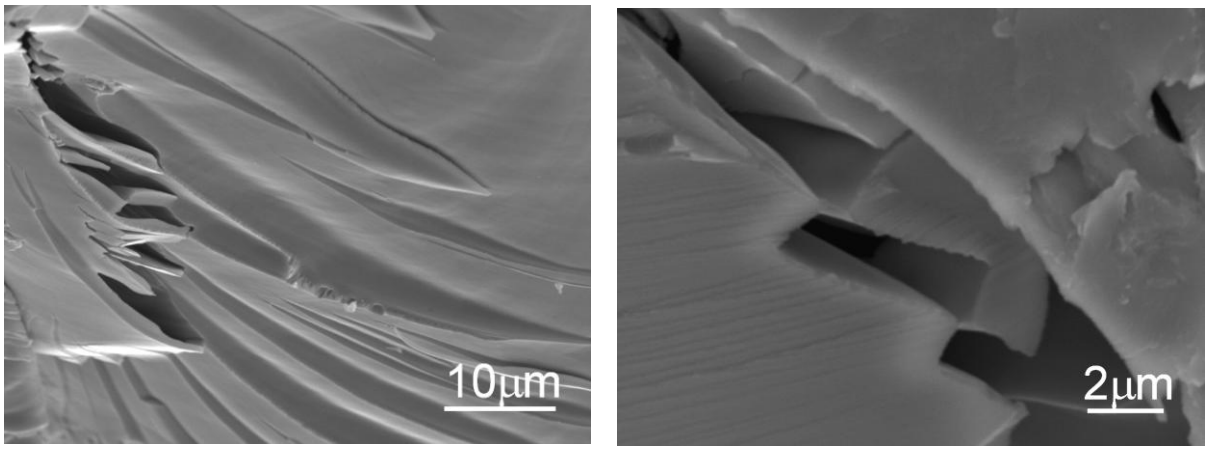

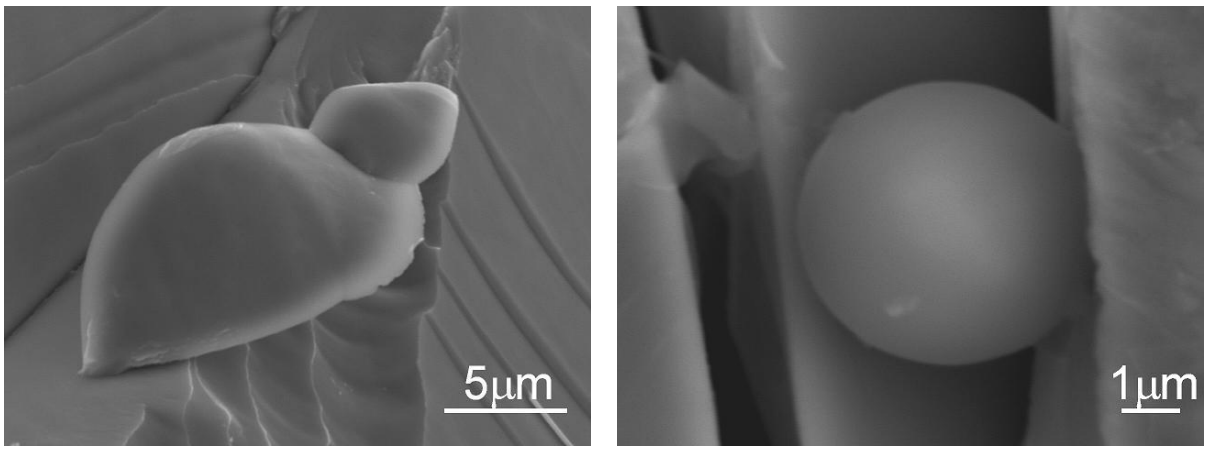

Figure 109: SEM images of fractures and features in $Ti_{40}Zr_{40}Ni_{20}$ 3 mm quenched rod, after being gently crushed in the mortar.

In contrary with melt spinning, where secondary phases are well distributed and finely dispersed in predominant matrix phase, in quenched rods, the areas of secondary phases are much bigger and thus better visible with back-scattered electrons. According to vertical section of Ti-Zr-Ni phase diagram along a line of equal Ti and Zr, reported by Kelton et al. in 2002, due to reports of Lefaix et al. in 2008, and our XRD and EDS data, dendritic phase in Figure 110 (a-d) must be either C14 Laves phase or mixture of this and β-(Ti,Zr) solid solution. The size of these dendrites is too small for exact EDS quantification, namely for that we need at least 2 square micrometer big homogenous area, which was difficult to find in our samples. So, the estimated error of our quenched rods EDS quantification was somewhere from three to five % for dendrite size close to previously mentioned conditions, whereas for smaller features this error became bigger (10% and more) since the matrix i-phase was taken into account as well.

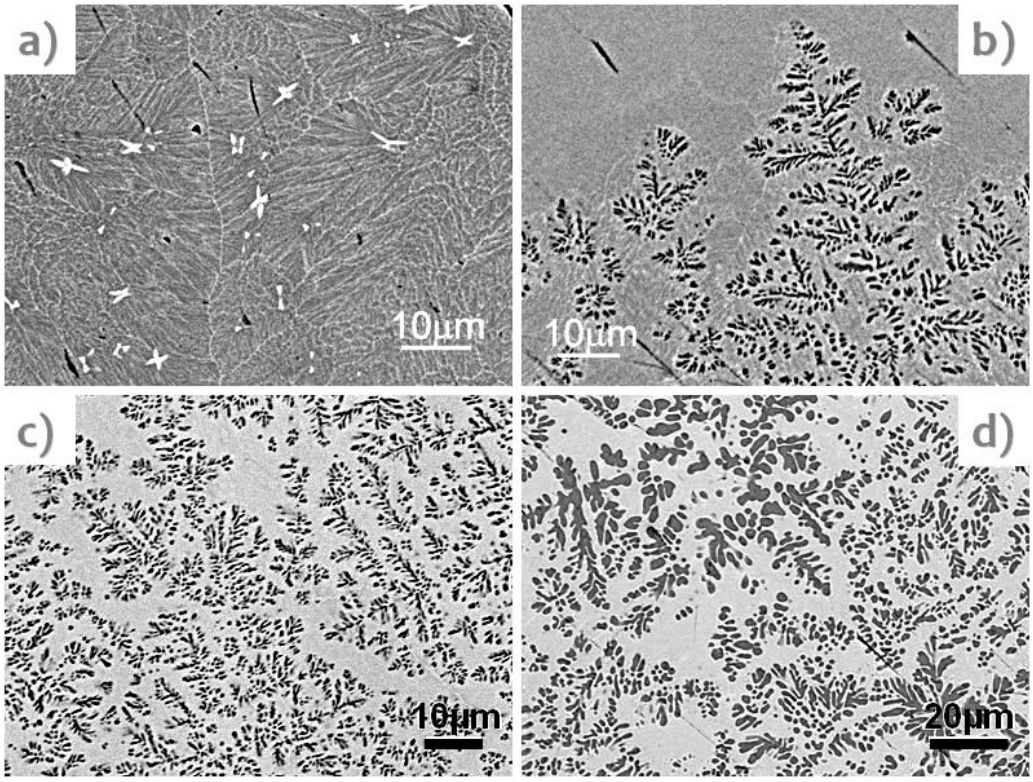

Figure 110: SEM Z-contrast images of 3 mm quenched rods taken from polished cross-section surfaces; a) $Ti_{33}Zr_{41}Ni_{21}Cu_5$, b) $Ti_{40}Zr_{40}Ni_{20}$, c) $Ti_{45}Zr_{35}Ni_{17}Cu_3$, and d) $Ti_{53}Zr_{27}Ni_{20}$.

In case of point EDS analysis (window), phase size is taken as a diameter of circle with origin in the point, which denotes the middle of electron beam, and with radius to the first secondary phase. In case of square EDS analysis (window), analysis area size is taken as a side of the square, which defines the area,

analyzed by electron beam.

a)

Phase	Window	Size (μm)	Ti	Zr	Ni	Cu
dark matrix	point	2	33.3	40.4	17.0	9.2
white star #1	point	1	22.0	55.6	15.4	7.1
white star #2	square	2	25.1	52.0	15.5	7.3
white star #3	point	1	21.1	57.3	14.7	7.0
total matrix	square	10	31.8	44.2	15.0	9.0

b)

Phase	Window	Size (μm)	Ti	Zr	Ni	Cu
dendrite #1	point	1	41.9	44.8	13.3	-
dendrite #2	point	2	49.2	48.4	2.4	-
dendrite #3	point	2	49.1	48.6	2.3	-
matrix	square	2	40.2	44.5	15.4	-

c)

Phase	Window	Size (μm)	Ti	Zr	Ni	Cu
matrix	point	2	47.9	31.6	17.8	2.72
dendrite #1	point	1	63.9	28.7	7.4	-
dendrite #2	point	1	68.7	27.8	3.5	-

d)

Phase	Window	Size (μm)	Ti	Zr	Ni	Cu
matrix	point	5	52.6	28.9	18.5	-
dendrite #1	point	5	73.0	23.4	3.6	-
dendrite #2	point	5	73.4	23.2	3.4	-

Table 8: EDS quantification data of phases shown in Figure 110; a) $Ti_{33}Zr_{41}Ni_{21}Cu_5$, b) $Ti_{40}Zr_{40}Ni_{20}$, c) $Ti_{45}Zr_{35}Ni_{17}Cu_3$, and d) $Ti_{53}Zr_{27}Ni_{20}$, respectively.

According to the results of EDS analysis, given in Table 8, we can correlate our data to the corresponding structures, reported by Qiang et al. in 2004. These structures are in good accordance with our XRD patterns. Thus, for instance dendrites in $Ti_{40}Zr_{40}Ni_{20}$ rods correspond to β-$Ti_{50}Zr_{50}$ solid solution, since the solubility of nickel in that phase is very low, and the measured and simulated XRD spectra match at BCC lattice constant a= 3.425 Å. Chemical composition of i-phase matrix is few atomic % off the nominal composition, namely Zr content is higher due to nickel. Further, in $Ti_{45}Zr_{35}Ni_{17}Cu_3$ 3 mm quenched rods we observed by XRD a BCC β-$Ti_{66}Zr_{34}$ solid solution phase with lattice parameter a= 3.387 Å. These results, again, match to our EDS findings.

Interesting feature has been observed by SEM using SEI detector, shown in Figure 111, namely we noticed the fracture along dendritic secondary phase, which is thus obviously more ductile than icosahedral matrix, which is known to be brittle at room temperatue.

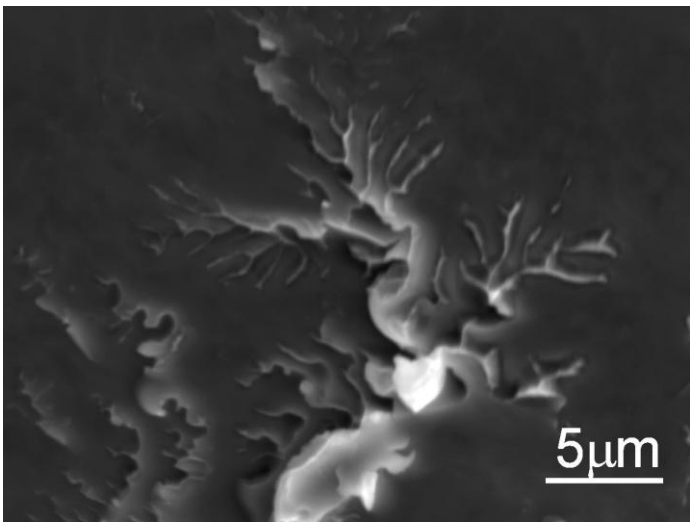

Figure 111: SEM (SE) image of fractured surface of 3 mm $Ti_{40}Zr_{40}Ni_{20}$ quenched rod is showing ductile nature of dendritic secondary phase, whereas i-phase matrix is brittle.

3.4.3 VSM results

We tested magnetic response of 3 mm quenched rods upon hydrogenation by VSM. Data in Figure 112a show significant increase (10-times) of maximum magnetization (at field 1 Tesla) and susceptibility for $Ti_{40}Zr_{40}Ni_{20}$ sample, which due to XRD data contained primarily i-phase, minor amount of β-phase and almost no C14 Laves phase. On the other hand, graphs in Figure 112d show only slight increase of maximum magnetization and susceptibility, which we think is not due to the 2-times smaller amount of bonded hydrogen compared to $Ti_{40}Zr_{40}Ni_{20}$ sample, but rather due to much higher content of crystalline phases, especially C14 Laves phase, beside icosahedral phase. If the increase was due to hydrogen content, then $Ti_{53}Zr_{27}Ni_{20}$ sample should have at least 12-times higher susceptibility compared to $Ti_{40}Zr_{40}Ni_{20}$ sample, but it is only 3-times higher, Figure 112c. And both alloys contain the same atomic % of nickel. We again think that the reason for such a behaviour is higher content of crystalline phases in $Ti_{53}Zr_{27}Ni_{20}$ sample, Figure 112b.

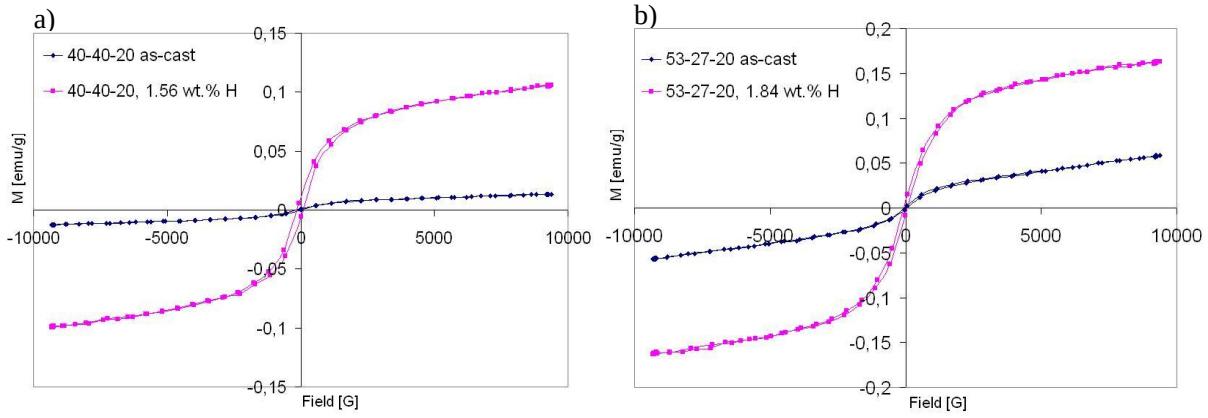

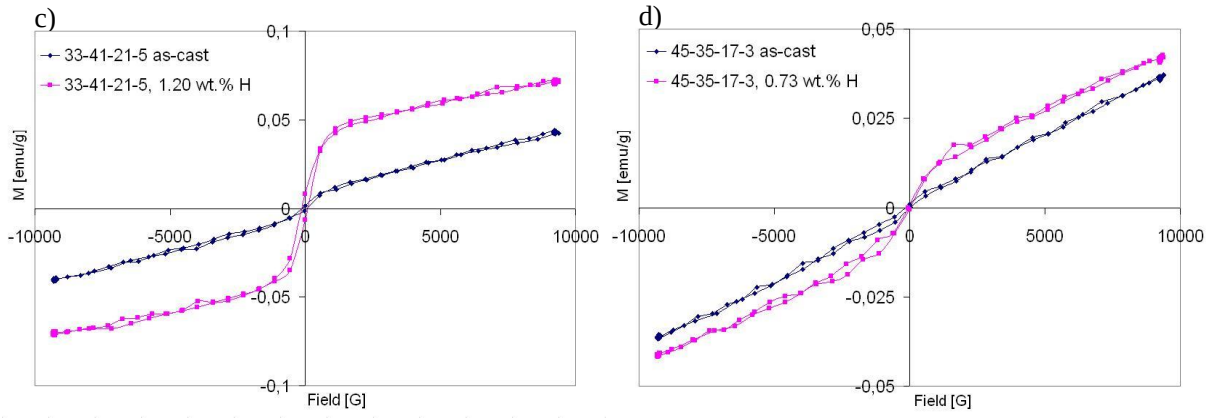

Figure 112: VSM data of as-cast and hydrided a) $Ti_{40}Zr_{40}Ni_{20}$, b) $Ti_{53}Zr_{27}Ni_{20}$, c) $Ti_{33}Zr_{41}Ni_{21}Cu_5$ and d) $Ti_{45}Zr_{35}Ni_{17}Cu_3$ 3 mm rods.

3.5 Arc-melting

3.5.1 X-ray diffraction of cross-section

Clearly XRD spectra of $Ti_{40}Zr_{40}Ni_{20}$ arc-melted button and annealed powder at 700°C for 2 hours are very different, Figure 113. There is no sign of C14 Laves phase and low energy α-solid solution in arc-melted samples. At 37° there is a widened peak belonging to β-Ti/Zr solid solution phase. This widening is an indication of different amounts of elements in the solution, or it might be even due to diffuse phase transformation from high temperature cubic β-Ti/Zr to low temperature hexagonal α-Ti/Zr solid solution. But this is, however, less-likely, since no indication of α-phase formation has been observed in both examined 5 gram arc-melted buttons, Figure 114.

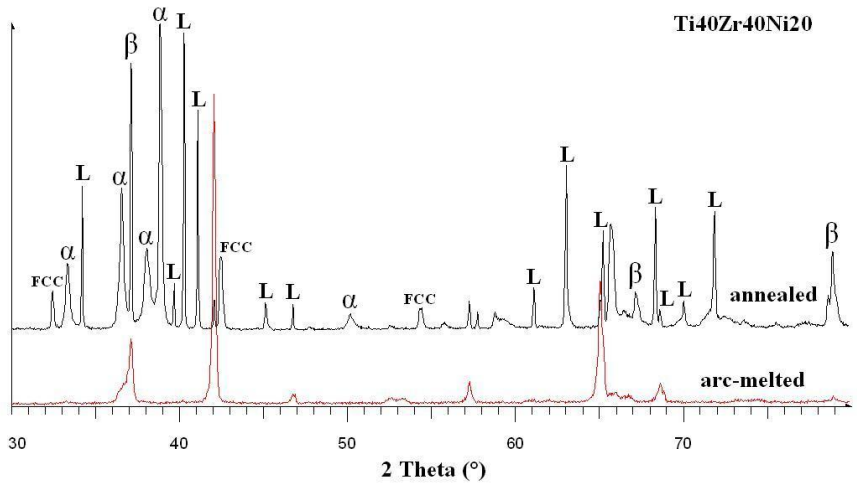

Figure 113: XRD spectra of cross-section surface of arc-melted $Ti_{40}Zr_{40}Ni_{20}$ button and annealed, crystalline powder with the same chemical composition.

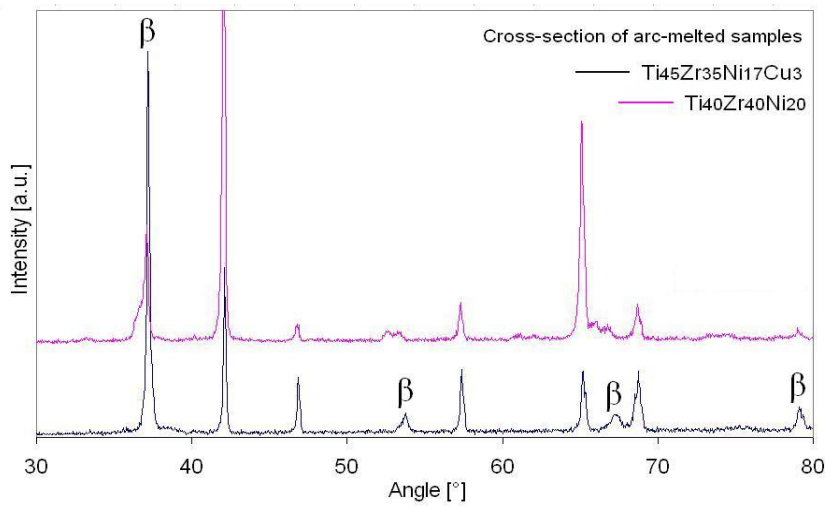

Figure 114: XRD spectra of $Ti_{40}Zr_{40}Ni_{20}$ and $Ti_{45}Zr_{35}Ni_{17}Cu_3$ arc-melted buttons. Spectra were taken on flat and polished cross-section surface.

In order to increase natural cooling rate of arc-melted buttons we prepared smaller samples, i.e. 1 gram instead of 5 grams. We hoped that we will be able to see some indication of Laves or solid solutions phase formation. Results in Figure 115 are showing that this was not the case, namely even for previously mentioned phases there should be some critical cooling rate reached, like for amorphous and icosahedral.

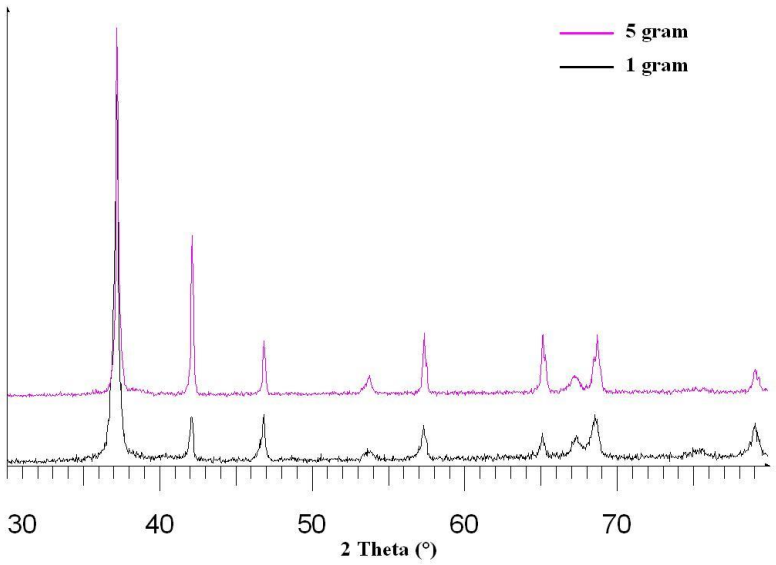

Figure 115: XRD patterns of polished cross-sections of 1 and 5 gram $Ti_{45}Zr_{35}Ni_{17}Cu_3$ arc-melted buttons.

3.5.2 SEM/EDS analysis

Cross-section of 5 gram arc-melted $Ti_{45}Zr_{35}Ni_{17}Cu_3$ button was investigated by back-scattered electrons, Figure 116, and corresponding EDS analysis of matrix and dendritic phase was performed, Table 9. According to XRD data and low Ni content in EDS spectra, dark dendrites are β-(Ti,Zr) solid solution phase with lattice parameter a= 3.416 Å, which should correspond to 54 at. % Ti and 46 at. % Zr. Our EDS data show that contents of Ti and Zr in those dendrites are 61 and 36 at. %, respectively. If this was pure solid solution of Ti and Zr, then its calculated lattice constant would be a= 3.395 Å. Since dendrites contain about 2 at. % of Ni, we think this slightly increases the lattice of the β-phase.

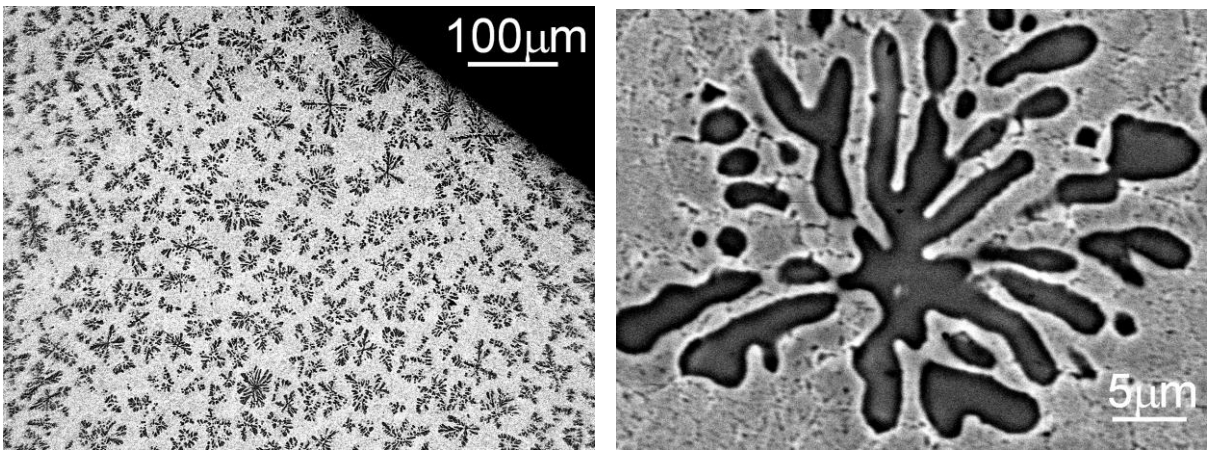

Figure 116: BEI of cross-section of 5 gram arc-melted $Ti_{45}Zr_{35}Ni_{17}Cu_3$ button.

In case of point EDS analysis (window), phase size is taken as a diameter of circle with origin in the point, which denotes the middle of the electron beam, and with radius to the first secondary phase. In case of square EDS analysis (window), analysis area size is taken as a side of the square, which defines the area, analyzed by the electron beam.

Phase	Window	Size (µm)	Ti	Zr	Ni	Cu
grey matrix #1	point	60	40.9	34.6	20.7	3.8
grey matrix #1	square	15	41.2	34.2	20.5	4.2
grey matrix #2	square	20	41.4	34.1	20.7	3.8
dendrite #1	point	3	61.3	35.8	2.9	-
dendrite #2	point	4	61.2	35.9	2.2	0.8
dendrite #3	square	2	61.0	36.0	2.3	0.8
bright areas	point	below 2	39.8	38.5	17.8	3.9

Table 9: EDS analysis data of phases in 5 gram arc-melted $Ti_{45}Zr_{35}Ni_{17}Cu_3$ button.

3.5.3 VSM results

Magnetic measurements of as-cast arc-melted buttons revealed paramagnetic behaviour, with practically the same susceptibility for 5 gram $Ti_{40}Zr_{40}Ni_{20}$ and $Ti_{45}Zr_{35}Ni_{17}Cu_3$ buttons, Figure 117. 1 gram $Ti_{45}Zr_{35}Ni_{17}Cu_3$ button showed slightly higher susceptibility, which we think is only due to the smaller size of the button, meaning that more of the sample is within high density magnetic field. Namely, the structure of 5 and 1 gram button is the same.

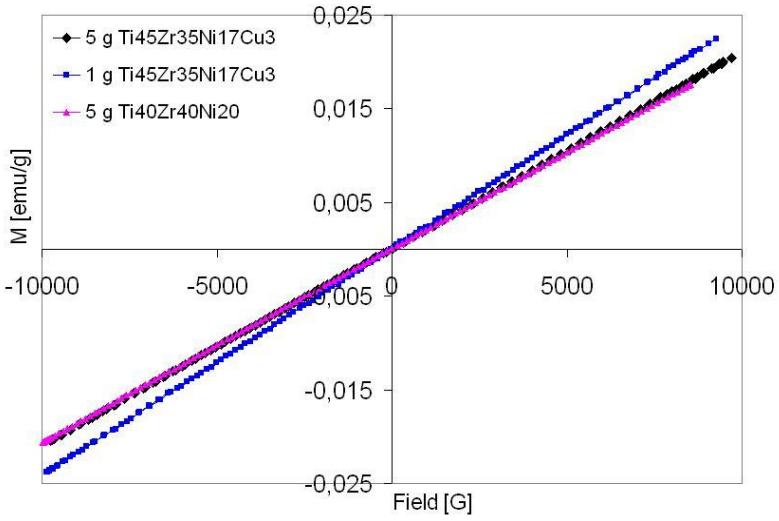

Figure 117: VSM measurements on $Ti_{40}Zr_{40}Ni_{20}$ and $Ti_{45}Zr_{35}Ni_{17}Cu_3$ arc-melted buttons.

3.5.4 Density measurements

By Archimed method we were able to measure density of arc-melted buttons with different compositions, Table 10. As we expected density is decreasing with titanium content, since it is almost two times lighter than zirconium, Figure 118. Since all points follow the line, with practically no deviations, we may say that this method is fairly precise for measuring densities of solid samples.

$Ti_{33}Zr_{41}Ni_{21}Cu_5$	$Ti_{40}Zr_{40}Ni_{20}$	$Ti_{45}Zr_{35}Ni_{17}Cu_3$	$Ti_{53}Zr_{27}Ni_{20}$	$Ti_{58}Zr_{24}Ni_{18}$
6.45	6.23	6.11	5.90	5.77

Table 10: Densities of arc-melted buttons with increasing content of titanium. Units are g/cm³.

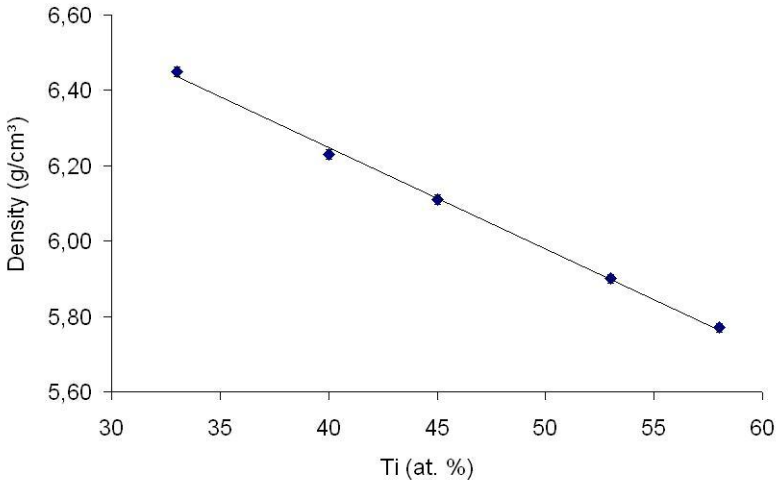

Figure 118: Density plot (g/cm³) versus titanium concentration (at. %) in Ti-Zr-Ni-(Cu) 5 g arc-melted buttons.

4 Discussion

4.1 Mechanical alloying

Due to reports of Konstanchuck (2001) and Takasaki (2004) we expected that we will not be able to produce icosahedral Ti-Zr-Ni quasicrystals directly by mechanical alloying. Namely, as mentioned before, Konstanchuck prepared i-phase material just by ball-milling of the elemental powders for two hours only, even though i-phase was the minor phase, embedded in the amorphous matrix. But Takasaki has reported that i-phase can not be formed just upon mechanical treatment. Heat-treatment must be applied to the amorphous sample as well. If we make an overview of all experimental conditions used in their and our mechanical alloying experiments we see that Konstanchuck used the most severe conditions, namely ball-to-sample ratio 20:1 and the ball acceleration 400 ms^{-2}. Takasaki used roughly three times lower acceleration and ball-to-sample ratio, i.e. 150 ms^{-2} and 8:1, respectively. In our case the ball acceleration was only 55 ms^{-2}, almost 8 times lower than in Konstanchuck's case, and ball-to-sample ratio was 15:1. From these observations it is obvious that the ball acceleration is the key parameter for direct i-phase formation by mechanical alloying. Ball-to-sample ratio determines only the rate at which this transformation occurs, i.e. the amount of the material subjected to kinetic energy of milling balls.
Unlike normal solidification processes, mechanical alloying technique alloy elemental powders mostly by dynamic force (mechanical collision), which leads to a chemical inhomogenity of the final products, making it difficult to produce a single quasicrystal phase powder.

The DSC results suggest a complex crystallisation process in both alloys, which mainly takes place during a single exothermic phase transformation between 500 and 550 °C. The enthalpy of the crystallisation for the $Ti_{40}Zr_{40}Ni_{20}$ alloy increases with alloying time and heating rate, while for $Ti_{40}Hf_{40}Ni_{20}$ the enthalpy is almost constant. However, the activation energy suggests that the $Ti_{40}Hf_{40}Ni_{20}$ sample crystallises more easily than the $Ti_{40}Zr_{40}Ni_{20}$.

We discovered that modification of magnetization depends on atmosphere in the milling vial during mechanical alloying of elemental Ti, Zr (Hf) and Ni powders. Namely, when argon gas is used, the magnetization drop is significant, whereas is case of hydrogen M drop is modest. We assume that the reason for this behaviour is that Ni d-states remain unmodified, since Ti and Zr rather reacted with hydrogen forming stable TiH_2 and ZrH_2 hydrides. And yet, a quotation of J.M. Dubois in his book *Useful Quasicrystals* (Dubois, 2005) confirms our observations: »Distribution of s-p states is modified upon alloying in the vicinity of the Fermi energy, and even more so after introducing large amounts of hydrogen in the icosahedral material«.

4.2 Melt spinning

As we expected, structure of melt-spun ribbons is affected by the cooling rate, i.e. cooling wheel speed, and so changes the thickness of ribbons. What we did not expect is that the magnetization (at 1 Tesla) and susceptibility of ribbons were unmodified, even though their structural states undergo phase transitions from amorphous to crystalline via icosahedral. According to reports of Molokanov and Chebotnikov in 1990, and publication of Qiang in 2004, we as well expected that i-phase will be formed directly by melt spinning in relatively wide interval of compositions. And our observations have confirmed their findings. In general, we showed that i-phase is formed directly from the melt via melt spinning route in relatively wide intervals of wheel speeds, as well as compositions. By calculating quasilattice cell parameters, a_q, from XRD data of i-phase samples with various compositions, we found out that a_q is fairly linearly decreasing with the content of titanium and copper on account of zirconium, i.e. with ([Ti]+[Cu])/[Zr] ratio. This correlation was preserved when these samples were all loaded to similar extent, which corresponded to about 5.5 % expansion of a_q. The increase of quasilattice constant, calculated from the 110000 (20/32) peak of the quasicrystalline alloys containing 20 at. % of Ni was observed by Qiang et al. in 2004 as well. Namely, the constant increased from 0.5054 to 0.5259 nm as Zr increased at the expense of Ti. For this purpose they have used the same Cahn's scheme (Cahn et. al, 1986) as we did.

BSE analysis of as-spun ribbons (not powder) revealed that they were homogenous on both, free and wheel sides. Even though some areas on both sides were implying on two phase system, we invalidate these findings by SE imaging, which showed that those were merely topological features. EDS analyses have shown that the starting or nominal composition of ribbons corresponds to measured atomic values in the frame of 2 % relative experimental error.

TEM revealed the size and distribution of i-phase grains embedded in amorphous matrix of melt-spun ribbons. We observed that the average grain size on the free side of the ribbons was about 5 times larger, i.e. 250 nm, than on the wheel side. This makes sense, since the cooling rate at the wheel side in higher, thus smaller grains grew there. At the same time, no preferential grain growth direction due to either thermodynamic or casting flow conditions has been observed. With 5-, 3- and 2-fold SAED patterns we confirmed that those grains have icosahedral structure.

Using standard route for calculation of layer thicknesses from XPS data, we can conclude that the thickness of an oxide layer on our $Ti_{45}Zr_{35}Ni_{17}Cu_3$ ribbons is 7 ± 1 nm. It can be calculated by subtracting minimum and maximum oxygen concentrations and dividing this value by two. The obtained concentration of oxygen gives us corresponding depth on the X-axis (oxide layer thickness) in accordance with the oxygen XPS curve (red) in Figure 66.

This result was quite unexpected, since Huang et al., 2008, reported XPS data of oxide layer thickness on suction-cast $Ti_{45}Zr_{35}Ni_{17}Cu_3$ quasicrystalline rods, exposed to ambient air for about two months. Their measurements showed that an oxide layer thickness on the surface of rods was 70 nm, which is about 15 times thicker than our oxide layers. We do not think that this difference is due to the different cooling regime.

4.3 Hydriding

Mass-spectra of desorbed hydrogen molecules from i-phase and amorphous material are actually very tricky results, since these two structures undergo phase transitions according to the previously described TTT diagram in Chapter 1 and kinetics of crystallization steps obtained by DSC experiments, described in Chapter 3. According to these observations we may claim that icosahedral grains start to grow in the amorphous sample at around 500°C, and icosahedral-to-crystalline transformation starts somewhere around 700°C. Thus, the last peak (~ 740°C) in mass-spectra is characteristic for all three, structurally different samples. But anyhow, the shapes of mass-spectra of these samples are different at lower temperatures, which gives us information about the sample structure like its fingerprint, whether it is amorphous, icosahedral or crystalline. Furthermore, with the combination of TG results we observed that hydrogen is more reversible bonded the more crystalline or periodic the structure is. The term more reversible refers to higher content of desorbed gas (mass %), which is starting to release at lower temperature (T_D). For instance, in case of $Ti_{40}Zr_{40}Ni_{20}$ material, crystalline modification has 1.7 mass % H and T_D= 290°C, i-phase has 1.31 mass % H and T_D= 500°C, and amorphous gives 1.22 mass % H and T_D= 495°C. The same study of $Ti_{45}Zr_{35}Ni_{17}Cu_3$ material gives following numbers, crystalline 1.84 mass % H and T_D=345°C, i-phase 1.56 mass % H and T_D= 495°C, and amorphous 0.82 mass % H and T_D= 485°C.

Interesting feature has been recognized when we hydrided melt-spun ribbons. Upon hydrogen absorption at 300°C (45 bar), Laves phase and β-(Ti, Zr) phase peaks were substancially diminished, but the icosahedral quasicrystal structure was conserved, though its lattice expanded due to the interstitial hydrogen. Does this mean that hydrogen induces i-phase formation? We think that in a way hydrogen lowers the activation energy for the formation of i-phase from Laves and β-(Ti, Zr) phases. We also confirmed that this phase transition is hydrogen induced, since crystalline peaks remained unmodified after heat-treatment at 300°C for 1000 min in vacuum. Contradictory results were obtained by loading fully crystalline samples, prepared by annealing at 800°C for 5 hours in vacuum. Namely, in this case we do not get any diminishing of Laves phase or any other crystalline peaks. Even more, all initial crystalline peaks are conserved after hydrogenation at 300°C (45 bar), only shifted due to the lattice expansion.

Decreasing of crystalline peaks occured only at high hydrogen pressure loading, because when we did hydriding of i-phase samples, initially showing no sign of parazitic crystalline phases, at normal pressure, Laves and β-phase peaks have showed-up. Therefore we might conclude that protons in these alloys increase the mobility of metals atoms, thus lowering the activation energy of particular phase transformations. It seems that thermal regime has an imporant role in determining the direction of this equilibrium Laves-to-icosahedral phase transition. The major question that still remains unanswered is why does diminishing of Laves peaks occur in partially crystallized, melt-spun samples (predominantly icosahedral), but not in fully crystalline samples, obtained by annealing at 800°C for few hours in vacuum.

No significant differences between the two structural modifications, amorphous and icosahedral, of the

same alloy were found by deuterium NMR analysis. The observed 8 % larger activation energy for the deuterium hopping among the interstitial sites and the 10 % larger static spectrum width of the amorphous phase, as compared to the icosahedral phase, can be accounted for by the larger deuterium content of the investigated amorphous sample. From the deuterium dynamics point of view, the icosahedral phase is not special compared to the amorphous modification of the same material. This is in agreement with the recently reported investigations of the amorphous and icosahedral $Zr_{69.5}Cu_{12}Ni_{11}Al_{7.5}$ alloy (Apih et al., 2005, and Dolinšek et al., 2007), where the same conclusion was reached, i.e. the activation energy for hydrogen hopping depends on the hydrogen content. When more hydrogen is absorbed, larger lattice expansion occurs and thus hopping barriers increase due to larger distances between the atoms. Our results suggest that short-range atomic order on the scale of nearest-neighbour atoms exists in the amorphous phase as well and is not much different from that of the quasicrystalline phase.

VSM measurements of amorphous $Ti_{40}Zr_{40}Ni_{20}$ and $Ti_{45}Zr_{35}Ni_{17}Cu_3$ samples mechanically alloyed for 68 and 65 hours, respectively, showed minor modification of susceptibility. These results can be explained due to the lack of crystallinity and thus absence of magnetocrystalline anisotropy, which originates from anisotropic (quasi)lattice expansion. Namely, interatomic distances in amorphous samples increase uniformly in all directions. These results confirmed that hydrogenation of amorphous phase gives negligible contribution to the total magnetization of multiphase samples, like melt-spun ribbons.

When we performed magnetic measurements on crystalline $Ti_{40}Zr_{40}Ni_{20}$ and $Ti_{45}Zr_{35}Ni_{17}Cu_3$ samples, we have obtained contradictory resutls. Namely, for first sample we observed about 65 % increase of magnetization at 1 Tesla, whereas for the last one approximately 70 % decrease of the same quantity has been detected. The only difference between these two samples was chemical composition and heat-treatment conditions via samples that were prepared from as-spun i-phase ribbons. Namely, $Ti_{40}Zr_{40}Ni_{20}$ sample was annealed for 2 hours at 700ºC, whereas $Ti_{45}Zr_{35}Ni_{17}Cu_3$ one was heat-treated for 4 hours at 800ºC. But nevertheless, both XRD patterns imply on same crystalline phases. The only difference could be bigger grains in $Ti_{45}Zr_{35}Ni_{17}Cu_3$ sample, since they have more time and higher temperature to grow.

4.4 Quenched rods

If we compare XRD results of melt spun and vacuum-cast Ti-Zr-Ni alloys we quickly see the difference. Namely, the structure of alloys obtained by melt spinning changes from amorphous at highest wheel speeds (50 m/s) to quasicrystalline in a large interval of wheel speeds (16-45 m/s), and finally to crystalline at wheel speeds below 15 m/s. On the other side, at vacuum-casting cooling rate is controlled by the diameter of the copper cold mould, 1.5 mm, 2 mm and 3 mm. It is easy to understand that the cooling rate decreases with the increasing diameter. So, XRD and SEM analysis of as-quenched rods showed that the mixture of dendritic C14 Laves phase and i-phase matrix co-existed in 3 mm rods, independent of the composition, except for the $Ti_{40}Zr_{40}Ni_{20}$ one, where almost single i-phase has formed.

In 2 mm rods we observed substancial decrease of parazitic crystalline phases for all compositions and nearly single i-phase has formed in all rods, as mentioned. This happens due to lower cooling rate, related to a smaller diameter of the copper mould, similar as lower wheel speed results in smaller cooling rate at melt spinning proceedure. When we decreased the diameter of the cold mould some more, namely just for half of milimeter, i.e. from 2 mm to 1.5 mm, we have got surprising results. Namely, due to previous results obtained by 3 and 2 mm moulds, we expected to get single i-phase rods. But XRD patterns revealed us different story, since the situation was similar to 3 mm rods. Again, the co-existence of icosahedral and hexagonal phases was observed in all 1.5 mm quenched rods, except in $Ti_{53}Zr_{27}Ni_{20}$ rod, where the amount of Laves phase is much lower than in other 1.5 mm rods.

However, by hydriding all 3 mm quenched rods, except $Ti_{58}Zr_{24}Ni_{18}$ one, we have got quite impressive results, which confirmed all findings related to hydriding of melt-spun ribbons and mechanically alloyed (amorphous) powders. Namely we confirmed strong relationship between mass-spectra of desorbed hydrogen and the structure of the sample, especially in the low temperature regime. Mass-spectra of desorbed hydrogen from melt-spun ribbons and quenched rods slightly differ due to the fact that ribbons contained no crystalline phases, only mixture of icosahedral and amorphous phase, whereas quenched rods presumably contained no amorphous phase, since the cooling rate at vacuum-casting is not so drastic, especially if 3 mm Cu mould is used. Instead of that they contained more or less crystalline phases, depending on the composition. So, the final mass-spectrum of such mixure is a sum of pure crystalline and pure i-phase spectrum in proper ratio. It should be noted at this point, that mixing of icosahedral and crystalline data at quenched rods is more obvious, than mixing of amorphous and icosahedral data at melt-spun ribbons, since the highest peak of mass-spectrum of amorphous phase is located at the position (~ 740ºC), where both, i-phase and amorphous phase, become crystalline. The second highest peak of amorphous sample almost overlapps the highest i-phase peak, since they are just about 10ºC apart. On the

contrary, the highest peaks of crystalline and icosahedral samples do not overlap, since they are about 200ºC apart, and thus presence of phase mixture in quenched rods can be easily detected from mass-spectra of desorbed H_2.

VSM measurements provided very interesting and what is more important, consistent results about modification of magnetic properties upon hydrogenation. Namely, it seems like i-phase expansion has the cruical influence in increase of the total susceptibility of the sample, whereas in more crystalline rods like $Ti_{45}Zr_{35}Ni_{17}Cu_3$ the susceptibility increase was not so significant at all. These findings are in good correlation with VSM results obtained from hydrided melt-spun i-phase and crystalline (subsequently annealed) ribbons.

4.5 Arc-melting

Even though arc-melting of Ti-Zr-Ni alloys was not the primar aim of our investigation, it gave interesting results. Namely, we did not expect that X-ray diffraction patterns of arc-melted buttons will be substancially different from the material, obtained by thermal treatment at 700°C, since they showed no sign of Laves phase present. This difference is due to lower cooling rate at arc-melting procedure.

VSM measurements of arc-melted buttons revealed their paramagnetic behaviour, with similar susceptibilities as melt-spun ribbons and quenched-rods.

We performed density measurements of these samples as well, in order to investigate how the density varies with titanium content.Almost perfect linear fit of density versus at. % of Ti has been detected.

5 Conclusions

Preparation, hydrogenation and characterization of $Ti_{40}Zr_{40}Ni_{20}$, $Ti_{45}Zr_{38-x}Ni_{17}Cu_x$ (x=3, 5), $Ti_{53}Zr_{27-x}Ni_{20}Cu_x$ (x=3, 5) and $Ti_{58}Zr_{24-x}Ni_{18}Cu_x$ (x=3, 5) alloys have confirmed previous findings of various authors and provided some new, unpublished information about the nature of these alloys. Especially, mass-spectrometry and TG of desorbed hydrogen and modification of magnetic properties upon hydrogen absorption are new findings. Essential contributions of this thesis are findings of structure influence on the shape of mass-spectra of desorbed hydrogen. Namely, hydrogen bonding sites are strongly related to the material structure, i.e. amorphous, icosahedral and crystalline, and to the minor extent to the chemical composition.

By mechanical alloying we were not able to produce quasicrystals directly, since subsequent annealing at temperatures determined by DSC and literature data had to be applied. Also, by this route we have got not negligible amount of secondary crystalline phases, such as FCC $(Ti/Zr)_2Ni$, FCC $Ti_{50}Zr_{50}$ solid solution and Zr_2Ni phase, that were not present in melt-spun samples.

We optimized parameters for melt-spinning and found out that the structure and thickness of ribbons depend on the cooling wheel speed. On the other hand, magnetization of ribbons at 1 Tesla is practically constant. Quasi-lattice cell parameter fairly linearly decreases with Ti and Cu content on expense of Zr, which was also confirmed by Qiang et al. in 2004. By TEM nanosized i-phase grains could be detected, imbedded in an amorphous matrix of the ribbon. EDS on the same microscope revealed i-phase and amorphous phase have the same composition. Oxidized Ti and Zr formed 7 nm thick film on melt-spun ribbons in one month from melt-spinning, which prevents further oxidation, like at aluminium metal. From overall hydriding experiments we observed that from amorphous alloys (obtained by mechanical alloying) the lowest amount of hydrogen has been desorbed, and this content is the same for 8 and 16 hours loading time. No sign of any stable hydride was recorded upon loading, as was reported by Takasaki et al. in 2004. Furthermore, we showed that slightly more hydrogen was released from crystalline samples, loaded for 8 hours than for 16 hours, but the total amount was the highest of all three studied structures. And even more, hydrogen started to release already at 100°C from crystalline alloys, whereas from icosahedral and amorphous this temperature was delayed till 300 – 400°C.

By vacuum-casting we were able to perform low quenching rate experiments, which enabled us preparation of samples with mixture of icosahedral and crystalline phases. By hydriding these samples we were able to see great influence of crystalline phases on the shape of mass-spectra. Also, we showed the influence of i-phase content on susceptibility increase of loaded samples.

By comparing structures of samples obtained by melt-spinning and vacuum-casting we have got better insight in the cooling process and phases that are formed. Namely, Kelton et al. (2002) have shown in Figure 3 that β-(Ti,Zr) and C14 Laves phase are formed directly from the liquid and are thus less thermodynamically stable than icosahedral phase, which is formed from those phases via peritectoid reaction, but only at modest cooling rates, i.e. as at vacuum-casting. This is why there are always some crystalline peaks in XRD patterns of quenched-rods present. On the other hand, i-phase is formed directly from the melt in case of melt-spinning, because with sufficient undercooling, metastable i-phase nucleates in preference to crystalline phases, suggesting a local icosahedral order in the liquid. Namely, there are no crystalline peaks present in XRD spectra of ribbons, melt-spun above 22 m/s.

By adding fourth element to Ti-Zr-Ni alloy system does not improve i-phase formation ability, since our samples with copper in general contained more C14 phase. We observed this by replacing 3 and 5 at. % of Zr with Cu. Huang et al. in 2007 reported similar observations since they claim that when Co is continually substituting Ni in suction-cast 3 mm rods, the forming ability of the Ti–Zr–(Ni, Co) i-phase is reduced. With one exception, namely at certain Co content they obtained single i-phase sample.

6 Acknowledgements

I would like to thank all the people who supported me on exciting way in the world of science and research.

First and most important acknowledgement goes to Slovenian Ministry of Science and Higher Education for the financial support, under Grant No. 3311-04-831079.

Special thanks goes to my supervisor and head of our department **Prof. Dr. Spomenka Kobe** for accepting and giving me the opportunity to work in her group at the Department for Nanostructured Materials at the Jožef Stefan Institute and to realize my Ph.D. research work and this dissertation. Her self-confidence and trust often gave me the strength to better present my results on seminars and conferences in the early days of my young researcher career. Also, I am very grateful to all other members of our research group.

First, to my co-supervisor **Dr. Paul J. McGuiness** for his dedicated mentorship and assistance at the laboratory and at paper work. Thank you for all the support and encouragements you gave me for the entire time spent in the laboratory, at formal in informal meetings, conferences, business trips and at Jožef Stefan Institute in general. I have learned a lot and I progressed considerably under your supervision. At the end he did all language corrections of this thesis. Thank you very much.

Dr. Tina Žužek gave me the first contact and insight into the world of quasicrystals with her collection of papers related to this topic. She also was always prepared to share her time and experience with me and help me to learn the theory of materials and practical work in the laboratory. At our formal group meetings she often brought out fresh ideas how to present results more clear and what else should be done or measured.

Dr. Matej Komelj is deserved for his effort to explain magnetic properties of Ti-Zr-Ni based allyos and for interpreation of magnetization dependence on the temperature for three different structures, obtained by SQUID technique.

This thesis would not be here without unselfish help of the following scientists. **Dr. Aleksander Rečnik** and **Mrs. Medeja Gec** did all work on TEM and sample preparation, respectively. At TEM sessions with Sandi I had a real lifetime opportunity to assist the first observation of titanium based quasicrystals at our institute. Since Sandi is geologist, dedicated crystallographer and microscopist, he was more than thrilled to see 5-fold electron diffraction and corresponding HRTEM image for the first time on any electron microscope. Namely, if he stuck in the ceramic world he would be deprived of the beauty of complex metallic alloys. When we first got these images, it was a really joyful moment. At this point it is worth mentioning that 5-fold HRTEM image was put on a cover page on one of the editons of JSI's internal newspaper, called *Novice IJS*. Medeja has made a little magic sample preparation work on our melt-spun i-phase ribbons, so we were able to observe the as-grown grains as well. This job really took all her experience and skills, since i-phase ribbons are extremely brittle and thus complicated for TEM sample preparation. Thank you both.

Dr. Zoran Samardžija was very helpful with his microanalysis instructions by which he taught me to use SEM and EDS. Also, his sample preparation lessons were unavoidable here.

Dr. Marjeta Maček from JSI Department of Advanced Materials gave me a quick course of mass-spectrometry and thermogravimetry on their TG-DTA/DSC with Gas Analytical System QMS 403 C Aëolos (STA 449 C/6/G Jupiter®-QMS 403 C, Netzsch, Germany) thermal analyzer with attached mass-spectrometer, and further assistance with Netzsch Proteus software. We often compete, who will be more precize and carefull with the equipment. Since the micro balance is a very sensitive piece of equipment, she has often warned me five times before she left in the office. Nothing went wrong, though, but then she goes again. And again. She definitely won the prize of the most responsible, careful, precize and suspicious scientist I ever met. At this point I should thank **Prof. Dr. Danilo Suvorov**, head of JSI Department of Advanced Materials, for using their very sensitive piece of equipment, which provided us a lot of results,

that are contained in this Ph.D thesis. Without his permission this would not be possible.

Prof. Dr. Jani Dolinšek from JSI Department of Solid State Physics gave us the opportunity to deuterize our melt-spun samples (at his collaborators in Korea) and subsequently perform ²H NMR measurements at his department by one of his Ph.D students, **Mr. Anton Gradišek**, which provided enough data to publish a scientific paper (Gradišek et. al, 2008). I hope we will collaborate on future projects and publish many more interesting papers!

Dr. Edi Kranjc from National Chemistry Institute took care for X-ray diffraction of our powders, ribbons and solid lumps. This work was often done surprisingly quick, sometimes on the same day. XRD data represent the majority of research work and basics of this Ph.D dissertation. Thank you Edi, and keep on the good work!

Dr. Janez Kovač from JSI Department of Surface Engineering and Optoelectronics has done XPS analysis of our melt-spun ribbons, which was the proof of surface oxide film presence that inhibits hydrogen uptake in these alloys. Dr. Kovač was very kind and explained every detail of experimental work and result of the analysis to me.

Prof Dr. Zvonko Jagličič and his assistant **Mr. Marko Jagodič** from Faculty of Mathematics and Physics in Ljubljana performed temperature dependent SQUID measurements of samples with different crystallographic structures. This information is beside mass-spectrometry a real added value of this disseertation, since no reports on this topic have been published yet.

Dr. Maša Rajić Linarić from Brodarski Institut in Zagreb is grateful for performing DSC measurements on mechanically alloyed powders and did calculation of crystallization activation energies.

At the end I would like to thank to all other co-workers at Jožef Stefan Institut who helped me in one way or another. **Mr. Benjamin Podmiljšak** and I are the dream team in the laboratory. We can fix nearly any technical or other kind of a problem one can face in scientific life. He is a member of our group, a Ph.D student working on magnetocaloric materials and uses arc-melting and melt spinning routes of material preparation as well. We actually set most of that equipment work properly. He taught me to use our VSM device as well. And many others too. Thanks for all your help.There is even a nice scientific contribution from us in MRS review from August 2008, a picture taken at MRS Fall Meeting, Boston 2007.

Retired chemical engineer, **Mr. Tone Porenta**, was my first contact with a practical work at the Department of Nanostructured Materials, JSI, when I came here in April 2003, as a young student of chemical engineering. He kindly showed me every piece of basic equipment and demonstrated how it works; new and old glove-boxes, old arc-melter, electric furnaces, turbo-vacuum pump system, hydraulic press, hot press, magnetic pulser, vacuum dryer, where the glassblower workshop is, and…how to cook coffe de luxe. Really an old school guy! Hvala Tonček!

The work was done at the Jožef Stefan Institute, Ljubljana, Slovenia. It was financially supported by the Slovenian Ministry of Science and Higher Education, under Grant No. 3311-04-831079

7 References

APIH, T., BOBNAR, M., DOLINŠEK, J., JASTROW, L., ZANDER, D., and KÖSTER, U.. *Solid State Commun.*, vol. 134, 2005, pp. 337

BALL, M.D., and LLOYD, D.J.. *Scripta Metall.*, vol. 19, 1985, pp. 1065-1068

BAUNACK, S., KAMACHI MUDALI, U., and GEBERT, A.. Characterization of oxide layers on amorphous Zr-based alloys by Auger electron spectroscopy with sputter depth profiling, *Applied Surface Science*, vol. 252, 2005, pp. 162–166

BELIN-FERRÉ, E., HENNIG, R.G., DANKHAZI, Z., SADOC, A., KIM, J.Y., and KELTON, K.F.. Theoretical and experimental investigation of the electronic structure of Ti–Zr–Ni and Ti–Zr–Ni:H alloys, *Journal of Alloys and Compounds*, vol. 342, 2002, pp. 337-342

CAHN, J.W., SHECHMAN, D., GRATIAS, D.. Indexing of icosahedral quasiperiodic crystals, *Journal of Materials Research*, 1986, vol. 1, pp. 13-26

CAHN, R.W., *Physical Metallurgy*, Third edition, Elsevier Science Publishers B.V., 1983

CHEN, W., WANG, Y., QIANG, J., and DONG, C.. *Acta Materialia*, vol. 51, 2003, pp. 1899-1907

CHERNIKOV, M.C., BERNASCONI, A., BEELI, C., SCHILLING, A., and OTT, H.R.. *Physical Review B*, vol. 48, 1993, pp. 3058

CODDENS, G., VIANO, A.M., GIBBONS, P.C., KELTON, K.F., and KRAMER, M.J.. *Solid State Community*, vol. 104, 1997, pp. 179

DAVIES, J.P., MAJZOUB, E.H., SIMMONS, J.M., and KELTON, K.F.. *Mater. Sci. Eng.*, vol. 294-296, 2000, pp. 104

DOLINŠEK, J., APIH, T., KLANJŠEK, M., KIM, H.J., and KÖSTER, U.. *Catal. Today*, vol. 120, 2007, pp. 351

DONG, C., WANG, Y., QIANG, J., and CHEN, W.R.. *Materials Transactions JIM*, vol. 45, 2004, 1177-1179

DUBOIS, J.M.. *Materials Science and Engineering A*, vol. 294-296, 2000, pp. 4-9

DUBOIS, J.M.. Useful Quasicrystals, *World Scientific Publishing Co. Pte. Ltd.*, Nancy, France, 2005.

ELSER, V.. *Physics Review B*, vol. 32, 1985, pp. 4892

GAVILANO, J.L., RAU, D., BEELI, C., WELLER, M., OTT, H.R., and TSAI, A.P.. Magnetic properties of amorphous and quasicrystalline $Al_{75}Cu_{15}V_{10}$

GAVILANO, J.L., RAU, D., MUSHKOLAJ, Sh., OTT, H.R., DOLINŠEK, J., and URBAN, K.. *Physical Review*, vol. 65, 2002, pp. 214202

GRADIŠEK, A., KOCJAN, A., McGUINESS, P.J., APIH, T., KIM, H.J., and DOLINŠEK, J.. Deuterium dynamics in the icosahedral and amorphous phases of the $Ti_{40}Zr_{40}Ni_{20}$ hydrogen-absorbing alloy studied by ^2H NMR, *Journal of Physics: Condensed Matter*, vol. 20, 2008, pp. 1-7

GUO, X.Q., LOUZGUINE, D.V., YAMAURA, S., MA, L.Q., SUN, W., HASEGAWA, M., and INOUE, A.. Hydrogen absorption in Ti–Zr–Ni–Cu amorphous alloy, *Materials Science and Engineering A*, vol. 338, 2002, pp. 97–100

HUANG, H. G., QIANG, J. B, BAI, B., DONG, P., ZHANG, P. C.. Effect of Co substitution for Ni on the Ti–Zr–(Ni, Co) pseudo-ternary quasicrystal formation, *Journal of Non-Crystalline Solids*, vol. 353, Issues 16-17, 2007, pp. 1670-1675

HUANG, H., DONG, P., YIN, C., ZHANG, P., BAI, B., and DONG, C.. Characterization and hydrogen absorption at low temperature of suction-cast $Ti_{45}Zr_{35}Ni_{17}Cu_3$ quasicrystalline alloy, *International Journal of Hydrogen Energy*, vol. 33, 2008, pp. 722-727

HUTTUNEN-SAARIVIRTA, E.. *Journal of Alloys and Compounds*, vol. 363, 2004, pp. 150-174

INOUE, A., *Acta Materialia*, vol. 48, 2000, pp. 279-306

KELTON, K.F., and GIBBONS, P.C.. *MRS Bulletin*, vol. 22, no. 11, 1997, pp.69

KELTON, K.F., GANGOPADHYAY, A.K., LEE, G.W., HANNET, L., HYERS, R.W., KRISHNAN, S., ROBINSON, M.B., ROGERS, J., and RATHZ, T.J., *Journal of Non-Cryst. Solid*, Vol. 312-314, 2002, pp.305-308

KELTON, K.F., *in Quasicrystals: Preparation, Properties and Applications*, Eds. DUBOIS, J.M., THIEL, P.A., TSAI, A.P., and URBAN, K.. *Materials Research Society*, Warrendale, 1999, pp. 471

KELTON, K.F., KIM, W.J., and STROUD, R.M.. *Applied Physics Letters*, vol. 70, 1997, 3230-3232

KIM, J.Y., GIBBONS, P.C., and KELTON, K.F.. *Journal of Alloys and Compounds*, vol. 266, 1998, pp. 311

KONSTANCHUK, I.G., IVANOV, E.Yu., BOKHONOV, B.B., and BOLDYREV, V.V.. Hydriding properties of mechanically alloyed icosahedral phase $Ti_{45}Zr_{35}Ni_{17}Cu_3$, *Journal of Alloys and Compounds*, vol. 319, Issues 1-2, 2001, pp. 290-295

LASJAUNIAS, J.C., SULPICE, A., KELLER, N., PRÉJEAN, J.J., and de BOISSIEU, M.. *Physical Review B*, vol. 52, 1995, pp. 886

LEE, G.W., CROAT, T.K., GANGOPADHYAY, A.K., and KELTON, K.F.. *Phil. Mag. Lett.*, vol. 82 (4), 2002, pp. 199–205

LEFAIX, H., VERMAUT, P., JANICKOVIČ, D., SVEC, P., PORTIER, R., and PRIMA, F.. Processing and characterization of rapidly quenched Ti-based alloys: Influence of solidification rate on the as-quenched structures, *Journal of Alloys and Compounds*, article in press, 2008, pp. 1-5

LIBERMANN, H., and GRAHAM, C., Production Of Amorphous Alloy Ribbons And Effects Of Apparatus Parameters On Ribbon Dimensions, *IEEE Transactions on Magnetics*, Vol 12, No 6, 1976

LIU, B., WANG, J., WU, Y., and WANG, L.. Crystallographic and electrochemical characteristics of $Ti_{45}Zr_{35}Ni_{17}Cu_3$ quasicrystalline alloy ball milled with nickel powder, *Electrochimica Acta*, vol. 51, no. 17, 2006, pp. 3586-3591

LIU, B., WU, Y., and WANG, L.. Crystallographic and electrochemical properties of ball-milled quasicrystalline $Ti_{45}Zr_{35}Ni_{17}Cu_3$ alloy with 20 mass % Ni, *Journal of Alloys and Compounds*, vol. 425, no. 1-2, 2006, pp. 296–301

LIU, B., WU, Y., and WANG, L.. Kinetic and electrochemical properties of icosahedral quasicrystalline $Ti_{45}Zr_{35}Ni_{17}Cu_3$ powder, *International Journal of Hydrogen Energy*, vol. 31, no. 10, 2006, pp. 1394–1400

LIU, B.Z., WU, Y.M., and WANG, L.. *Journal of Non-Crystalline Solids*, vol. 352, 2006, pp. 3936

LIU, B.Z., WU, Y.M., and WANG, L.. *Journal of Power Sources*, vol. 159, 2006, pp. 1458

LIU, B., FAN, G., WANG, Y., MI, G., WU, Y., and WANG, L.. Chrystallographic and electrochemical characteristics of melt-spun Ti-Zr-Ni-Y alloys, *International Journal of Hydrogen Energy*, vol. 33, Issue 20, 2008, pp. 5801-5805

LÖFFLER, J.F., Intermetallics, vol. 11, 2003, pp. 529-540

MECHLER, S., ABROMEIT, C., WANDERKA, N., MACHT, M.P., ZUMKLEY, T., SCHUMACHER, G., and KLAUMÜNZER, S.. Phase transformation quasicrystalline-amorphous in Zr-Ti-Ni-Cu by swift heavy ions, *Nuclear Instruments and Methods in Physics Research, Section B: Beam Interactions with Materials and Atoms*, vol. 245 (1), 2006, pp. 133–136

MIO, H., KANO, J., and SAITO, F.. Scale-up method of planetary ball mill, *Journal of European Ceramic Society*, vol. 59 (24), 2004, pp. 5909-5916

MIZUTANI, U., TAKEUCHI, T., and SATO, H.. *Progress in Materials Science*, vol. 49, 2004, pp. 227-261

MOLOKANOV, V.V., and CHEBOTNIKOV, V.N.. Quasicrystals and amorphous alloys in Ti-Zr-Ni system: Glass-forming ability, structure and properties, Journal of Non-Crystalline Solids, vol. 117/118, 1990, pp. 789-792

MOULDER, J.F., STICKLE, W.F., SOBOL, P.E., and BOMBEN, K.D.. Handbook of X-Ray Photoelectron Spectroscopy, *Physical Electronics Inc., Eden Prairie*, Minnesota, USA, 1995

POON, S.J.. *Advanced Physics*, vol. 41, 1992, pp. 303

QIANG, J., WANG, Q., WANG, Y., HUANG, H., WU, J., and DONG, C.. Formation of e/a-constant

phases in the Ti-Zr-Ni-Cu system, *Materials Science and Engineering A*, vol. 448-451, 2007, pp. 565–568

QIANG, J.B., WANG, Y.M., WANG, D.H., KRAMER, M., THIEL, P, and DONG, C.. Quasicrystals in the Ti-Zr-Ni alloy system, Journal of Non-Crystalline Solids, vol. 334&335, 2004, pp. 223-227

RAU, D., GAVILANO, J.L., BEELI, C., CHERNIKOV, M., and OTT, H.R.. *Condensed Matter*/0304262

RUD, A.D., SCHMIDT, U., ZELINSKA, G.M., LAKHNIK, A.M., PEREKOS, A.E., KOLBASOV, G.Ya, and DANILOV, M.O.. Peculiarities of structural state and hydrogen storage proeprties of Ti-Zr-Ni based intermetallic compounds, *Journal of Alloys and Compounds*, vol. 404-406, 2005, pp. 515-518

SATO, T.J., ABE, E., and TSAI, A.P.. *Jpn. Journal of Applied Physics*, vol. 36, 1997, pp. L1038-L1039

STADNIK, Z.M.. Physical Properties of Quasicrystals, *Springer, Berlin, Germany*, 1999

STROUD, R.M., VIANO, A.M., GIBBONS, P.C., KELTON, K.F., and MISTURE, S.T.. *Applied Physics Letters*, vol. 69, 1996, pp. 2998-3000

TAKASAKI, A., HUETT, V.T., KELTON, K.F.. Hydrogenation of Ti-Zr-Ni quasicrystals synthesized by mechanical alloying, *Journal of Non-crystalline Solids*, vol. 334 & 335, 2004, pp. 457-460

TAKASAKI, A., KELTON, K.F.. *International Journal of Hydrogen Energy*, vol. 31, 2006, pp. 183-190

TREBIN H.R.. Quasicrystals Structure and Physical Properties, *Wiley-vch GmbH & Co. KGaA*, 2003

TSAI, A.P., INOUE, A., and MASUMOTO, T.. *Jpn. Journal of Applied Physics*, vol. 26, 1987, pp. L1505-L1507

VIANO, A.M., MAJZOUB, E.H., STROUD, R.M., KRAMER, M.J., MISTURE, S.T., GIBBONS, P.C., and KELTON, K.F.. *Phil. Mag. A*, vol. 78, 1998, pp. 131–141

VIANO, A.M., STROUD, R.M., GIBBONS, P.C., McDOWELL, A.F., CONRADI, M.S., and KELTON, K.F.. Hydrogenation of titanium-based quasicrystals, *Physical Review B*, 1995, vol. 51, pp. 12026–12029

WANG, L., and INOUE, A.. Icosahedral and amorphous phases in melt-spun Ti-Zr-Ni-Cu alloys, *Materials Transactions*, vol. 42, 2001, pp. 2637-2640

WANG, L., MA, L., and INOUE, A.. Formation and mechanical properties of Ti-Zr-Ni-Cu amorphous alloy containing icosahedral nanoscale quasicrystalline phase, *Materials Transactions*, vol. 43, no. 9, 2002, pp. 2346-2349

WANG, L., MA, L., MA, C., and INOUE, A.. Formations of amorphous and quasicrystal phases in Ti-Zr-Ni-Cu alloys, *Journal of Alloys and Compounds*, vol. 361, no. 1-2, 2003, pp. 234–240

WANG, W.H., DONG, C., and SHEK, C.H., *Material Science and Engineering*, vol. R44, 2004, pp. 45-89

WANG, Y.M., QIANG, J.B., WONG, C.H., SHEK, C., and DONG, J.. *Journal of Materials Research*, vol. 18, 2003, pp. 642-648

WANG, L., LIU, B., MA, L., MA, C., and INOUE, A.. Phase separation and crystallization in a melt-spun $Ti_{45}Zr_{35}Ni_{17}Cu_3$ alloy, *Journal of Non-Crystalline Solids*, vol. 354, 2008, pp. 1010 – 1014

WU, Y., HUI, X.D., LU, Z.P., LIU, Z.Y., LIANG, L., and CHEN, G.L.. Effects of metalloid elements on the glass-forming ability of Fe-based alloys, *Journal of Alloys and Compounds*, vol. 467 (1-2), 2009, pp.187-190

Index of Figures

Figure 1: Schematic representation of a) 3-fold, b) 4-fold and c) 6-fold crystallographic symmetry..... 2
Figure 2: a) Illustration of »forbbiden« 5-fold symmetry shows that rhomboedral interstitials are formed while trying to fill 2D plane with regular pentagons, b) simulation for a Laue pattern (X-ray) from an icosahedral quasicrystal, whereby the X-ray beam is along one of the five-fold axes. 3
Figure 3: Schematic vertical section of Ti-Zr-Ni phase diagram along a line of equal Ti and Zr, showing the phases that form in equilibrium (Kelton et al., 2002). 5
Figure 4: Compositional range for the formation of quasicrystalline phases in rapidly solidified Ti-Ti_2Ni-Zr_2Ni-Zr alloys is denoted by dash line, Molokanov and Chebotnikov, 1990. 5
Figure 5: Ternary phase formation section for Ti-Zr-Ni alloys. Green line denotes the phase field of Ti-Zr-Ni quasicrystals revealed by Qiang et al., 2004. Their predicted ternary i-$Ti_{40}Zr_{40}Ni_{20}$ (red point), located at the crossing point of two e/a-variant lines Ti_2Ni-to-Zr and Zr_2Ni-to-Ti, is just slightly different from reported (Kelton et al., 2002) ternary quasicrystals composition i-$Ti_{41.5}Zr_{41.5}Ni_{17}$ (blue point). 6
Figure 6: Thermodynamic stability of phases in Ti-Zr-Ni alloy system. 7
Figure 7: XRD patterns of $Ti_{45}Zr_{35}Ni_{17}Cu_3$ ribbons, melt-spun at a) 10 m/s (86 ± 5 μm thick), and b) 35 m/s (20 ± 2 μm thick); Wang et al. 2003a. 7
Figure 8:XRD patterns of cast $Ti_{45}Zr_{35}Ni_{17}Cu_3$ bulk samples with diameters of 3, 2 and 1 mm (Wang, 2003a). 8
Figure 9: Icosahedron, with corresponding 5-, 3- and 2-fold rotation zone axes. 9
Figure 10: The first Brillouin zone of icosahedral quasicrystal. 9
Figure 11: C14 Laves phase structure from several perspectives. Green spheres denote A (Ni) atoms. 14
Figure 12: Hydrogenation kinetics of the $Ti_{45}Zr_{38}Ni_{17}$ i-phase at 230°C: (1, 3) 2 hours of mechanical alloying only, (2, 4) MA (2 h) and annealing at 440 °C in Ar for 5h; (1, 2) $P(H_2)$ = 0.8 bar, (3, 4) $P(H_2)$ = 13.5 bar (Konstanchuck et al., 2001). 16
Figure 13: Auger depth profile for icosahedral $Ti_{45}Zr_{38}Ni_{17}$ stored in air for 30 days. Oxide coating is approximately 15 nm thick (Viano et al., 1998). 16
Figure 14: XRD spectra of $Ti_{45}Zr_{38}Ni_{17}$ i-phase with different contents of hydrogen ([H]/[M]). Patterns from b) to e) were obtained by desorbing hydrogen at 400 °C for b) 5, c) 10, d) 30 and e) 180 min. The peak denoted by c(111) is a reflection from the FCC (Ti/Zr)H_2 phase (Viano et al., 1998). 17
Figure 15: Expansion of the quasilattice constant a_q as a function of hydrogen concentration in icosahedral $Ti_{45}Zr_{38}Ni_{17}$ icosahedral phase. 17
Figure 16: a) schematic diagram of the planetary ball-mill b) the movement of a ball in a pot, (Mio et al., 2004). 18
Figure 17: Schematic presentation of melt spinning performance. After the alloy is melted by RF coil induction, it is ejected through the crucible nozzle onto the rotating copper cooling wheel, producing long and thin ribbons. 20
Figure 18: Temperature-time-transformation diagram of Ti-Zr-Ni alloy system (Wang et al., 2003a). 20
Figure 19: Processing route of melt-spun ribbons. 21
Figure 20: Edmund Bühler, Melt Spinner SC device. 21
Figure 21: Schematic presentation of Sievert's apparatus for hydrogen absorption from gas phase. 22
Figure 22: Photography of our stainless-steel Sievert's apparatus for high-pressure hydrogen absorption. 23
Figure 23: a) Edmund Bühler MAM-1 Arc-Melter, and b) melting chamber. 24

Figure 24: Arc-melted buttons of Ti-Zr-Ni alloys. Each weights about 5 grams. 24
Figure 25: 3 mm rod cast in arc-melter MAM 1, and suction casting copper crucible plate. 25
Figure 26: Interference of X-ray light, scattered on crystal planes. 26
Figure 27: PHI-TFA XPS spectrometer produced by Physical Electronics Inc. 26
Figure 28: Scanning electron microscope (purdue.edu). 27
Figure 29: Transmission electron microscope, (findtarget.com). 28
Figure 30: TG-DTA/DSC with Gas Analytical System QMS 403 C Aëolos (STA 449 C/6/G Jupiter® - QMS 403 C, Netzsch, Germany) thermal analyzer with attached mass-spectrometer. On the right, corresponding schematics is shown. 29
Figure 31: LakeShore vibrating-sample magnetometer and related schematics on the right. 30
Figure 32: Superconducting quantum interference device (SQUID): Josephson junction pair within a superconducting ring. A change in flux produces a voltage variation across the JJ pair. 30
Figure 33: Archimedes' principle of volume measurement via displaced water mass. 31
Figure 34: XRD patterns (a) of the $Ti_{40}Zr_{40}Ni_{20}$ and (b) $Ti_{40}Hf_{40}Ni_{20}$ after alloying for 0, 20, 40, 60, 80 and 100 h. 32
Figure 35: SEM micrographs of a) agglomerated non-polished powder particle, consisting of much smaller particles, and b) z-contrast image of polished agglomerate revealed presence of Zr-rich phase in the bulk. 33
Figure 36: EDS spectrogram of polished $Ti_{45}Zr_{38}Ni_{17}$ agglomerate of ~ 5 μm² dark grey area, shown in Figure 35b. 33
Figure 37: DSC results of $Ti_{40}Zr_{40}Ni_{20}$ and $Ti_{40}Hf_{40}Ni_{20}$ samples, mechanically alloyed for various times, recorded at heating rate 10 K/min. 34
Figure 38: Heat of crystallisation vs. alloying time, for both compositions, measured at five different heating rates: 2, 5, 10, 15 and 20 °C/min. 34
Figure 39: DSC curves recorded at five different heating rates for (a) $Ti_{40}Zr_{40}Ni_{20}$ and (b) $Ti_{40}Hf_{40}Ni_{20}$ powder mechanically alloyed for 100 h. 35
Figure 40: An example of the Kissinger plot of $Ti_{40}Hf_{40}Ni_{20}$ (after 100 h of mechanical alloying) for determining the activation energies. 35
Figure 41: Dependence of activation energy of crystallization on alloying time for Zr- and Hf-based alloys. 36
Figure 42: VSM hysteresis curves of a) Zr-based and b) Hf-based alloys, measured after 0, 20, 40, 60 and 80 hours of milling. 37
Figure 43: Magnetization (at 1 Tesla) of Zr- and Hf-based alloys decreases with alloying time. After 100 hours it is reduced for more than 95 %. 37
Figure 44: Magnetization (at 1 Tesla) plot of $Ti_{40}Zr_{40}Ni_{20}$, $Ti_{40}Hf_{40}Ni_{20}$ and pure Ni samples versus alloying time. 38
Figure 45: XRD patterns (a) of the $Ti_{40}Zr_{40}Ni_{20}$ and (b) $Ti_{40}Hf_{40}Ni_{20}$ after alloying for 60 h and heat treating at various temperatures. The heating rate was 10 K/min. 38
Figure 46: XRD spectra of samples mechanically alloyed in a hydrogen atmosphere. 39
Figure 47: SEM image of submicrometer particles of $Ti_{40}Zr_{40}Ni_{20}$ powder after 40 hours of mechanical alloying in a hydrogen atmosphere. 39
Figure 48: Magnetization (at 10 kOe) decrease is significant when alloyed in argon, but not so significant when alloyed in hydrogen. 40
Figure 49: XRD spectra of a) $Ti_{40}Zr_{40}Ni_{20}$ and b) $Ti_{45}Zr_{35}Ni_{17}Cu_3$ ribbons melt-spun at different wheel speeds. 40
Figure 50: VSM data of $Ti_{40}Zr_{40}Ni_{20}$ samples, melt-spun at series of wheel speeds and therefore having diffrrent structural states. 41
Figure 51: Thickness and magnetization at 1 Tesla of ribbons spun at various wheel speeds for the $Ti_{40}Zr_{40}Ni_{20}$ and $Ti_{45}Zr_{35}Ni_{17}Cu_3$ materials. 41
Figure 52: XRD spectra of $Ti_{53}Zr_{27}Ni_{20}$ ribbons, melt-spun at various wheel speeds. 42
Figure 53: XRD data of ribbons with various compositons, all spun at 22 m/s. 42

Figure 54: Ternary phase diagram. Alloys marked with blue and green stars form i-phase when melt-spun around 22 m/s. Alloy marked with yellow circle forms i-phase by vacuum-casting only (Chapter 3.4). Red crosses denote compositions at which i-phase is not formed at any wheel speed. On the right side of the figure is a list of compositions. Blue color denotes compositions that have not been published yet. 43

Figure 55: Decrease of icosahedral cell parameter a_q with Ti and Cu content by substituting Zr. The same trend is preserved for an expanded quasilattice with the highest amount of hydrogen we could obtain for each sample..... 43

Figure 56: XRD spectra of ribbons melt-spun at 22 m/s, a) $Ti_{40}Zr_{40-x}Ni_{20}Cu_x$ (x= 0, 3, 5), b) $Ti_{45}Zr_{38-x}Ni_{17}Cu_x$ (x= 0, 3, 5), c) $Ti_{53}Zr_{27-x}Ni_{20}Cu_x$ (x= 0, 3, 5) and d) $Ti_{58}Zr_{24-x}Ni_{18}Cu_x$ (x= 0, 3, 5). 44

Figure 57: SEM images of melt-spun ribbons 45

Figure 58: BSE image of a) free side and b) wheel side of $Ti_{58}Zr_{24}Ni_{18}$ melt-spun ribbon. 45

Figure 59: SEM images of the same area on the free-side of $Ti_{58}Zr_{24}Ni_{18}$ melt-spun ribbon, taken by a) back-scattered electrons, and b) secondary electrons..... 46

Figure 60: Crystallites of the $Ti_{45}Zr_{35}Ni_{17}Cu_3$ phase scattered in an amorphous matrix. 46

Figure 61: HRTEM images of i-phase grain and corresponding SAED patterns in a), b) 5-fold, c), d) 3-fold and e), f) 2-fold zone axes, respectively. 47

Figure 62: XRD spectra of $Ti_{40}Zr_{40}Ni_{20}$ and $Ti_{45}Zr_{35}Ni_{17}Cu_3$ crystalline alloys, obtained by annealing of the i-phase ribbons at 700 °C for 2 hours and 800°C for 4 hours in high vacuum, respectively. 47

Figure 63: TEM characterization of crystallized $Ti_{40}Zr_{40}Ni_{20}$ sample upon annealing at 700°C for 2 hours. BF images a) and b) show the same area only differently tilted, namely dark grain is in the zone axis. 48

Figure 64: XRD spectra of ribbons, melt-spun at 40 m/s. Material of the crucible has obvious effect on the structure of both a) $Ti_{40}Zr_{40}Ni_{20}$ and b) $Ti_{45}Zr_{35}Ni_{17}Cu_3$ samples. 49

Figure 65: XRD spectrum of $Ti_{40}Zr_{40}Ni_{20}$ ribbons, melt-spun at 32 m/s using quartz crucible..... 49

Figure 66: Depth profile of elements in $Ti_{45}Zr_{35}Ni_{17}Cu_3$ melt-spun ribbon. 50

Figure 67: 3-nm-deep XPS binding energy analysis of ribbons melt-spun by BN and graphite crucibles. 50

Figure 68: X-ray photoelectron absorption peaks of a) Ti 2p, b) Zr 3d, c) Ni 2p, and d) Cu $2p_{3/2}$ electrons. Intervals correspond to etching depths that are roughly 1.5 nm apart, same as points in Figure 66. 51

Figure 69: Typical X-ray photoelectron spectra and binding energies of a) titanium, b) zirconium, c) nickel, d) copper, and e) boron. Data were obtained by monochromated Al Kα radiation (from Moulder et al., 1995). 52

Figure 70: XRD spectra of $Ti_{40}Zr_{40}Ni_{20}$ samples, amorphous, i-phase and crystalline, that were used for SQUID (and VSM) experiments. 53

Figure 71: VSM hysteresis curves of amorphous, icosahedral and crystalline $Ti_{40}Zr_{40}Ni_{20}$ samples. 53

Figure 72: Results of SQUID analysis of amorphous, icosahedral and crystalline $Ti_{40}Zr_{40}Ni_{20}$ samples. Black arrows denote cooling and heating, respectively..... 54

Figure 73: TG curves of hydrogen desorption from amorphous, icosahedral and crystalline $Ti_{45}Zr_{35}Ni_{17}Cu_3$ samples, all subjected to the same loading conditions. 54

Figure 74: Comparison of mass contents of desorbed hydrogen from five different samples, obtained by TG and by weighing before and after desorption using Carbolite furnace attached to dynamic vaccum via silica tube. 55

Figure 75: Plot of areas under mass-spectra normalized to sample mass versus mass content of desorbed hydrogen, measured by TG. In graph a) points are divided according to date of measurement, whereas in b) points are sorted due to composition (density). 56

Figure 76: Mass-spectra of desorbed hydrogen are strongly dependent just on the structure of samples, and only slightly dependent on the composition or hydrogen content; a) $Ti_{40}Zr_{40}Ni_{20}$ and b) $Ti_{45}Zr_{35}Ni_{17}Cu_3$. 56

Figure 77: Mass-spectra of desorbed hydrogen from $Ti_{53}Zr_{27}Ni_{20}$ i-phase samples, containing different amount of hydrogen, i.e. hydrided for various extent of time. 57

Figure 78: Mass-spectra of desorbed hydrogen from i-phase samples with different compositions and highest content of hydrogen. 57
Figure 79: H_2 mass-spectra of a) $Ti_{53}Zr_{27-x}Ni_{20}Cu_x$ and b) $Ti_{58}Zr_{24-x}Ni_{18}Cu_x$ samples loaded with comparable amount of hydrogen. 58
Figure 80: XRD spectra of amorphous $Ti_{40}Zr_{40}Ni_{20}$ and $Ti_{45}Zr_{35}Ni_{17}Cu_3$ powders, hydrided for 1000 min at 300°C and 45 bar. 59
Figure 81: FFT of amorphous XRD spectra. The shift of amorphous halo indicates the interatomic distances increased upon interstitial protons, and it is proportional with the content of hydrogen obtained by TG. 59
Figure 82: Mass-spectra of desorbed hydrogen from amorphous $Ti_{40}Zr_{40}Ni_{20}$ and $Ti_{45}Zr_{35}Ni_{17}Cu_3$ samples, both loaded at 300°C and 45 bar for 1000 min. 60
Figure 83: Mass-spectra of hydrogen desorption from $Ti_{45}Zr_{35}Ni_{17}Cu_3$ amorphous samples, loaded for 500 and 1000 min. The same amount of hydrogen was desorbed from both samples. 61
Figure 84: Lattice expansion of hexagonal C14 Laves phase and cubic (Zr, Ti) solid solutions due to interstitially bonded protons. 61
Figure 85: Mass-spectra of desorbed hydrogen from crystalline a) $Ti_{40}Zr_{40}Ni_{20}$ and b) $Ti_{45}Zr_{35}Ni_{17}Cu_3$ samples, loaded for 500 and 1000 min. 62
Figure 86: XRD spectra of as-prepared, loaded and unloaded $Ti_{53}Zr_{27}Ni_{20}$ i-phase implies that this material can be already fully unloaded at low desorption temperature (see Figure 77). No stable hydrides have been formed. 62
Figure 87: VSM data of $Ti_{53}Zr_{27}Ni_{20}$ i-phase ribbons; as-prepared, loaded with two different H_2 contents, and finally desorbed at 500°C. Even though almost all hydrogen was desorbed, by VSM measurements we can see irreversible magnetic response (red curve). 63
Figure 88: Mass-spectra of desorbed hydrogen from fully loaded $Ti_{58}Zr_{24}Ni_{18}$ i-phase (1.81 wt. %) and the same sample, after hydrogen was desorbed at the first and most intense desorption peak (510 °C). 63
Figure 89: XRD spectra of ribbons hydrogenated at normal hydrogen pressure, subjected to various thermal activation regimes. HT denotes heat-treatment. 64
Figure 90: Mass-spectra of desorbed hydrogen from icosahedral samples, hydrided at normal hydrogen pressure, at different heating regimes. 64
Figure 91: Hydrogen desorption temperature distribution is practically independent of the way the sample was loaded, i.e. high (45 bar) or low (1 bar) pressure loading. 65
Figure 92: XRD spectra of as-spun and loaded $Ti_{45}Zr_{35}Ni_{17}Cu_3$ i-phase ribbons. 65
Figure 93: XRD spectra of $Ti_{58}Zr_{19}Ni_{18}Cu_5$ melt-spun material indicates mixture of icosahedral and Laves phase in as-spun and vacuum annealed samples. Clearly, hydrogen induces Laves phase-to-icosahedral phase transformation. 66
Figure 94: a) Comparison of H_2 mass-spectra from sample mechanically alloyed in hydrogen for 40 hours by 5-times refilling of hydrogen, and amorphous sample with the same composition, loaded with hydrogen from gas phase at 300°C, 1000 min and 45 bar; b) corresponding XRD spectra. 66
Figure 95: a) VSM curves of as-spun, annealed and hydrided $Ti_{45}Zr_{35}Ni_{17}Cu_3$ i-phase samples. Approximately 30 % increase of magnetization at 10 kOe has been observed for hydrided sample, containing 1.56 wt. % H; b) corresponding XRD spectra reveal the formation of crystalline phases upon annealing of the i-phase ribbons, which disappear after hydrogenation. 67
Figure 96: VSM curves of as-spun (22 m/s) $Ti_{53}Zr_{27}Ni_{20}$ i-phase and hydrided at 1 bar of hydrogen by multi-step thermal activation, containing 1.53 wt. % H. 68
Figure 97: VSM and XRD data of $Ti_{53}Zr_{27-x}Ni_{20}Cu_x$ (x= 0, 3, 5) predominantly icosahedral alloys; a) and c) as-spun at 22 m/s, b) and d) hydrided at 300 °C for 16 hours, all containing comparable amounts of hydrogen. 68
Figure 98: VSM and XRD data of $Ti_{58}Zr_{24-x}Ni_{18}Cu_x$ (x= 0, 3, 5) predominantly icosahedral alloys; a) and c) as-spun at 22 m/s, b) and d) hydrided at 300 °C for 16 hours, all containing comparable amounts of hydrogen. 69
Figure 99: VSM study of hydrided and as-prepared amorphous a) $Ti_{40}Zr_{40}Ni_{20}$ and b) $Ti_{45}Zr_{35}Ni_{17}Cu_3$ samples, obtained by mechanical alloying of melt-spun ribbons. 69

Figure 100: VSM data of as-annealed and hydrided crystalline a) $Ti_{40}Zr_{40}Ni_{20,}$ b) $Ti_{45}Zr_{35}Ni_{17}Cu_3$ and c) $Ti_{53}Zr_{27}Ni_{20}$ samples. 70
Figure 101: XRD spectra of a) amorphous and b) icosahedral $Ti_{40}Zr_{40}Ni_{20}$ samples in unloaded state and after deuterium loading..... 71
Figure 102: The temperature-dependent deuterium NMR spectra of a) icosahedral and b) amorphous sample. For amorphous sample, the Gaussian fit of the static spectrum at T = 80 K is shown in c), whereas a Lorenzian fit of the motionally narrowed spectrum at T = 400 K is shown in d). 72
Figure 103: The temperature-dependent full width at half-maximum $\Delta\nu_{1/2}$ of the ^2H NMR spectra of the icosahedral (ICO) and amorphous (A) samples. 72
Figure 104: Mass-spectra of desorbed hydrogen from 3 mm quenched rods with different compositions, all loaded under same conditions, i.e. 300°C and 45 bar for 1000 minutes. 73
Figure 105: XRD spectra of as-cast and hydrided (300°C, 1000 min) 3 mm rods of four different compositions; a) $Ti_{33}Zr_{41}Ni_{21}Cu_5$, b) $Ti_{40}Zr_{40}Ni_{20}$, c) $Ti_{45}Zr_{35}Ni_{17}Cu_3$ and d) $Ti_{53}Zr_{27}Ni_{20}$. 74
Figure 106: XRD spectra of a) 1.5 mm, b) 2 mm and c) 3 mm vacuum-cast rods of various compositions, all predominantly containing icosahedral phase and minority of hexagonal C14 Laves and FCC β-(Ti, Zr) solid solution. 75
Figure 107: XRD spectra of quenched rods with five different compositions: a) $Ti_{33}Zr_{41}Ni_{21}Cu_5$, b) $Ti_{40}Zr_{40}Ni_{20}$, c) $Ti_{45}Zr_{35}Ni_{17}Cu_3$, d) $Ti_{53}Zr_{27}Ni_{20}$, e) $Ti_{58}Zr_{24}Ni_{18}$. Rods with three different diameters (3, 2 and 1.5 mm) were quenched for each composition. 76
Figure 108: XRD spectra of as-spun (22 m/s) and as-cast (2 mm rod) $Ti_{33}Zr_{41}Ni_{21}Cu_5$ alloy. 77
Figure 109: SEM images of fractures and features in $Ti_{40}Zr_{40}Ni_{20}$ 3 mm quenched rod, after being gently crushed in the mortar. 78
Figure 110: SEM Z-contrast images of 3 mm quenched rods taken from polished cross-section surfaces; a) $Ti_{33}Zr_{41}Ni_{21}Cu_5$, b) $Ti_{40}Zr_{40}Ni_{20}$, c) $Ti_{45}Zr_{35}Ni_{17}Cu_3$, and d) $Ti_{53}Zr_{27}Ni_{20}$. 78
Figure 111: SEM (SE) image of fractured surface of 3 mm $Ti_{40}Zr_{40}Ni_{20}$ quenched rod is showing ductile nature of dendritic secondary phase, whereas i-phase matrix is brittle. 80
Figure 112: VSM data of as-cast and hydrided a) $Ti_{40}Zr_{40}Ni_{20}$, b) $Ti_{53}Zr_{27}Ni_{20}$, c) $Ti_{33}Zr_{41}Ni_{21}Cu_5$ and d) $Ti_{45}Zr_{35}Ni_{17}Cu_3$ 3 mm rods. 81
Figure 113: XRD spectra of cross-section surface of arc-melted $Ti_{40}Zr_{40}Ni_{20}$ button and annealed, crystalline powder with the same chemical composition. 81
Figure 114: XRD spectra of $Ti_{40}Zr_{40}Ni_{20}$ and $Ti_{45}Zr_{35}Ni_{17}Cu_3$ arc-melted buttons. Spectra were taken on flat and polished cross-section surface. 82
Figure 115: XRD patterns of polished cross-sections of 1 and 5 gram $Ti_{45}Zr_{35}Ni_{17}Cu_3$ arc-melted buttons. 82
Figure 116: BEI of cross-section of 5 gram arc-melted $Ti_{45}Zr_{35}Ni_{17}Cu_3$ button. 83
Figure 117: VSM measurements on $Ti_{40}Zr_{40}Ni_{20}$ and $Ti_{45}Zr_{35}Ni_{17}Cu_3$ arc-melted buttons. 83
Figure 118: Density plot (g/cm³) versus titanium concentration (at. %) in Ti-Zr-Ni-(Cu) 5 g arc-melted buttons. 84

Index of Tables

Table 1: Crystallographic data of the reported Ti/Zr-rich phases in the Ti-Zr-Ni alloy system, (Qiang et al., 2004). 6
Table 2: Table of dimensionless parameters for 6-index notation of the four most intense i-phase XRD peaks. 12
Table 3: Indexation of $Ti_{45}Zr_{35}Ni_{17}Cu_3$ i-phase XRD spectrum for quasi-lattice cell parameter a_q determination. 12
Table 4: Preparation conditions for the $Ti_{40}Zr_{40}Ni_{20}$ and $Ti_{40}Hf_{40}Ni_{20}$ quasicrystals by mechanical alloying with subsequent annealing. 19
Table 5: Quantitative analysis of energy-dispersive spectrum (EDS) of three random ~ μm² areas on $Ti_{45}Zr_{38}Ni_{17}$ polished aglomerate. 33
Table 6: EDS data on free- and wheel-side of the melt-spun $Ti_{58}Zr_{24}Ni_{18}$ ribbon, predominantly containing i-phase. 45
Table 7: Desorption temperatures of highly bonded protons from two different compositions with 0, 3 and 5 atomic % of copper addition. 59
Table 8: EDS quantification data of phases shown in Figure 110; a) $Ti_{33}Zr_{41}Ni_{21}Cu_5$, b) $Ti_{40}Zr_{40}Ni_{20}$, c) $Ti_{45}Zr_{35}Ni_{17}Cu_3$, and d) $Ti_{53}Zr_{27}Ni_{20}$, respectively. 79
Table 9: EDS analysis data of phases in 5 gram arc-melted $Ti_{45}Zr_{35}Ni_{17}Cu_3$ button. 83
Table 10: Densities of arc-melted buttons with increasing content of titanium. Units are g/cm³. 84

Bibliography

Articles

KOCJAN, A., McGUINESS, P.J., RAJIĆ LINARIĆ, M., and KOBE, S.. Amorphous-to-quasicrystalline transformations in the Ti-Zr-Ni and Ti-Hf-Ni systems. *Journal of Alloys and Compounds*, 2008, vol. 457, p. 144-149.

ŠKULJ, I., KOCJAN, A., McGUINESS, P.J., and ŠUŠTARŠIČ, B.. Hydrogen absorption by Ti-Zr-Ni-based alloys (Absorpcija vodika v zlitinah Ti-Zr-Ni). *Mater. tehnol.*, 2007, vol. 41, št. 6, str. 279-282.

GRADIŠEK, A., KOCJAN, A., McGUINESS, P.J., APIH, T., KIM, H.J., and DOLINŠEK, J.. Deuterium dynamics in the icosahedral and amorphous phases of the $Ti_{40}Zr_{40}Ni_{20}$ hydrogen-absorbing alloy studied by ^{2}H NMR, *Journal of Physics: Condensed Matter*, vol. 20, 2008, pp. 1–7.

Conferences

KOCJAN, A., McGUINESS, P.J., REČNIK, A., and KOBE, S.. Direct production of the Ti-Zr-Ni-Cu icosahedral phase for hydrogen-storage applications by rapid quenching from the melt. In *Proceedings of 2007 MRS Fall Meeting*, Materials Research Society, Boston, MA, 2008, vol. 1042, 7 str.

DRAŽIĆ, G., KOCJAN, A., McGUINESS, P.J., SARANTOPOULOU, E., KOLLIA, Z., CEFALAS, A.C., and KOBE, S.. Analytical electron microscopy of Ti-Zr-Ni based quasi-crystals prepared by melt-spinning and pulsed laser deposition. In *Proceedings of ACMM-20 & IUMAS-IV, 20th Australian Conference on Microscopy and Microanalysis and 4th Congress of the International Union of Microbeam Analysis Societis*, Australian Microscopy and Microanalysis Society, Perth, Western Australia, 2008, str. 421-422.

RAJIĆ, M., McGUINESS, P.J., KOCJAN, A., TOMAŠIĆ, N., and KOBE, S.. The crystallization of quasicrystals in Ti-based systems. V *13. konferenca o materialih in tehnologijah (program in knjiga povzetkov)*, Inštitut za kovinske materiale in tehnologije, Portorož, Slovenija, 2005, str. 119.

KOCJAN, A., McGUINESS, P.J., and KOBE, S. Preparation and characterization of $Ti_{45}Zr_{38}Ni_{17}$ and $Ti_{40}Hf_{40}Ni_{20}$ quasicrystals. In *Programme and book of abstracts of 4th Symposium of science and technology of nanomaterials in Slovenia, SLONANO 2005*, Jozef Stefan Institute & National Institute of Chemistry, Ljubljana, Slovenia, 2005, str. 24-25.

KOCJAN, A., McGUINESS, P.J., KOBE, S., and RAJIĆ LINARIĆ, M.. Kvazikristali za shranjevanje vodika Ti-Zr(Hf)-Ni (Ti-Zr(Hf)-Ni quasicrystals for hydrogen storage). V *14. konferenca o materialih in tehnologijah (program in knjiga povzetkov)*, Inštitut za kovinske materiale in tehnologije, Portorož, Slovenija, 2006, str. 51.

KOCJAN, A., McGUINESS, P.J., REČNIK, A., and KOBE, S.. Direct production of the Ni-Ti-Zr icosahedral phase for hydrogen-storage applications by rapid quenching from the melt. In *Program and exhibit guide of MRS 2007 Fall meeting*, Materials Research Society, Boston, MA, 2007, str. 445.

KOCJAN, A., McGUINESS, P.J., REČNIK, A., and KOBE, S.. Priprava ikozaedrične faze Ni-Ti-Zr za shranjevanje vodika z ultra-hitrim kaljenjem (Direct production of the Ni-Ti-Zr icosahedral phase for hydrogen-storage applications by rapid quenching from the melt). V *15. konferenca o materialih in tehnologijah (program in knjiga povzetkov)*, Inštitut za kovinske materiale in tehnologije, Portorož, Slovenija, 2007, str. 37-38.

KOCJAN, A., McGUINESS, P.J., REČNIK, A., and KOBE, S.. Study of Ti-Zr-Ni-(Cu) alloys and hydride forming ability. In *Abstract book of Hot nano topics 2008 : incorporating SLONANO 2008, 3 overlapping workshops on current hot subjects in nanoscience*, Portorož, Slovenia, 2008, str. 248.

KOCJAN, A.. Melt-spinning and hydrogen storage in Ti-Zr-Ni quasicrystals. In *Abstract book of WomenInNano Winter School*, Kranjska Gora, Slovenia, 2008, str. 71.